DOE-ER-0313/70
ORNL/SPR-2021/2151
Distribution
Categories
UC-423, -424

FUSION MATERIALS
SEMIANNUAL PROGRESS REPORT
FOR THE PERIOD ENDING

June 30, 2021

Prepared for
DOE Office of Fusion Energy Sciences
(AT 60 20 10 0)

DATE PUBLISHED: August 2021

Prepared by
OAK RIDGE NATIONAL LABORATORY
Oak Ridge, Tennessee 37831
Managed by
UT-Battelle, LLC
For the
U.S. DEPARTMENT OF ENERGY

FOREWORD

This is the seventieth in a series of semiannual technical progress reports on fusion materials science activity supported by the Fusion Energy Sciences Program of the U.S. Department of Energy. It covers the period ending June 30, 2021. This report focuses on research addressing the effects on materials properties and performance of exposure to the neutronic, thermal and chemical environments anticipated in the chambers of fusion experiments and energy systems. This research is a major element of the national effort to establish the materials knowledge base for an economically and environmentally attractive fusion energy source. Research activities on issues related to the interaction of materials with plasmas are reported separately.

The results reported are the products of a national effort involving a number of national laboratories and universities. A large fraction of this work, particularly in relation to fission reactor irradiations, is carried out collaboratively with partners in Japan, Russia, and the European Union. The purpose of this series of reports is to provide a working technical record for the use of program participants, and to provide a means of communicating the efforts of fusion materials scientists to the broader fusion community, both nationally and worldwide.

This report has been compiled by Stephanie Melton, Oak Ridge National Laboratory. Her efforts, and the efforts of the many persons who made technical contributions, are gratefully acknowledged.

Daniel Clark
Research Division
Office of Fusion Energy Sciences

TABLE OF CONTENTS

TABLE OF CONTENTS

TABLE OF CONTENTS

TABLE OF CONTENTS

TABLE OF CONTENTS

1. FERRITIC/MARTENSITIC STEEL DEVELOPMENT

1.1 ADVANCE CASTABLE NANOSTRUCTURED ALLOYS FOR FIRST-WALL/BLANKET APPLICATIONS—L. Tan, W. Tang, Y. Yang, Y. Katoh (Oak Ridge National Laboratory), K.G. Field (University of Michigan)

OBJECTIVE

To establish a US-RAFM (reduced-activation ferritic-martensitic) steel based on the carbide-castable nanostructured alloys (CNAs) to demonstrate the viability and advantage of CNAs through the production and performance evaluation of industry-scale heats for use in integrated first-wall and blanket systems.

SUMMARY

The project, sponsored by ARPA-E and FES, was initiated recently with an executive period of 3/2021-3/2024. The order of industry-scale CNA heats was placed and is being produced in the US. Meanwhile, welding wires for CNA are being ordered.

PROGRESS AND STATUS

Introduction

The current reference RAFM steels (e.g., Eurofer97 and F82H) have a small applicable temperature window (~350-550°C) and have been scaled up to industry-scale heats. CNAs were recently developed in laboratory scale at Oak Ridge National Laboratory. Seven-aspect property comparison among carbide-CNAs, carbonitride-CNAs, Eurofer97/F82H, and 14YWT oxide-dispersion-strengthened alloy indicated the best-balanced properties of carbide-CNAs.

Experimental Procedure

As shown in Figure 1, with procuring industry-scale carbide-CNA heats as the core of this project, multiple tasks will be pursued to accomplish the objective, which include assessing weldability, mechanical properties, ion and neutron radiation resistance, coolant compatibility, and microstructures, as well as simulations to provide physics-based support for the experimental designs and observations.

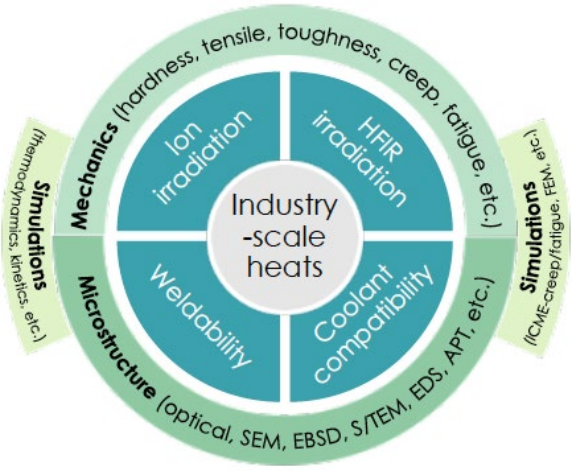

Figure 1. Synergy of the major tasks to accomplish the objective of this project.

Results

A purchase order for two 3-ton ingots, to be converted into 0.75” and 1” thick plates, was placed. In the meantime, a purchase order for a 0.5-ton ingot, to be converted into 1”-diameter rods and 0.045’-diamter welding wires, is being placed.

1.2 REFINING CARBON CONTENT IN CARBIDE-VERSION CASTABLE NANOSTRUCTURED ALLOYS: MICROSTRUCTURES, MECHANICAL PROPERTIES, AND ION IRRADIATION RESPONSES—L. Tan, Y. Yang, W. Zhong, T. Graening (Oak Ridge National Laboratory), P. Patki, K.G. Field (University of Michigan)

OBJECTIVE

The preliminary systematic performance comparison showed the advantages of carbide-CNAs (Castable Nanostructured Alloys) over carbonitride-CNAs. To further improve carbide-CNAs, one direction is to refine the alloying composition. Carbon is a critical element in the alloy to stabilize the austenite phase over a larger temperature range and to determine the number of carbides to be formed. This work is to understand the effects of carbon content on the microstructures, mechanical properties, and ion irradiation responses of carbide-CNAs.

SUMMARY

Two new heats of CNAs, called CNA8 and CNA9, were fabricated, with CNA9 having about one order of magnitude lower $M_{23}C_6$ amount but comparable MC amount with CNA8. Microstructural characterization indicated comparable grain structures with MC in two levels of sizes in the two steels, with noticeable $M_{23}C_6$ in CNA8 but undetected $M_{23}C_6$ in CNA9. Mechanical testing is in progress. Ion irradiation has completed two doses and ready for post-irradiation examinations.

PROGRESS AND STATUS

Introduction

Because of the high coarsening rate of Cr-rich $M_{23}C_6$, minimizing the $M_{32}C_6$ amount while maintaining a high density of MC (M=Ti/Ta/W/etc.) is hypothesized to provide better mechanical properties to ferritic-martensitic steels, including CNAs. Therefore, two steels were designed with different carbon content using computational thermodynamics to promote maximized amount of MC but significantly different amounts of $M_{23}C_6$. Two new heats were fabricated because the previous two heats showed noticeably different grain structures. Figure 1 shows the calculated temperature-dependent phase mole fractions using the measured chemistry with the solid and dashed lines denoting the phases in CNA8 and CNA9, respectively. Other than comparable MC amount, the $M_{23}C_6$ amount is about one order of magnitude reduced in CNA9. The reduced carbon also decreased the austenite temperature range in CNA9 and thus altered its normalization temperature as described next.

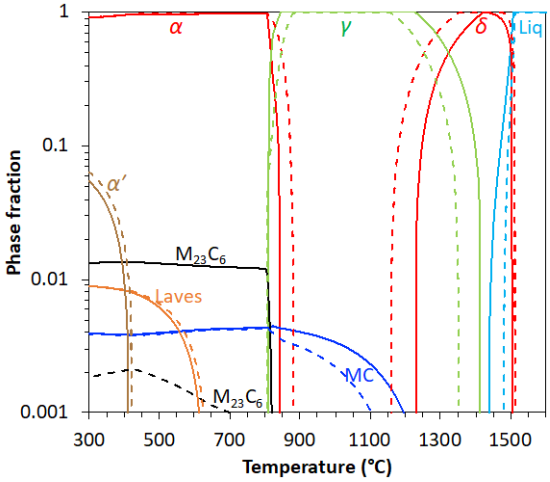

Figure 1. Calculated temperature-dependent phase mole fraction in alloys CNA8 and CNA9.

Experimental Procedure

Two new laboratory-scale (~1 lb.) steels of CNA8 and CNA9 were vacuum arc melted into large buttons and then drop cast into 25.4 × 25.4 × ~152 mm. The steels were hot rolled into 6.3-mm thick plates and finally normalized at 1100°C and 1050°C, respectively, for 15 min and tempered at 750°C for 30 min with air cooling. Tensile (type SS-3 specimens) and Charpy V-notch impact (half-size specimens in the T-L orientation) specimens were machined from the two steels for tensile, creep, and Charpy impact tests. Small coupons were machined from the two steels for ion irradiation study. Electron backscatter diffraction (EBSD) and transmission electron microscopy (TEM) with energy dispersive spectroscopy (EDS) were used to characterize the grain structures and precipitates, respectively.

Results

Figure 2 shows the EBSD inverse-pole figure (IPF) taken from CNA8 and CNA9, showing fine structures in a lath form. It indicates comparable grain sizes without preferred grain orientations.

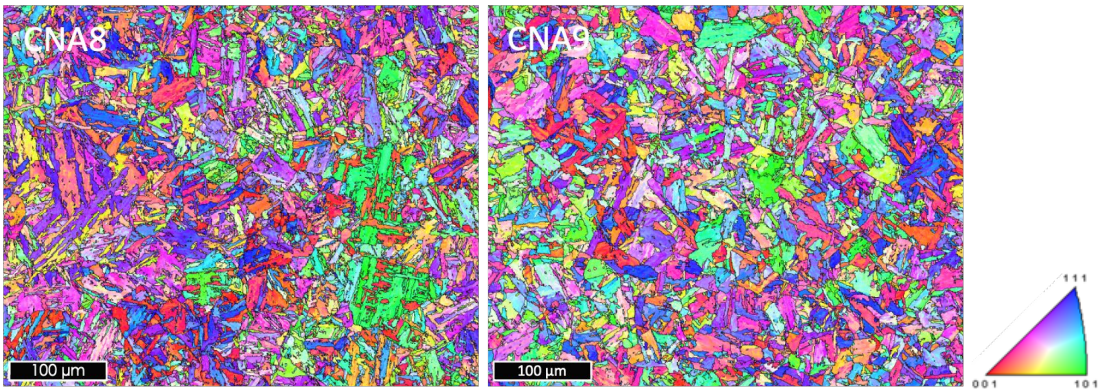

Figure 2. EBSD IPF of CNA8 and CNA9 indicating the grain structures and orientations.

Figure 3 shows the EDS maps of Cr and Ti, indicating that CNA8 contains both MC and $M_{23}C_6$ while CNA9 only shows MC because the small $M_{23}C_6$ amount in CNA9 is difficult to be detected under TEM, which is consistent with the alloy design. MC precipitates have coarse and fine sizes. MC in CNA8 is not as uniform as that in CNA9, which is comparable to the fine MC in the CNA9 Ti-map Figure 3 (right) in some regions but much less fine MC in other regions.

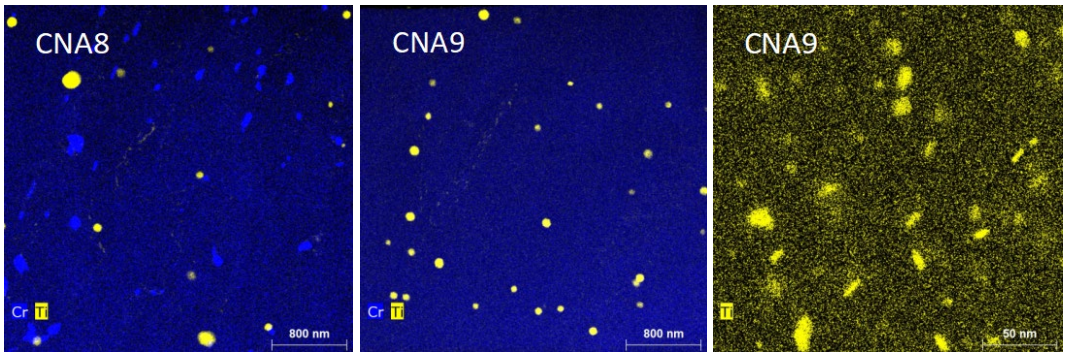

Figure 3. EDS maps of Cr and Ti from CNA8 and CNA9 indicating the distribution Cr-rich and Ti-rich precipitates.

Tensile tests and Charpy impact toughness testing have been completed. Creep testing is in progress. Ion irradiation with either single beam of Fe^{3+} ions or dual-beam of He^{2+} and Fe^{3+} ions have completed 100 and 50 displacements per atom (dpa) without or with 10 appm He/dpa at 500°C at University of Michigan. Post-irradiation microstructural characterization and nanoindentation testing will be pursued.

1.3 MICROSTRUCTURE CHARACTERIZATION OF F82H-IEA AFTER LOW DOSE HFIR NEUTRON IRRADIATIONS AT 300 °C—A. Bhattacharya, S.M. Levine, J. Poplawsky, P.D. Edmondson, J.W. Geringer, Y. Katoh (Oak Ridge National Laboratory), T. Nozawa, H. Tanigawa (National Institutes for QST)

OBJECTIVE

F82H-IEA steel was irradiated in HFIR to ITER-TBM relevant conditions of 3.5 dpa, at target 300 °C in RB15J campaign. Previously, Vickers microhardness indentation tests were performed on these samples which revealed irradiation-induced hardening. Here, microstructure characterization using STEM and APT were performed to identify the nano-scale evolution of the material that contributes to hardening-embrittlement.

SUMMARY

STEM characterization revealed irradiation-induced dislocation loops in the microstructure with diameters ranging between ~8-20 nm. The loops were homogeneously distributed inside the martensitic laths. The **g.b** analysis revealed both a<100> and a/2<111> type dislocation loops in the microstructure, which is surprising because ion irradiations typically report only a/2<111> loops in Fe-Cr based alloys for $T_{irr} \leq$ 350 °C. This suggests different temperature dependent Burgers vector of loops in RAFM/FeCr alloys after neutron and ion irradiations that requires careful overarching analysis. APT experiments were also performed on the same materials, which revealed extensive co-clustering of Mn-Si in the steel. The Mn-Si clusters were both homogeneously distributed and heterogeneously nucleated on different defects such as dislocation loops and dislocation lines. The extensive irradiation-induced nanoclustering of minor alloying elements is expected to deleteriously contribute to low temperature hardening embrittlement (LTHE) in RAFM steels.

PROGRESS AND STATUS

<u>STEM analysis on F82H-IEA steels</u>

- Campaign: RB15J
- Conditions: 3.5 dpa, 300 °C
- Sample ID: OX1 and OX2
- Two FIB samples characterized

Diffraction contrast and analytical STEM characterization of F82H-IEA irradiated to 3.5 dpa/300 °C was performed using FEI F200X Talos STEM at the LAMDA lab. Figure 1 presents a high throughput energy dispersive X ray spectroscopy (EDX) map of the irradiated foils. Cr/W/V rich carbides were seen, expected to be the $M_{23}C_6$ carbide phase. No evidence of pure Ta/V rich MX phase was detectable. Chemical distributions across PAGB and lath boundaries was also studied. Figure 2 shows a grain boundary (GB) triple point in the sample where it is evident that Cr/Si segregated to GBs, while W and V depleted. Characterization of control samples is necessary to quantify any radiation driven GB microchemistry changes. STEM-EDX in Figure 2 also indicates some unexpected Ni presence on the grain boundaries. Because RAFM steels do not typically contain much Ni, this result is surprising. More advanced analysis, using modern statistical data analysis tools is ongoing to better understand if Ni distribution is real or if it is an unknown artifact.

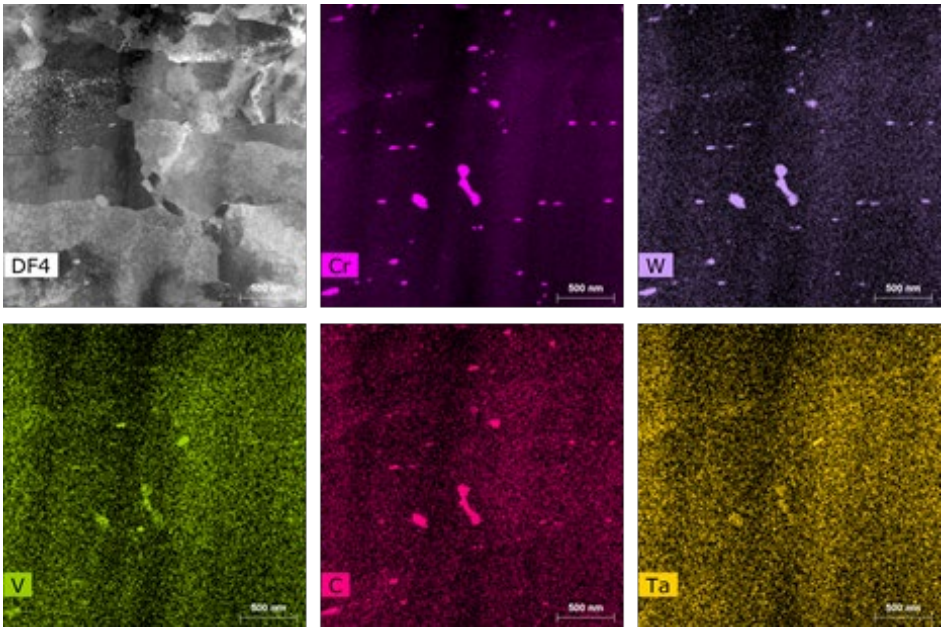

Figure 1. STEM-EDX overview of irradiated F82H-IEA heat, 3.5 dpa, 300 °C. Cr rich $M_{23}C_6$ carbide phases are visible. No clear evidence of MX particles was detectable.

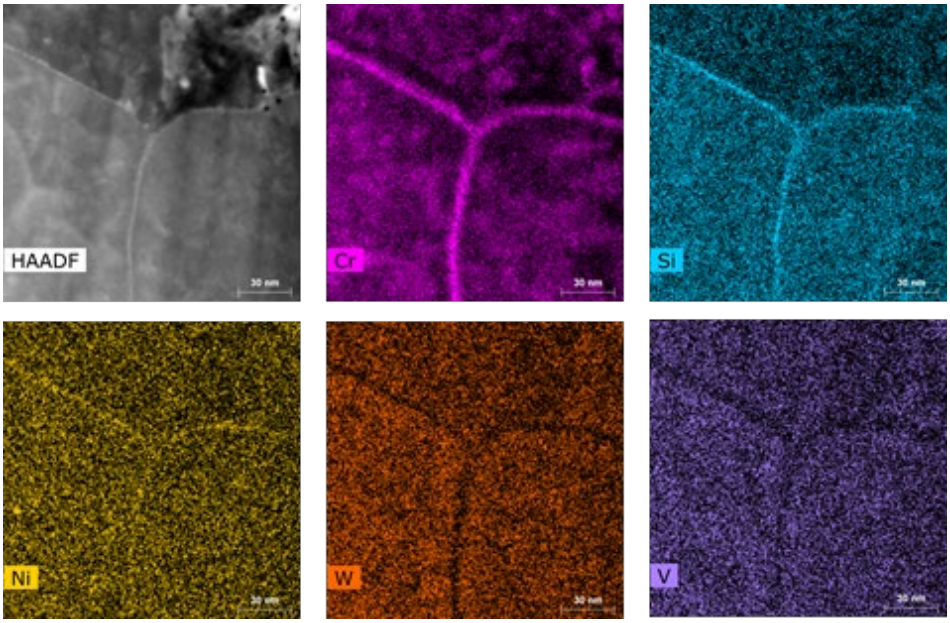

Figure 2. STEM-EDX mapping of a GB triple point in irradiated F82H-IEA heat, 3.5 dpa, 300 °C, showing elemental segregation of Cr/Si/Ni and W/V depletion.

In addition to elemental characterization, TEM/STEM was used to detect and quantify the irradiation-induced extended defects. After irradiation, dislocation loops formed in the material. Figure 3 presents different areas of the foil imaged in STEM mode where the dislocation loop microstructure overview is visible. Most dislocation loops were between ~8-20 nm in diameter.

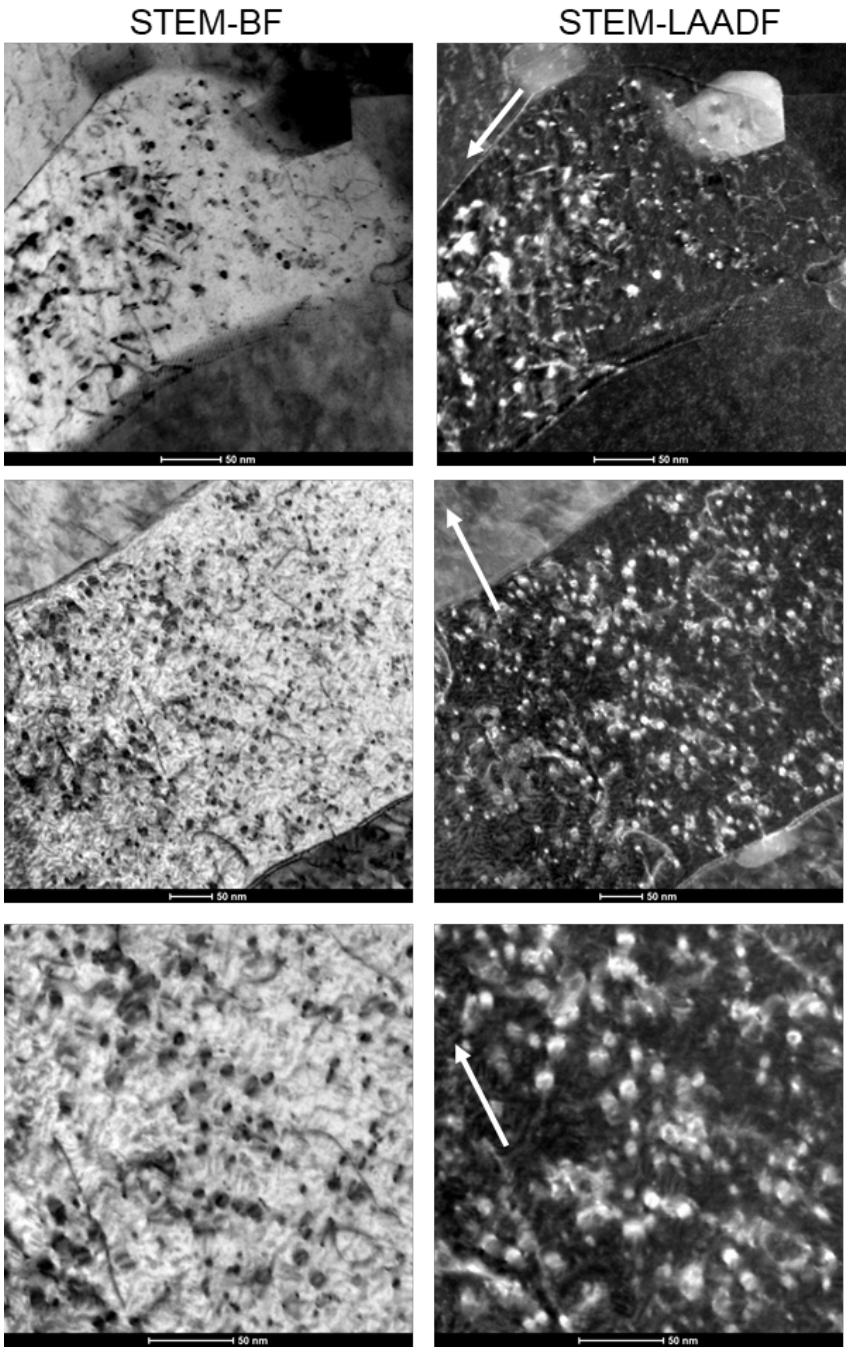

Figure 3. Bright field (BF) and low angular annular dark field (LAADF) STEM images of dislocation loops in HFIR irradiated F82H-IEA heat, 3.5 dpa, 300 °C. Imaging performed with <110> type g vector indicated by the white arrows, close to [001[zone axis, deviation parameter s>0.

Using **g.b** analysis, Burgers vector of the dislocation loops was identified. An example of this is shown in Figure 4, where the same nanograin was tilted along different g vectors to identify the visibility-invisibility patterns of the loops. The study revealed both a<100> and a/2<111> type dislocation loops in the sample. In Figure 4, blue arrows point to a<100> type loops while the red arrows point to a/2<111> type loops. The concentration of both the loop families was nearly equal in proportions.

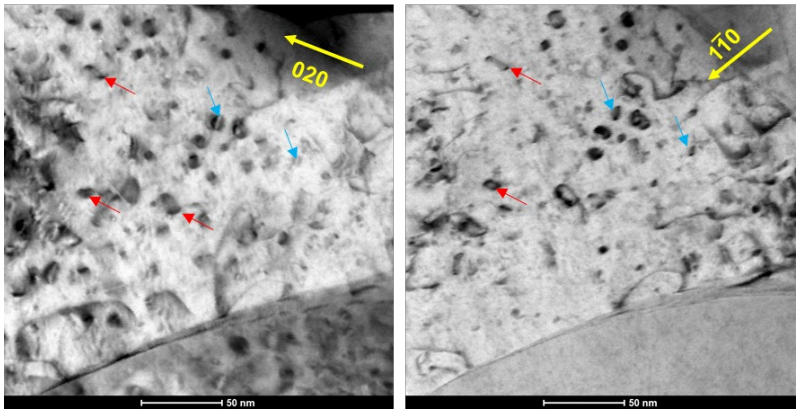

Figure 4. STEM-BF images showing a<100> loops (blue arrows) and a/2<111> type loops (red arrows), in HFIR irradiated F82H-IEA heat, 3.5 dpa, 300 °C. Same area was tilted and analyzed using different g vectors. In this example, zone axis = [001], deviation parameter s>0. The direction of the g vectors is annotated.

APT analysis on F82H-IEA steels

- Campaign: RB15J
- Conditions: 3.5 dpa, 300 °C
- Sample ID: OX1

After STEM characterization, APT studies were also performed to understand irradiation-induced microchemistry reorganization in F82H. The experiments were performed in voltage mode at 40 K, using CAMECA LEAP 4000X HR APT at the CNMS facility of ORNL. The needle samples required for the study were prepared using LAMDA FIB machines. Figure 5a presents APT atom maps from a needle where radiation induced clustering of Mn and Si is evident. Figure 5b presents an iso-concentration plot where Mn and Si clustered regions can be identified, including a dislocation loop. Clustering on a dislocation loops is further evidenced in Figure 6 where local atom maps and 2D contour plots of an identified loop are presented. It is evident that MnSiP seems to cluster at the dislocation cores, while there seems to be presence of Cr inside the loop (i.e., on the habit plane). More data analysis is ongoing to thoroughly quantify the radiation induced nanoclustering phenomenon in this steel, including testing control samples.

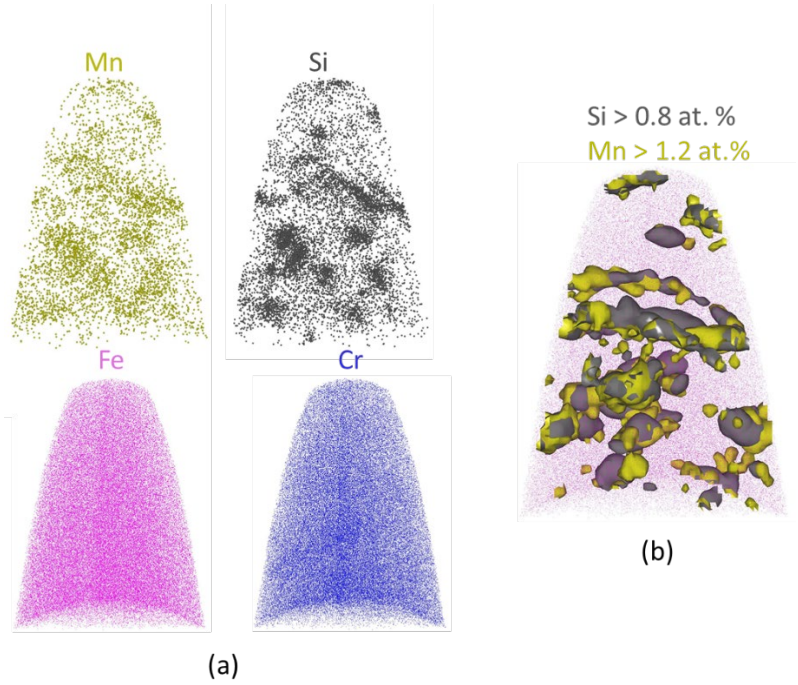

Figure 5. The APT of HFIR irradiated F82H-IEA heat, 3.5 dpa, 300 °C. (a) Atom maps. (b) Iso concentration surface contour plots showing MnSi segregation/clustering in the material, including RIS to dislocation loops. More data analysis is ongoing with an improved open-source APT software, OSCAR (S. Levine, A. Bhattacharya, C. Pareige, S.J. Zinkle et al. ORNL Fusion Semi Annual 2021).

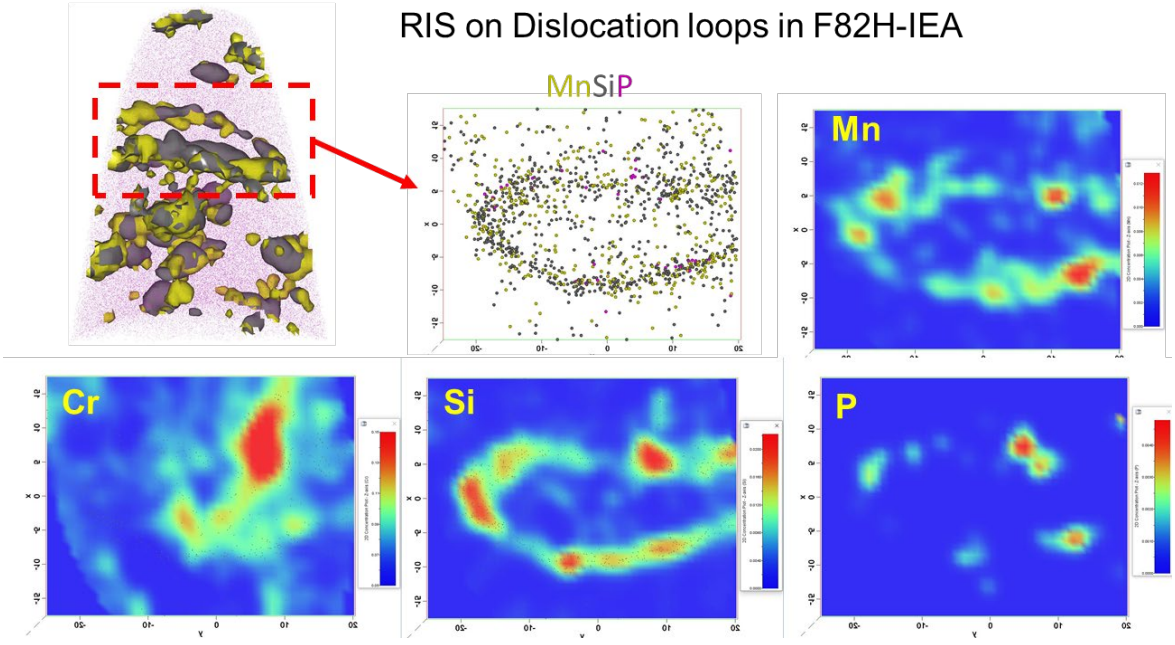

Figure 6. The APT study of RIS on dislocation loops in HFIR irradiated F82H-IEA heat, 3.5 dpa, 300 °C. The figure shows 2D contour plots of elemental segregation on a dislocation loop.

Future Plans

More data analysis of the APT reconstructed needles to quantify the segregated regions. Analysis of microstructure data using dispersed barrier hardening model to quantify the mechanical properties.

References

[1] E. Gaganidze and J. Aktaa. Assessment of neutron irradiation effects on RAFM steels. Fus. Eng. Des (88) 2013 (118-128).
[2] Y. Dai, G. Odette, Y. Yamamoto, The effects of helium in irradiated structural alloys, Comprehensive Nuclear Materials (2012), vol. 1, pp. 141-193
[3] S.J. Zinkle et al. Development of next generation tempered and ODS reduced activation ferritic/martensitic steels for fusion energy applications. Nucl. Fusion (57) 2017 092005

1.4 HFIR IRRADIATION-INDUCED MECHANICAL PROPERTY CHANGES IN A ^{54}Fe-DOPED F82H STEEL—A. Bhattacharya, J. Reed, J.W. Geringer, Y. Katoh (Oak Ridge National Laboratory), T. Nozawa (National Institutes for QST)

OBJECTIVE

The F82H-IEA and ^{54}Fe based F82H were neutron irradiated in JP29 irradiation campaign, to understand the effect of helium (He) on low temperature hardening-embrittlement (LTHE). The neutron dose was ~66 dpa at T_{irr} = 292-302 °C. This report details a comparison of Vickers hardness and tensile properties of the steels.

SUMMARY

Vickers microhardness indentation tests were completed on ^{54}Fe-F82H and F82H-IEA irradiated in the same capsules to quantify the effect of He. In absence of an ^{54}Fe F82H archival sample to verify the starting isotopic distribution, we assume the sample to be constituted of >99% ^{54}Fe , thereby generating ~160 appm He. Indentation testing revealed no major effect on irradiation hardening between the two tested materials. Uniaxial tensile tests were performed on the ^{54}Fe-F82H sample and compared with data on F82H-IEA irradiated under same conditions. The tests revealed unexpected results. The yield stress and ultimate tensile stress of the ^{54}Fe based sample was lower than the sample without He. However, the uniform and total elongation of sample with ^{54}Fe was nearly twice lower. Unirradiated archival material is needed to better understand the irradiated properties.

PROGRESS AND STATUS

Understanding the effect of He on mechanical property degradation of RAFM and ODS steels is a critical challenge to predict the in-service performance of fusion first-wall/blanket and plasma facing structures [1]. Currently, the effect of He on LTHE degradation and on high temperature He embrittlement is not well-understood that may pose serious fusion reactor design challenge [2]. A major challenge is unavailability of a fusion prototypic neutron source (FPNS) where fusion relevant He along with high neutron doses may be achieved for testing RAFM/ODS steels. In absence of FPNS, isotopic tailoring of RAFMS steels with elements that have high (n, α) reaction cross-section in HFIR spectrum, combined with HFIR irradiations is a unique approach that allows us to access moderate-to-high He generation rates. In this context, F82H steels produced using ^{54}Fe isotope were irradiated in HFIR in the JP29 experiments. F82H-IEA and ^{54}Fe-F82H samples from JP29 campaign were hardness and tensile tested to quantify the effect of He generation due to the presence of ^{54}Fe. Nuclear transmutation of ^{54}Fe to produce He in steels in the HFIR spectra is expected by the following reaction:

$$^{54}Fe_{26} + {}^{1}n_{0} \rightarrow {}^{51}Cr_{24} + {}^{4}He_{2}$$

The samples were tested in the hot cells using Vickers microhardness indentation tests on the head/grip sections of undeformed SS-J3 flat tensile samples, with 1 kg load, 15 s dwell time in accordance with ASTM E384 Standard Test Method for Micro indentation Hardness of Materials. Table 1 summarizes the results obtained from each indentation test. Data from Table 1 is plotted in Figure 1 where no major effect of ^{54}Fe addition, thereby the effect of He, was noticeable on the irradiated hardness values. However, as compared to unirradiated F82H-IEA, it is evident that both irradiated materials hardened profusely.

Table 1. Vickers microhardness tests – comparing ^{54}Fe-F82H with F82H-IEA

Material	Target dose (dpa)	Target T_{irr} (°C)	Sample IDS	Vickers Hardness (HV) , x9.8 MPa (value of each tested indent)					
F82H-IEA	~66	292	O64	347.3	401.4	367.1	350.4	363.8	X
				348.9	342.8	397.7	356.6	314.9	X
^{54}Fe-F82H	~66	302	S60	359	393.1	380.6	385	360.6	363.8
				358.2	374.6	369.6	350.4	386.8	X

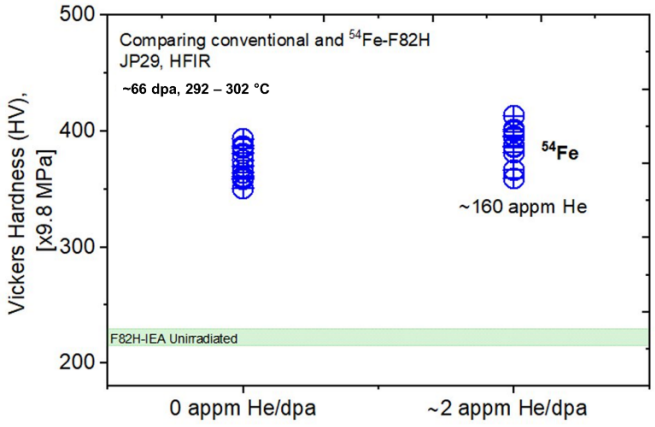

Figure 1. Scatter plot of Vickers microhardness data.

Uniaxial tensile tests were performed on the ^{54}Fe-F82H and compared with high dose F82H-IEA and unirradiated F82H-IEA results. Like results obtained by hardness tests, materials hardened significantly upon irradiation as compared to unirradiated condition. However, hardness gain in F82H-IEA was slightly higher than the ^{54}Fe specimen, which is little surprising that requires a further careful interpretation of the thermometry data from the capsule. However, the ductility of the ^{54}Fe sample was severely reduced as compared to F82H-IEA which seems to suggest potential embrittlement due to the presence of He. A summary of the tensile properties is provided in Table. 2. The tensile tests were performed on SSJx specimens in the hot-cells with guidance from ASTM E8 Standard Test Methods for Tension Testing of Metallic Materials, using a strain rate of 10^{-3} s^{-1} ($5x10^{-3}$ mm/s extension rate). The specimens were shoulder-loaded for testing using an Instron 3367 tensile machine equipped with a 5kN load cell and connected with an Instron Bluehill3 analysis software. Please note that the elastic portion of the stress-strain curves suffers from machine compliance, because the elongation was estimated using machine stroke in absence of a contact/non-contact extensometer. As a result, the slope of this region varied for different samples. However, data summarized in Table 1 was tabulated using the tangent modulus method which is not affected by compliance issues in the elastic regime.

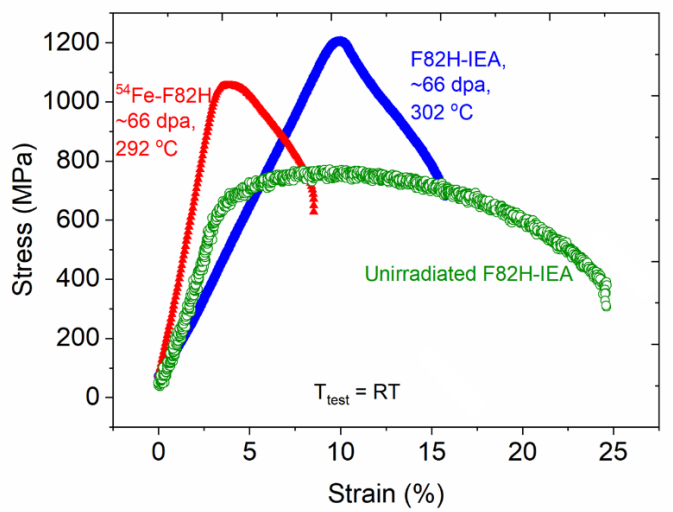

Figure 2. Engineering stress-strain curves of ^{54}Fe-F82H, F82H-IEA and unirradiated F82H-IEA, revealing irradiation induced hardening and loss of ductility.

Table 2. Summary of the unirradiated and irradiated tensile properties. σ_{YS} = yield stress, σ_{UTS} = ultimate tensile stress, UEp = uniform plastic elongation, TEp = total plastic elongation

Steels	σ_{YS} MPa	σ_{UTS} MPa	Elongation plastic	
			UE_p %	TE_p %
Unirradiated F82H-IEA	612	771	5.8	16.7
Irradiated F82H-IEA	1198	1203	0.61	10.1
Irradiated ^{54}Fe-F82H	1052	1057	0.34	6.2

Future Plans

First APT runs have already been performed on 54Fe specimen that has revealed Si clustering on dislocation loops. More APT data analysis combined with STEM characterization will be performed on the ^{54}Fe specimen to develop structure-property relationship. In addition, effort will be devoted to locating the highly precious ^{54}Fe F82H, which is needed to validate the experimental results.

References

[1] E. Gaganidze and J. Aktaa. Assessment of neutron irradiation effects on RAFM steels. Fus. Eng. Des (88) 2013 (118-128).

[2] Y. Dai, G. Odette, Y. Yamamoto, The effects of helium in irradiated structural alloys, Comprehensive Nuclear Materials (2012), vol. 1, pp. 141-193.

[3] S.J. Zinkle et al. Development of next generation tempered and ODS reduced activation ferritic/martensitic steels for fusion energy applications. Nucl. Fusion (57) 2017 092005.

1.5 ON THE EFFECTS OF IRRADIATION ENHANCED THERMAL SOFTENING ON THE CREEP PROPERTIES OF 9Cr TEMPERED MARTENSITIC STEELS—M.E. Alam, T. Yamamoto, G.R. Odette (University of California Santa Barbara, CA)

OBJECTIVE

The objective of this study is to assess the effect of higher temperature irradiation softening on the primary creep properties Grade 91 type tempered martensitic steels.

SUMMARY

Acceleration of thermal creep rates by irradiations above ≈ 450 °C could have a deleterious effect on the creep properties of Grade 91 type 9Cr tempered martensitic steels (TMS), such as Eurofer97. Here we model the effects of softening on the creep rate and strain-time curves. The softening, and its effect on creep, is approximately athermal between 450 and 550 °C. The effects of softening are mainly manifested at higher primary strains and failure metrics like the dpa onset of tertiary creep. A rough rule of thumb is that at above ≈ 450 °C, a nominal dpa rate of 10^{-6}/s, the creep failure times are reduced by an average factor of ≈ 2.5 under softening irradiation conditions for failure at around 100 dpa. For fusion structures the effects of softening would be experienced in regions with low He/dpa. Notably, high He/dpa ≈ 10 would have a beneficial effect of creep times if the failure criteria are not met before ≈ 50 dpa.

BACKGROUND

We previously reported a comprehensive model for the effects of irradiation on the constitutive properties of TMS, with a focus on changes in the yield stress, σ_y, including for fusion relevant irradiation conditions as: $\Delta\sigma_y$ = f(dpa, He/dpa, T), where T is the irradiation and test temperatures [1]. Typical fission reactor irradiations, with He(appm)/dpa ratios << 1, cause hardening at T ≤ 400 °C, while at higher T the steels can gradually soften. At fusion first wall relevant He/dpa ≈ 10, the steels initially irradiation soften, but begin to re-experience increases in $\Delta\sigma_y$ at He > ≈ 400 appm. We showed the likely reason for the softening at such low T is radiation enhanced diffusion (RED); RED shifts purely thermal softening regime (> 600°C > 10^3 h) to lower temperatures and shorter times. We further noted that the main effects of softening are expected to be increases in thermal creep rates (ε'), since ε' is proportional to $[\sigma/\sigma]^n$, where n is a large number (typically ≥ 15). We also previously reported models to predict a variety of creep properties for a range of TMS heats [2]. We found that creep could be best modeled based on a normalized stress power law, $\varepsilon' \alpha (\sigma/\sigma_u)^n$, where σ_u is the ultimate tensile stress of a particular steel at the creep temperature. Here, we combine the softening and creep models to assess the effect of irradiation on the creep strains (ε_x) as a function of dpa. The basic creep model was previously fitted to a Eurofer97 creep database [3] and $\sigma_y(dpa)/\sigma_{yo} \approx (\sigma_u(dpa)/\sigma_{uo})$ was fitted to data from 450 to 600°C irradiations. The combined model was used to calculating the creep strain (ε) and creep rate (ε') as a function of dpa for T = 450, 500 and 550ºC at various σ, both with and without softening. To a good approximation, the dpa to specified strain ε_x with softening (dpa_s) is given by a relation in the form $dpa_s = C dpa_t^m$, where dpa_t is the corresponding pseudo dpa at ε_x without irradiation enhanced softening. As expected, the effect of softening increases with increasing dpa. For example, for ε_x = 2% (close to the thermal tertiary creep strain), $dpa_s = 1.3284(dpa_t)^{0.735}$. Thus, if dpa_t = 100 dpa, without softening, dpa_s would be ≈ 39 dpa.

PROGRESS AND STATUS

<u>The softening model</u>

The effect of high temperature exposures for long times leading to softening both with (under creep) and without (under thermal aging) stress is well established [4–11]. Thermal aging effects are generally manifested above ≈ 600°C and time more than 10,000 h. Softening under stress also occurs near and beyond the tertiary creep strain and time. While there are several different microstructural evolution

mechanisms leading to thermal softening, they generally share a common rate controlling dependence on the thermal diffusion coefficient (D_{th}). Thus, the excess defects produced by displacement damage result in higher radiation enhanced diffusion (RED) coefficients (D*). RED shifts the microstructural evolutions to lower temperatures and shorter times. Figure 1a shows best estimate D_{th} and D* as a function of 1/T. The banded region marks temperatures ranging from 450 to 550 °C, where D* is nearly athermal. It has also been found that thermal and irradiation softening data can be superimposed by a temperature adjustment with an activation energy of about 260 kJ/mole. Thus, softening, which begins thermally at about 600 °C, would be expected to start at about 400 °C under irradiation. While the thermal softening rates increase with temperature above ≈ 600 °C, the corresponding kinetics under irradiation would be expected to be roughly athermal at lower temperatures. The softening model was developed by fitting both the long-term thermally-aged [4–11] and RED adjusted [1] σ_y/σ_{yo} at 450, 500, 550 and 600 ºC as shown in Figure 1b.

$$\sigma_y/\sigma_{yo} = A - B \log (dpa) \qquad (1)$$

Here σ_{yo} is the unirradiated yield stress. The data is highly scattered but yield the fits summarized in Table 1. The fit results are very similar for the 450 to 550°C data, which is not surprising given the athermal D*. The average slope (B) and offset (A) over this temperature range is also shown in Table 1. In these cases, σ_y/σ_{yo} falls below 1 at > ≈ 4.6 dpa and σ_y/σ_{yo} = 0.85 at 200 dpa. The softening slope is larger and the dpa at σ_y/σ_{yo} = 1 is smaller for the 600 °C data. Thus, the overall softening process is described by a bilinear function shown in Figure 1c. The σ_u/σ_{uo} is assumed to be the same as σ_y/σ_{yo}. Time and dpa are related, based on an assumed dpa rate of 10^{-6} /s. The dashed lines show the effect of rehardening by a He/dpa ratio of 10 appm/dpa.

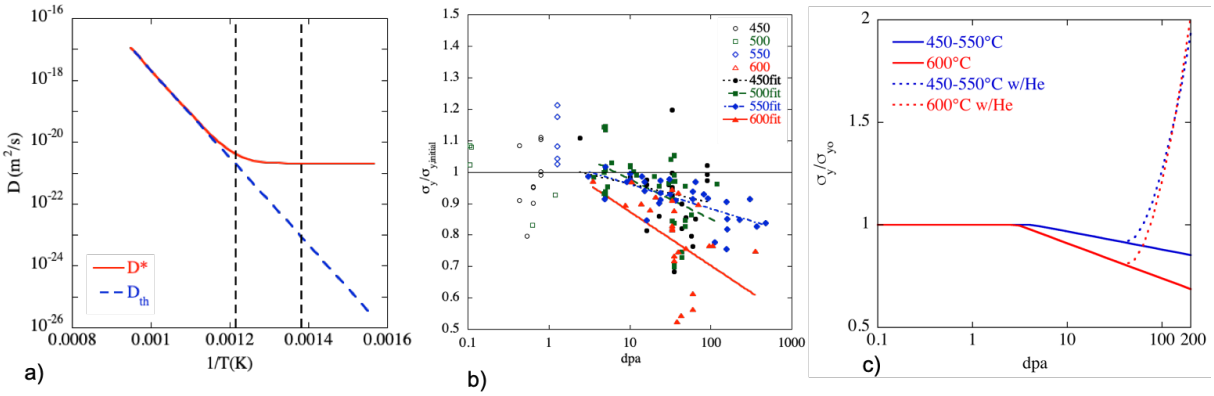

Figure 1. a) D_{th} and D* as a function of 1/T; b) σ_y/σ_{yo} vs dpa for combined thermally aged and RED-adjusted softening; and c) the average softening from 450 to 550 and 600 °C (solid line) and rehardening at He/dpa = 10 in units of appm/dpa (dashed line).

Table 1. Parameters for softening model

Parameters	450 ºC	500 ºC	550 ºC	Average of (450-550 ºC)	600 ºC
A (offset)	1.029	1.1037	1.0372	1.05659	1.08175
B (slope)	-0.06055	-0.1266	-0.07791	-0.08835	-0.17135

The creep model

A previously developed σ/σ_u primary creep model [2], derived for Eurofer97 [3], predicts the time (t_x) to reach a specified strain (ε_x) from 0.1 to 5 % as a function of σ/σ_u and T. The model is

$$t(\varepsilon) = (C_1+C_2\varepsilon+C_3\varepsilon^2)\exp\{S(\sigma/\sigma_u)\}\exp(Q/RT) \quad (2)$$

Here, C_i's are the intercept and slope fit parameters, and Q is the effective activation energy. The fit parameters for 450 to 600 °C are summarized in Table 2. The effective activation energy is fixed at 250 kJ/mole. Figure 2a shows a predicted versus measured t_x. While the times are scattered, the model predicts a robust trend. Figure 2b shows an example of predicted and measures $\varepsilon(t)$ at 500 °C and σ = 240 MPa. The results of the model are presented in two ways. The first is log-log plots of the creep rate (ε' in units of /s) versus dpa. The creep rate equations are then integrated to predict continuous creep strain curves, ε(dpa).

The effect of irradiation softening is estimated by simply by replacing the unirradiated constant σ/σ_u with the σ/σ_u(dpa) ratio, which increases with dpa. The ε' is adjusted in small ε increments and again integrated to predict ε(dpa) for the softening case. Since it results in longer creep times and dpa, the effect of softening increases with decreasing σ.

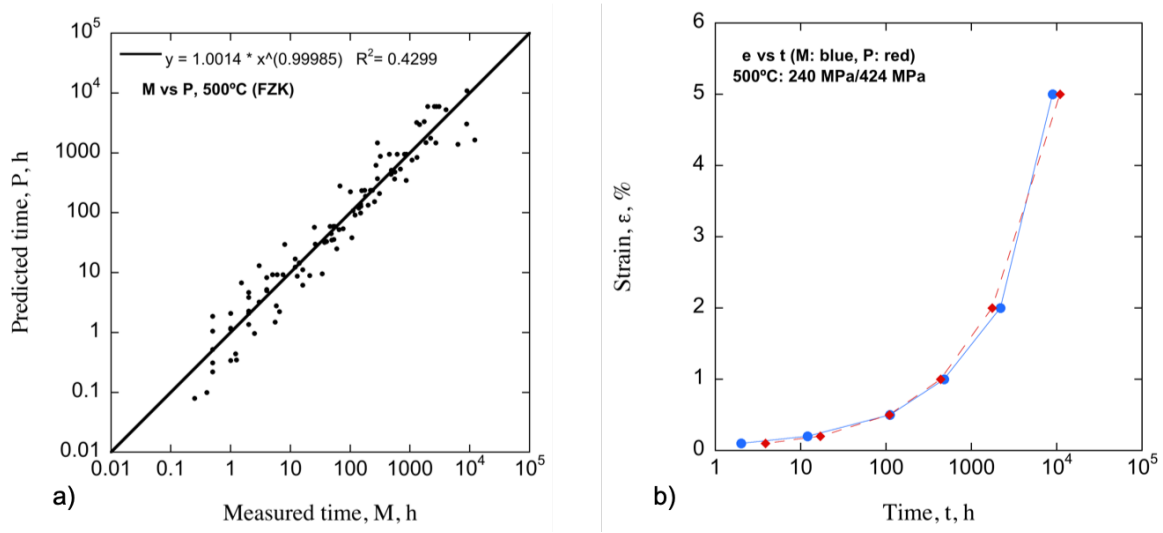

Figure 2. a) The σ/σ_u model for Eurofer97 data showing the measured vs predicted time for 500 ºC [2,3]; and, b) measured (blue dots) and predicted (red diamond) creep curve (ε vs t) at 500 ºC for σ = 240 MPa and σ_u = 424 MPa [3].

Table 2. Parameters for σ/σ_u model at different T ($\varepsilon_{x = 0.1\text{-}5\%}$) for Eurofer97 creep database [3]

Parameters	450 ºC	500ºC	550 ºC
C_1	-1.4×10^{-11}	-1.55×10^{-11}	9×10^{-10}
C_2	3.19×10^{-8}	2.7×10^{-10}	-5×10^{-7}
C_3	6.2475×10^{-5}	1.3×10^{-4}	5.5255×10^{-3}
S	-24.22	-25.9	-32.04
Q	250,000	250,000	250,000

Figure 3a shows the ε' versus dpa results at 450 °C for σ = 190 to 340 MPa. The dashed and solid lines are for the softening and non-softening cases, respectively. At the highest σ = 340 MPa, the dpa are too low for there to be any softening effect. The dpa increase, along with the difference between the softening and non-softening curves, with decreasing σ. Figure 3b shows the corresponding integrated ε(dpa) curves. Note again that for the non-softening case the dpa represent time for 10^{-6} dpa/s. Thus, the very high nominal dpa for the non-softening case at the lowest stress, simply means that the corresponding actual unperturbed thermal creep times are longer than 30 to 60x10^3 h. Table 3 summarizes the 450 °C results. Figures 4 and 5 and Tables 4 and 5 repeat these results for 500 and 550°C at the indicated σ values. Note that the minima in the ε'(dpa) curves represent the onset of tertiary creep, which occurs at various ε especially for the non-hardening case.

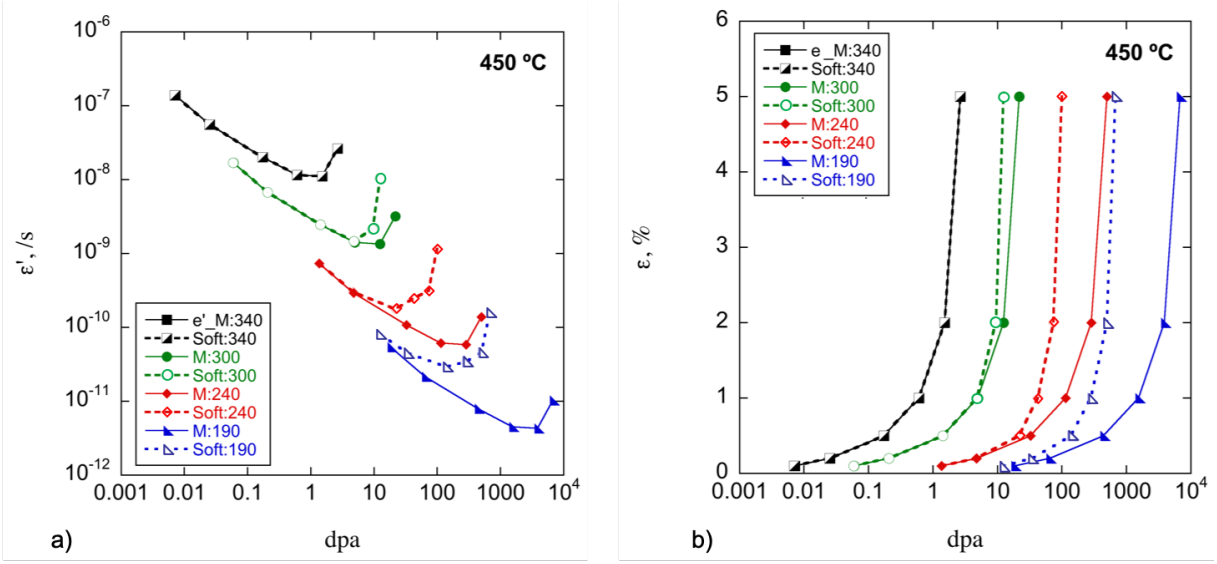

Figure 3. Softening and non-softening curves at 450 °C and varying σ, with the initial σ_u = 464 MPa: a) log-log plot of ε' vs dpa; and b) ε vs dpa creep curves.

Table 3. Irradiation enhanced thermal creep softening effect at 450 ºC as a function of σ and ε_x

Temp, K (3)	Creep Stress, S, Mpa	Yield, Sy, Mpa	Ultimate, Su, Mpa	S/Su	Measured strain, %	Original time (h)	Original dpa	Original Strain rate between strains, /s	Sy/Syo between strains (avg)	Softened Su, Su_s	Softened S/Su_s	Softened total time ts, h	Soften dpa, dpa_s	Strain rate after softening, e'_s, /s	e'_s/e'
723	340	429	464	0.73276	0.1	2	0.0072	1.39E-07	1.000	464.0	0.73276	2	0.007	1.39E-07	1.0
723	340	429	464	0.73276	0.2	7	0.0252	5.56E-08	1.000	464.0	0.73276	7	0.025	5.56E-08	1.0
723	340	429	464	0.73276	0.5	48	0.1728	2.03E-08	1.000	464.0	0.73276	48	0.173	2.03E-08	1.0
723	340	429	464	0.73276	1	168	0.6048	1.16E-08	1.000	464.0	0.73276	168	0.605	1.16E-08	1.0
723	340	429	464	0.73276	2	419	1.5084	1.11E-08	1.000	464.0	0.73276	419	1.508	1.11E-08	1.0
723	340	429	464	0.73276	5	736	2.6496	2.63E-08	1.000	464.0	0.73276	736	2.650	2.63E-08	1.0
723	300	429	464	0.64655	0.1	16.48	0.059328	1.69E-08	1.000	464.0	0.64655	16	0.059	1.69E-08	1.0
723	300	429	464	0.64655	0.2	57.6	0.20736	6.76E-09	1.000	464.0	0.64655	58	0.207	6.76E-09	1.0
723	300	429	464	0.64655	0.5	394.8	1.42128	2.47E-09	1.000	464.0	0.64655	395	1.421	2.47E-09	1.0
723	300	429	464	0.64655	1	1381.6	4.97376	1.41E-09	0.998	463.1	0.64779	1341	4.828	1.47E-09	1.0
723	300	429	464	0.64655	2	3446	12.4056	1.35E-09	0.983	456.2	0.65767	2642	9.512	2.13E-09	1.6
723	300	429	464	0.64655	5	6053	21.7908	3.70E-09	0.965	447.7	0.67005	3440	12.383	1.05E-08	3.3
723	240	429	464	0.51724	0.1	376	1.3536	7.39E-10	1.000	464.0	0.51724	376	1.354	7.39E-10	1.0
723	240	429	464	0.51724	0.2	1320	4.752	2.94E-10	0.999	463.4	0.51791	1298	4.675	3.01E-10	1.0
723	240	429	464	0.51724	0.5	9048	32.5728	1.08E-10	0.968	449.2	0.53429	5987	21.554	1.78E-10	1.6
723	240	429	464	0.51724	1	31665	113.994	6.14E-11	0.926	429.7	0.55857	11640	41.905	2.46E-10	4.0
723	240	429	464	0.51724	2	78975	284.31	5.87E-11	0.902	418.7	0.57318	20435	73.567	3.16E-10	5.4
723	240	429	464	0.51724	5	138721	499.3956	1.39E-10	0.886	411.0	0.58398	27663	99.588	1.15E-09	8.3
723	190	429	464	0.40948	0.1	5114	18.4104	5.43E-11	0.961	445.7	0.42632	3401	12.244	8.17E-11	1.5
723	190	429	464	0.40948	0.2	17947	64.6092	2.16E-11	0.941	436.4	0.43534	9594	34.539	4.49E-11	2.1
723	190	429	464	0.40948	0.5	123032	442.9152	7.93E-12	0.894	414.9	0.45791	38121	137.236	2.92E-11	3.7
723	190	429	464	0.40948	1	430596	1550.1456	4.52E-12	0.854	396.2	0.47956	78825	283.771	3.41E-11	7.6
723	190	429	464	0.40948	2	1073924	3866.1264	4.32E-12	0.829	384.7	0.49391	138923	500.124	4.62E-11	10.7
723	190	429	464	0.40948	5	1886370	6790.932	1.03E-11	0.812	376.8	0.50420	190542	685.952	1.61E-10	15.7

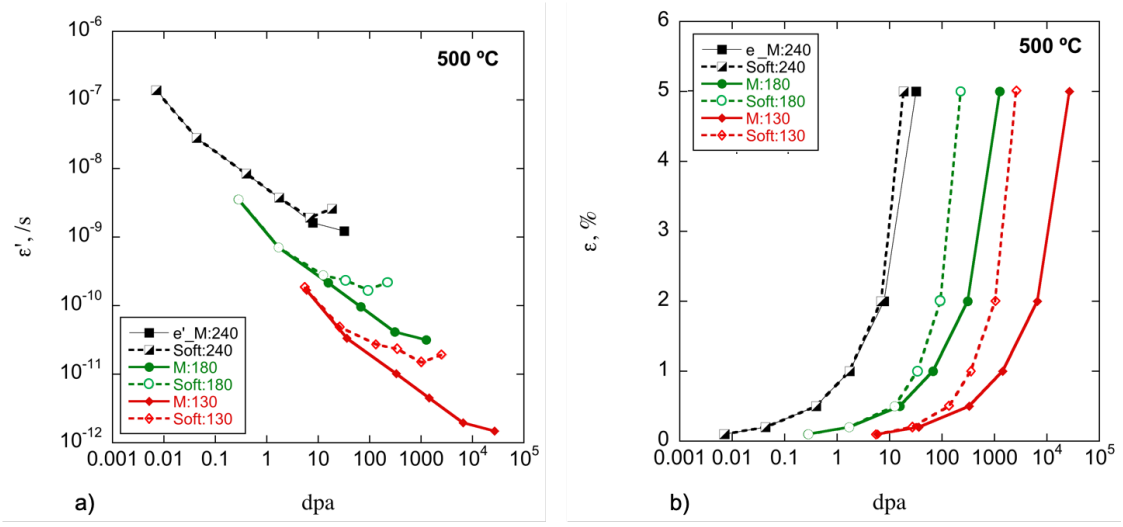

Figure 4. Softening and non-softening curves at 500 °C and varying σ, with the initial σ_u = 424 MPa: a) log-log plot of ε' vs dpa; and b) ε vs dpa creep curves.

Table 4. Irradiation enhanced thermal creep softening effect at 500 ºC as a function of σ and ε_x

Temp, K (t1)	Creep Stress, S, Mpa	Yield, Sy, Mpa	Ultimate; Su, Mpa	S/Su	Measured strain, %	Original time (h)	Original dpa	Original Strain rate between strains, /s	Sy/Syo between strains (avg)	Softened Su, Su_s	Softened S/Su_s	Softened total time ts, h	Soften dpa, dpa_s	Strain rate after softening, e'_s, /s	e'_s/e'
773	240	404	424	0.56604	0.1	2	0.0072	1.39E-07	1.000	424.0	0.56604	2.0	0.007	1.39E-07	1.0
773	240	404	424	0.56604	0.2	12	0.0432	2.78E-08	1.000	424.0	0.56604	12.0	0.043	2.78E-08	1.0
773	240	404	424	0.56604	0.5	111	0.3996	8.42E-09	1.000	424.0	0.56604	111.0	0.400	8.42E-09	1.0
773	240	404	424	0.56604	1	480	1.728	3.76E-09	1.000	424.0	0.56604	480.0	1.728	3.76E-09	1.0
773	240	404	424	0.56604	2	2190	7.884	1.62E-09	0.991	420.3	0.57108	1922.0	6.919	1.93E-09	1.2
773	240	404	424	0.56604	5	8955	32.238	1.23E-09	0.964	408.6	0.58744	5134.8	18.485	2.59E-09	2.1
773	180	404	424	0.42453	0.1	78	0.2808	3.56125E-09	1.000	424.0	0.42453	78	0.281	3.56E-09	1.0
773	180	404	424	0.42453	0.2	469	1.6884	7.10425E-10	1.000	424.0	0.42453	469	1.688	7.10E-10	1.0
773	180	404	424	0.42453	0.5	4335	15.606	2.15554E-10	0.980	415.5	0.43324	3460	12.457	2.79E-10	1.3
773	180	404	424	0.42453	1	18748	67.4928	9.63636E-11	0.941	398.8	0.45132	9374	33.747	2.35E-10	2.4
773	180	404	424	0.42453	2	85537	307.9332	4.15903E-11	0.902	382.4	0.47065	25899	93.235	1.68E-10	4.0
773	180	404	424	0.42453	5	349766	1259.1576	3.15383E-11	0.865	366.9	0.49054	68206	227.543	2.23E-10	7.1
773	130	404	424	0.30660	0.1	1653	5.9508	1.68E-10	0.991	420.2	0.30941	1537	5.533	1.81E-10	1.1
773	130	404	424	0.30660	0.2	9937	35.7732	3.35E-11	0.961	407.6	0.31896	7213	25.968	4.89E-11	1.5
773	130	404	424	0.30660	0.5	91947	331.0092	1.02E-11	0.900	381.5	0.34075	37954	136.636	2.71E-11	2.7
773	130	404	424	0.30660	1	397607	1431.3852	4.54E-12	0.850	360.3	0.36079	97716	351.778	2.32E-11	5.1
773	130	404	424	0.30660	2	1814082	6530.6952	1.96E-12	0.811	343.9	0.37800	285365	1027.315	1.48E-11	7.5
773	130	404	424	0.30660	5	7417890	26704.404	1.49E-12	0.773	327.7	0.39676	719428	2589.940	1.92E-11	12.9

The non-softening tertiary creep strain is typically around 5 %, or a little less, while it is 2 % or less for the softening case. A log-log plot of the non-softening versus softening dpa at 0.2 and 5 % is shown in Figure 6. The curves are similar and least square fits:

$$dpa_s = 1.3284\ dpa_t^{0.735} \text{ for } \varepsilon_x = 2\ \% \quad (3a)$$

and

$$dpa_s = 1.2843\ dpa_t^{0.727} \text{ for } \varepsilon_x = 5\ \% \quad (3b)$$

The corresponding data from 0.2 to 5% strains are shown in Table 6.

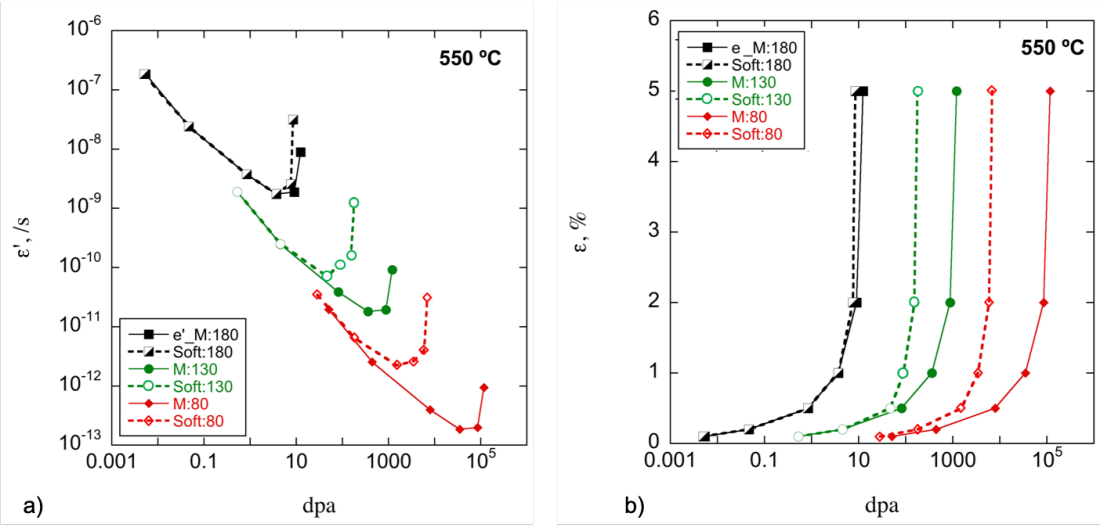

Figure 5. Softening and non-softening curves at 550 °C and varying σ, with σ_u = 350 MPa: a) log-log plot of ε' vs dpa; and b) ε vs dpa creep curves.

Table 5. Irradiation enhanced thermal creep softening effect at 550 ºC as a function of σ and ε_x

Temp, K (84)	Creep Stress, S, Mpa	Yield , Sy, Mpa	Ultimate, Su, Mpa	S/Su	Measured strain, %	Original time (h)	Original dpa	Original Strain rate between strains, /s	Sy/Syo betwee strains (avg)	Softened Su, Su_s	Softened S/Su_s	Softened total time ts, h	Soften dpa, dpa_s	Strain rate after softening, e'_s, /s	e'_s/e'
823	180	340	350	0.51429	0.1	1.5	0.0054	1.85E-07	1.000	350.0	0.51429	1.5	0.005	1.85E-07	1.0
823	180	340	350	0.51429	0.2	13	0.0468	2.42E-08	1.000	350.0	0.51429	13.0	0.047	2.42E-08	1.0
823	180	340	350	0.51429	0.5	235	0.846	3.75E-09	1.000	350.0	0.51429	235.0	0.846	3.75E-09	1.0
823	180	340	350	0.51429	1	1030	3.708	1.75E-09	1.000	350.0	0.51429	1030.0	3.708	1.75E-09	1.0
823	180	340	350	0.51429	2	2505	9.018	1.88E-09	0.989	346.3	0.51981	2105.1	7.578	2.58E-09	1.4
823	180	340	350	0.51429	5	3439	12.3804	8.92E-09	0.976	341.8	0.52670	2369.0	8.528	3.16E-08	3.5
823	130	340	350	0.37143	0.1	146	0.5256	1.90259E-09	1.000	350.0	0.37143	146	0.526	1.90E-09	1.0
823	130	340	350	0.37143	0.2	1264	4.5504	2.48486E-10	0.999	349.8	0.37166	1255	4.517	2.51E-10	1.0
823	130	340	350	0.37143	0.5	22850	82.26	3.86053E-11	0.954	333.9	0.38932	12881	46.372	7.17E-11	1.9
823	130	340	350	0.37143	1	100149	360.5364	1.79677E-11	0.896	313.7	0.41436	25319	91.148	1.12E-10	6.2
823	130	340	350	0.37143	2	243565	876.834	1.93682E-11	0.873	305.7	0.42526	42952	154.629	1.58E-10	8.1
823	130	340	350	0.37143	5	334380	1203.768	9.17616E-11	0.860	301.2	0.43166	49868	179.524	1.23E-09	13.1
823	80	340	350	0.22857	0.1	14210	51.156	1.95E-11	0.928	324.6	0.24643	8018	28.865	3.46E-11	1.8
823	80	340	350	0.22857	0.2	122977	442.5372	2.56E-12	0.892	312.2	0.25621	50704	182.534	6.51E-12	2.5
823	80	340	350	0.22857	0.5	2222024	7999.2864	3.97E-13	0.816	285.6	0.28014	425780	1532.808	2.22E-12	5.6
823	80	340	350	0.22857	1	9738998	35060.3928	1.85E-13	0.760	265.8	0.30094	958424	3450.325	2.61E-12	14.1
823	80	340	350	0.22857	2	23685535	85267.926	1.95E-13	0.734	256.7	0.31161	1653014	5950.849	4.00E-12	20.1
823	80	340	350	0.22857	5	32516817	117060.5412	9.44E-13	0.720	252.0	0.31742	1925207	6930.745	3.06E-11	32.4

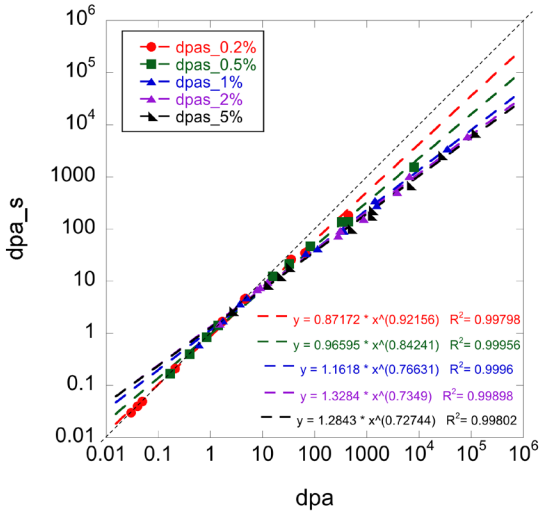

Figure 6. Creep dpa before and after softening from 0.2 to 5 % strains at varying T and σ.

Table 6. Creep dpa before and after softening from 0.2 to 5% strains at varying T and σ

Temperature, ºC	Stress, MPa	dpa_0.2%	dpa_s 0.2%	dpa_0.5%	dpa_s 0.5%	dpa_1%	dpa_s 1%	dpa_2%	dpa_s 2%	dpa_5%	dpa_s 5%
450	340	0.03	0.03	0.17	0.17	0.60	0.60	1.51	1.51	2.65	2.65
450	300	0.21	0.21	1.42	1.42	4.97	4.83	12.41	9.51	21.79	12.38
450	240	4.75	4.67	32.57	21.55	113.99	41.90	284.31	73.57	499.40	99.59
450	190	64.61	34.54	442.92	137.24	1550.15	283.77	3866.13	500.12	6790.93	685.95
500	240	0.04	0.04	0.40	0.40	1.73	1.73	7.88	6.92	32.24	18.49
500	180	1.69	1.69	15.61	12.46	67.49	33.75	307.93	93.23	1259.16	227.54
500	130	35.77	25.97	331.01	136.64	1431.39	351.78	6530.70	1027.31	26704.40	2589.94
550	180	0.05	0.05	0.85	0.85	3.71	3.71	9.02	7.58	12.38	8.53
550	130	4.55	4.52	82.26	46.37	360.54	91.15	876.83	154.63	1203.77	179.52
550	80	442.54	182.53	7999.29	1532.81	35060.39	3450.32	85267.93	5950.85	117060.54	6930.74

A pertinent metric of creep life dpa to the onset of tertiary creep (dpa_{tc}). The tertiary creep strain (ε_{tc}) varies with the loading condition, especially for the softening case. Figure 7 shows a log-log plot dpa_{tc} for no softening versus softening cases. As an example, the plot shows that to reach $dpa_{tc} \approx 100$ dpa with softening, the dpa_{tc} without softening must be ≈ 300 dpa, or ≈ 2.8×10^5 h at the reference dpa rate of 10^{-6}/s (500 ºC/180 MPa).

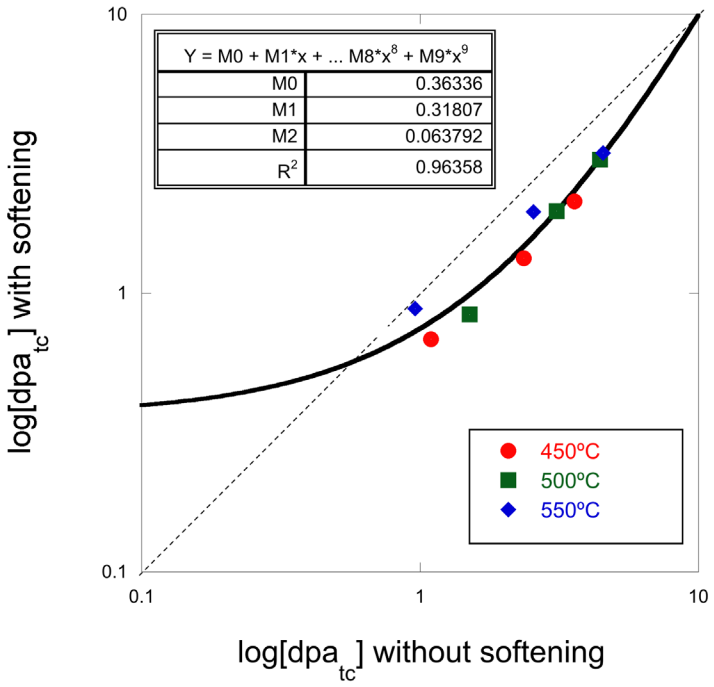

Figure 7. The log[dpa_{tc}] without versus with softening in log-log plot.

Effects of He Hardening

The results summarized above do not consider the effects of rehardening by He illustrated in Figure 1c. Helium makes an approximately athermal contribution to hardening above 450 °C starting at a threshold of a threshold of ≈ 430 appm and increasing with the √He. Thus, He hardening would be expected to greatly extend the creep life if softening failure (by whatever criteria) does not occur before about the threshold of 500 appm He. For typical first wall He/dpa ≈10, 50 dpa is a good metric for when the beneficial (to creep) effects of He to begin to emerge. However, detailed modeling of He effects on creep is the subject of ongoing research and will be described in future reports.

Discussion

At high temperatures the softening effects of irradiation must be considered. A rough rule of thumb is that at above ≈ 450 °C a nominal dpa rate of 10^{-6}/s, the creep failure times are reduced by about a factor of 3, under irradiation. For fusion structures the effects of softening would be experience in regions with low He/dpa. Notably, high He/dpa ≈ 10 would have a beneficial effect of creep times if the failure criteria is not met before ≈ 50 dpa.

Acknowledgments

We acknowledge the support provided by U.S. Department of Energy through the Office of Fusion Energy Sciences (8-442520-22419-3).

References

[1] T. Yamamoto, G.R. Odette, Constitutivd models for hardening of tempered matensitic steels irradiated at 300 to 500 °C up to high dpa abd He, DOE Fusion React. Mater. Progr. Semiannu. Prog. Rep. DOE/ER/68 (2020) 55–67.
[2] M.E. Alam, T. Yamamoto, G.R. Odette, Global Thermal Creep Models Derived from a Comprehensive Multiple Heat Database on 9Cr Tempered Martensitic Steels, DOE Fusion React. Mater. Progr. Semiannu. Prog. Rep. 69 (2020) 24–37.
[3] M. Rieth, M. Schirra, A. Falkenstein, P. Graf, S. Heger, H. Kempe, R. Lindau, H. Zimmermann, EUROFER 97. Tensile, charpy, creep and structural tests, in: (No. FZKA--6911). Forschungszentrum Karlsruhe GmbH Technik und Umwelt (Germany). Inst. fuer Materialforschung., 2003.
[4] C.G. Panait, W. Bendick, A. Fuchsmann, A.F. Gourgues-Lorenzon, J. Besson, Study of the microstructure of the Grade 91 steel after more than 100,000 h of creep exposure at 600 °C, Int. J. Press. Vessel. Pip. 87 (2010) 326–335.
[5] F. Masuyama, T. Yamaguchi, New ferritic steels beyond Grade 92 and its creep degradation assessment by hardness method for Grade 91, in: ASME Symp. Elev. Temp. Appl. Mater. Foss. Nucl. Petrochemical Ind., 2014: pp. 1–8.
[6] H.-Y. Lee, W.G. Kim, Influence of Thermal Aging on Material Strength Behavior in Grade 91 Steeel, in: Transacctions Korean Nucl. Soc. Autumn Meet., 2015: pp. 3–5.
[7] J. Zhao, J. Gong, A. Saboo, D.C. Dunand, G.B. Olson, Dislocation-based modeling of long-term creep behaviors of Grade 91 steels, Acta Mater. 149 (2018) 19–28.
[8] S. Khayatzadeh, D.W.J. Tanner, C.E. Truman, P.E.J. Flewitt, D.J. Smith, Influence of thermal ageing on the creep behaviour of a P92 martensitic steel, Mater. Sci. Eng. A. 708 (2017) 544–555.
[9] M. Li, W.Y. Chen, Microstructure-based prediction of thermal aging strength reduction factors for grade 91 ferritic-martensitic steel, Mater. Sci. Eng. A. 798 (2020) 140116.
[10] T. Nagasaka, M. Ando, H. Tanigawa, H. Sakasegawa, T. Tanaka, T. Muroga, A. Sagara, Tensile properties of F82H steel after aging at 400–650 °C for 1000–30,000 h, Fusion Eng. Des. 124 (2017) 1011–1014.
[11] Y. Yano, T. Tanno, Y. Sekio, H. Oka, S. Ohtsuka, T. Uwaba, T. Kaito, Tensile properties and hardness of two types of 11Cr-ferritic/martensitic steel after aging up to 45,000 h, Nucl. Mater. Energy. 9 (2016) 324–330.

1.6 CROSS-WELD CREEP-RUPTURE CHARACTERIZATION IN MODIFIED 3Cr BAINITIC STEELS—Y. Yamamoto (Oak Ridge National Laboratory)

OBJECTIVE

This work aims to develop new bainitic steels, based on 3Cr-3WVTa bainitic steels originally developed at ORNL. The goal is to obtain mechanical properties of both base metal and weldments superior to those of existing commercial bainitic steels or ferritic-martensitic (F-M) steels, together with no requirement for post-weld heat treatment (PWHT). The target applications are high-temperature structural components in fusion reactors such as helium cooled vacuum vessels operating up to 450°C and blanket support structures up to 550°C. Improvements of creep performance and1.6 room-temperature toughness are targeted via optimization of alloy composition and thermo-mechanical treatment. The present study focused on investigating and understanding the cross-weld creep rupture characteristics in newly developed 3Cr-3WVTa base bainitic steels, as a function of test temperature.

SUMMARY

Evaluation of the cross-weld creep-rupture mode in the modified 3Cr-3WVTa bainitic steel weldments (ID: MLC02T) was conducted. Cross-sectional microstructure characterization indicated a severe creep-deformation as well as the creep-rupture occurred at the inter-critical heat affected zone when tested at or above 550°C, whereas the specimens ruptured inside the base metal at 500°C. The results suggested that, by comparing with the base metal performance, very limited reduction of the cross-weld creep performance would be expected in the modified steel at or below 500 °C. Since the base metal was subjected to the normalization-and-tempering prior to the weldment, it is suggested that the base metal should be used in as-normalized condition before applying the weldment for the improved creep-deformation resistance.

PROGRESS AND STATUS

Cross-weld creep performance of newly proposed modified 3Cr-3WVTa bainitic steel was evaluated. The heat (ID: MLC02T) contains higher Mn and lower C than the original 3Cr-3WVTa steel to expect maintaining high hardenability and reducing the as-normalized hardness, targeting a reduced property inhomogeneity across the weldment in as-welded (no PWHT) condition. The nominal compositions of the original and modified steels are summarized in Table 1. The composition of new heat is close to that of previously evaluated heat MSLC2, although MSLC2 contains more Si than either the new MLC02T or the original 3Cr-3WVTa steels. A vacuum-induction-melted ingot of MLC02T was homogenized at 1200°C, hot-rolled and annealed at 1100°C, and then air-cooled to RT (normalization). The rolled plate was tempered at 700°C for 1h, followed by air-cooling to RT (tempering). A gas tungsten arc weld (GTAW) with a filler metal wire made of original 3Cr-3WVTa steel was applied to the tempered plates to prepare the cross-weld specimens.

Table 1. Nominal composition of 3Cr-3WVTa base bainitic steels (balanced Fe)

Name	Alloy composition, wt.%	Remarks
MLC02T	3Cr-3W-0.2V-0.16Si-2.0Mn-0.1Ta-0.05C	Modified (newly proposed)
MSLC2	3Cr-3W-0.2V-0.50Si-2.0Mn-0.1Ta-0.05C	Modified (high Si, previously reported)
Original	3Cr-3W-0.2V-0.16Si-0.4Mn-0.1Ta-0.1C	Require PWHT

Figure 1 illustrates the creep-rupture test results of MLC02T base and cross-weld specimens tested at 500 and 550°C. The results of original 3C-3WVTa steel at 550°C were also plotted for comparison. The base and cross-weld creep-rupture test results of MLC02T at 500°C were mostly overlapped to each other, indicating that the Weld Strengthening Reduction Factor (WSRF) is nearly 1 and the weldment would not cause the reduction of creep-rupture lives. The results at 550°C indicated that the base metal creep-rupture strength was ~30% lower than the original 3Cr-3WVTa steel in the range of stress studied. On the other hand, the cross-weld creep-rupture test of MLC02T at 550°C (only one test was completed to date) showed the creep-rupture strength comparable to (or slightly better than) that of original 3Cr-3WVTa steel weldment.

It should be noted that two long-term tests targeting more than 10,000h, one for the base metal and the other for the cross-weld sample, are currently in progress.

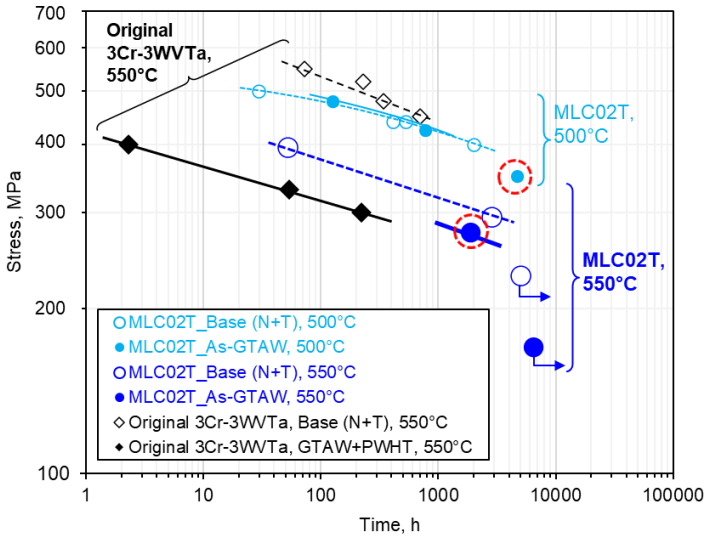

Figure 1. Creep-rupture test results of MLC02T base and cross-weld specimens tested at 500 and 550°C, together with those of original 3Cr-3WVTa steel [1].

Cross-sectional microstructure characterization of the cross-weld creep-ruptured specimens was conducted. Figure 2 represents two montaged optical micrographs showing the macroscopic cross-sectional images of two different creep-rupture specimens tested at 500 (upper) and 550°C (lower), corresponding to the samples indicated by the red circles in Figure 1. Both images showed the weld metal near the center, and the heat affected zone (HAZ) and the inter-critical heat affected zone (ICHAZ) were adjacent to the weld metal. The HAZ area was heated above Ac3 temperature and then austenitized during the welding process, so that the area consisted of newly formed bainitic ferritic structure with untempered condition. The ICHAZ area was heated between Ac1 and Ac3, which resulted in a partially austenitized + partially over-tempered condition. The upper image in Figure 2 indicated that the creep-rupture occurred inside the base metal suggesting that the HAZ/ICHAZ would not negatively impact on the creep-rupture performance of the modified steel at 500°C, and the base metal properties dominated the cross-weld creep-rupture performance at the temperature. The observation result was also consistent with the creep-rupture test results at 500°C, discussed in Figure 1. On the other hand, the lower image illustrated the creep-rupture occurred along the ICHAZ. The close observation revealed that the large distortion was accumulated at the inside of the over-tempered base metal, suggesting that the over-tempered region has less deformation resistance than the other areas at 550°C.

A similar observation was conducted in all cross-weld creep-ruptured specimens including MLC02T (500 and 550°C), MSLC2 (550 and 600°C), and original 3Cr-3WVTa steel (550°C), tested in the as-welded condition. As summarized in Table 2, all materials tested at or above 550°C resulted in rupturing at the ICHAZ in the stress range studied. It should be noted that the specimens applied a post-weld heat treatment also showed the same result at 550°C. Only MLC02T was tested at 500°C to date, and all specimens were ruptured inside the base metal, indicating that, at least for MLC02T, the transition of the rupture mode appears between 500 and 550°C. Two trail cross-weld creep-rupture tests of MSLC2 and original 3Cr-3WVTa steels have been prepared to evaluate the rupture mode of them at 500°C, targeting to find the transition of the rupture mode in these materials. The tests are to be conducted once the creep-test frames become available. In addition, preparation of new cross-weld specimens is currently in progress which use the as-normalized plate as the base metal for the weldments, targeting the improved deformation resistance at the ICHAZ at or above 550°C.

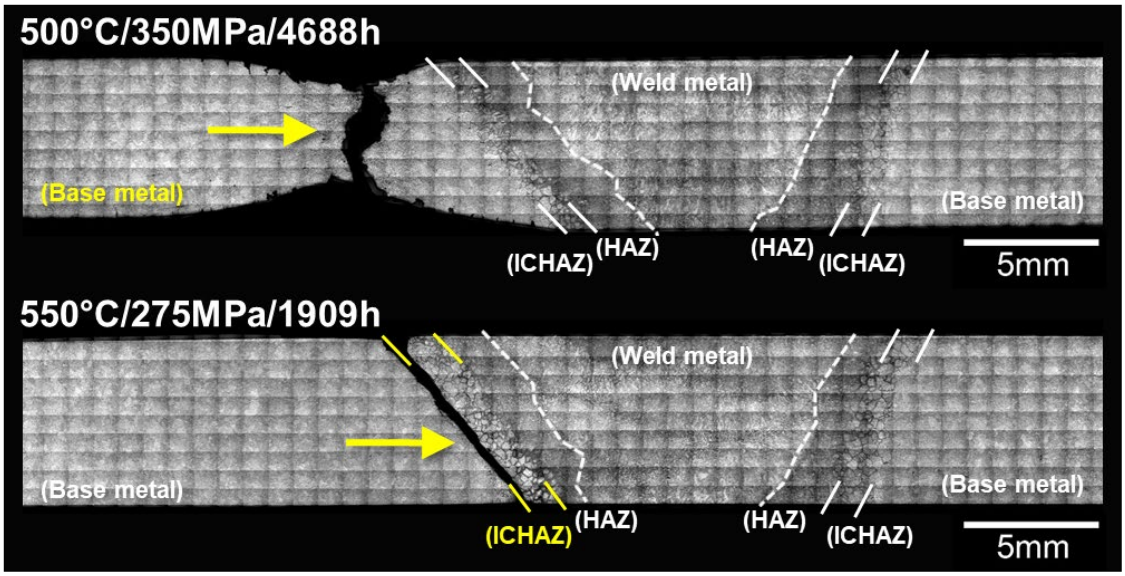

Figure 2. Cross-sections of creep-rupture tested cross-weld MLC02T at 500 (upper) and 550°C (lower); the upper specimen ruptured at the base metal, whereas the lower rupture at the ICHAZ.

Table 2. Ruptured location of the modified 3Cr-3WVTa steels in the cross-weld creep testing; the test samples include MLC02T (500 and 550°C), MSLC2 (550 and 600°C), and original steel (550°C), tested in the as-welded condition

Temperature, °C	Stress, MPa								
	480	425	400	350	330	300	275	250	170
600	-	-	-	-	-	-	-	ICHAZ	-
550	-	-	ICHAZ	-	ICHAZ	ICHAZ	ICHAZ	-	ICHAZ
500	Base	Base	-	Base	-	-	-	-	-

Future Plans

The MLC02T with optimized microstructure (fine prior austenite grain size, untempered) are to be welded to evaluate the cross-weld creep-rupture performance with an expected improvement of creep-deformation resistance at or above 550°C. Charpy impact toughness tests of both base metal and the cross-weld specimens will also be performed to evaluate the effect of grain refinement on the DBTT.

References

[1] R.L. Klueh et al., Int. J. Pressure Vessels and Piping, 84 (2007) 29-36.

1.7 ADVANCED CHARACTERIZATION OF RAFM STEEL MICROSTRUCTURES—C. M. Parish (Oak Ridge National Laboratory)

OBJECTIVE

The overarching objective of this work is to develop new, state-of-the-art characterization techniques for application to the expected future needs of the Fusion Materials program.

SUMMARY

In this reporting period, software codes were refined to provide computationally efficient machine learning results from large-area, high-throughput X-ray spectrum imaging (XSI) of carbides from an AM RAFM (additively manufactured reduced-activation ferritic/martensitic) steel. The computer codes described in the last reporting period have been improved significantly and provide high-fidelity machine learning results. Samples were provided via collaboration with A. Bhattacharya, L. Tan, and the ORNL Manufacturing Demonstration Facility.

PROGRESS AND STATUS

Prior work in the ORNL Fusion Materials program has used the *carbon extraction replica* method to make scanning transmission electron microscopy (STEM) specimens. In the carbon extraction replica method, the hard precipitates (i.e., carbides, oxycarbonitrides, etc.) from a steel are embedded in a thin, electron-transparent film of amorphous carbon and that film, with the embedded carbides, is analyzed. This technique has two major advantages. First, large areas (potentially square millimeters) are obtained; with FIB samples, specimens are a few square microns, at most. Second, the precipitates are not embedded in the FM matrix, so their cation content can be measured without confounding effects from the matrix. Thermo Scientific "MAPS" software on Talos F200X STEM in the LAMDA laboratory was used to obtain a large dataset, a 10×10 grid of XSIs was obtained, where each XSI was 1024×1024 pixels in space and 4096 channels in spectral space.

Figure 1 (left) shows the 10×10 tile set of HAADF (high angle annular dark field) images; large numbers of carbides (bright) are seen on the carbon-film background (dark).

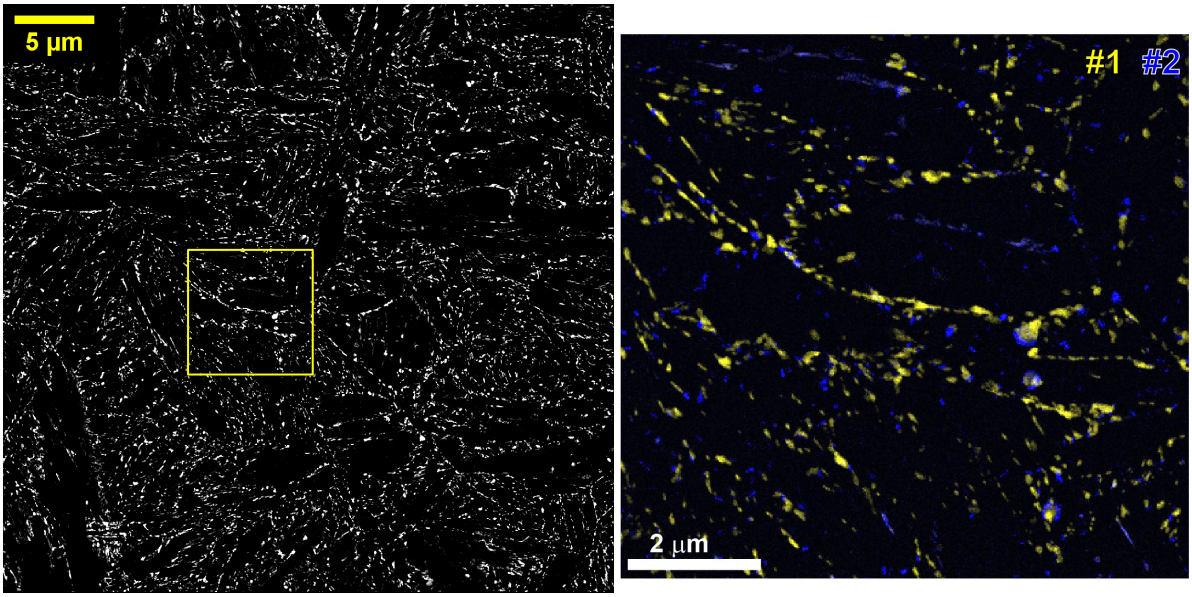

Figure 1. (left) HAADF montage of the 10×10 STEM tiles. The effective size, with overlap at the edges of panels, is roughly 7100×7100 pixels (50 megapixels). (right) A small region of the naïve, fully weighted analysis of the dataset. Yellow #1: $M_{23}C_6$; blue #2: V(C,N).

As discussed last reporting period, the data size (10×10×1024×1024×4096) is ≈4.3×10^{11} data elements. At 4 bytes per data element, this would be roughly 1.6 TB of data, and analysis of a dense 1.6 TB dataset is obviously intractable without high performance computing resources, but XSI data is handled in a truncated and sparse manner, which is very efficient computationally and in storage terms. As reported previously (Figure 1 (right)), M23C6 and V(C,N) precipitates were identified by the machine learning approach.

An important consideration is that the algorithm used performs scaling for Poisson noise, making the dataset more homoscedastic and tractable for analysis. However, recent literature has indicated that with low and varying X-ray count rates, as in a nanoparticle XSI, a different noise pre-treatment is required. This code was implemented and run with many different parameters on the dataset, which resulted in a far deeper noise floor and therefore far more ability for the algorithm to identify small number-density phases and to find variations in phases the human analyst would assume are a single phase.

Specifically, instead of two precipitates in the old weighting scheme, six precipitate types are found, Figures 2-3:

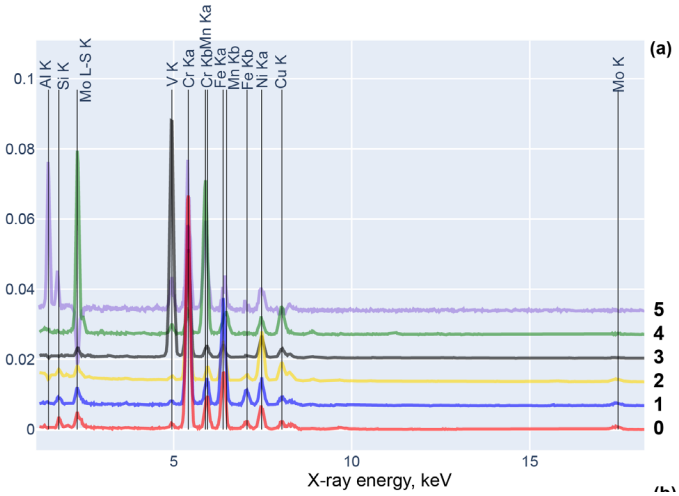

Figure 2. Spectral endmembers extracted by machine learning. #0 and #1 are $M_{23}C_6$-type, with slightly different cation ratios. #2 is the background spurious X-rays from the nickel sample grid. #3 is the V(C,N). #4 is MnS. #5 is an Al-Si-Cr-oxide.

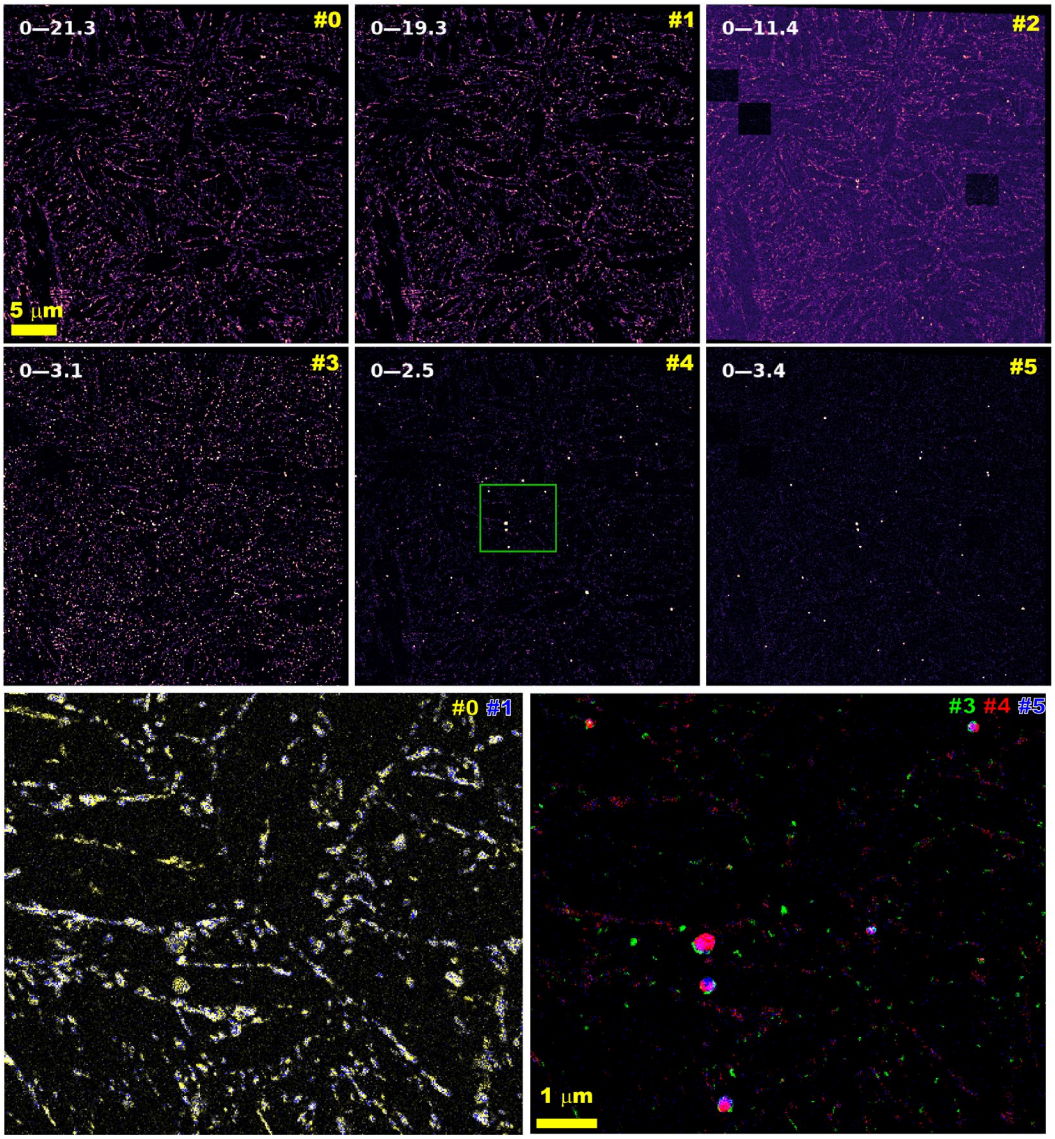

Figure 3. Panels #0-#5 are the abundance maps of the endmembers seen in Figure 9a from the nanoprecipitate dataset. #0 and #1 are the $M_{23}C_6$-type carbides. Panel #2 shows the Ni-rich background component. Panel #3 is the VX-type nanoprecipitate. Panel #4 shows the MnS precipitates. #5 shows the Al-Si-Cr-oxides. The bottom row shows false color overlays. The left overlay shows the two $M_{23}C_6$ components as yellow and blue; the right overlay shows the VX, MnS, and Al-Si-Cr components.

This exciting result—that improved pretreatment for the noise—results in improved visibility of the small number density precipitates will allow improved analysis of future specimens from the fusion program. In particular, the Al-Si-Cr-O phase is not anticipated, and the MnS phase was erroneously rolled into the $M_{23}C_6$ by the prior algorithm. Also, the $M_{23}C_6$ phase is seen to consist of two separate endmembers. Although much of the aggregate $M_{23}C_6$ appears to be an intermediate mixture of the two endmembers, some of the $M_{23}C_6$ pockets (such as along lath boundaries) appear to be almost purely one of the endmembers.

Additionally, during this reporting period, codes were written to streamline the reporting pipeline to reduce the data analysis cycle time.

A publication is under review at *Microscopy and Microanalysis*. The dataset has been published open source (https://doi.ccs.ornl.gov/ui/doi/353). The codes are undergoing final approval for open-source publication (https://code.ornl.gov/nmp/eds_montage).

Future Work

Future work will involve implementation of machine vision to count and size the particles.

2. ODS AND NANOCOMPOSITED ALLOY DEVELOPMENT

2.1 TEMPERATURE AND DOSE EFFECTS ON PHASE SEPARATION IN NEUTRON IRRADIATED PM2000 AND MA957—Samara Levine, Steven Zinkle (University of Tennessee), Arunodaya Bhattacharya, Jonathan Poplawsky, David Hoelzer, Yutai Katoh (Oak Ridge National Laboratory)

OBJECTIVE

The objective of this study was to understand the effects of temperature and dose on nano-scale phase separation in oxide dispersion strengthened (ODS) alloys PM2000 and MA957 using atom probe tomography (APT).

SUMMARY

The Fe-Cr based oxide dispersion strengthened (ODS) alloys PM2000 (19% Cr – 5% Al base) and MA957 (14% Cr base) were irradiated in the High Flux Isotope Reactor (HFIR) to doses ranging from 4.5 to 50.7 dpa with temperatures ranging between 285 and 500°C ± 20°C. Here, APT was used to explore the evolution of secondary phase particles and solute clusters under irradiation with temperature and dose so that the contribution of nano-scale phase separation phenomena to low temperature hardening and embrittlement (LTHE) may be understood. At all conditions, there was a high number density of Cr-rich clusters. In addition, significant clustering of Al/Ti in PM2000 and Ni/Ti in MA957 was observed in samples irradiated at 500°C.

PROGRESS AND STATUS

Low temperature hardening and embrittlement (LTHE) of reduced activation ferritic-martensitic (RAFM) steels and ODS alloys currently constrains the lower operating temperature for fusion reactor first wall/blanket (FW/B) structures. Recent evidence from Vickers microhardness testing of ODS variants PM2000 and MA957 irradiated in the High Flux Isotope Reactor (HFIR) has revealed that contrary to RAFM steels, irradiation induced hardening may persist in some ODS alloys for irradiation temperatures up to ~ 500 °C [1]. The underlying cause of this irradiation hardening in ODS alloys is not well understood.

The APT experiments were conducted on samples of PM2000 and MA957 following irradiation in the HFIR to doses ranging from 4.5 to 50.7 dpa with temperatures ranging between 285 and 500°C ± 20°C. Needle shaped samples were milled in the Low Activation Materials Development and Analysis (LAMDA) laboratory using a FEI Quanta Focused Ion Beam (FIB). The needle shaped tips were then characterized using the Local Electron Atom Probe (LEAP) 4000X HR at the Center for Nanophase Materials Sciences (CNMS). Data was acquired at a temperature of 50 K in voltage mode with a pulse rate of 200 kHz, a pulse fraction of 0.2, and a detection rate of 0.5. Reconstructions of the tip volumes were done using Cameca's Integrated Visualization and Analysis Software (IVAS). The plane spacing of an indexed pole was used to calibrate the depth (z) direction of each reconstruction. The field factor (k) and image compression factor (ICF) of reconstructions varied between 4.1 – 6.1 and 1.4 – 1.65, respectively. Subsequent cluster analysis was then performed using the Open-Source Characterization of APT Reconstructions (OSCAR) program [2]. Parameters used for cluster analysis are provided in Table 1.

Table 1. Cluster analysis parameters

Material	Solute Atom	Concentration Threshold (c_{th}) (at. %)	Linking Distance (d_{link}) (nm)	Minimum Solute Atoms per Cluster (N_{min})
PM2000	Cr	34.0	0.46	20
PM2000	Ti	5.0	1.16	8
MA957	Cr	30.0	0.45	16
MA957	Ni	5.5	0.90	8

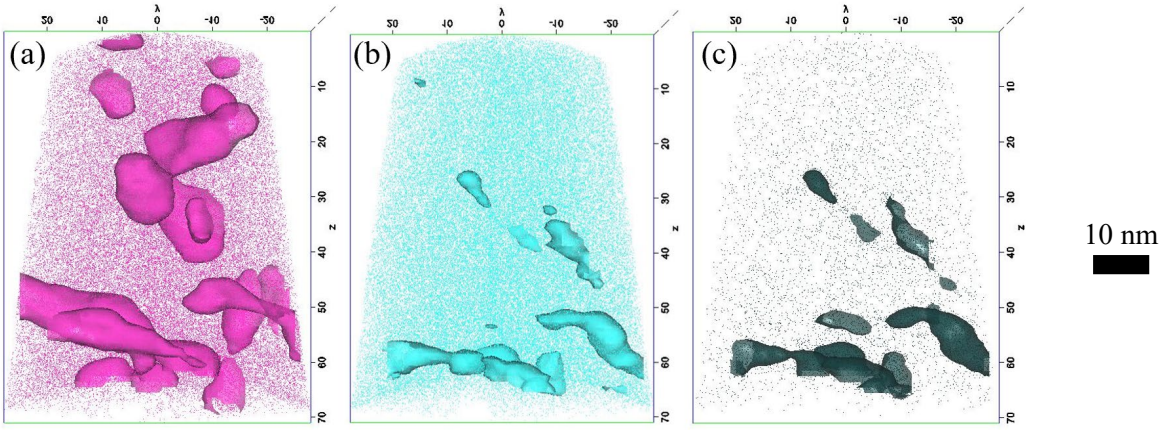

Figure 1. Atom maps from PM2000 irradiated at 500°C to 8.7 dpa. (a) Cr map with 30 at. % iso-surfaces (b) Al map with 15 at. % iso-surfaces (c) Ti map with 3 at. % iso-surfaces.

Select atom maps from a typical volume of neutron irradiated PM2000 after 8.7 dpa at 500°C are provided in Figure 1. For PM2000, Cr-rich clusters were observed at all irradiation conditions. Table 2 contains size, density, and compositional information. Given the chromium content of this alloy, radiation enhanced precipitation of α' is expected [3]. It is notable that average core concentrations of Cr were well below the 80 – 90 at. % Cr core concentration that is typically observed in neutron irradiated Fe-Cr binary alloys and that is expected based on the Fe-Cr equilibrium phase diagram. Further analysis is needed to rule out trajectory aberrations. However, these relatively low core Cr concentrations are consistent with previous results from APT studies of neutron irradiated FeCrAl alloys [4, 5]. Ab initio calculations by Li et al. [6] indicate that Al increases the formation energy of α' and thus destabilizes α' phase. Size and number density of α' did not vary significantly at 285 – 335°C as irradiation dose increased from 4.5 to 50.7 dpa. This is consistent with previous studies of Fe-Cr binary alloys where α' reaches equilibrium at low (< 1.0 dpa) irradiation doses [7]. For the irradiations between 285 – 449 °C, the average Guinier radius of the Cr clusters was ~1.4 –1.6 nm and the number density of clusters was ~ 2 x 10^{24} – 4 x 10^{24} m^{-3}. On the other hand, for the irradiation conducted at 500 °C, the average Guinier radius of the Cr clusters was ~ 4.5 nm and number density of Cr clusters dropped an order of magnitude to ~ 2.4 x 10^{23} m^{-3}. The dramatic increase in Cr cluster size corresponded to the onset of significant Al/Ti clustering. Table 3 contains size, density, and compositional information. Al/Ti rich clusters were observed adjacent to Cr-rich clusters. This suggests that the formation of α' and Al/Ti rich clusters may be linked. Similar Al/Ti rich clustering occurring heterogeneously at α' interfaces was observed by Capdevilla et. al. [8] in thermally aged PM2000. The core composition of the Al/Ti rich clusters in this study was close to the β' phase ($Fe_2AlTi_{0.6}Cr_{0.4}$) proposed in [8].

Table 2. Quantitative results on Cr-rich clusters in neutron irradiated PM2000

Irradiation Temp. (°C)	Dose (dpa)	Avg. Radius (nm)	Density (m^{-3})	Avg. Core Fe (at. %)	Avg. Core Cr (at. %)	Avg. Core Al (at%)
285 ± 20	50.7	1.49 ± 0.11	1.44 x 10^{24}	45.4 ± 3.3	43.0 ± 3.1	8.86 ± 0.6
335 ± 20	4.5	1.43 ± 0.12	3.95 x 10^{24}	43.5 ± 3.4	45.9 ± 3.6	9.60 ± 0.8
449 ± 20	5.5	1.57 ± 0.08	1.72 x 10^{24}	45.9 ± 2.4	45.2 ± 2.4	9.82 ± 0.5
500 ± 20	8.7	4.83 ± 0.72	2.43 x 10^{23}	39.9 ± 5.9	51.4 ± 7.7	7.51 ± 1.1

Table 3. Quantitative results on Al/Ti rich clusters in neutron irradiated PM2000

Irradiation Temp. (°C)	Dose (dpa)	Avg. Radius (nm)	Density (m^{-3})	Avg. Core Fe (at. %)	Avg. Core Cr (at. %)	Avg. Core Al (at%)	Avg. Core Ti (at%)
285 ± 20	50.7	n/a	0	n/a	n/a	n/a	n/a
335 ± 20	4.5	n/a	0	n/a	n/a	n/a	n/a
449 ± 20	5.5	1.66 ± 0.68	2.99×10^{22}	55.6 ± 22.7	18.9 ± 7.7	14.4 ± 5.9	8.7 ± 3.5
500 ± 20	8.7	5.29 ± 1.16	1.13×10^{23}	50.4 ± 11.0	13.4 ± 2.9	19.6 ± 4.3	14.4 ± 3.2

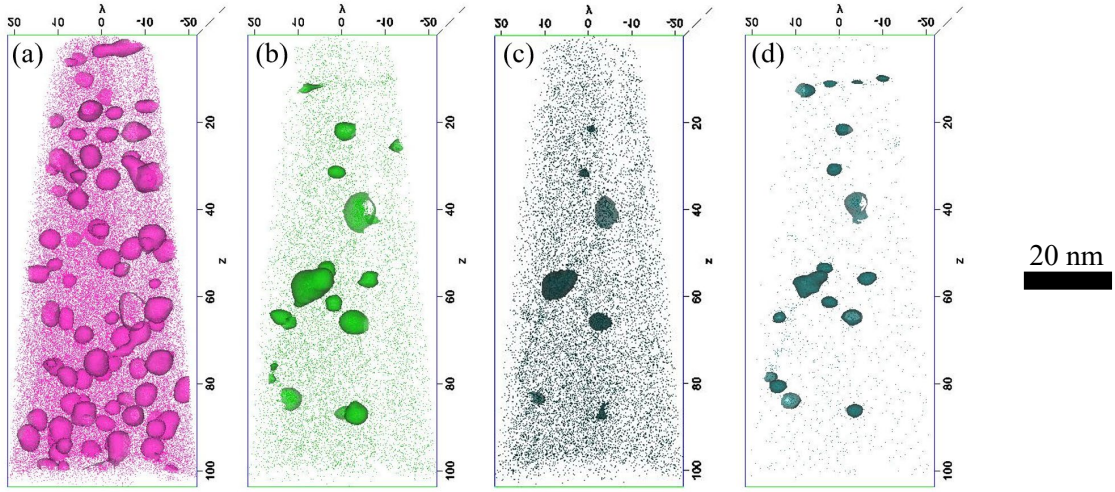

Figure 2. Atom maps from MA957 irradiated at 500°C to 8.7 dpa. (a) Cr map with 25 at. % iso-surfaces (b) Ni map with 3 at. % iso-surfaces (c) Ti map with 3 at. % iso-surfaces (d) TiO map with 2 at. % iso-surfaces.

Select atom maps from a typical volume of neutron irradiated MA957 after 8.7 dpa at 500°C are provided in Figure 2. Like PM2000, Cr-rich clusters was also observed in MA957 at all irradiation conditions. Table 4 contains size, density, and compositional information. The formation of α' in MA957 under irradiation at 500°C is somewhat surprising given that at 500°C the solubility limit of Cr in Fe is close to 14 wt. % according to [3]. By comparison, α' was observed in MA957 containing 13.8 wt. % Cr after irradiation in the Fast Flux Test Facility–Materials Open Test Assembly (FFTF–MOTA) to 109 – 113 dpa at 412°C, but not at 550 and 670°C [9]. In this study, Cr-rich clusters appear to coarsen from 335 – 500°C as irradiation temperature increases. Interestingly, the Cr-rich clusters also seem to coarsen at 285 – 335°C with increasing dose. As α' is expected to reach equilibrium by ~1 dpa [7], this result needs to be further understood. As an alternative to coarsening, it is also possible that during irradiation at 285°C to 50.7 dpa, ballistic effects may have caused the dissolution of smaller clusters. For all irradiation conditions, measured Cr cluster core concentration was less than fully mature α' (80 – 90 at. % Cr). Further work is needed to determine whether this is due to APT trajectory aberrations or if α' formation is being suppressed.

Table 4. Quantitative results for Cr-rich clusters in neutron irradiated MA957

Irradiation Temp. (°C)	Dose (dpa)	Avg. Radius (nm)	Density (m^{-3})	Avg. Core Fe (at. %)	Avg. Core Cr (at. %)
285 ± 20	50.7	1.68 ± 0.10	1.44×10^{24}	43.0 ± 2.5	53.9 ± 3.1
335 ± 20	4.5	1.16 ± 0.05	3.95×10^{24}	53.6 ± 2.4	44.9 ± 2.0
449 ± 20	5.5	1.35 ± 0.06	1.72×10^{24}	49.1 ± 2.0	49.3 ± 2.0
500 ± 20	8.7	1.95 ± 0.11	2.43×10^{23}	38.5 ± 2.3	60.2 ± 3.5

In addition to Cr-rich clusters, Ni/Ti rich clusters were also observed in MA957. This is consistent with previous work, where multivariate statistical analysis (MVSA) was used to characterize scanning transmission electron microscopy (STEM) high through-put energy dispersive X-ray spectroscopy (EDS) maps of MA957 following irradiation at 285°C to 50.7 dpa [10]. Table 5 contains size, density, and compositional information for each irradiation condition. After irradiation at 500°C, Ni and Ti enrichment was most pronounced, and clusters also included ~ 3 at. % Si. For irradiations between 285 and 449°C, a portion of the Ni/Ti rich clusters were found at the interface of the oxides. In contrast, following the irradiation at 500°C, almost all Ni/Ti clusters were associated with an oxide. With respect to dose, Ni/Ti clusters continued to nucleate beyond 4.5 – 8.7 dpa and roughly doubled in number density by 50.7 dpa. The ratio of Ni to Ti in these clusters was ~2. As this ratio does not match with any common precipitate phase, the clusters do not seem to be secondary phase particle precursors. Given that Ni, Ti, and Si were observed enriching grain boundaries, it is possible that the formation of these Ni/Ti clusters is caused by radiation induced segregation, especially to the interface of the oxides.

Table 5. Quantitative results from Ni/Ti rich clusters in neutron irradiated MA957

Irradiation Temp. (°C)	Dose (dpa)	Avg. Radius (nm)	Density (m^{-3})
285 ± 20	50.7	1.68 ± 0.10	1.44×10^{24}
335 ± 20	4.5	1.16 ± 0.05	3.95×10^{24}
449 ± 20	5.5	1.35 ± 0.06	1.72×10^{24}
500 ± 20	8.7	1.95 ± 0.11	2.43×10^{23}

Irradiation Temp. (°C)	Dose (dpa)	Avg. Core Fe (at. %)	Avg. Core Cr (at. %)	Avg. Core Ni (at. %)	Avg. Core Ti (at. %)	Avg. Core Si (at. %)
285 ± 20	50.7	67.6 ± 4.9	7.2 ± 0.5	12.0 ± 0.9	3.8 ± 0.3	0.6 ± 0.0
335 ± 20	4.5	65.7 ± 8.2	9.3 ± 1.2	12.6 ± 1.6	6.1 ± 0.8	1.2 ± 0.1
449 ± 20	5.5	48.1 ± 5.2	8.7 ± 0.9	12.7 ± 1.4	6.1 ± 0.7	0.9 ± 0.1
500 ± 20	8.7	72.8 ± 13.1	6.6 ± 1.2	21.4 ± 3.8	11.9 ± 2.1	3.3 ± 0.6

Future Work

Further analysis to determine the effect of neutron irradiation on the oxides in MA957 will be conducted. The results from this study will be applied to the dispersed barrier hardening model to determine expected change in yield strength under irradiation. The calculated changes in yield strength will be compared to microhardness and tensile data recently collected from these irradiated alloys. To expand upon the current APT results, TEM characterization of PM2000 and MA957 after 8.7 dpa at 500°C will be conducted. Finally, additional APT experiments involving another ODS variant, 12YWT (12% Cr base), irradiated in HFIR in the same campaign may be performed to elucidate the role of initial sink strength on LTHE.

References

[1] Bhattacharya, A., et al. "Neutron irradiation induced hardening in RAFM and ODS steels." DOE/ER-O313/69, Volume 69, December 31, 2020.
[2] Levine, S., et al. "Development of Open-Source, High-Fidelity APT Data Analysis Algorithms for Characterizing Nuclear Structural Materials." DOE/ER-O313/69, Volume 69, December 31, 2020.
[3] Xiong, W., et al. "Phase Equilibria and Thermodynamic Properties in the Fe-Cr System", Critical Reviews in Solid State and Materials Sciences, 35:2 (2010): 125-152.
[4] Edmondson, P., et al. "Irradiation-enhanced α' precipitation in model FeCrAl alloys." Scripta Mater., 116 (2016): 112-116.
[5] Massey, C., et al. "Deconvoluting the Effect of Chromium and Aluminum on the Radiation Response of Wrought FeCrAl Alloys After Low-Dose Neutron Irradiation." J. Nucl. Mater., 549 (2021): 152804.
[6] Li, W. et. al. "The effect of Al on the 475 C embrittlement of Fe–Cr alloys." Comp. Mater. Sci., 74 (2013): 101-106.

[7] Bergner, F., et. al. "Estimation of the solubility limit of Cr in Fe at 300 C from small-angle neutron scattering in neutron-irradiated Fe–Cr alloys." *Scripta Mater.,* 61:11 (2009): 1060-1063.
[8] Capdevilla et al. “Strengthening by intermetallic nanoprecipitation in Fe–Cr–Al–Ti alloy”. Acta Mater., 107 (2016): 27-37.
[9] Bailey, N., et al. "Atom probe tomography analysis of high dose MA957 at selected irradiation temperatures." J. Nucl. Mater., 459 (2015): 225-234.
[10] Levine, S., et. al. “Neutron irradiation induced phase separation in oxide dispersion strengthened alloys.” ORNL/TM2020/1837, December 2020.

3. CERAMIC COMPOSITE STRUCTURAL MATERIAL DEVELOPMENT

3.1 X-RAY CHARACTERIZATION OF ANISOTROPIC DEFECT FORMATION IN SiC UNDER IRRADIATION WITH APPLIED STRESS—Takaaki Koyanagi, Yutai Kato (Oak Ridge National Laboratory), David J. Sprouster, Lance Snead (Stony Brook University)

Extended abstract of a manuscript in Scripta Materialia 197 (2021) 113785

Irradiation creep can be a serious life limiting factor for nuclear fusion reactor core components. In silicon carbide (SiC) materials, which possess very limited strain tolerance, irradiation creep could be an important stress mitigating mechanism. High-energy x-ray diffraction (XRD) is employed to gain insight into the irradiation-induced creep behavior of SiC (Figure 1). Polycrystalline β-SiC specimens were simultaneously exposed to elevated temperature neutron-irradiation and mechanically applied stresses. The structural disordering was subsequently examined using two-dimensional x-ray diffraction. The intensity of the (111) shoulder peak, an indication of stacking disorder, increased when the specimens were irradiated under tensile stress (Figure 2). This is the first observation of nanoscale stress-induced stacking disorder in SiC at low neutron fluences. These findings suggest stress-induced preferential nucleation and/or growth of defect clusters as a key creep mechanism in neutron irradiated SiC.

Figure 1. Experimental procedure for the XRD experiment: (a) appearance of creep specimen, (b) preparation of the specimen for XRD, and (c) XRD setup.

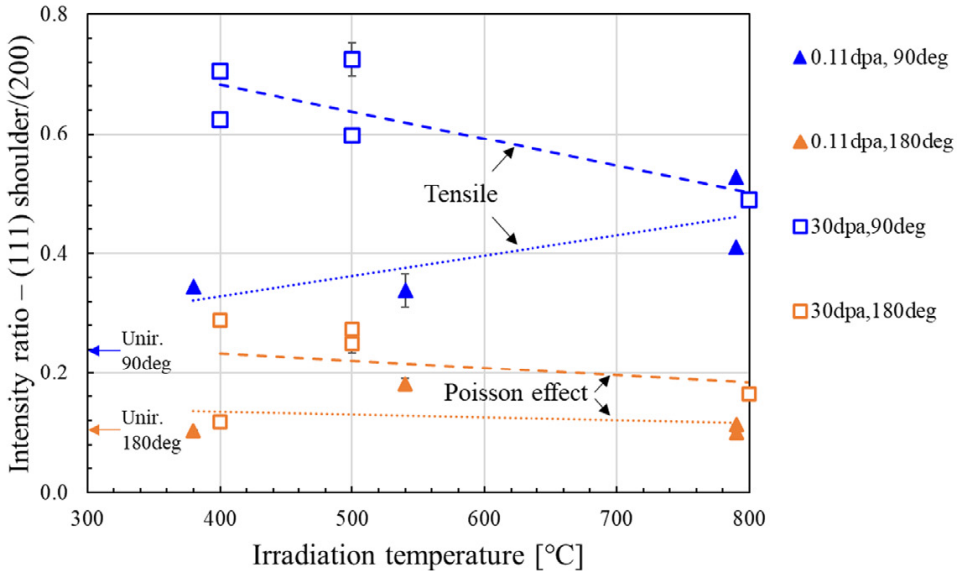

Figure 2. Intensity of (111) shoulder peaks normalized to that of (200): irradiation temperature and neutron damage dependences for 90 ±5 ° (tensile) and 180 ±5 ° (Poisson effect) azimuth slices from the 2D detector. The dotted lines are drawn for better visibility of the data trend.

4. PLASMA-FACING AND HIGH HEAT FLUX MATERIALS AND COMPONENT TESTING

4.1 PROPERTIES AND CHARACTERIZATION OF THE 2nd GENERATION OF Cu-Cr-Nb-Zr ALLOYS FOR FUSION ENERGY APPLICATIONS—Ying Yang, Ling Wang (Oak Ridge National Laboratory), Steven Zinkle (University of Tennessee), Lance Snead (Stony Brook University)

OBJECTIVE

This study aims at developing high creep strength and high thermal conductivity Cu-Cr-Nb-Zr alloys with reduced Nb contents for long pulse fusion high heat flux structures, through an accelerated approach of computational thermodynamics guided alloy design.

SUMMARY

Work performed during the reporting period (01/01/2021-06/30/2021) is to design a second generation of Cu-Cr-Nb-Zr alloys, to investigate the creep properties of the newly developed alloys, and to compare the creep properties with the reference 1st generation Cu-Cr-Nb-Zr and commercial CuCrZr alloys at 500°C in protective Ar atmospheres under various applied stress levels.

PROGRESS AND STATUS

In previous work [1,2], we have successfully developed 1st generation of Cu-Cr-Nb-Zr (CCNZ) alloys with improved creep properties. However, due to the high Nb content in those alloys, clustered laves Cr_2Nb phase was observed to have solidified from the liquid, which can serve as crack initiation sites. In addition, the high Nb content is also undesirable because it will increase residual radioactivity in fusion applications.

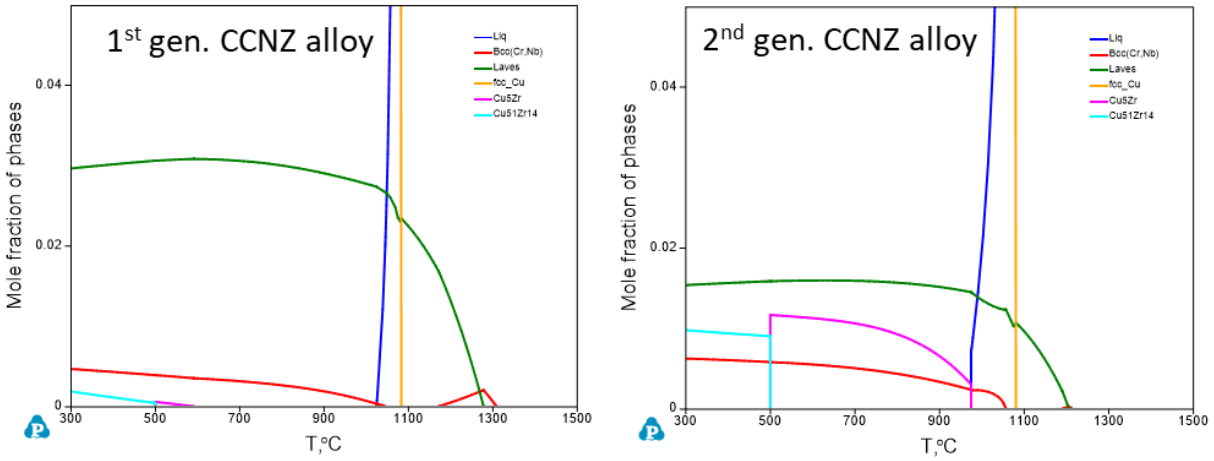

Figure 1. Calculated mole fractions of various precipitate vs temperature in the 1st and 2nd generation of CCNZ alloys.

In FY2021, we designed the 2nd generation of CCNZ alloy with reduced Nb content. The composition design was aided by computational thermodynamics. The comparison on calculated precipitate fraction vs temperature between the 1st and 2nd CCNZ alloys are shown in Figure 1, showing the following several improvements: 1) the melting temperature of laves_Cr2Nb in new alloy is lower, which helps to reduce the amount of clustered laves phase formed from the liquid; 2) we increased the amount of matrix precipitates including Cr and CuZr intermetallic compounds. We anticipate that more matrix precipitates will be beneficial to the material's overall strength. The ingot was made in an argon protected arc-melting furnace followed by drop-casting into the shape of 1.25 × 1.25 × 0.75 cm bar, with an approximate mass of 100 g. The as-cast bar was then subjected to multi-pass cold rolling at room temperature for a total 70% or 50% reduction in thickness. The as-rolled materials were solution annealed at 970 °C for 20 min, followed by

water quench. The final aging treatment was conducted at 475 °C for 3 h on the solutionized samples, followed by air cooling.

The aged samples were then subjected to creep testing in accordance with the American Society for Testing and Materials (ASTM) standard E139-11, Standard Test Methods for Conducting Creep, Creep-Rupture, and Stress-Rupture Tests of Metallic Materials. All tests used the type SS-3 miniature sheet tensile specimens that were machined from the cold-worked + solutionized + aged alloys, parallel to the rolling direction. The gauge section of the tensile specimen was of 7.62×1.52×0.76 mm. Tensile creep-rupture testing was conducted at 500 °C in inert gas environment under applied stress levels of 90, 110, and 125 MPa, using an extensometer which was not directly attached on the specimens but rather on the loading rod. The creep stress-strain curves of the 2nd gen. CCNZ alloy (CCNZ_HZ) are shown in Figure 2 and compared to those from the 1st gen. CCNZ alloy (CCNZ_HP) and the ITER grade (CCZ) alloy. The results suggested that the 2nd gen. CCNZ alloy has longer creep life than the 1st gen. CCNZ and CCZ alloy, especially for the higher applied stress levels. The creep strains for the 2nd gen. CCNZ alloy are also greater than those of the other two alloys.

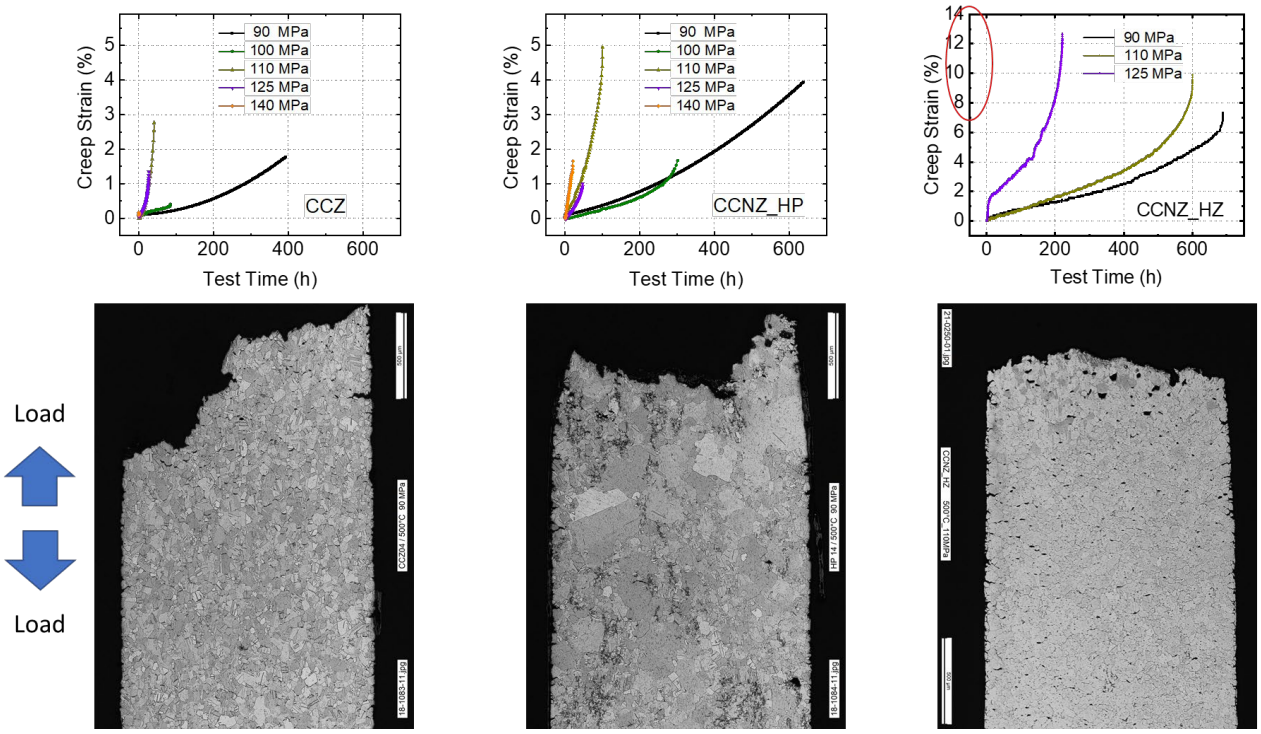

Figure 2. Creep stress strain curves of the CCZ, 1st gen. CCNZ and 2nd gen. CCNZ alloys tested at 500°C in inert gas atmosphere under various applied stress levels and the associated optical images at locations close to the fracture surface. The scale bar is 500μm bar in all three images.

The optical images at the location close to the fracture surface for the three alloys were also shown in Figure 2. The CCZ alloy shows no grain boundary precipitates, unimodal grain size and uniform crack distribution. The 1st gen. CCNZ alloy shows clustered and heterogeneous precipitates at grain boundaries, bimodal grain size and heterogenous crack distribution. The 2nd gen. CCNZ alloy shows uniformly distributed grain boundary precipitates, unimodal grain size and uniform crack distribution. The improved creep properties are believed to be associated with the presence of uniformly distributed grain boundary precipitates and may also be due to increased amount of matrix precipitates. Detailed TEM characterization on matrix precipitates is currently on going, together with in-depth creep mechanistic analysis.

Future Work

1) Continue TEM characterization and synchrotron XRD analysis to obtain the volume fraction, mean radius and number density of both grain boundary and matrix precipitates and correlate the precipitate characteristics with improved creep properties and the underlying mechanism.
2) Write a manuscript for the microstructure-property relationship in the 2nd CCNZ alloy and their comparison with that for the 1st CCNZ alloy and commercial CCZ alloy.

References

[1.] Yang, Y., Wang, L., Snead, L., & Zinkle, S. J. (2018). Development of novel Cu-Cr-Nb-Zr alloys with the aid of computational thermodynamics. Materials & Design, 156, 370-380.

[2.] Wang, L., Zheng, C., Kombaiah, B., Tan, L., Sprouster, D. J., Snead, L. L., ... & Yang, Y. (2020). Contrasting roles of Laves_Cr2Nb precipitates on the creep properties of novel CuCrNbZr alloys. Materials Science and Engineering: A, 779, 139110.

4.2 RADIATION ENHANCED GRAIN GROWTH IN TUNGSTEN AND TUNGSTEN ALLOYS—H. Gietl, T. Koyanagi, Y. Kato (Oak Ridge National Laboratory), X. Hu (Sichuan University)

OBJECTIVE

Tungsten (W) is the main plasma facing material under consideration for fusion devices. This task is evaluating material changes after neutron irradiation at 850 ˚C and above (nominally 1100˚C).

SUMMARY

Pure W and several W alloys were subjected to mixed spectrum neutron irradiation in HFIR at a temperature of 850 ˚C and above (nominally 1100˚C) with calculated fast fluences of 2.08 and 2.36×10^{25} n/m^2 (E > 0.1 MeV) (~0.42-0.47dpa). After neutron irradiation, softening and grain growth of W and W alloys was observed and the recrystallisation fraction was quantified by EBSD analysis. A quantitative predication of the shift in recrystallisation temperature during irradiation was made by considering radiation-enhanced diffusion.

PROGRESS AND STATUS

In fusion reactors, W is exposed to high temperatures which can lead to an alteration of the microstructure by recovery, recrystallisation and grain growth. These microstructural changes lead to a loss in strength, embrittlement, and an increased ductile to brittle transition temperature. Thus, it is important to analyze the recrystallisation under fusion reactor relevant temperatures with neutron interaction.

Microstructural analysis using SEM-EBSD (Figure 1) found significant grain growth after irradiation.

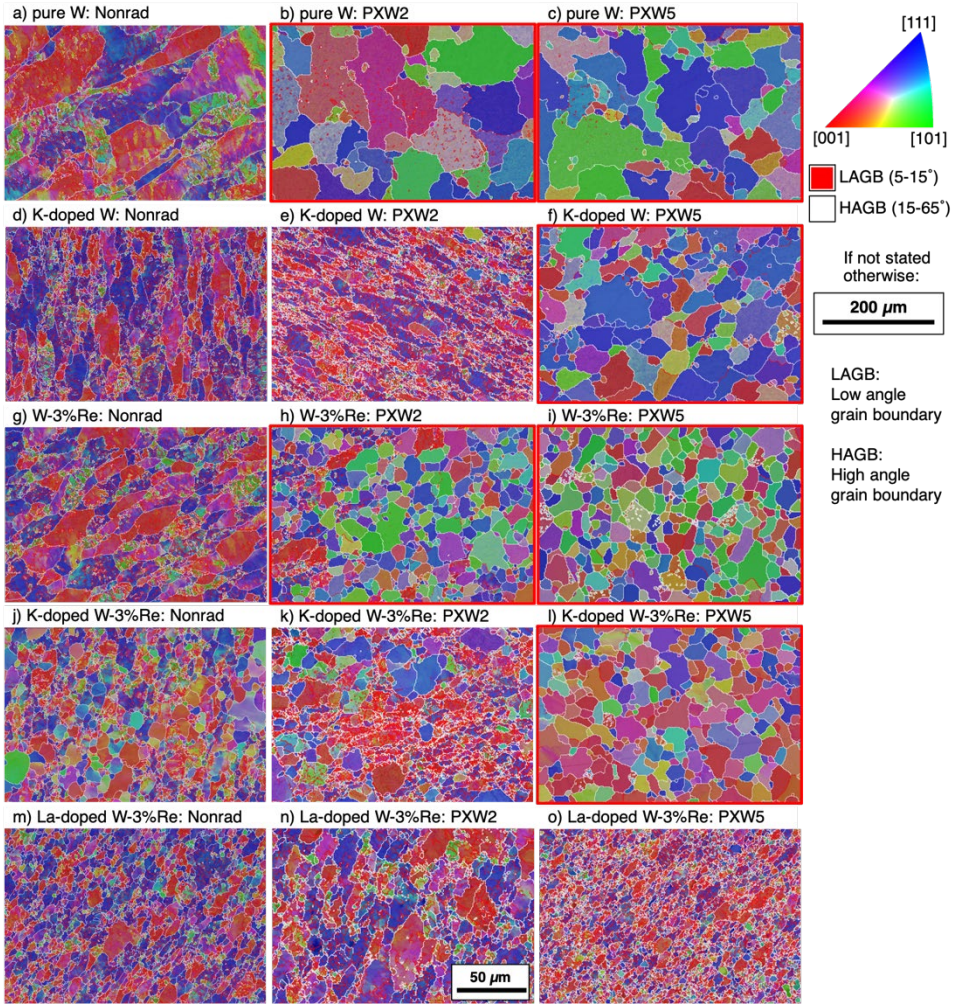

Figure 1. EBSD images of W and W alloys after neutron irradiation at different temperature (PXW2: 0.42 dpa at 850˚C and PXW5: 0.47 dpa at nominally 1100˚C)

In partially recrystallized samples, it is essential to distinguish between the grains which are already recrystallized and those which are not, to understand how recrystallization evolves. Such a procedure is always somewhat subjective because there is no precise definition for a recrystallized grain. There have been many parameters deduced from EBSD data for the discrimination of recrystallized grains and quantifying the recrystallization kinetics [1]. These are generally based on the quality of diffraction patterns [2] and measures of internal misorientations such as: the Grain Orientation Spread (GOS) [3], the Kernel Average Misorientation (KAM), and grain boundary analysis. Furthermore, the size and shape (i.e., aspect ratio) of recrystallized grains were considered in several cases. The misorientation-based method is the more reliable one for the identification of recrystallized grains. In addition, several papers have suggested the use of GOS to detect recrystallized grains [3-8]. Based on preliminary tests and reported evaluations [9, 10] a combination of three parameters was used to define a recrystallized grain. A grain was defined as recrystallized if

i) the internal misorientation within a grain is less than 1°,
ii) the area of a grain is larger than 70 μm^2 , and

iii) the grain is at least partially surrounded by high angle boundaries with misorientations larger than 15°.

The result of that evaluation is shown in Figure 2 and there is significant recrystallisation of W and W-3%Re if irradiated at 850 ˚C (irradiation ID: PXW2). After the irradiation at a nominal 1100 ˚C (irradiation ID: PXW5) nearly all W materials show recrystallisation. La-doped W-3%Re seems to be unaffected by both irradiation conditions.

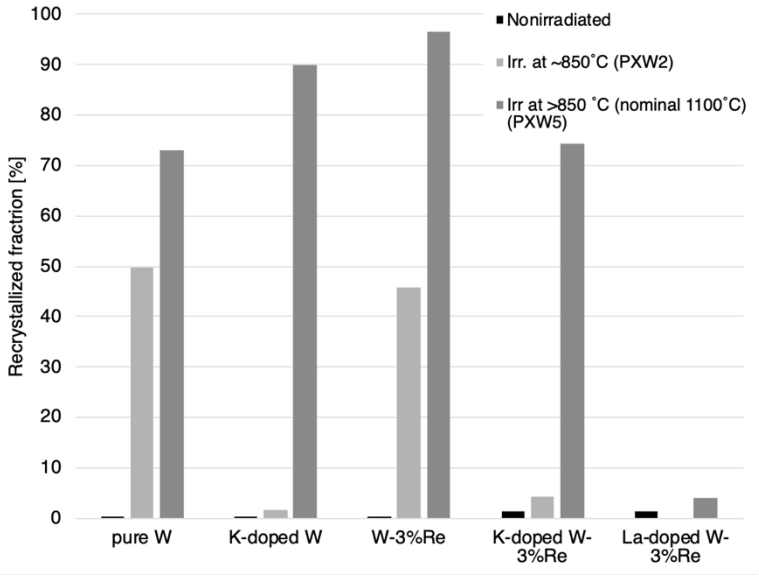

Figure 2. Calculated recrystallization fraction based on EBSD analysis after neutron irradiation.

The EBSD recrystallisation analysis is in good agreement with the softening seen for W and W alloys in this study (Figure 3).

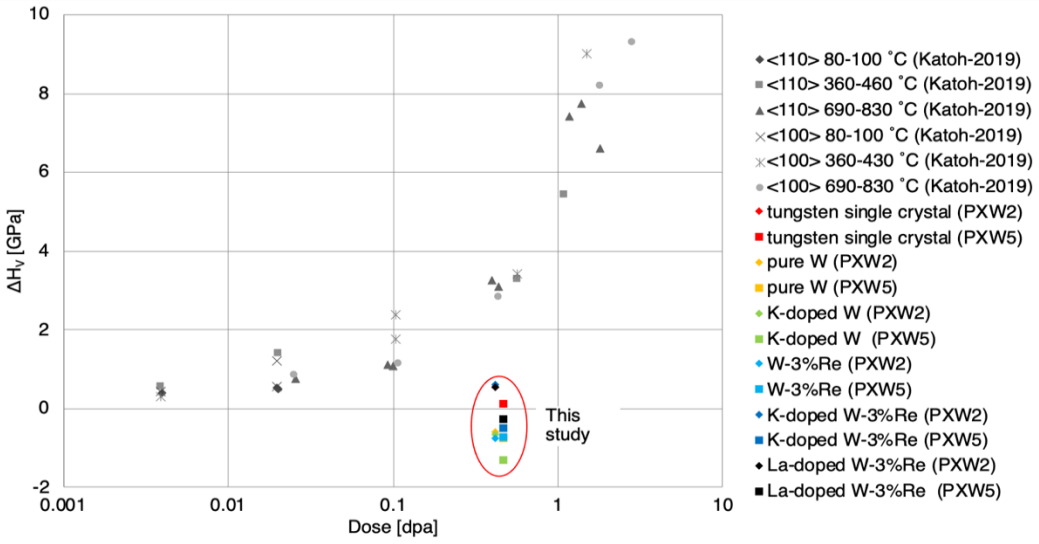

Figure 3. Comparison of hardness after neutron irradiation with literature values [11].

A quantitative predication of the shift in recrystallisation temperature during irradiation could be made by assuming that the acceleration of recrystallisation kinetics is solely due to radiation-enhanced diffusion [12]. The radiation enhanced diffusion coefficient (D_{rad}) is given as $D_{rad} = D_v C_v + D_i C_i$ ($D_{v,i}$ = diffusivity of vacancies or interstitials, $C_{v,i}$ = point defect concentration of vacancies or interstitials) [13-15]. The following equations and assumptions are based on [13-15]. For the calculations of D_{rad} three different temperature regions which are defined by the melting temperature (T_m) were considered: the low temperature ($T \lesssim 0.1 - 0.2\, T_m$), moderate temperature ($0.2\, T_m \lesssim T \lesssim 0.4\, T_m$), and high temperature region ($T \gtrsim 0.4 - 0.6\, T_m$). At low temperature the rate of thermal vacancy creation (K_{th}) is negligible and the concentration of irradiation-produced vacancies becomes high enough that direct recombination with interstitials begins to dominate over diffusion to fixed sinks.

In the low temperature region D_{rad} is calculated as: $D_i C_i \cong D_v C_v \cong \sqrt{\frac{D_i D_v K}{\alpha}}$ with K = atomic displacement rate, α = recombination coefficient $\cong \frac{4\pi(D_i + D_v)}{a^2}$ and a = lattice spacing. For $D_i \gg D_v$ follows $\alpha = \frac{4\pi D_i}{a^2}$ and is calculated with $D_{rad} \cong \sqrt{\frac{K D_v a^2}{4\pi}}$.

In the moderate temperature range, most vacancies and interstitials are lost to fixed sinks, which leads to: $D_i C_i \cong \frac{K}{k_i^2}$ and $D_v C_v \cong \frac{K}{k_v^2}$ with k_v^2 = fixed sink strength for vacancies ($k_v^2 = 4\pi \bar{r}_c \rho_c + Z_v \rho_d + k_{gb}^2$), k_i^2 = fixed sink strength for interstitials ($k_i^2 = 4\pi \bar{r}_c \rho_c + Z_i \rho_d + k_{gb}^2$), k_{gb}^2 = sink strength of grain boundaries ($k_{gb}^2 = \frac{6k}{d}$) (k = is the square root of sink strength for the grain interior due to dislocations and voids, d = grain size), $\bar{r}_c$ = mean void radius, ρ_c = void number density, ρ_d = dislocation line density and $Z_{v,i}$ = dislocation sink strength constant for vacancies or interstitials. This leads to $D_{rad} = \mathrm{K}\left(\frac{k_i^2 + k_v^2}{k_i^2 * k_v^2}\right) \approx \frac{2K}{k_i^2}$.

At the higher temperature ($T \gtrsim 0.4 - 0.6\, T_m$) the irradiation-induced defects anneal out very rapidly and, in addition $K_{th} \gg \mathrm{K}$. As such, the D_{rad} is neglectable at high temperature and the diffusion is equal to the thermal diffusion coefficient (D_{th}). As the calculation of D_{rad} strongly depends on the various sinks present in the material, D_{rad} was determined from available literature data of point defect of single crystal and polycrystalline W [16, 17]. In addition, D_{rad} of polycrystalline W - were grain boundaries act as strong sinks - is much smaller than D_{rad} of W single crystal. Based on the limited available data for high temperature irradiated W, the calculation is tentative and only values for pure W without any transmutation products were considered. Figure 4 shows the calculated temperature dependent diffusion coefficients for a damage production rate of 1.9×10^{-7} dpa/s which is equal to the W irradiated in this study. In addition, the thermal diffusion coefficient of W is given from Huang et al. [18].

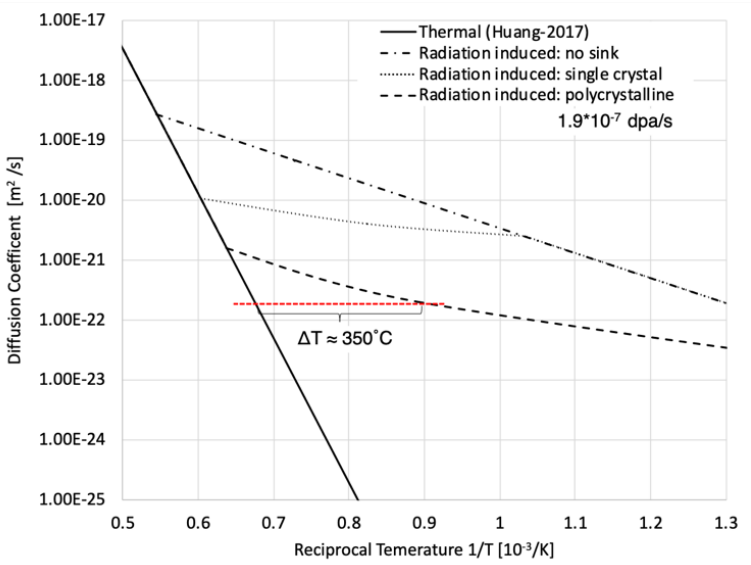

Figure 4. Thermal and radiation enhanced diffusion coefficient for W. The radiation enhanced diffusion coefficient at 850 ˚C is predicted to be comparable to the thermal diffusion coefficient at 1200 ˚C for polycrystalline tungsten. This results in a shift of 350 ˚C if irradiated at 850 ˚C, which is a reasonable explanation for the observed grain growth.

Without any sinks considered, D_{rad} increases rapidly until the thermal diffusion coefficient dominates the effects of irradiation-enhanced diffusion at around 1550˚C. The most reasonable case is that there are strong sinks present which lower D_{rad}. This leads to the result that the material irradiated at 850 ˚C in HFIR has a D_{rad} ~2×10^{-22}. This calculated D_{rad} is comparable to a thermal diffusion coefficient at ~1200˚C.

By comparing the calculated diffusion values with previous annealing experiments W and W alloys [19-21] for long term annealing above 1100 ˚C of pure W, softening caused by recovery and recrystallization is expected. The shown calculation for D_{rad} predicts that such material degradation in W can take place at lower temperatures.

However, the strong dependence of the recrystallisation of W on the manufacturing condition, such as degree of deformation [20, 21], makes it nearly impossible to generalize the results. In addition, transmutation products were not considered in these calculations. It is worth mentioning that Re and Os form dumbbells with W which are highly mobile. Nevertheless, it can be concluded that the neutron irradiation increases the diffusion coefficient which can lead to a premature grain growth in W compared to only thermal annealing and thus narrows the design space for tungsten in fusion reactors.

Future Plans

Reference samples are currently annealed and will be examined. This evaluation will give insights in neutron irradiation contribution to the grain growth kinetics.

References

[1.] Schwartz, A.J., et al., *Electron backscatter diffraction in materials science*. Vol. 2. 2009: Springer.

[2.] Tarasiuk, J., P. Gerber, and B. Bacroix, *Estimation of recrystallized volume fraction from EBSD data.* Acta materialia, 2002. **50**(6): p. 1467-1477.
[3.] Field, D.P., *Quantification of partially recrystallized polycrystals using electron backscatter diffraction.* Materials Science and Engineering: A, 1995. **190**(1-2): p. 241-246.
[4.] Alvi, M.H., et al., *Cube texture in hot-rolled aluminum alloy 1050 (AA1050)—nucleation and growth behavior.* Acta materialia, 2008. **56**(13): p. 3098-3108.
[5.] Barbier, D., et al., *Microstructures resulting from the interaction between ferrite recrystallization and austenite formation in dual-phase steels.* Journal of Materials Science, 2015. **50**(1): p. 374-381.
[6.] Diehl, M., et al., *Site-specific quasi in situ investigation of primary static recrystallization in a low carbon steel.* Materials Science and Engineering: A, 2019. **755**: p. 295-306.
[7.] Gerber, P., et al., *Estimation of the recrystallized volume fraction from local misorientation calculations.* Archives of Metallurgy and Materials, 2005. **50**(3): p. 747.
[8.] Rollett, A.D., M.L. Taheri, and B.S. El-Dasher. *Texture-Dependent measurement of recrystallization kinetics using electron backscatter diffraction*. in *Plasticity'02: the 9 th Intl. Symposium on Plasticity and its Current Applications*. 2002. Citeseer.
[9.] Ayad, A., et al., *Quantifying primary recrystallization from EBSD maps of partially recrystallized states of an IF steel.* Materials Characterization, 2021. **171**: p. 110773.
[10.] Lopez, A.A., *Thermal stability of warm-rolled tungsten.* Fusion Engineering and Design (FED), 2015. **98**(99): p. 1924-1928.
[11.] Katoh, Y., et al., *Response of unalloyed tungsten to mixed spectrum neutrons.* Journal of Nuclear Materials, 2019. **520**: p. 193-207.
[12.] Zinkle, S., G. Kulcinski, and L. Mansur, *Radiation-enhanced recrystallization in copper alloys.* Journal of Nuclear Materials, 1986. **141**: p. 188-192.
[13.] Sizmann, R., *The effect of radiation upon diffusion in metals.* Journal of Nuclear Materials, 1978. **69**: p. 386-412.
[14.] Russell, K.C., *Phase stability under irradiation.* Progress in Materials Science, 1984. **28**(3-4): p. 229-434.
[15.] Was, G.S., *Fundamentals of radiation materials science: metals and alloys*. 2016: springer.
[16.] Fukuda, M., et al., *Neutron energy spectrum influence on irradiation hardening and microstructural development of tungsten.* Journal of Nuclear Materials, 2016. **479**: p. 249-254.
[17.] Koyanagi, T., et al., *Microstructural evolution of pure tungsten neutron irradiated with a mixed energy spectrum.* Journal of Nuclear Materials, 2017. **490**: p. 66-74.
[18.] Huang, C.-H., et al., *Mechanism of nucleation and incipient growth of Re clusters in irradiated W-Re alloys from kinetic Monte Carlo simulations.* Physical Review B, 2017. **96**(9): p. 094108.
[19.] Tsuchida, K., et al., *Recrystallization behavior of hot-rolled pure tungsten and its alloy plates during high-temperature annealing.* Nuclear Materials and Energy, 2018. **15**: p. 158-163.
[20.] Alfonso, A., et al., *Thermal stability of a highly-deformed warm-rolled tungsten plate in the temperature range 1100–1250° C.* Fusion Engineering and Design, 2015. **98**: p. 1924-1928.
[21.] Alfonso, A., et al., *Recrystallization kinetics of warm-rolled tungsten in the temperature range 1150–1350 C.* Journal of Nuclear Materials, 2014. **455**(1-3): p. 591-594.

4.3 ELECTRICAL CONDUCTIVITY EVALUATION OF NEUTRON IRRADIATED TUNGSTEN MATERIALS FROM THE PHENIX COLLABORATION—J. R. Echols, L. M. Garrison (Oak Ridge National Laboratory)

OBJECTIVE

The goal of the PHENIX collaboration is to expand the database on neutron irradiation effects in tungsten materials. This task evaluates the effects of irradiation at elevated temperatures on electrical resistivity.

SUMMARY

Electrical resistivity measurements conducted on single and polycrystalline tungsten samples exposed to neutron radiation between 0.2 and 0.7 displacements per atom (dpa) show increased resistivity, but dpa alone cannot explain the trends. Re content, rather, appears to be the dominant effect. Results examining the effects of grain orientation in polycrystalline samples with elongated grains show measurable variation in resistivity depending on sample orientation with respect to the applied current. This variation is used to calculate grain boundary resistivity in the direction of the current.

PROGRESS AND STATUS

The US-Japan collaboration, PHENIX, aims to investigate tungsten and tungsten-based materials' (>1500 total samples) response to neutron irradiation for use in future fusion reactors. These samples were exposed to neutron radiation in the RB*19J irradiation capsule in the High Flux Isotope Reactor (HFIR) to doses of ~0.2-0.7 dpa. Irradiation temperatures (measured/calculated through SiC thermometry and extrapolation) for three different subcapsules were 430-670, 740-960, and 880-1080°C. A gadolinium shield was utilized to reduce the thermal neutron flux, and therefore the rate of W to Re/Os transmutations, to more fusion relevant values than previous irradiations such as TITAN.

Tungsten's high thermal conductivity is critical for its use in future fusion reactors and is one of the reasons tungsten is the leading candidate material for high heat flux regions of reactors. Neutron irradiation in a reactor environment, however, degrades the thermal conductivity of tungsten. To separate the phonon and electron contributions to thermal conductivity, and the transmutant element contributions to scattering-induced loss of thermal conductivity, electrical conductivity measurements need to be taken and compared against thermal conductivity measurements. For the purposes of this report, electrical resistivity (the inverse of conductivity) is given. The details of this calculation can be found in previous reports [1]. Testing was conducted at room temperature and normalized to 20°C

Small, 3mm diameter testing disks provided two distinct advantages. First, limiting the dose to the testing individual. Second, the uniform geometry (for example, compared to tensile bars) allows samples with elongated grains to be rotated such that the grain boundary density in the direction of the current varies. Figure 1 shows a diagram of the resistivity testing apparatus used and how rotation affects the grain boundary (GB) density

Resistivity was measured for thick plate ALMT-produced polycrystalline tungsten (PCW) with elongated grains (material codes AT and BT) and single-crystal tungsten (SCW, material code UE). For the PCW samples, samples were cut in different orientations with respect to the elongated grains: A – where grains are equiaxed relative to the applied current, and B – where grains are not equiaxed relative to the applied current. Resistivity results as a function of calculated dpa are shown in Figure 2. In general, there is no simple trend between resistivity and DPA. Notably, significant grain growth has been observed in some materials from the 880-1080°C capsule, so the highest temperature samples may be expected to have

significant changes in microstructure. GB effects will be discussed in more detail further in this report. However, the reduction in total GBs crossed may be a cause of the reduction in resistivity observed in the samples from the highest temperature capsule.

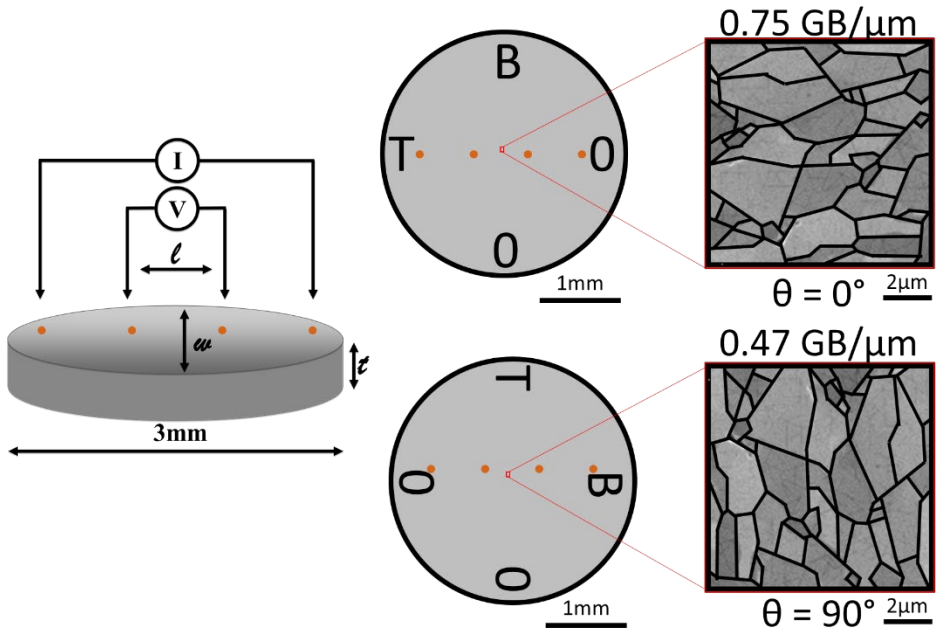

Figure 1. (Left) Diagram of 3mm electrical resistivity testing device. Cu electrodes are shown in orange. (Right) Effect of sample orientation and GB density in the direction of the current. Rotating samples with elongated grains will capture different GB densities in resistivity measurements. Although sample ID engraving is shown, engraving is always opposite the measurement side.

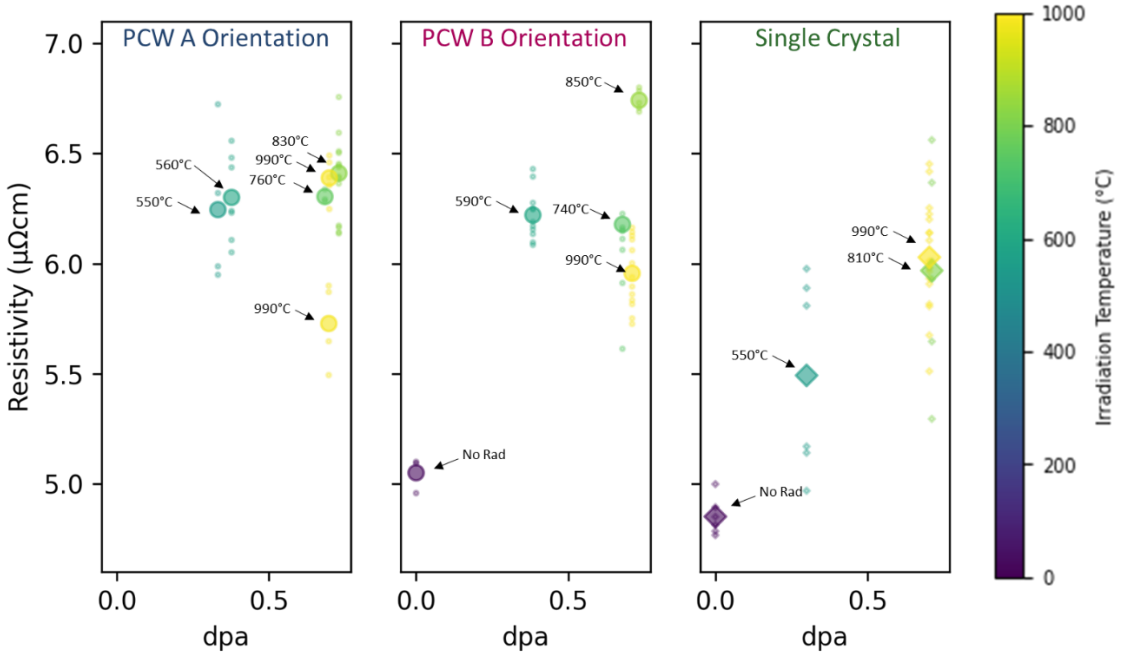

Figure 2. Electrical resistivity, as a function of dpa, for SCW and PCW materials. Irradiation temperature estimates are indicated by color with callouts in the figure. Average values are shown in large, solid marks with individual measurements given with smaller, lighter marks.

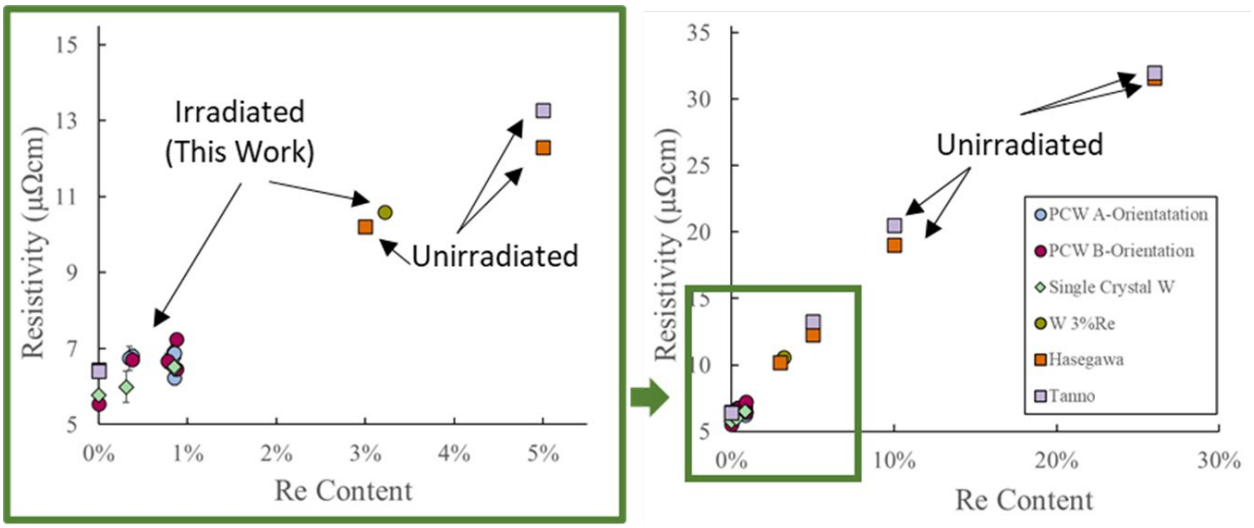

Figure 3. Electrical resistivity, as a function of calculated Re content, for SCW and PCW materials, compared directly with unirradiated W-Re alloys from Hasegawa [2] and Tanno [3].

Transmutant Re (which has an almost 4× higher resistivity, ~19.3 μΩcm, than tungsten, ~5.3) presents a compelling trend when compared to the observed resistivity changes. In Figure 3, we plot expected transmutant Re content (calculated at time of capsule exit from HFIR) against measured resistivity. In addition to the SCW and PCW samples discussed earlier, a single W-3%Re alloyed sample (pre-irradiation)

is included. These values are shown alongside those from unirradiated W-Re alloys produced and measured by Hasegawa [2] and Tanno [3]. We find our samples to fall along the trend observed in these works, suggesting that Re transmutation may play a dominant effect in changes to electrical resistivity upon irradiation. Notably, both authors report resistivities of ~5.9 μΩcm for the pure W case, which is ~15% greater than our reported value of ~5.1 μΩcm for B-orientation PCW (which is also more in-line with literature values of tungsten's resistivity).

Measurement on angular dependence of resistivity for a range of samples is shown in Figure 4. Unirradiated and low-temperature irradiated B-series PCW (which doesn't have equiaxed grains relative to the current for different rotations) shows a resistivity that oscillates with measurement angle. However, samples which are likely recrystallized (BT08), equiaxed relative to the current (AT01) or have no grains (UE06), do not exhibit this behavior. Sine fits (constrained to a period of 180°) were applied to the oscillatory data and the amplitude in these fits is taken as the GB effect on resistivity.

In Figure 5, peak, midpoint, and trough resistivities from the oscillatory samples are plotted against the maximum, mid, and minimum GB densities measured in [4]. Applying a linear fit to this data, we can estimate the resistivity-per-GB in the direction of the current for each irradiation condition. Resistivity with respect to DPA is shown in Figure 6 – with and without subtracting the calculated GB effects. When subtracting the GB effects, the PCW data falls into relatively good agreement with the SCW data

Future Plans

Future work will attempt to generalize these observations into a mathematical framework and make comparisons between resistivity and thermal conductivity.

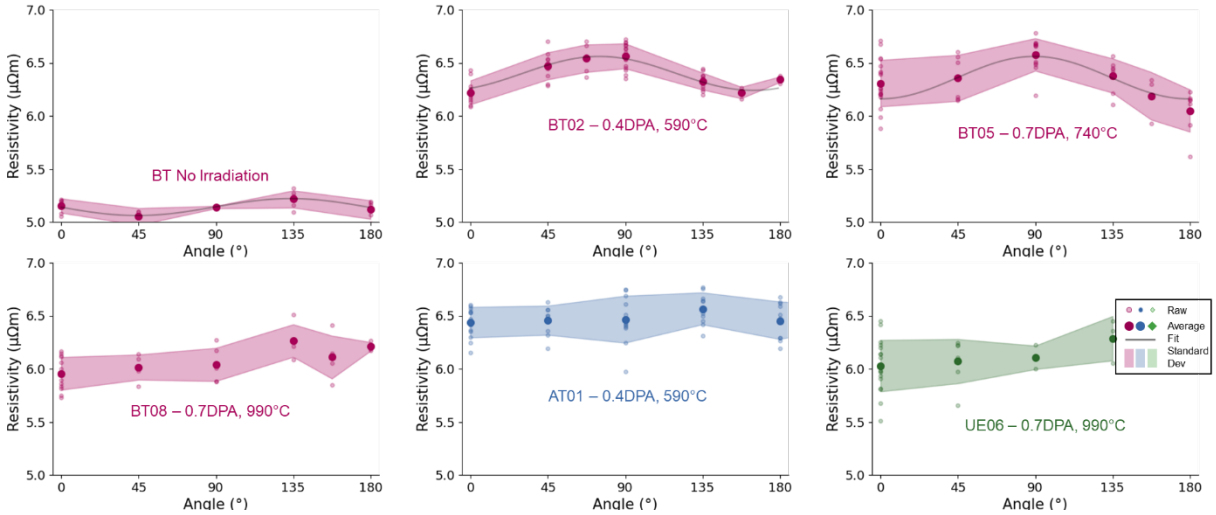

Figure 4. Resistivity of B-orientation samples as a function of arbitrary measurement angle. Average values are shown in large, solid marks with individual measurements given with smaller, lighter marks. A sine wave fit is shown in the first row, approximating expected resistivity for any angle. Samples in the bottom row exhibit no such orientation dependence. The 0° angle is arbitrary for each sample.

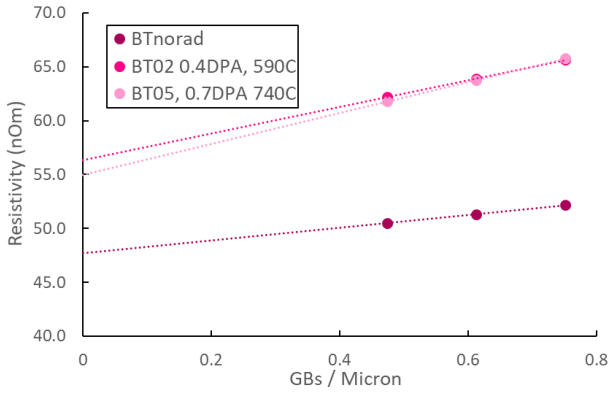

Figure 5. BT-series resistivity averages plotted against GB density in the direction of the current, with a linear fit applied to approximate the zero-grain case.

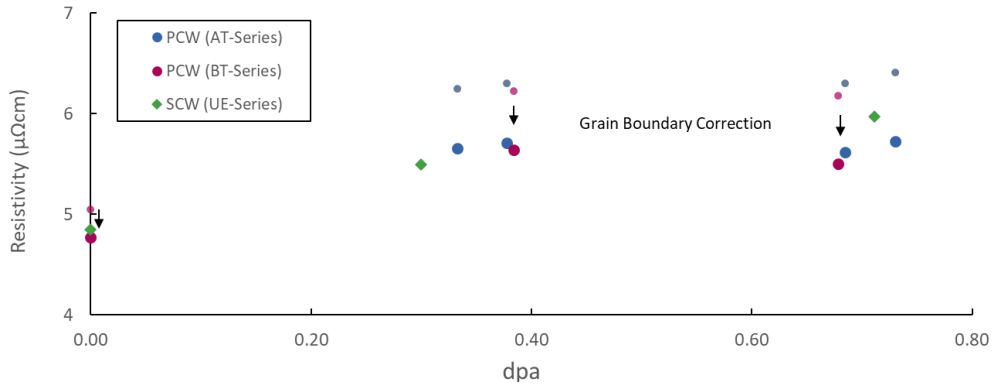

Figure 6. Adjustments to measured resistivity based on removing the fitted GB effects. Small circles represent unmodified resistivity results, while large circles represent the adjusted results which remove GB effects.

References

[1] Echols, John et al. " ELECTRICAL CONDUCTIVITY EVALUATION OF NEUTRON IRRADIATED TUNGSTEN MATERIALS FROM THE PHENIX CAMPAIGN." Fusion Materials Research at Oak Ridge National Laboratory in Fiscal Year 2020 (2020).

[2] Hasegawa, Akira, et al. "Property change mechanism in tungsten under neutron irradiation in various reactors." Journal of nuclear materials 417.1-3 (2011): 491-494.

[3] Tanno, T., et al. "Effects of transmutation elements on the microstructural evolution and electrical resistivity of neutron-irradiated tungsten." Journal of Nuclear Materials 386 (2009): 218-221.

[4] Garrison, Lauren, et al. "4.6 MICROSTRUCTURE AND MECHANICAL PROPERTIES OF TUNGSTEN IN THE PHENIX COLLABORATION IRRADIATION." Fusion Materials Research at Oak Ridge National Laboratory in Fiscal Year 2017 (2017): 45.

4.4 THERMAL TRANSPORT EVALUATION OF NEUTRON IRRADIATED TUNGSTEN MATERIALS FROM THE PHENIX AND TITAN COLLABORATIONS—J. R. Echols, L. M. Garrison, Y. Katoh (Oak Ridge National Laboratory)

OBJECTIVE

The goal of the PHENIX and TITAN collaborations is to expand the database on neutron irradiation effects in tungsten materials. This task evaluates the effects of neutron dose, thermal neutron shielding, and temperature on the thermal transport in single and poly-crystalline tungsten.

SUMMARY

Thermal diffusivity measurement is underway for samples irradiated in the PHENIX and TITAN campaigns at Oak Ridge National Laboratory. A phased plan has been developed to quickly provide insight into variables captured by these campaigns, including irradiation temperature, fluence, and shielding of thermal neutrons. Initial thermal diffusivity measurements have been completed on unirradiated, single crystalline tungsten.

PROGRESS AND STATUS

The TITAN and PHENIX programs neutron irradiated thousands of tungsten and tungsten alloy samples in the High Flux Isotope Reactor (HFIR) at Oak Ridge National Laboratory. These samples were irradiated at a variety of fluences (0.02-20 $x10^{25}$ n/m^2, E>0.1MeV) and temperatures (100-1000°C). The PHENIX campaign utilized a Gd shield to filter out a large quantity of thermal neutrons (and therefore greatly reducing transmutation), while the TITAN campaign exposed samples to the full HFIR neutron spectrum. Tabs of tested tensile specimens from both campaigns can undergo thermal diffusivity testing at Oak Ridge. This presents a unique opportunity to greatly expand the thermal conductivity database of neutron irradiated tungsten, while investigating the effects of irradiation dose, temperature, and spectrum.

Figure 1 shows a comparison of the single crystalline tungsten (SCW) samples from both campaigns, while highlighting several planned phases of testing for these materials. Phase 1 focuses on evaluating the materials which have the most similar fast fluxes and temperatures, while varying the thermal shielding (and therefore transmutation) of the samples. Phase 2 focuses on the effects of varying temperature at low and high dose for unshielded material, while Phase 3 fills in the effects at mid-doses.

Diffusivity measurements are carried out on a Netzsch LFA467, which utilizes the laser-flash method of thermal diffusivity measurement. The tensile tab is thinly coated with a graphene spray to reduce reflectivity, then fitted to a custom fixture within the device, and finally placed under vacuum. A brief laser pulse (order 0.1ms) heats one side of the tab while the temperature on the other side is monitored to determine the rate of heat transfer through the material. An example curve is shown in Figure 2. For each sample, five measurements are taken at each testing temperature. Tests begin at room temperature, after which the device will heat the material and take additional measurements at 50°C increments up to the irradiation temperature (minus a safety margin). Measurements are taken in 100°C intervals back to room temperature to ensure that radiation damage has not been annealed out by exceeding the maximum radiation temperature (which would exhibit as an increase in diffusivity).

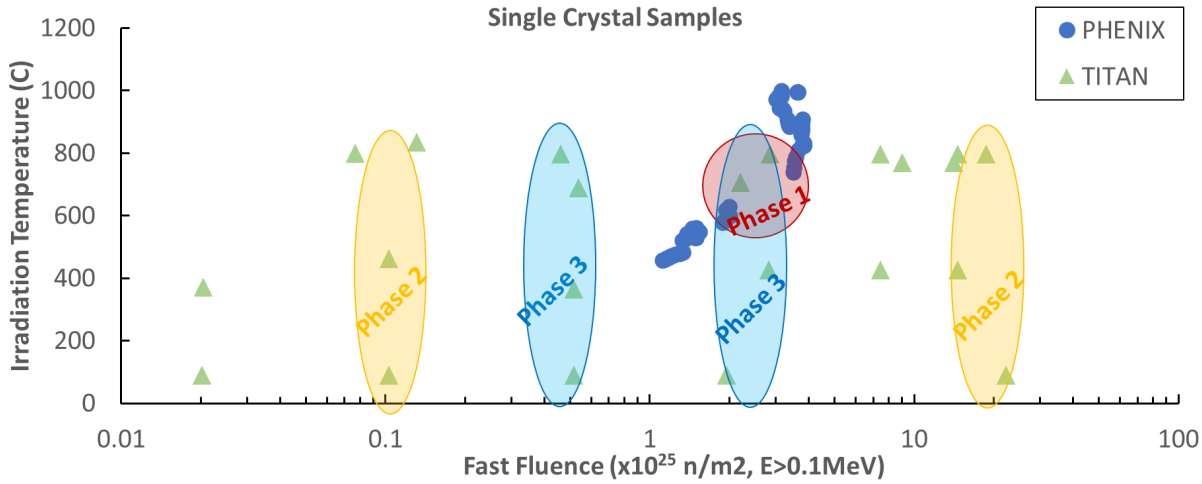

Figure 1. Temperature/fast fluence relationship for all SCW tungsten tensile samples from the PHENIX and TITAN projects. Initial work is divided up into phases (represented by the colored ovals) to maximize early insight into thermal effects.

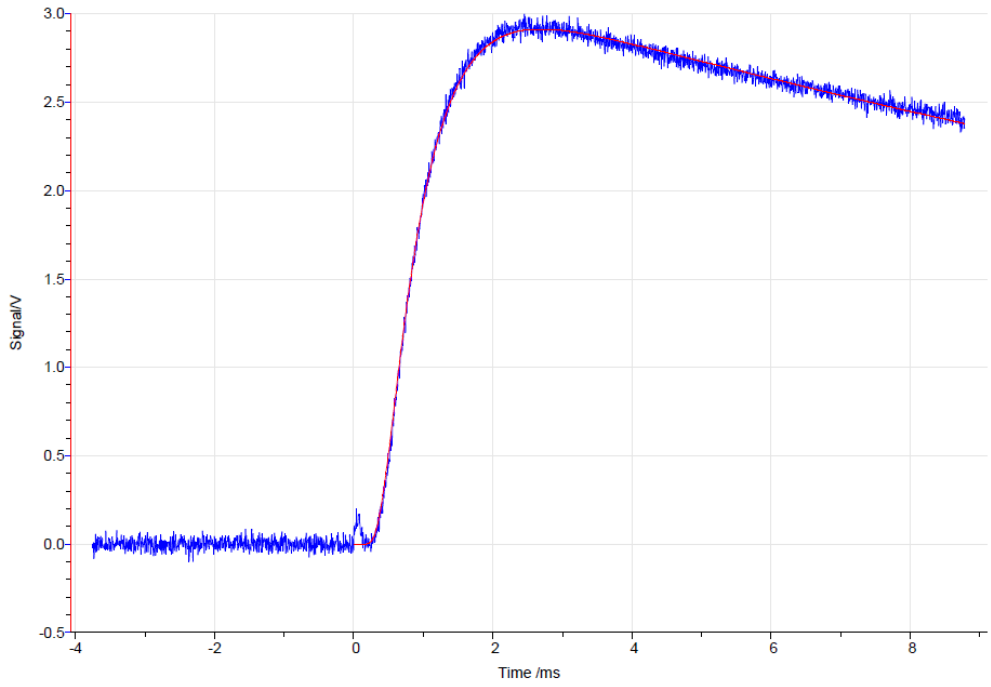

Figure 2. Example voltage (vertical axis) /time (horizontal axis) signal measured by the LFA467 taken on unirradiated SCW at 500°C, which is used to calculate thermal diffusivity. Note the small amount of flash-through observed from 0-0.1ms. Measured data is shown in blue, while the fit used to calculate diffusivity is shown in red.

Initial unirradiated testing has been completed on unirradiated SCW and is shown in Figure 3. This data is consistent with expected curves from the literature and the small spread indicates that the custom fixture for tensile tabs is performing as desired. Phase 1 testing is currently underway and is composed of samples shown in Table 1.

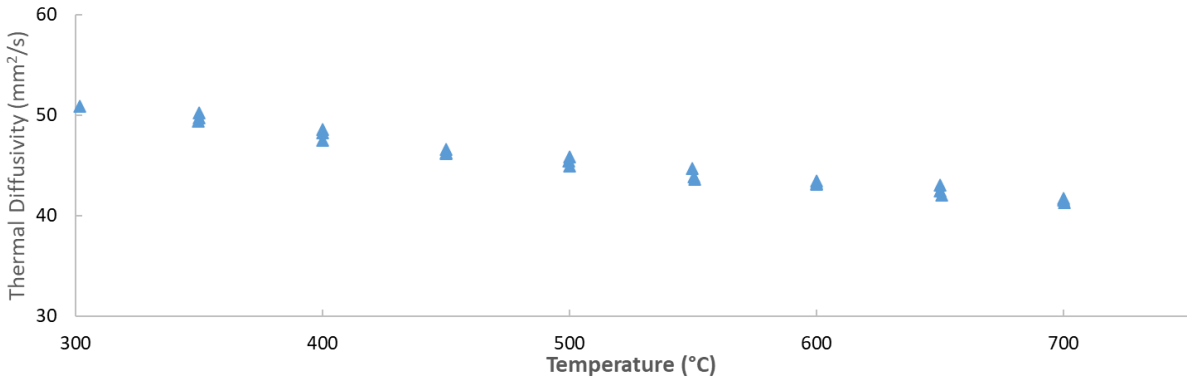

Figure 3. Measured thermal diffusivity of SCW from 300°C to 700°C.

Table 1. Phase 1 samples with calculated fluence, irradiation temperature, and associated campaign

Sample ID	*Fluence (E > 0.1MeV)*	*Irradiation Temp (°C)*	*Campaign*
W07	2.8	430	TITAN
W18	2.2	700	TITAN
1W27	2.8	800	TITAN
UE03	1.3	480	PHENIX
UE0G	3.8	830	PHENIX
UE0L	3.2	933	PHENIX

Future Plans

Future work will include measurement of materials from all phases, and correlation with irradiation conditions and electrical resistivity.

4.5 MEASURING AND TRACKING DEFORMATION IN DUCTILE PHASE TOUGHENED W-NiFe HEAVY ALLOYS USING IN-SITU MECHANICAL TESTING AND COMPUTER VISION—Jing Wang, James V. Haag IV, Amra Peles, Wahyu Setyawan, Danny J. Edwards (Pacific Northwest National Laboratory), Mitsu Murayama (Virginia Tech), Jonathan Roman (Carnegie Mellon University)

OBJECTIVE

This work seeks to directly measure, and track deformation of ductile phase toughened (DPT) W-NiFe heavy alloys in microscopic level, utilizing in-situ mechanical testing, computer vision, and machine learning techniques.

SUMMARY

This report summarizes the progress in utilizing in-situ mechanical testing, computer vision (CV), and machine learning (ML) to measure and track deformation process at microscopic scale in ductile phase toughened (DPT) W-NiFe alloys at PNNL. Preliminary exploration suggests that conventional computer vision-based techniques are useful in determining local strains based only on in-situ mechanical testing data.

PROGRESS AND STATUS

Introduction

We aim to develop machine learning tools to help analyze in-situ mechanical testing data and to better understand deformation behavior of materials in microscopic level. Specifically, we are interested in in-situ tensile testing in SEM, which could provide materials deformation information at a wide range of magnification levels for the entire testing duration. Most analysis of in-situ mechanical testing is still conducted manually either frame by frame or on selected static images. In the past several years, there are an increasing number of publications on developing software tools/techniques to help the analysis. A well-known approach is the digital image correlation (DIC), which estimates true strain data. Some open-source or commercial software, e.g., μDIC, DICe, and Ncorr, are available. The high resolution DIC approach has been used to study slip band formation, crack propagation, and deformation mapping across a wide range of grains[1].

For this study, we analyze ductile phase toughened W-NiFe alloys. Performing in-situ mechanical testing allows us to collect SEM images during the tensile tests that enable us to gain direct insights in the effect of imposed deformation on microstructure. As opposed to static SEM images, this technique creates a series of images at time intervals that correlate with the test parameters (e.g., strain rates). The time-series evolution could help us better understand the deformation and crack propagation in DPT W-NiFe composite.

Typically, DIC requires applying a speckle pattern to the specimen surface as a feature to track local movements. However, this approach could obscure microstructure information and is not desired in our study. Instead, we use local microstructure features themselves for the movement tracking. Another method to achieve pixel-wise accuracy is called optical flow [2-4]. Both methods have been tested and we favor the optical flow method due to various open-source packages in python that are available. Corresponding strains are calculated and inspected qualitatively.

Experimental Procedure

<u>In-situ mechanical testing</u>

In-situ mechanical testing was conducted on wire electrical discharge machined (EDM) and polished micro-tensile dog-bone specimens with a gauge section geometry of nominally 5 × 1 × 0.1 mm. Specimens were

strained using a Kammrath & Weiss micro-tensile tester, shown in Figure 1, equipped with a 200N load cell in a uniaxial tension setup at a crosshead displacement rate of 100 nm/s (calculated 2×10^{-5} s^{-1} strain rate) until failure. The micro-tensile tester was placed in an FEI environmental scanning electron microscope (ESEM) to record video frames during straining. Individual frames were recorded in 9 s increments at an image pixel resolution of 1024×943. The ESEM was operated at an acceleration voltage of 30 kV, and frames were recorded using a backscattered electron detector. This detector allows for easy differentiation between the two constituent phases as the primary contrast generation mechanism with this detector is based on the atomic number, making the light grey domains the tungsten particles, and the dark grey domains NiFe matrix. We focused on as-received DPT W (90W-0R) for simplicity. Several test geometries, namely un-notched, one notched, and doubly notched were tested. The experimental test matrix is listed in Table 1. Snapshots of an obtained in-situ video from an un-notched specimen are shown in Figure 2.

Table 1. Specimen matrix in this report

Materials	Notches	Number of Dataset
90W-0R	0	2
	1	2
	2	1

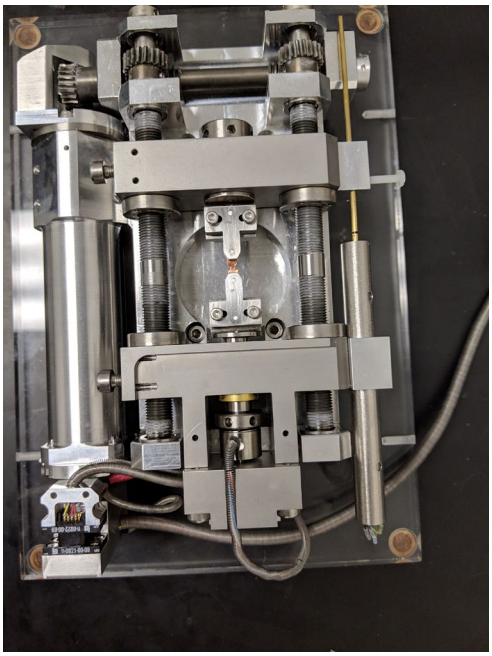

Figure 1. A picture of the Kammrath & Weiss micro-tensile tester at Virginia Tech.

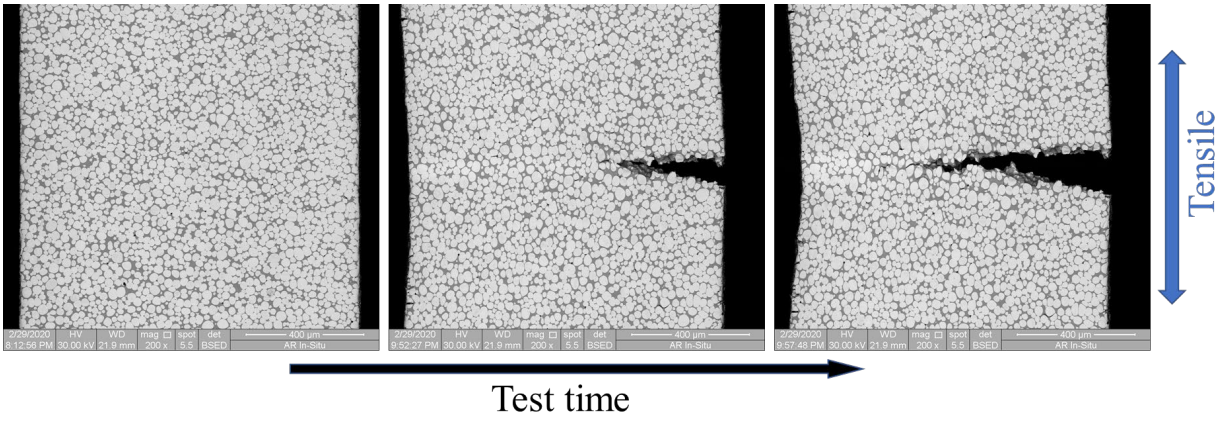

Figure 2. Snapshots from in-situ mechanical testing video of an un-notched specimen. The tensile loading direction is along the vertical direction.

Preliminary Results

Microstructure

More detailed overviews of the general microstructure of W-NiFe alloy samples have been presented in previous reports [5-7]. Figure 3 shows a typical microstructure of surface of as-sintered W-NiFe (90W-0R) specimens used for this study. The microstructure resembles two typical phases in this set of materials: a NiFe phase, which serves as the ductile matrix; and a W phase, which provides strength and high temperature mechanical performance.

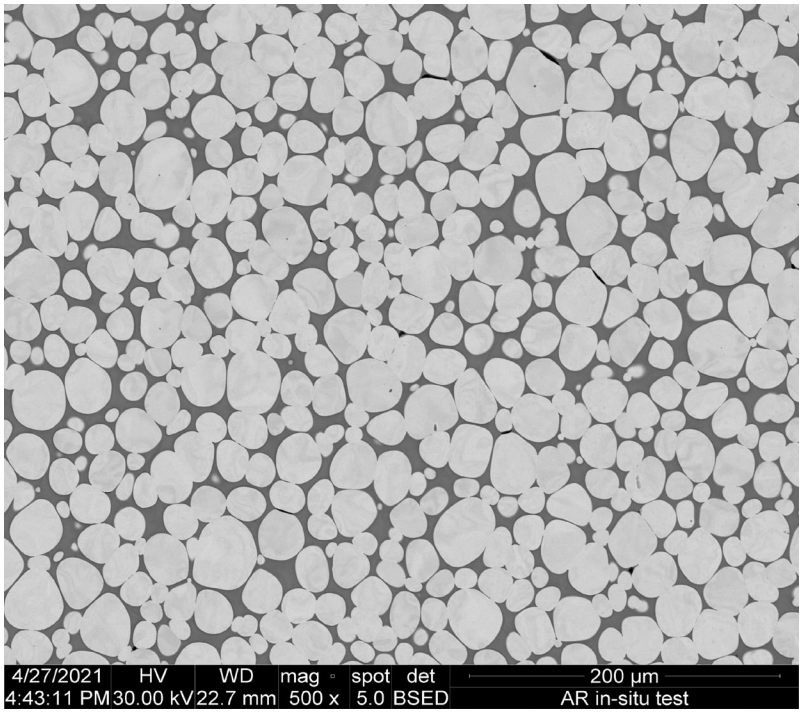

Figure 3. Typical microstructure of as-received DPT W-NiFe (90W-0R) in SEM BSE mode. The bright region corresponds to W dominant particles while the darker gray regions are NiFe matrix.

Estimate local strain using computer vision techniques

One dataset from un-notched 90W-0R specimen is used for demonstration in the following. Firstly we employed the *tvl1* optical flow algorithm to calculate the frame-to-frame displacement field [2]. Part of the obtained result is shown in Figure 4. Note what shown here is the estimated pixel-wise displacements rather than local strains. The color of the displacement field is proportional to the magnitude of displacement at that pixel. We can see that from frame to frame, the upper and lower part of specimen exhibited displacement either to left up/left down (Frame 5, Frame 33) or mostly up or down (Frame 15), with a V-shape region ahead of crack tip remains low displacements. The upper and lower boundary of this low displacement field region is about 30° from the horizontal axis. It is also clear that near end of this dataset with crack propagate, the low displacement field region shrinks, and the displacement field in other regions grows in magnitude.

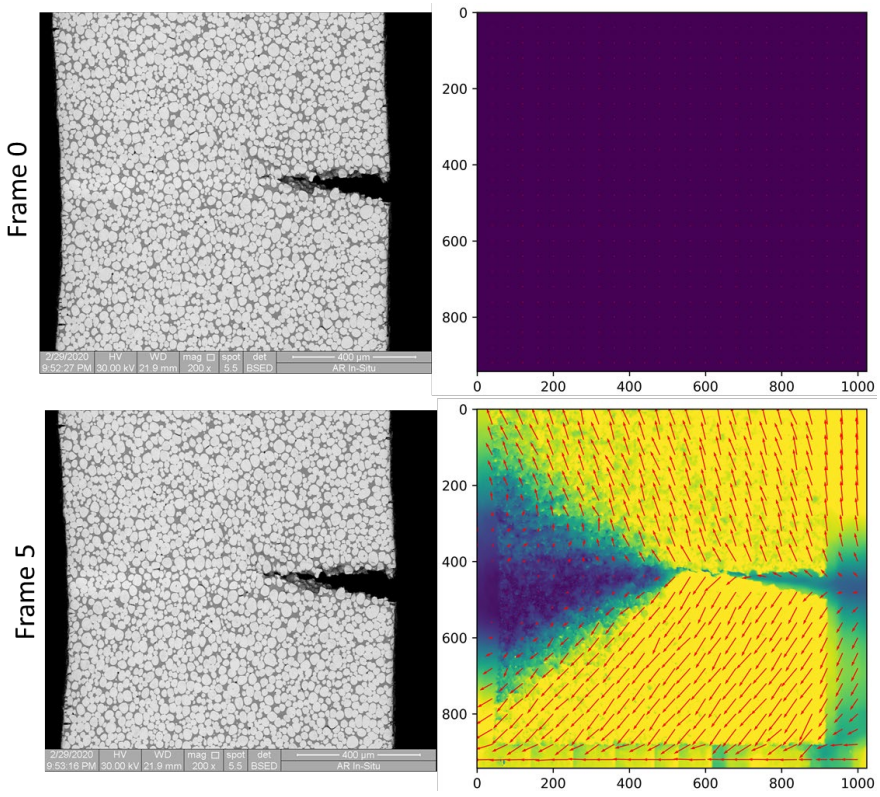

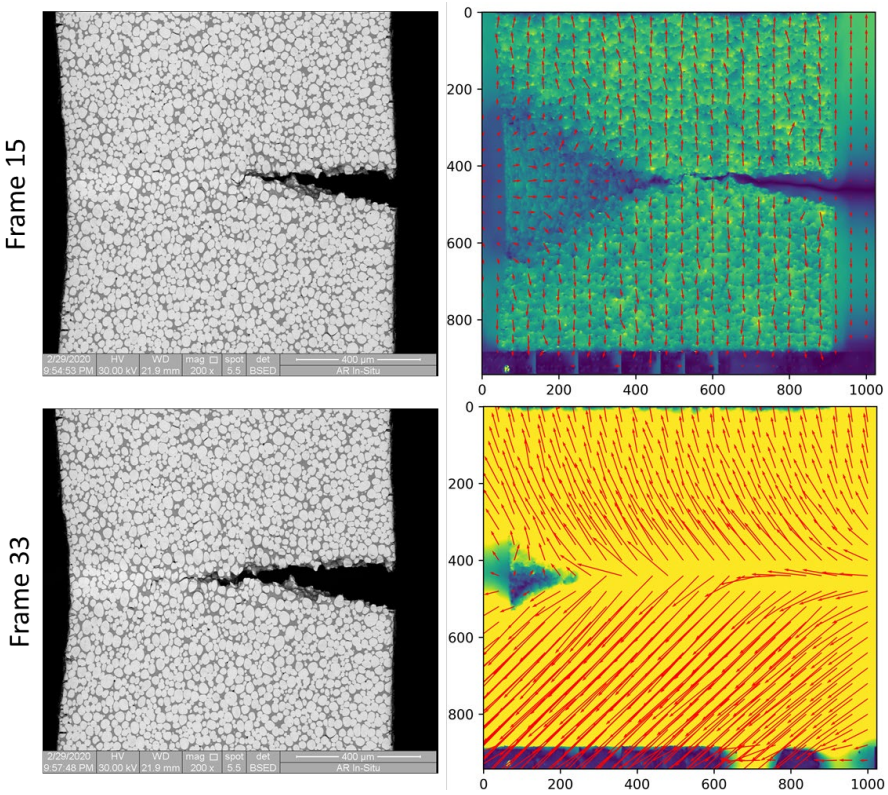

Figure 4. (Left) BSE images. (Right) Calculated displacement fields between each frame. The red arrow represents the displacement direction and the length of the arrow represent the magnitude of the displacement vector. The color in the right panels correspond to the magnitude of displacement field. Displacement field of frame *i* is with respect to frame *i-1*.

Frame-to-frame strain can be calculated from the pixel level displacement field. The result for shear strain ε_{xy} is shown in Figure 5. Note a positive shear strain means two originally orthogonal vectors now have a larger angle in between them compared to a previous frame. The histogram shows an interesting bimodal distribution with more regions experiencing a negative shear strain, presumably due to the Poisson effect. Strain along vertical and horizontal axis is not shown here, mainly because they are quite noisy due to frame-to-frame calculation. We will incorporate a cumulative strain or apply a moving average to reduce the noise.

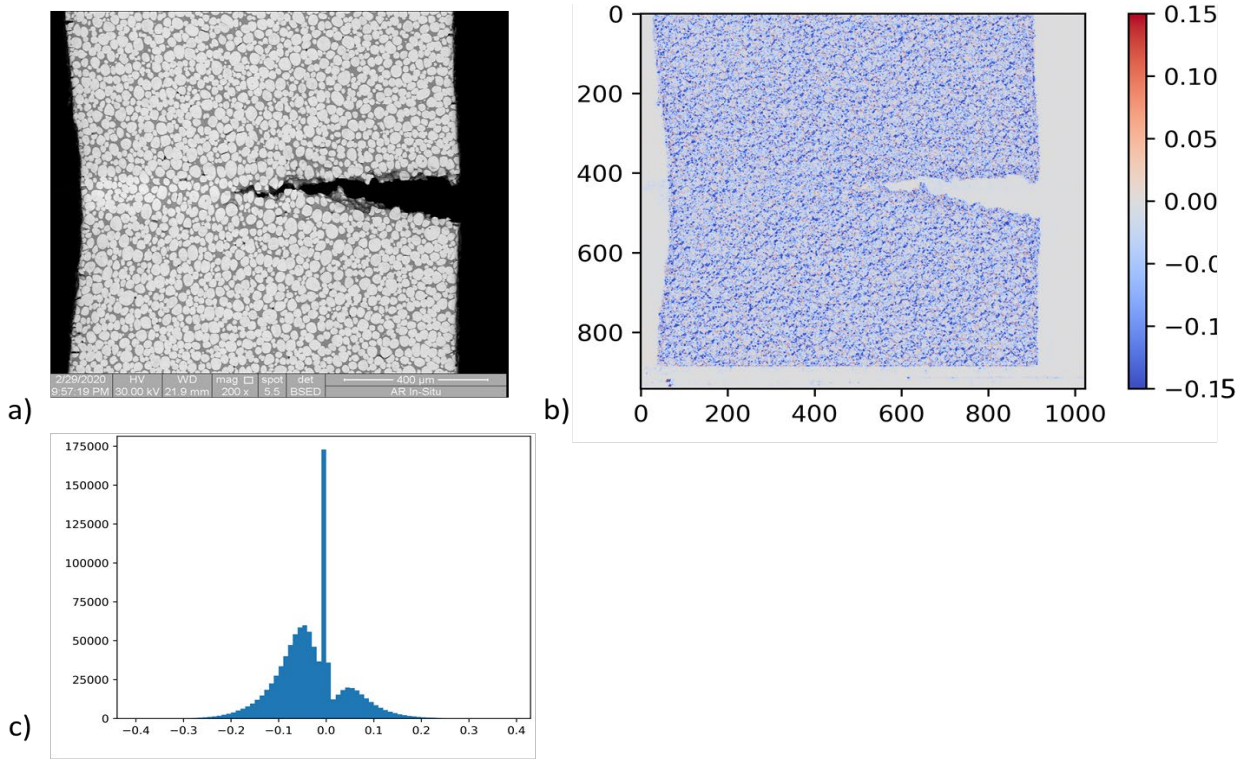

Figure 5. a) BSE of frame 30 of test data; b) calculated shear strain (between frames) map; c) histogram of shear strain. The major peak at 0 correspond to regions outside specimen or background that does not move at all.

Tracking microstructure features using machine learning

Another capability we are interested in is to be able to track microstructure features of interests during in-situ mechanical testing. Feature tracking can be achieved with conventional computer vision techniques, such as using particle filter algorithm. An example of tracking a randomly selected, pre-defined microstructure feature patch is plotted in Figure 6. In addition, theoretically nothing prevents multiple particle filters to run in parallel to track multiple features of interests during testing [8]. This approach can be used to track both W particles, and other features, e.g., growth of a small crack, during the testing, enabling measurement of individual feature characteristics throughout the deformation process.

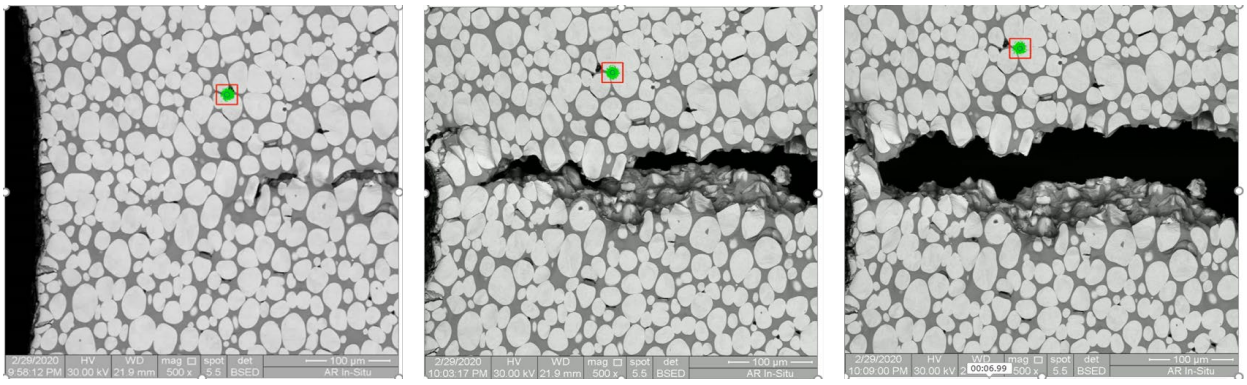

Figure 6. Microstructure feature tracking using particle filter method. From left to right images: test time increases.

A key limitation of computer vision technique is the selection of those feature to track. Though automatic feature selection techniques, such as Harris corner detection, and Scale-invariant feature transform (SIFT), exist, those techniques lack the capacity to pick microstructure features meaningful to researchers. Machine learning techniques, specifically deep learning models, can be a good alternative to perform multiple objects tracking with semantic meanings. There are a couple of ways to achieve multiple objects tracking in deep learning, one approach is to train a model on one instance of feature of interest and later expand it to run multiple instances; a second one is to directly build-in multiple objects tracking capacity. Either way, it requires a significant amount of human effort in labeling those features. Example of data to be labeled is shown in Figure 7. An entire series of images for one in-situ testing consist hundreds to thousands of such images, which renders manual labeling of moving and deforming objects impractical.

Alternatively, we can create a synthetic dataset that resembles main feature characteristics, imposing artificial movements with a noise addition, to mimic real dataset. Figure 8 shows an example of these synthetic images. The synthetic images were generated iteratively with randomized overlap of 3 ellipsoids for each particle. The size distribution is enforced to match those of real data. Next step is to train the synthetic data using a model called masked R-CNN (Region based convolutional neural network) for multiple objects tracking capability and deformation characteristics extraction [9], and other potential models [10, 11].

Summary

In summary, we have collected a fair amount of good quality data from in-situ mechanical testing in SEM to better measure and perform in-depth analysis of deformation behavior of DPT W. Exploration into conventional computer vision and state-of-the-arts deep learning shows great potential to facilitate our goal. Although more work, e.g., testing on deep learning models, needs to be done, we are confident the resulting outcome will be beneficial to gain insights into the correlation between microstructure and deformation behaviors.

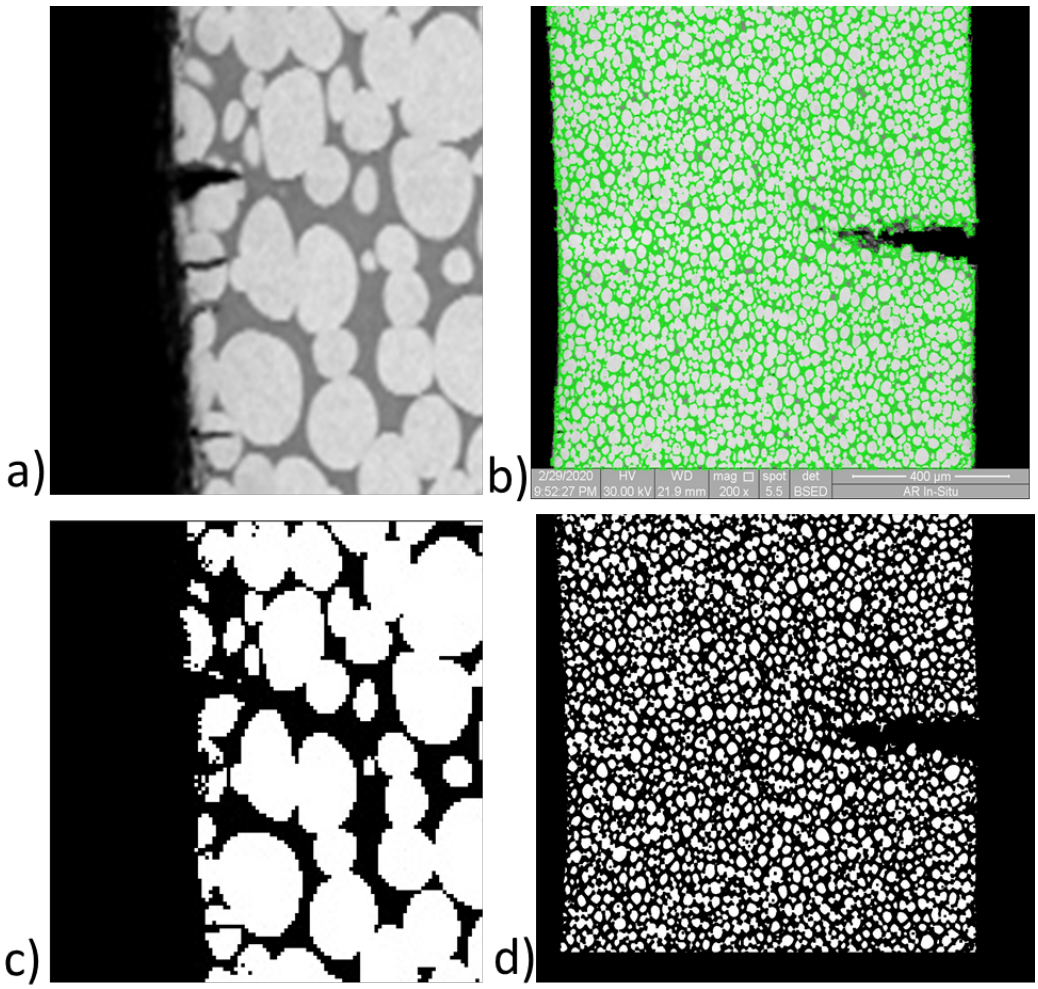

Figure 7. a) magnified BSE images of DPT W; b) segmented image (green is NiFe matrix); c) enlarged binarized image (white is W phase); d) overview of a binarized image (white is W phase).

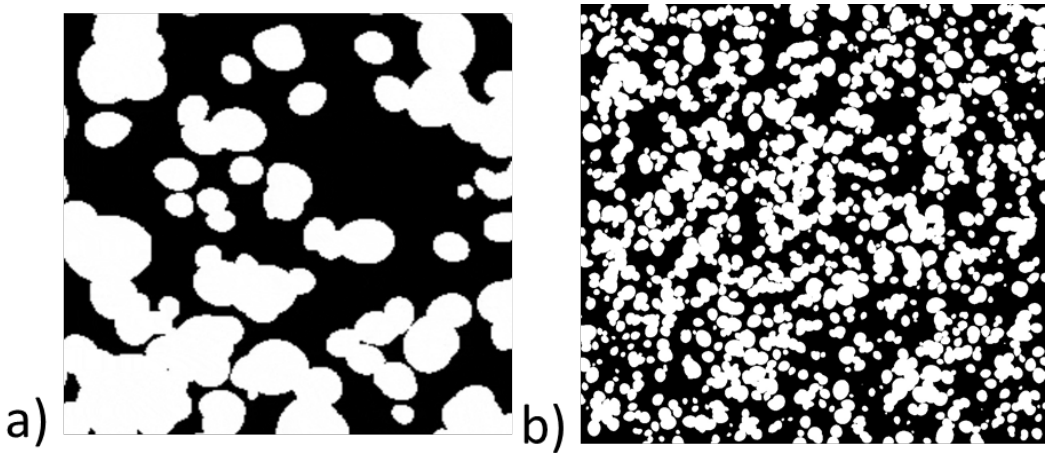

Figure 8. a) enlarged synthetic image; b) synthetic image for ML training.

Acknowledgements

This research was supported by Office of Fusion Energy Sciences, U.S. Department of Energy (DOE) under Contract DE-AC05-76RL01830.

References

[1.] Chen, Z. and S. Daly, *Active slip system identification in polycrystalline metals by digital image correlation (DIC).* Experimental Mechanics, 2017. **57**(1): p. 115-127.

[2.] Zach, C., T. Pock, and H. Bischof. *A duality based approach for realtime tv-l 1 optical flow*. in *Joint pattern recognition symposium*. 2007. Springer.

[3.] Lucas, B.D. and T. Kanade. *An iterative image registration technique with an application to stereo vision*. 1981. Vancouver, British Columbia.

[4.] Hartmann, C. and W. Volk. *Digital image correlation and optical flow analysis based on the material texture with application on high-speed deformation measurement in shear cutting*. in *International Conference on Digital Image & Signal Processing (DISP 2019), At Oxford, UK*. 2019.

[5.] Wang, J., et al., *Tensile testing and microstructural characterization of ductile phase toughened W-NiFe alloys*, In *Fusion Materials Semiannual Progress Report For The Period Ending June 30, 2020*. 2020.

[6.] Wang, J., et al., *Microstructural characterization and mechanical testing of ductile-phase toughened tungsten*, in *Fusion Materials Semiannual Progress Report For The Period Ending December 31, 2019*. 2019.

[7.] Wang, J., et al., *Microstructure-Mechanical Property Correlation in Ductile Phase Toughened W-NiFe Heavy Alloy*, in *Fusion Materials Semiannual Progress Report for the Period Ending December 31 2020*, D. Clark, Editor. 2020.

[8.] Smal, I., et al., *Particle filtering for multiple object tracking in dynamic fluorescence microscopy images: Application to microtubule growth analysis.* IEEE transactions on medical imaging, 2008. **27**(6): p. 789-804.

[9.] Wijesinghe, K., et al., *Characterization of microscopic deformation of materials using deep learning algorithms.* Materials & Design, 2021. **208**: p. 109926.

[10.] Pal, S.K., et al., *Deep learning in multi-object detection and tracking: state of the art.* Applied Intelligence, 2021: p. 1-30.

[11.] Xu, Y., et al. *How to train your deep multi-object tracker*. in *Proceedings of the IEEE/CVF Conference on Computer Vision and Pattern Recognition*. 2020.

4.6 MICROHARDNESS AND TENSILE PROPERTIES OF A HOT-ROLLED 90W-NiFe TUNGSTEN HEAVY METAL ALLOY—M.E. Alam, G.R. Odette (University of California Santa Barbara), J. Wang. C.H. Henager Jr., W. Setyawan (Pacific Northwest National Laboratory)

OBJECTIVE

The objective of this study is to understand the effects of hot-rolling on the microhardness and tensile strength of a 90W-7Ni3Fe tungsten heavy metal alloy (WHA).

SUMMARY

The hot-rolling (HR: 0, 62, 74 and 87% thickness reduction) effects on the microstructure and room temperature (RT) fracture toughness (K_{Jm} or K_{Ic} ≈ 97, 35, 35 and 116 MPa$\sqrt{m}$, respectively) for a PNNL's 90W-NiFe WHA are reported previously. Here, we have reported the Vickers microhardness (HV) of individual phases (at 10 gf load) and composite structures (at 100 to 1000 gf loads), and RT tensile properties of the HR 90W WHA. The HV for DP and W at 10 gf are lowest for 0R (348 ± 27, and 478 ± 19 kgf/mm^2, respectively) that reaches maximum for 62R (445 ± 52, and 569 ± 39 kgf/mm^2, respectively), remains stable due to saturation at 74R, followed by softening for 87R (395 ± 32 and 469 ± 34 kgf/mm^2, respectively). The composite HV follows the similar trends, irrespective of loading, though the hardness value reduces systematically with increasing load for the same HR %. The RT σ_y and σ_u also follow the same pattern as HV with the lowest σ_y/σ_u at 0R ≈ 621/891 MPa, and highest at 62R ≈ 930/1086 MPa. The 74R and 87R strength is somewhat similar to that of 62R and 0R, respectively. Tensile ductility and fracture toughness exactly follow the opposite trends to HV and strength.

PROGRESS AND STATUS

Introduction

Tungsten heavy metal alloys (WHAs), a class of bi-phase metallic composite, typically contains 78-98% W, along with a balance of lower melting point ductile phase (DP) metals like Ni, Fe, Cu and Co, are well known for their good room to high temperature tensile strength and ductility [1–4]. In addition to use in very high temperatures environments, like rocket nozzles, main applications of WHA, include use in ordnance, such as kinetic energy penetrators, counterbalances and flywheels, where high class densities are important [1,3,5]. Recently, various WHAs have been considered as potential structural plasma facing materials for fusion reactor divertor applications [6–13]. For example, Neu et al. [8,9] reported the use of 97W-2Ni-1Fe WHAs as divertor tiles for the mid-size tokamak ASDEX Upgrade facilities that experienced cyclic plasma heat flux up to 20 MW/m^2 and surface temperature up to 2200 ºC, and found lower cracking tendency for WHAs than pure W.

Various thermomechanical plastic deformation processing routes, like hot-rolling (HR), extrusion or swaging may increase the strength of WHA's [14–21]. Researchers at Pacific Northwest National Laboratory (PNNL) characterized the effects of the composite architecture on deep notch bend bar toughness for a 90 wt.% W-Fe-Ni WHA, with HR to different thickness reductions of 0, 62, 74 and 87 % [6]. Their hypotheses was that the deformed W and DP phases, which form a 'brick-and-mortar (BAM)' like microstructure, could improve strength by hot working, while enhancing ductility and toughness, by creating more distributed damage zone under deep notch bar loading [6,22]. We have performed fracture toughness on the fatigue precracked notch bend bars following ASTM E1921 [23] standard and reported previously with basic microstructural characterizations [24,25]. Here, we have investigated the effect of hot-rolling on the microhardness (both individual phases and as a composite structure, as a function of indentation loading variations) and RT tensile properties of the HR 90W WHA alloy. Details introduction can be found in [25].

Experimental Procedures

The RT Vickers microhardness measurements (HV) were performed on the bend bar polished surfaces at varying loads of 10, 100, 200, 500 and 1000 gf with a 10 second dwell, using a LECO M-400A semi-automated hardness tester. Smaller 10 gf load was used in an attempt to probe the individual DP and W phases, while higher 100 to 1000 gf loads were used to characterize HV at various length scales relative to the composite microstructure. SEM, rather than optical images, was used to measure the indentation diagonals to obtain more accurate readings. Ten to fifteen indentations were made in all cases, with average values and standard deviations calculated in accordance with ASTM standard E834 [26].

Uniaxial tensile tests at RT were performed on L-oriented flat dog-bone shaped sub-sized specimens that are EDM fabricated from the bend bars. The 20 mm long tensile specimens have a 5.0 mm gage section, 1.0 mm width and 0.7 mm thickness. The side and thickness tensile specimen surfaces were ground using 180 to 2000 grit paper to remove surface oxides, contamination, minor cracks and local residual stresses due to EDM. Tests were carried out on an MTS 810 servo-hydraulic universal testing machine. At least 3 tests per alloy were conducted at a strain rate of 10^{-3}/s. The tensile properties were obtained in general accordance with ASTM E8M-15a [27].

Results

Microstructure

The 3D SEM micrographs of the polished and etched HR 90WNiFe plates has been reported previously [24,25]. In summary, the 0R (as-received) 90W plate shows randomly oriented, roughly spheroidal ≈ 17 ± 7 μm W particles (particle aspect ratio, PAR: 1.2 ± 0.2) surrounded by an interconnected honeycomb web structure of the NiWFe ductile phase, DP ≈ 3.3 ± 1.7 μm thick (Fig. 1a and [24,28]). HR leads to increasingly oriented and anisotropically deformed W-particles to ≈ 44x27x10μm for 62R, 55x25x7μ for 74R and 79x27x5 μm for 87R alloys and thinner surrounding DP layers (Figure 1b-g). For example, the 62R HR flattens, extends, and welds the initially roughly spherical W particles (Figure 1e). The increment of deformation between the 62R and 74R produces layers of discrete and more regular bladelike W particles (Figure 1e,f). The 87R W phase is deformed into highly irregular, crenulated, wavy blades, with average dimensions of ≈ 79x27x5 μm in the rolling length direction (top and side views), width (top view) and thickness directions (side view), respectively (Figure 1b,c,g and Reference [25]). The 87R W blades are partly interconnected, forming irregular layers (bricks), separated by semi-continuous thin layers of the NiWFe DP (mortar). The multiphase 87R deformation is so large that some ductile and W phase particles are mechanically mixed (entrapped) to form roughly spherical inclusions inside the W blades (Figure 2g). Higher magnification SEM images in Figure 1h shows the micron size W grains inside the W particles in the 74R WHA, while Figure 1i shows even smaller submicron size grains in the 87R WHA (red arrows, Figure 1i). The ultra-fine grains are likely due to the dynamic recrystallizations during HR. Dynamic recrystallization was also observed for the DP phase with larger grains as indicated by the white arrows in Figure 1h, with more details in [29].

The average areal fraction of DP for the 0R plate is ≈ 17 ± 4 %, irrespective of the view orientation. However, the large deformations result in anisotropic plate view area fractions, which increase in the top and front view, and decrease in the side views, obeying conservation of volume requirements. For example, the side view areal DP fraction decreases as ≈ 17 %, 14 %, 13 % and 12 % for the 0R, 62R, 74R and 87R WHAs, respectively. The DP ligament thickness observed on the side and front faces of the HR WHAs decreases from 3.3 ± 1.7 μm for 0R to 2.5 ± 0.9, 1.5 ± 0.7 and 1.35 ± 0.5 μm for the 62, 74 and 87R alloys, respectively.

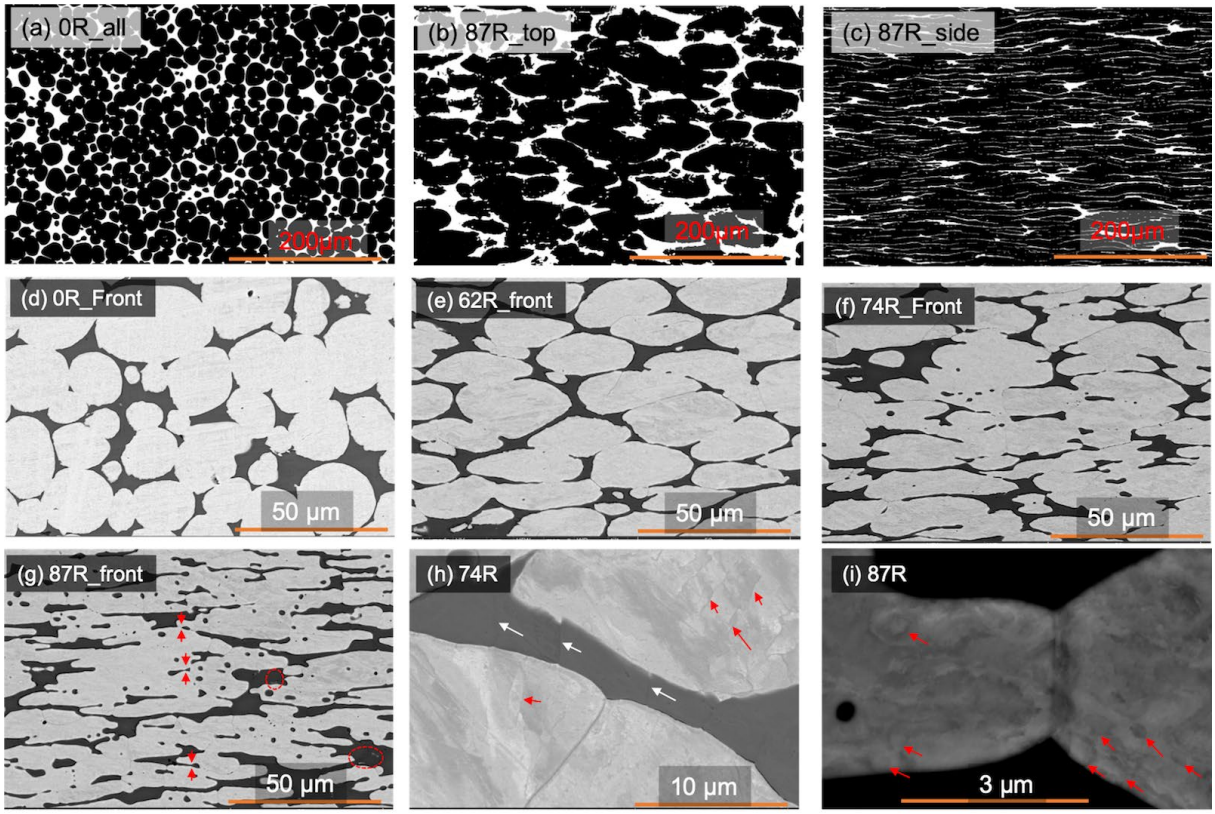

Figure 1. Binary black-white SEM images for the: (a) 0R; (b-c) 87R top and side views, respectively; showing the morphology of W particles (black) and DP phase (white); (d-g) BSE SEM images showing the front view of the 0R (d), 62R (e), 74R (f) and 87R (g) and demonstrating the evolution of the W and DP morphologies, including DP entrapment inside highly deformed W particles (red arrows in 2g) at large HR; and, (h and i) higher magnification SEM images revealing subgrain structures, indicated by red arrows (for W) and white arrows (for DP) in the 74 and 87R WHA, respectively.

Microhardness

Room temperature Vicker's microhardness (HV) measurements for the as received and HR 90W WHA are shown in Table 1 and plotted in Figure 2. The smallest 10 gf load was used to individually probe the DP and W phases; the HV are shown in Figure 2a and the indents are illustrated in Figure 2c. The larger 100 gf to 1000 gf loads measured the composite hardness; the HV are shown in 2b for the indents illustrated in Figure 2d. For the 10-gf load, the W HV first increases with HR from 0 to 62R (≈ 478 ± 19 kgf/mm^2 and 569 ± 39 kgf/mm^2, respectively), levels of at 74R (≈ 566 ± 37 kgf/mm^2), followed by a decrease at 87R (≈ 469 ± 34 kgf/mm^2). The HV of the DP follows a similar trend. The DP HV increases from 348 ± 27 for 0R to 445 ± 52 kgf/mm^2 for 62R, slightly softens to 432 ± 28 kgf/mm^2 at 74R, and then again drops to 395 ± 32 kgf/mm^2 at 87R. The initial increase in HV is expected, since HR increases the dislocation densities and refines W and DP grains or subgrains [15,16,21]. The saturation of HV is also not unexpected, assuming the dislocation substructure reaches a steady state. However, the lower HV in the 87R WHA is somewhat unexpected. This decrease may be due to a strain induced recovery/recrystallization processes, but there is not enough data to reach any firm conclusion. The decrease in the DP HV of the 87R WHA may be due to the 900 ºC heat treatment to remove H. However, this does not explain the softening of the W phase since its recovery temperature is much higher, especially for a short 1 h anneal time [30,31].

Note that, for the HR WHA, the average 10 gf indentation diagonal (d) varies between 5.5 to 6.5 μm for W and 6-8 μm for the DP, corresponding to indentation depths (h ≈ 0.14d) of ≈ 0.77 to 1.12 μm, based on Vickers 136 º diamond face angle. Thus, the HV for DP may be increased by the surrounding W particles given that the thickness of the ligament is only 3.3 μm for 0R to 1.35 μm for 87R, as seen in the side and front views in Figure 1. Note, the higher HV in the 10 gf tests is presumably also partly due to indentation size effects [32].

Table 1. RT Vickers microhardness (HV, kgf/mm^2) as a function of indentation loads on the individual phases and composite structures for all the HR WHAs

Loads	Phase	0R	62R	74R	87R
10 g_f	DP	348 ± 27	445 ± 52	432 ± 28	395 ± 32
	W	478 ± 19	569 ± 39	566 ± 37	469 ± 34
100 g_f	composite	359 ± 13	445 ± 28	441 ± 19	365 ± 13
200 g_f	composite	337 ± 8	429 ± 24	435 ± 28	344 ± 9
500 g_f	composite	312 ± 4	395 ± 9	400 ± 14	332 ± 7
1000 g_f	composite	308 ± 8	392 ± 5	391 ± 6	317 ± 3

The composite HV for all the HR WHA were measured over a range of loads from 100 to 1000 gf. The average HV increases with decreasing indentation load (Table 1 and Figure 2b). At 100 gf load, the indentation diagonal is ≈ 22 μm (top row of Figure 2d), which is close to the W-particles size. Thus, there is a higher probability that the indentation load probes more of the W-particles, which are much harder than the DP, resulting in higher HV values. At the highest 1000 gf load, the indentation is much deeper with a diagonal length of ≈ 76 μm as shown in Figure 2d. Since this load probes both the W particles and DP, the average HV decreases. Note there may be other indentation size effects between 100 and 500 gf. However, HV values for 500 gf and 1000 gf loads are nearly the same, indicating that a 500-gf load is sufficient to evaluate the composite HV.

Notably, the composite HV follows the same trends as observed in the individual phases: the composite HV increases from 0R to 62R, stabilizes at 74R, and then softens at 87R as shown in Table 1 and Figure 2a,b. Note that the 100-gf composite HV closely traces the 10 gf DP HV with an average difference of less than 5 %. Indentation cracking was not observed in any of the hardness tests, including for 1000 gf on 87R WHA (Figure 2c,d). However, as shown in Figure 2c, significant indentation pile-up were observed, especially in the 62R to 87R WHA; such pile ups are common in HR WHA [33].

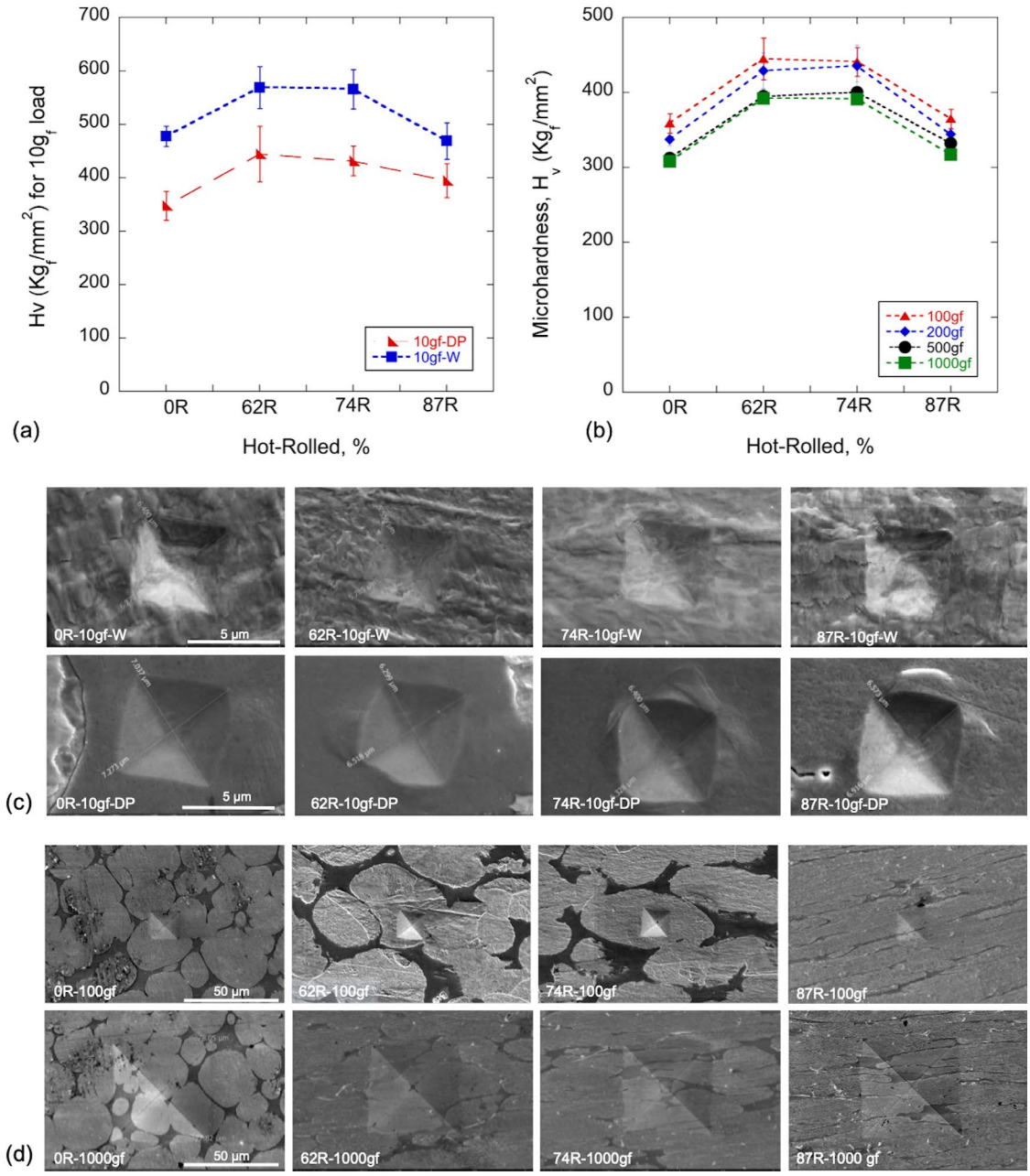

Figure 2. Plot shows the RT HV as a function of indentation loads and HR reductions: (a) the individual phases at a 10-gf load; (b) 100 to 1000 g_f loads probing the composite structures; (c) the W (top) and DP (bottom) indentations at the at 10 g_f load; and (d) the indentations for the 100 g_f (top) and 1000 g_f (bottom) loads.

Room temperature tensile properties

The RT engineering stress-strain (σ–ε) curves for all the HR WHA are plotted in Figure 3a, and the corresponding σ_y, σ_u and total elongation (ε_t) values are plotted in Figure 3b and summarized in Table 2.

The tensile σ_y and σ_u closely track the HV trends. The uniform, total elongation and reduction of area (RA) ductility follow the opposite trends, with ductility decreasing linearly with the WHA σ_y and σ_u [15,16,19,21].

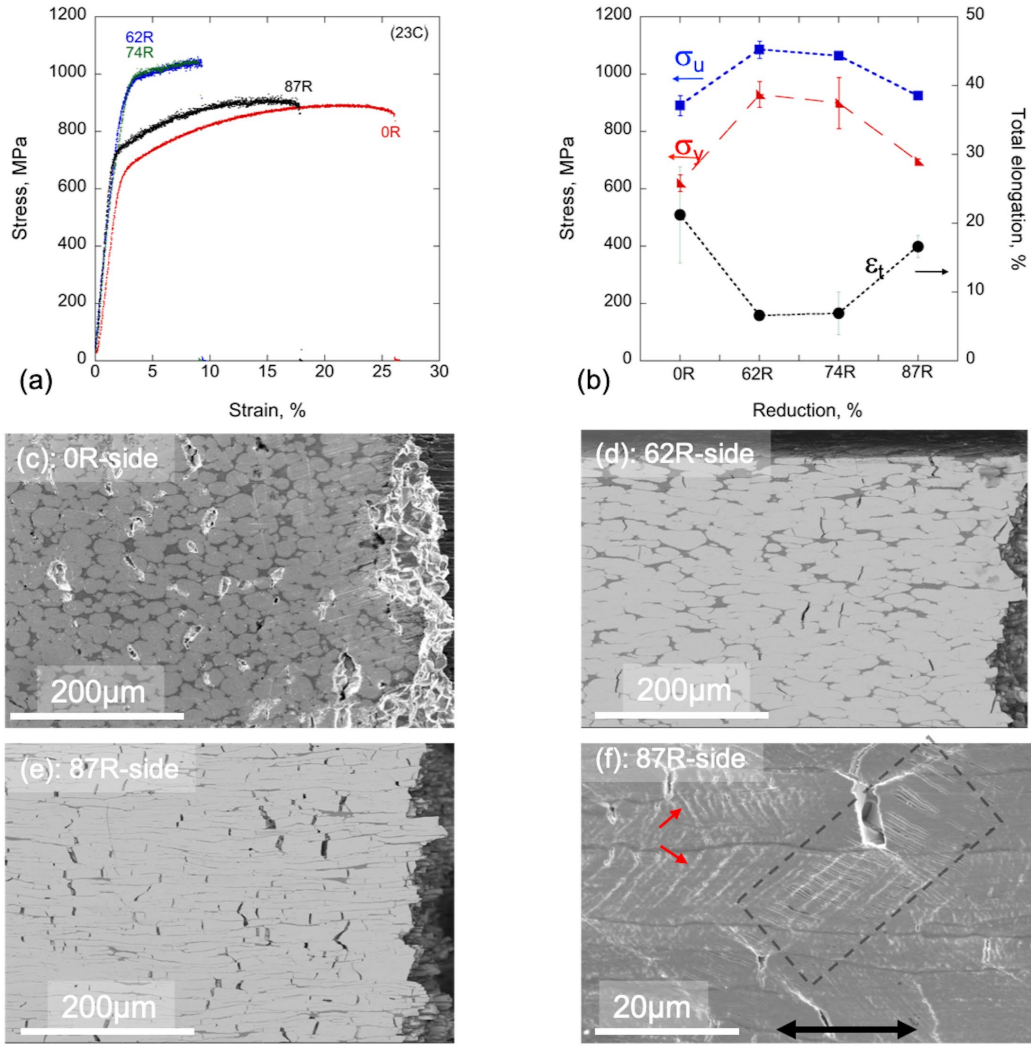

Figure 3. (a) RT engineering stress-strain (σ–ε) curves for all the HR WHA; (b) the tensile σ_y, σ_u and ε_t versus the HR reductions; (c-e) SEM side surface tensile micrographs for 0R (c), 62R (d), 87R (e); and (f) a high magnification micrograph showing slip steps in the 87R W phase. The loading direction is horizontal in all cases (indicated by black arrow in f).

Figure 3c to e show that the W particle microcracking increase with HR. The side surface view of the fractured 0R WHA shows that the W-particles deform in the direction of loading with little microcracking. Narrow isolated DP arrested microcracks, mostly oriented perpendicular to the loading direction, are observed in Figure 3d for the broken 62R (and 74R WHA, not shown due to the similarity to 62R). The minimal crack opening is not associated with higher local toughness. Rather, it is due to the early (low strain) linking of a planar array of the microcracks to form the fracture surface. The 87R WHA shown in Figure 3e has the largest number of microcracks, that are arrested and blunted and, in some cases locally linked, due to the larger strains needed to propagate the fracture surface cracks. Figure 3f is a higher magnification view of 45° slip steps in deformed in the 87R WHA.

Table 2. RT tensile properties of the HR 90W WHAs

HR, %	σ_y, MPa	σ_u, MPa	ε_u, %	ε_t, %	RA, %
0	621 ± 29	891 ± 35	17.9 ± 4.4	21.2 ± 7.0	25.8
62	930 ± 45	1086 ± 30	6.2 ± 0.7	6.6 ± 0.7	10.8 ± 1.1
74	899 ± 89	1064 ± 7.5	6.6 ± 2.8	6.9 ± 3.1	12 ± 2
87	697 ± 8	925 ± 6	12.3 ± 0.9	16.6 ± 1.6	21.7 ± 2.6

Figure 4 shows the SEM fractographs of the RT tensile fracture surfaces. The 0R WHA in Figure 4a shows the mix of all well-known local fracture modes: W-cleavage (WC), W-W interface fracture (WW), DP rupture (DR) and W-DP decohesion (WD) [28]. The 62R (and 74R) fracture surfaces in Figure 4b mostly show WC. The 87R fracture surface in Figure 4c again show the usual a mix of local fracture modes, as well as ductile rupture of the DP particles entrapped in the highly deformed W phase, shown in the higher magnification micrograph in Figure 4d.

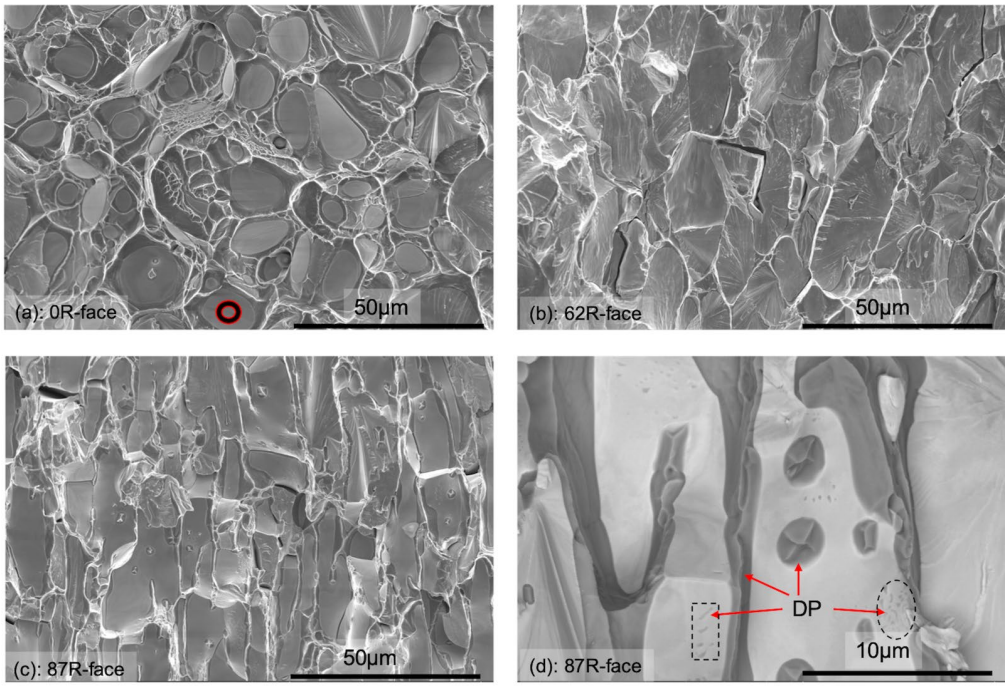

Figure 4. Tensile fracture surface micrographs for 87R showing: (a) a mix of local fracture mode for 0R; (b) W-cleavage dominated fracture for 62/74R; (c) WW dominated fracture mode for 87R; and (d) ductile rupture of large DP particles, along with small DP fragments in the W. The loading direction is out-of-plane as indicated in Figure 4a by the circle.

Summary

Here we explored the microstructure and RT microhardness and tensile properties of HR 90W WHA. While the as-received (0R) WHA is microstructurally homogeneous and isotropic, the HR WHA are highly

anisotropic in terms of W particles DP morphology and composite architecture. Both the W particles and DP are randomly textured, irrespective of the HR condition or direction. Both the WHA hardness and strength follow the same trends and vary with the amount of HR: first increasing to 62R, then saturating or slightly softening at 74R, then decreasing at 87R, for reasons that are not yet fully understood. There is a strong inverse relation between HR WHA fracture toughness/tensile ductility and the microhardness/tensile strength properties.

Future Work

The effect of high temperature annealing (1300 ºC/24 h) has been completed on the 0R WHAs and the characterization of microstructure, tensile strength and toughness of annealed WHA are in progress.

Additional characterization is needed to understand the effect of 74/87 HR conditions on the WHA strength and fracture toughness variations.

High temperature tests of fracture toughness and subcritical crack growth rates will be initiated.

Acknowledgement

We like to acknowledge the support provided by U.S. Department of Energy (DOE) through the Office of Fusion Energy Sciences PNNL under contract DE-AC05-76RL01830 and UCSB DOE-Fusion 8-442520-22419-3. The U.S. National Science Foundation supported California Nanoscience Institute provided facilities critical the success of this research.

References

[1] Y. Şahin, Recent progress in processing of tungsten heavy alloys, J. Powder Technol. 2014 (2014) 1–22.

[2] K. Hu, X. Li, X. Ai, S. Qu, Y. Li, Fabrication, characterization, and mechanical properties of 93W-4.9Ni-2.1Fe/95W-2.8Ni-1.2Fe/95W-2.8Ni-1.2Fe-1Al2O3 heavy alloy composites, Mater. Sci. Eng. A. 636 (2015) 452–458.

[3] X. Gong, J. Fan, F. Ding, Tensile mechanical properties and fracture behavior of tungsten heavy alloys at 25-1100 °C, Mater. Sci. Eng. A. 646 (2015) 315–321.

[4] U.R. Kiran, A. Panchal, M. Sankaranarayana, G.V.S.N. Rao, T.K. Nandy, Effect of alloying addition and microstructural parameters on mechanical properties of 93% tungsten heavy alloys, Mater. Sci. Eng. A. 640 (2015) 82–90.

[5] W.D. Cai, Y. L, R.J. Dowding, F.A. Mohamed, E.J. Lavernia, A review of tungsten-based alloys as kinetic energy penetrator materials, Rev. Part. Mater. 3 (1995) 71–131.

[6] C. Henager Jr, W. Setyawan, T. Roosendaal, N. Overman, B. Borlaug, E. Stevens, K. Wagner, R. Kurtz, G.R. Odette, B. Nguyen, K. Cunningham, Ductile-phase toughened tungsten for plasma-facing materials in fusion reactors, Int. J. Powder Metall. 53 (2017) 53–69.

[7] M. Scapin, Mechanical characterization and modeling of the heavy tungsten alloy IT180, Int. J. Refract. Met. Hard Mater. 50 (2015) 258–268.

[8] R. Neu, H. Maier, M. Balden, S. Elgeti, H. Gietl, H. Greuner, A. Herrmann, A. Houben, V. Rohde, B. Sieglin, I. Zammuto, Investigations on tungsten heavy alloys for use as plasma facing material, Fusion Eng. Des. 124 (2017) 450–454.

[9] R. Neu, H. Maier, M. Balden, R. Dux, S. Elgeti, H. Gietl, H. Greuner, A. Herrmann, T. Höschen, M. Li, V. Rohde, D. Ruprecht, B. Sieglin, I. Zammuto, Results on the use of tungsten heavy alloys in the divertor of ASDEX Upgrade, J. Nucl. Mater. 511 (2018) 567–573.

[10] H. Sattar, S. Jielin, H. Ran, M. Imran, W. Ding, P. Das Gupta, H. Ding, Impact of microstructural properties on hardness of tungsten heavy alloy evaluated by stand-off LIBS after PSI plasma irradiation, J. Nucl. Mater. 540 (2020) 152389.

[11] Q. An, A. Elshafiey, L. Huang, D.A. Hammer, M. Hassani, Plasma and X-ray radiation-induced damage mechanisms in a tungsten heavy alloy, J. Nucl. Mater. 539 (2020) 152325.

[12] G.R. Odette, M.E. Alam, K. Cunningham, Ductile-Phase Toughened Tungsten for Plasma Facing Materials, DOE-UCSB-ER54275, United States, 2019.
[13] T. Laas, K. Laas, J. Paju, J. Priimets, S. Tõkke, B. Väli, V. Shirokova, M. Antonov, V.A. Gribkov, E. V. Demina, V.N. Pimenov, M. Paduch, R. Matulka, M. Akel, Behaviour of tungsten alloy with iron and nickel under repeated high temperature plasma pulses, Fusion Eng. Des. 151 (2020).
[14] X. Gong, J.L. Fan, F. Ding, M. Song, B.Y. Huang, Effect of tungsten content on microstructure and quasi-static tensile fracture characteristics of rapidly hot-extruded W-Ni-Fe alloys, Int. J. Refract. Met. Hard Mater. 30 (2012) 71–77.
[15] X. Gong, J.L. Fan, F. Ding, M. Song, B.Y. Huang, J.M. Tian, Microstructure and highly enhanced mechanical properties of fine-grained tungsten heavy alloy after one-pass rapid hot extrusion, Mater. Sci. Eng. A. 528 (2011) 3646–3652.
[16] Z.S. Levin, K. Ted Hartwig, Hardness and microstructure of tungsten heavy alloy subjected to severe plastic deformation and post-processing heat treatment, Mater. Sci. Eng. A. 635 (2015) 94–101.
[17] Y. Yang, H. Lianxi, W. Erde, Microstructure and mechanical properties of a hot-hydrostatically extruded 93W-4.9Ni-2.1Fe alloy, Mater. Sci. Eng. A. 435–436 (2006) 620–624.
[18] Y. Yu, H. Hu, W. Zhang, X. Xu, Microstructure evolution and recrystallization after annealing of tungsten heavy alloy subjected to severe plastic deformation, J. Alloys Compd. 685 (2016) 971–977.
[19] Y. Yu, W. Zhang, E. Wang, Effect of heat treatment on microstructure and mechanical properties of hot-hydrostatically extruded 93W-4.9Ni-2.1Fe alloy, J. Alloys Compd. 622 (2015) 880–884.
[20] Z.H. Zhang, F.C. Wang, S.K. Li, L. Wang, Deformation characteristics of the 93W-4.9Ni-2.1Fe tungsten heavy alloy deformed by hydrostatic extrusion, Mater. Sci. Eng. A. 435–436 (2006) 632–637.
[21] Z. Zhaohui, W. Fuchi, Research on the deformation strengthening mechanism of a tungsten heavy alloy by hydrostatic extrusion, Int. J. Refract. Met. Hard Mater. 19 (2001) 177–182.
[22] B.N. Nguyen, C.H. Henager, J. Wang, W. Setyawan, Tailoring ductile-phase toughened tungsten hierarchical microstructures for plasma-facing materials, J. Nucl. Mater. 540 (2020) 152382.
[23] ASTM E1921-20, Standard Test Method for Determination of Reference Temperature , To , for Ferritic Steels in the Transition Range, in: Annu. B. ASTM Stand., ASTM International, 100 Barr Harbor Drive, PO Box C700, West Conshohocken, PA 19428-2959, United States, 2020: pp. 1–25.
[24] M.E. Alam, G.R. Odette, C.H. Henager, W. Setyawan, Fracture Toughness of Rolled 90WNiFe Tungsten Heavy Metal Alloy, Fusion React. Mater. Progr. Semiannu. Prog. Rep. DOE0313/67 (2019) 52–65.
[25] M.E. Alam, J. Wang, C.H. Henager, W. Setyawan, G.R. Odette, The effect of hot rolling on the strength and fracture toughness of 90W–7Ni3Fe tungsten heavy metal alloys, Mater. Sci. Eng. A. (2021) 141738.
[26] ASTM E384, Standard test methods for microindentation hardness of materials, in: Annu. B. ASTM Stand., ASTM International, West Conshohocken, PA, United States, 2006: pp. 1–33.
[27] ASTM E8M-15a, ASTM E8/E8M - 15a: Standard test methods for tension testing of metallic materials, in: Annu. B. ASTM Stand., ASTM International, 100 Barr Harbor Drive, PO Box C700, West Conshohocken, PA 19428-2959, United States, 2015.
[28] M.E. Alam, G.R. Odette, On the remarkable fracture toughness of 90 to 97W-NiFe alloys revealing powerful new ductile phase toughening mechanisms, Acta Mater. 186 (2020) 324–340.
[29] J. V. Haag IV, D.J. Edwards, C.H. Henager, W. Setyawan, J. Wang, M. Murayama, Characterization of Ductile Phase Toughening Mechanisms in a Hot-Rolled Tungsten Heavy Alloy, Acta Mater. 204 (2020) 116523.
[30] K. Tsuchida, T. Miyazawa, A. Hasegawa, S. Nogami, M. Fukuda, Recrystallization behavior of hot-rolled pure tungsten and its alloy plates during high-temperature annealing, Nucl. Mater. Energy. 15 (2018) 158–163.
[31] A. Alfonso, D. Juul Jensen, G.N. Luo, W. Pantleon, Thermal stability of a highly-deformed warm-rolled tungsten plate in the temperature range 1100-1250 °c, Fusion Eng. Des. 98–99 (2015) 1924–1928.
[32] J.G. Swadener, E.P. George, G.M. Pharr, The correlation of the indentation size effect measured with indenters of various shapes, J. Mech. Phys. Solids. 50 (2002) 681–694.

[33] P. Zhang, S.X. Li, Z.F. Zhang, General relationship between strength and hardness, Mater. Sci. Eng. A. 529 (2011) 62–73.

4.7 X-RAY DIFFRACTION STUDY OF W Fe-Ni LIQUID PHASE SINTERED TUNGSTEN HEAVY ALLOYS—D.J. Sprouster, L.L. Snead (Stony Brook University), M.E. Alam, G.R. Odette (University of California, Santa Barbara)

OBJECTIVE

In this work, we employ high-energy X-ray diffraction to identify and quantification of phases and microstructure in base WHAs with 90, 92.5, 95 and 97wt.%W Fe-Ni liquid phase sintered WHAs. We find a composition-dependent compressive residual strain in host BCC W phase, potentially due to the inclusion of the FCC NiWFe phase or processing. Lattice strain was quantified in the BCC W and FCC NiWFe phases, by 2D XRD mapping around the fracture surface. We find that the FWHMs of the BCC W peaks are large around fracture surface, presumably due to large fractions of dislocations and slip bands. Finally, the lattice strain in NiWFe is larger than that of the BCC host matrix.

SUMMARY

Tungsten is generally too brittle to serve as a structural material in extreme environments. However, the fracture toughness of W-Fe-Ni liquid sintered, biphasic tungsten heavy alloys (WHAs) is ~10 to 20 times larger than for monolithic W. This superior WHA toughness involves new mechanisms associated with arrest, blunting and bridging of microcracks, leading to crack tip stress field shielding and large amounts of plastic deformation, which is accommodated in the ductile W-Fe-Ni phase [1]. Both laboratory and synchrotron-based x-ray techniques are used to characterize the evolution of the local constituent phase stress and strain states, as well as dislocation structures and damage, in tensile specimens loaded to rupture. This unique database will be key to developing rigorous models of the remarkable new deformation and toughening mechanisms operating in WHAs. Future in situ experiments are planned.

PROGRESS AND STATUS

The XRD measurements were performed at the National Synchrotron Light Source-II (NSLS-II) using the high-energy X-rays available at The X-ray Powder Diffraction beamline (XPD). High signal to noise XRD patterns were collected at the top of the gauge section (away from fractures surface). A second set of XRD patterns were collected by 2D mapping the specimens from the fractured surface, up the gauge to the grip. This second set of measurements were performed to understand the evolution of lattice strain and any changes in the microstrain (2D defects) away from fractured surface for the 90, 92.5, 95 and 97wt.%W Fe-Ni liquid phase sintered WHAs.

All measurements were performed in transmission mode with an amorphous Silicon-based flat panel detector (Perken-Elmer) mounted orthogonal to and centered on the beam path. The sample-to-detector distances and tilts of the detector relative to the beam were refined using a LaB6 powder standard (NIST standard reference material 660c). The wavelength of the incident X-rays was 0.1917 Å (66.676 keV). The sample-to-detector distance was calculated to be 1387.81 mm. 300 individual patterns with detector exposures of 0.2s were collected for each specimen. All raw two-dimensional patterns were background corrected by subtracting the dark current image and the air scattering and Kapton background within IgorPro (Wavemetrics). Noticeable artefact regions of the detector (like the beam stop, dead pixels) were masked. The corrected and masked two-dimensional detector images were then radially integrated to obtain one-dimensional powder diffraction patterns. XRD patterns were collected from air, the broken gauge, all the way up the tensile specimen to the grip as shown in Figure 1. Phase identification was performed using Match3! (Crystal Impact, Bonn, Germany). The background subtracted XRD patterns were refined with the MAUD software package. The peak profiles were modeled by a modified pseudo-Voigt function. The instrument contribution to the broadening of the measured profiles was quantified by fitting

the LaB_6 NIST powder standard, with a known coherent grain size and negligible microstrain contribution. The Gaussian and Lorentzian-based broadening parameters were subsequently fixed during the analysis of the alloys under investigation to quantify the microstructure (coherent grain size and microstrain components). The phase fraction, lattice parameter, microstrain and coherent grain size components could vary for the different crystal phases present. The microstrain components for the FCC phases were not included in the refinements. Therefore, the refined coherent grain size parameters of these phases are lower limits.

Results

The XRD patterns for the WHA specimens are shown in Figure 2. All specimens have two components, including the BCC W and FCC NiWFe phase. From Figure 2 only subtle differences in peak positions (lattice parameters), and peak heights for the W and NiFeW phases are observable indicative that in the bulk, there are some Microstructural differences (coherent grain size, microstrain).

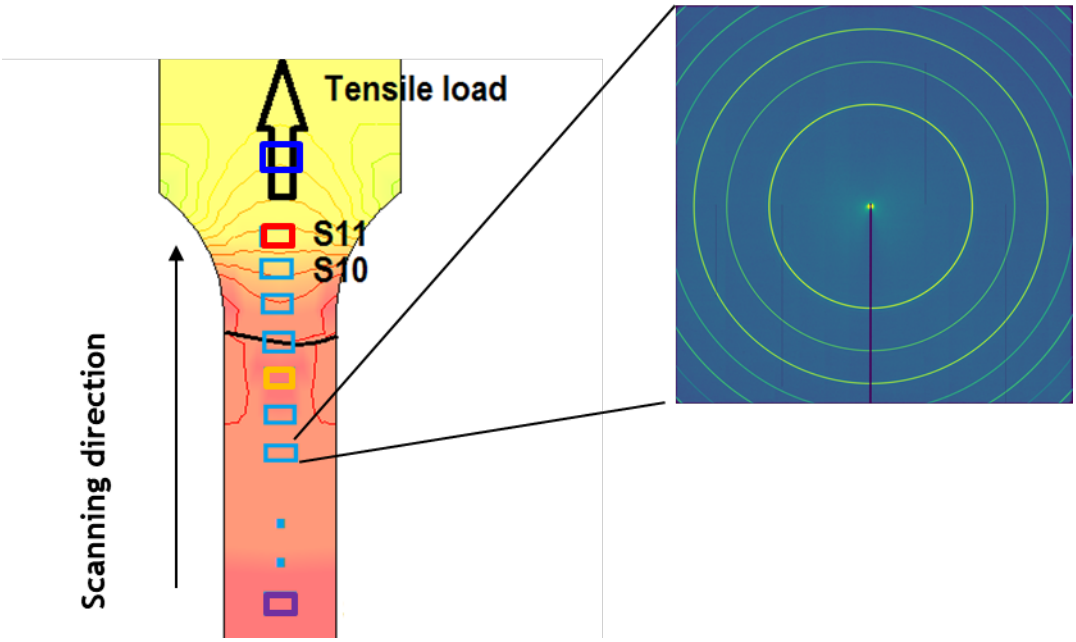

Figure 1. XRD pattern measurements for the WHA specimens.

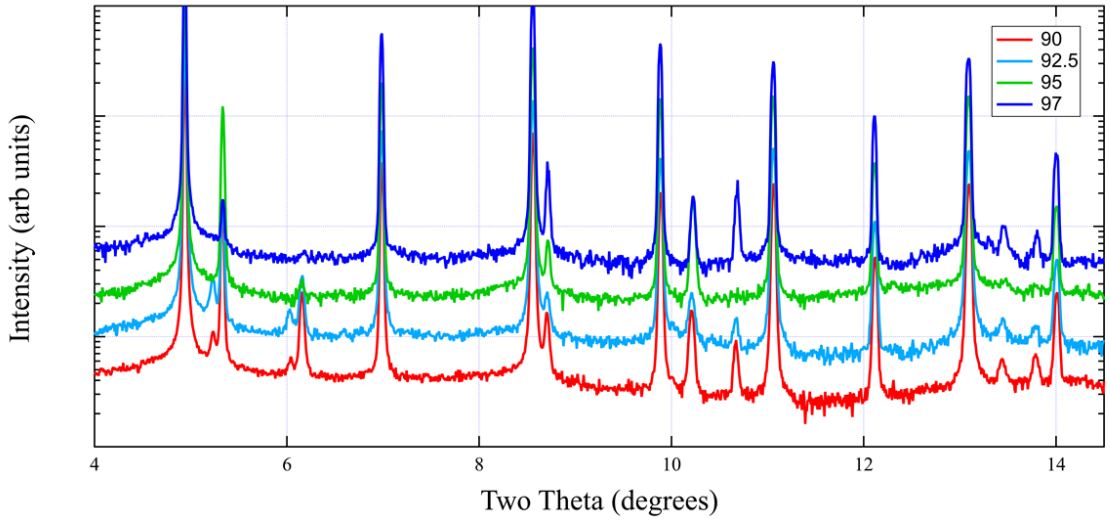

Figure 2. The XRD phase identification for 90 WHA specimen. The phases identified include FCC Fe (green), FCC NiW (orange) and BCC W (red).

The quantitative XRD refinement results are given in Figure 3 as a function of W content (%). In the base materials, the lattice parameters of the BCC W phase are contracted relative to bulk W. This is potentially due to the excess strain or from the inclusion of the FCC NiWFe phase (Eshelby) and compressive in nature. The microstructural parameters are similar across composition range and the Wt. fraction of NiWFe phase increases with Increasing Fe and Ni.

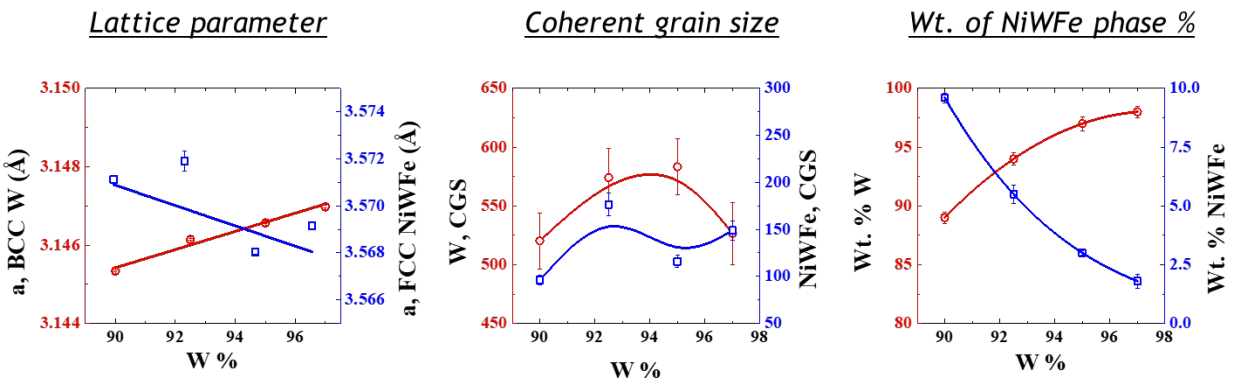

Figure 3. Quantitative XRD results for all WHA alloys studied.

Figure 4 shows a representative series of XRD patterns collected from different distances from the fractured surface. The position and FWHM of the XRD peaks shift and broaden (respectively) the closer to the fracture surface. Individual peaks (hkls) were refined, to capture the position and width of selected XRD peaks for the different compositions. The results from the XRD peak position analysis are shown in Figure 5 for the 90 and 95% WHA alloys for (110) and (211) planes. Small strains in the BCC W matrix from fracture surface are thus clearly observable from the position of XRD peaks. largest strains are observable at the fracture surface (relative to higher on the gauge). Similar trends were observable for all compositions.

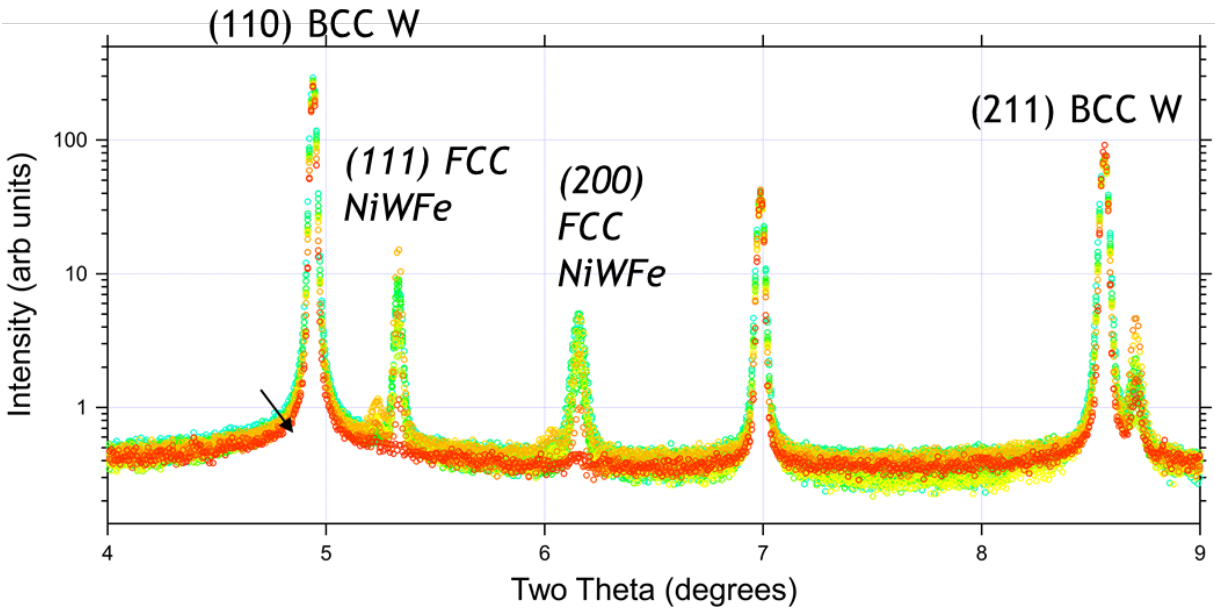

Figure 4. XRD patterns from 2D scanning experiment. The changes in the position and FWHM are subtle, and quantitative peak analysis is required to extract the changes with distance.

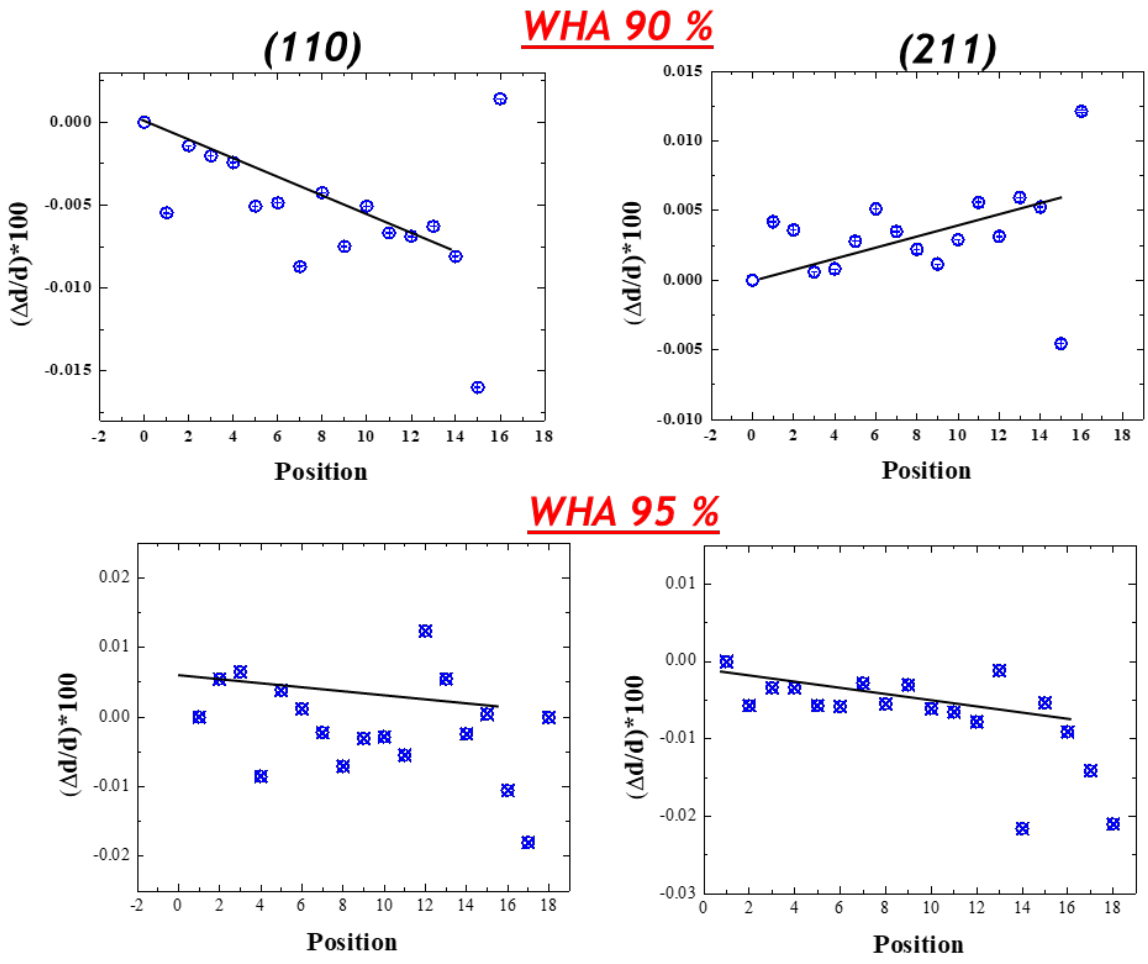

Figure 5. Changes in peak position for the (110) and (211) XRD peaks for the 90 and 95% WHA specimens.

The results from the XRD peak FWHM analysis are shown in Figure 6 for the 90 and 95% WHA alloys for (110) and (211) planes. Similar trends in FWHMs across sample matrix and hkl's were quantified (magnitudes and shape) from all specimens and indicate that 2D defects vary in the BCC W matrix phase and decrease in magnitude the further away from the fractured surface. The strain in the FCC NiWFe phase was also quantified from an identical fitting procedure. The results from the peak fitting for the NiFeW phase are shown in Figure 7. The strain in FCC NiWFe from fracture surface is observable as large changes in the position of XRD peaks, which appear to be ~ one order of magnitude larger than those determined for the BCC W matrix.

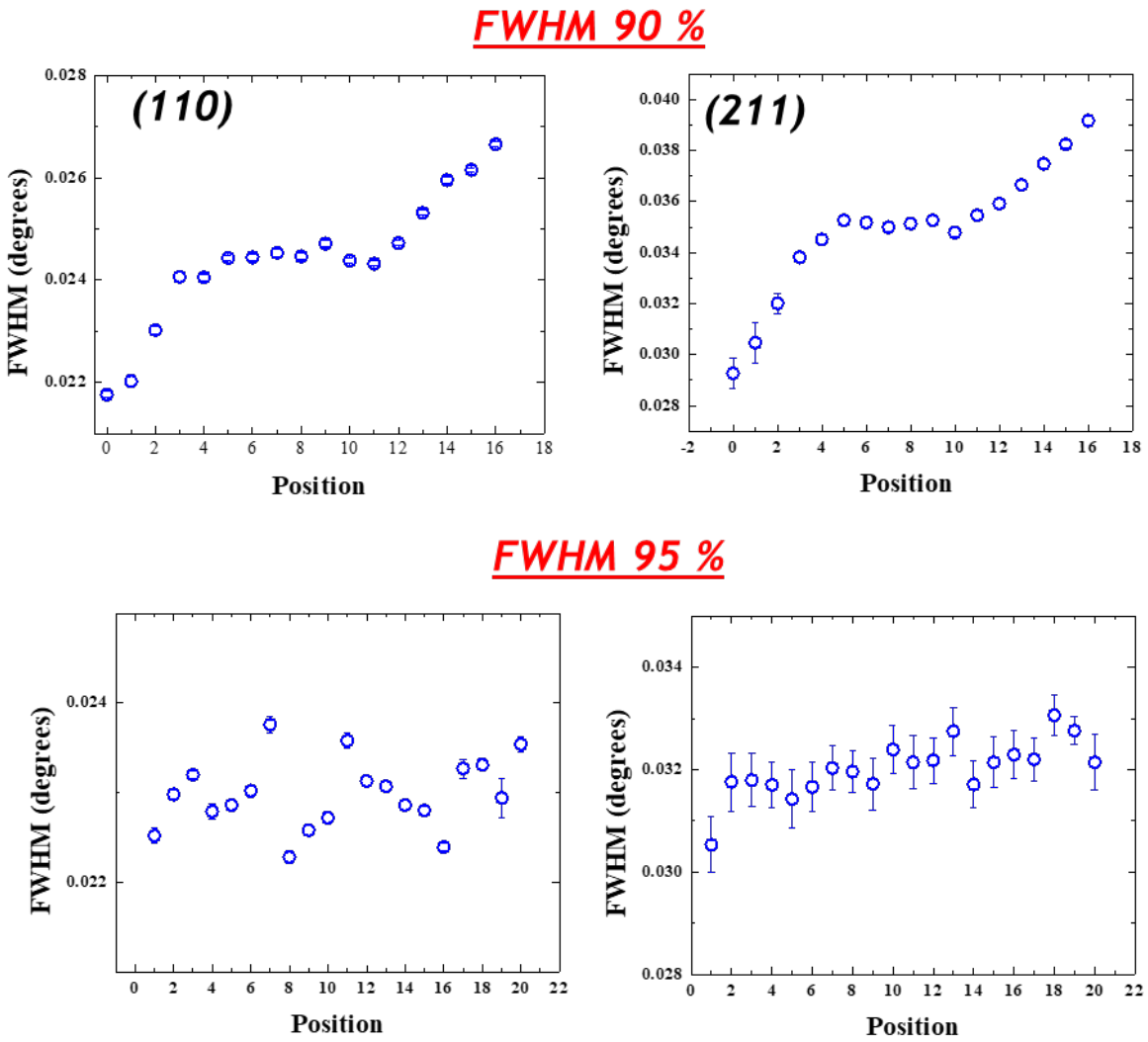

Figure 6. Changes in the FWHM for the (110) and (211) peaks for the 90 and 95% WHA specimens.

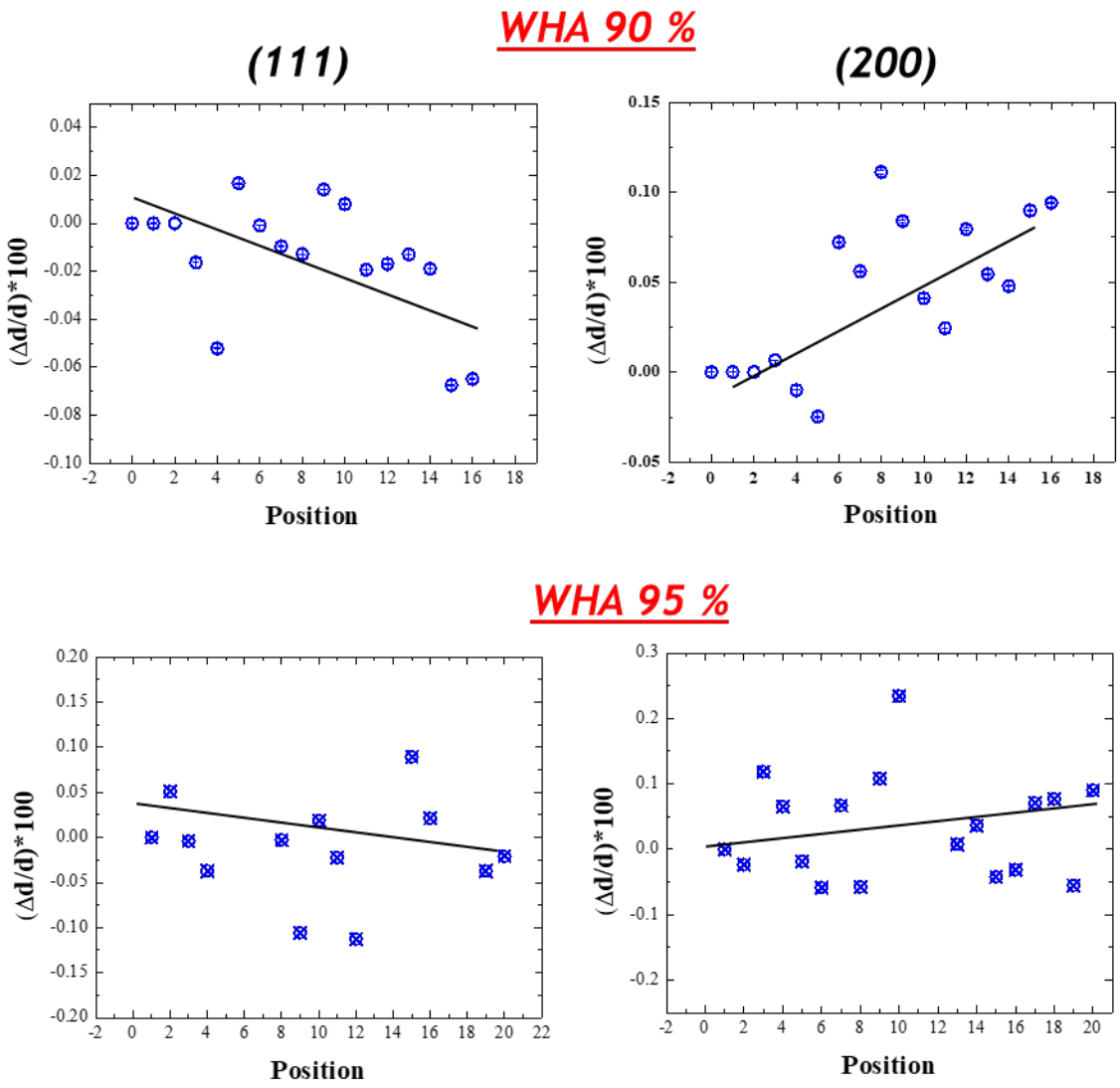

Figure 7. Changes in peak position for the NiWFe (111) and (200) XRD peaks in the 90 and 95% WHA specimens. Note the larger changes in the strain (order of magnitude) compared to the BCC phase.

Future Work

These initial results show that high energy XRD is particularly useful in providing detailed topological microstructural information in dense NiWFe. The 2D XRD scanning results show that the averaged structures show that the fractured surfaces display both an increased lattice strain and microstructural based broadening, that decrease away from the fractured surface. Future work will include analysis of different hkl's to correlate changes in BCC W and FCC NiWFe phases. Further analysis of the 2D XRD patterns, using horizontal and vertical components from the individual 2D XRD images, could be explored to access any anisotropic defect components introduced from the mechanical strain [2]. Future in situ XRD measurements at XPD or PDF with a mechanical stage are planned in following FY22.

Acknowledgements

These experiments and analysis were supported by the DOE Office of Fusion Energy Sciences under contract DE-SC0018322 with the Research Foundation for the State University of New York at Stony Brook. This research used The X-ray Powder Diffraction beamline of the National Synchrotron Light Source II, a U.S. Department of Energy (DOE) Office of Science User Facility operated for the DOE Office of Science by Brookhaven National Laboratory under Contract No. DE-SC0012704.

References

[1.] Alam, M.E. and G.R. Odette, *On the remarkable fracture toughness of 90 to 97W-NiFe alloys revealing powerful new ductile phase toughening mechanisms.* Acta Materialia, 2020. **186**: p. 324-340.

[2.] Koyanagi, T., et al., *X-ray characterization of anisotropic defect formation in SiC under irradiation with applied stress.* Scripta Materialia, 2021. **197**: p. 113785.

4.8 ON THE STRENGTH OF INTERPHASE BOUNDARIES IN A HOT-ROLLED TUNGSTEN HEAVY ALLOY—James V. Haag IV, Mitsu Murayama (Virginia Tech), Danny J. Edwards, Jing Wang, Wahyu Setyawan (Pacific Northwest National Laboratory)

OBJECTIVE

The goal of this study is the analysis of multiple tungsten – ductile phase boundaries in a thermo-mechanically processed tungsten heavy alloy to gain insight into their high interfacial strength.

SUMMARY

Recent progress has been made on the transmission electron microscope (TEM) characterization of a hot-rolled 90W-7Ni-3Fe alloy. This has been done to determine the role of the interphase boundary in the overall mechanical behavior of the system. The current hypothesis for the effective expression of both high stiffness and toughness in these alloys is that behavior depends on the strong adhesion between the tungsten phase and Ni-Fe-W phase. The TEM analysis of these boundary interfaces reveals surprising levels of lattice coherency despite the dissimilar crystal structures, lattice parameters, and kinetics of formation. Multiple boundaries have been noted to be faceted, with phase boundary structures theorized to be semi-coherent in nature. This faceting behavior and proposed semi-coherency may increase the strength of these boundaries by lowering the free energy and increasing their decohesion energy. This report represents the ongoing work in understanding the remarkable mechanical properties of these materials.

PROGRESS AND STATUS

Introduction

The material of interest to this study is a hot-rolled tungsten heavy alloy (WHA) produced by Pacific Northwest National Laboratory (PNNL) as a potential structural material in plasma facing components (PFCs) in nuclear fusion reactors [1-3]. This class of alloys is the subject of multiple prior and ongoing studies [1-10] into their viability for this role. Yet the exact response of these microstructures to the simulated thermal, mechanical, and irradiation stimuli of the fusion environment is still unknown. The expectation is that these materials will retain many of the properties which make polycrystalline tungsten an excellent plasma facing material, while exhibiting ductility far more than tungsten, even post-irradiation. The current goals of this extended research are to test the validity of this claim, and present results aimed at making an informed selection of materials for PFCs. Of particular interest in this study are what geometric, chemical, and microstructural factors give rise to the effective ductile phase toughening in these composites.

Prior semiannual reports have discussed the microstructural characterization of WHAs first from a bulk-scale perspective [4-5] and have necessarily progressed down to the TEM length-scale [5-6] to describe the behavioral phenomena noted in physical testing. This interplay of different phases, geometries, and relative boundary strengths seem to govern the ductile phase toughening behavior of these alloys and warrant further exploration as they are not well understood. The in-situ and ex-situ mechanical testing of these alloys [7-9] has revealed a surprising lack of fracture incidences at the FCC Ni-Fe-W phase and BCC tungsten phase interface, which has been theorized to be a dominant reason these microstructures can be hard while also retaining excellent deformability. This has ultimately led to a focused evaluation of what factors may lead to this high interphase adhesion and has motivated a TEM-based investigation of the FCC-BCC phase interface. If this interface is indeed what allows the simultaneous utilization of tungsten's hardness and the deformability of the FCC phase, then TEM observation of these boundaries may aid in the interpretation of the specific factors which appear to govern the mechanical behavior of these materials. This boundary-based analysis will allow for better determination of what gives rise to this high boundary adhesion, and then how to best take advantage of this effect for microstructural optimization.

Experimental

The TEM foils were prepared via the dimple grinding and low-kV Ar ion milling process detailed in [6], with the added caveat of all PIPS II ion milling now taking place at cryogenic temperatures (approximately -170°C) as opposed to room temperature. This condition was implemented in the preparation process for TEM foils as it was theorized that the lower temperatures combined with lower acceleration voltage (100eV) final milling steps with Ar ions would produce specimens with comparatively reduced damage from the thinning process as well as allow greater control over the removal speed by slowing the milling process. This thinner damage layer could then be removed with less aggressive flash electropolishing conditions, which would lead to the reduction of the effects of preferential material removal, and thereby final foil thickness variations. This uneven specimen thickness is caused by the difference in electrochemical properties of the W and Ni-Fe-W phases and would yield TEM foils with the more noble phase having a greater thickness than the less noble phase. This preferential electropolishing is a large downside to electrochemical thinning processes when considering materials with more than one phase and is an area worth pursing further to reduce or potentially eliminate preparation process induce damage in multiphase materials.

This newly implemented low-temperature ion milling process roughly doubled the active milling time to reach electron transparency but produced TEM foils with superior surface damage reduction as compared to conventionally prepared focused ion beam (FIB) liftout specimens, and qualitatively yielded more regions with less pronounced thickness variations between phases as compared to prior combined PIPS II thinning and flash electropolishing attempts. While the elimination of surface damage in TEM foils is not mission critical in this current analysis, it is essential that the upcoming analysis of irradiated WHA specimens contains as few preparation-induced defects as possible. Especially as these 'black spot' defects generated from ion beam based thinning techniques may mimic radiation damage, leading to incorrect quantification of defect structures and densities. Representative micrographs of this progression in making thinner and more damage free WHA TEM specimens have been provided in Figure 1 below.

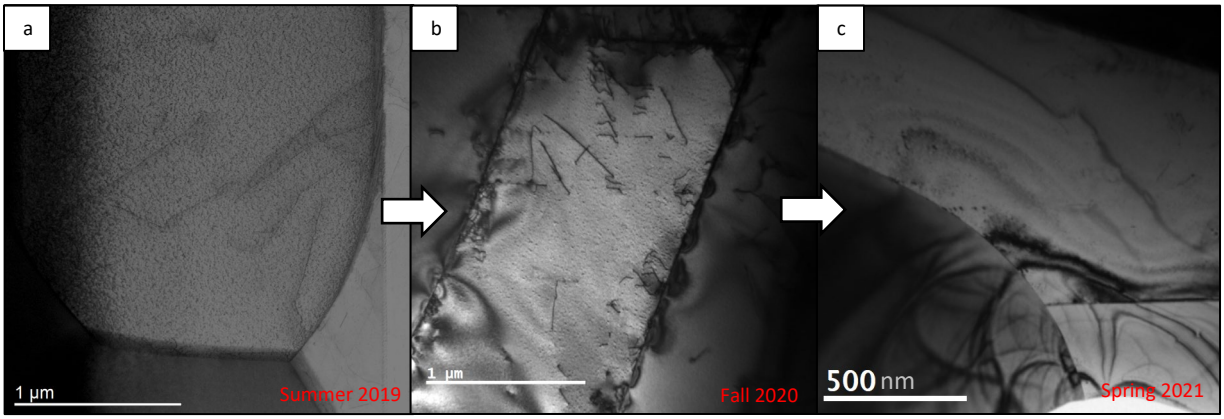

Figure 1. Bright field images of TEM foils from (a) FIB liftout with a 5kV Ga^+ final milling step, (b) Ar ion milled at room temperature with a 250eV final milling step, and (c) Ar ion milled at cryogenic temperature with a 100eV final milling step. The small black spots dotting the specimens are indicative of surface damage from specimen preparation.

Multiple interphase boundary regions from these specimens were then observed using a JEOL 2100 TEM for imaging and orientation analysis. Prior TEM analyses [6] had revealed a surprising degree of lattice matching and some regions which potentially exhibit semi-coherent boundary structures between the W and Ni-Fe-W phases, which may in part be due to the high symmetry of both crystal structures. However, no dominant orientation relationship between the two phases has been observed, either though EBSD or TEM analysis. This is not entirely surprising though, as these dual-phase microstructures are a result of liquid phase sintering and thermomechanical treatment rather than the precipitation of one phase from a

parent phase, where a limited number of orientation relationships would be expected. It is possible that crystallographic texturing of the W or Ni-Fe-W phase due to the hot-rolling process could induce some form of preferred angular misorientation between the phases, but plots of W to Ni-Fe-W phase misorientation angles follow the Mackenzie randomness distribution for boundary disorientation character almost perfectly, indicating seemingly no presence of preferred phase boundary orientations. This is the case for the material in both its liquid phase sintered state and after hot rolling. While there appears to be no statistically dominant boundary orientation relationship, TEM analysis of these boundaries will help to gain better insight into their appearance and respective grain orientations of these regions at the nanoscale.

Closer inspection of these interphase boundary regions in the hot-rolled material has revealed that many exhibit planar facets, like those marked by red dashed lines in Figure 2. This finding highlights the benefits of using a dimple ground and ion milled specimens due to their large areas for observation compared to the relatively small analytical areas provided by a conventional FIB liftout specimen. These specimens allow for more regions and larger areas of electron transparency in the analysis of specimens, like that shown in Figure 2a, which can then be used to generate a more comprehensive picture of the microstructure. This does come at the cost of a large decrease in site specificity for specimen preparation as compared to FIB liftouts. It is also noted that not all phase boundary regions exhibit this faceted appearance, and those that do appear to exhibit multiple different facets, even along the same boundary. These facets have been observed to vary in size from tens of nanometers up to over a micron in length and are typically of a size scale below the resolution limit of EBSD. Therefore, without relatively high magnification SEM imaging or TEM analysis, these facets may be overlooked entirely. Lower magnification observation of these structures may not provide the requisite spatial resolution to properly characterize these boundary regions, and this multi-faceted structure which would otherwise give the impression of a rounded or contoured boundary shape possesses a phase boundary structure composed of multiple planar facets which all satisfy one orientation relationship. These facets each have a boundary plane which is posited to represent some local energy minima, which reduces the overall interfacial energy of the system, with jogs or breaks in that plane, leading to another planar facet which satisfies the same orientation relationship, but a different low-energy boundary plane. The observed planar faceting is corroborated by prior research on dual-phase Ti-Al alloys in [11-12], and this postulated energy reduction by planar faceting may in-part be responsible for the high strength of these boundaries. Now this is theorized to be the case but requires confirmation in the boundary plane indexing of each facet in one of these multi-faceted regions and comparison to the expected energy if the boundary were to be contoured in appearance.

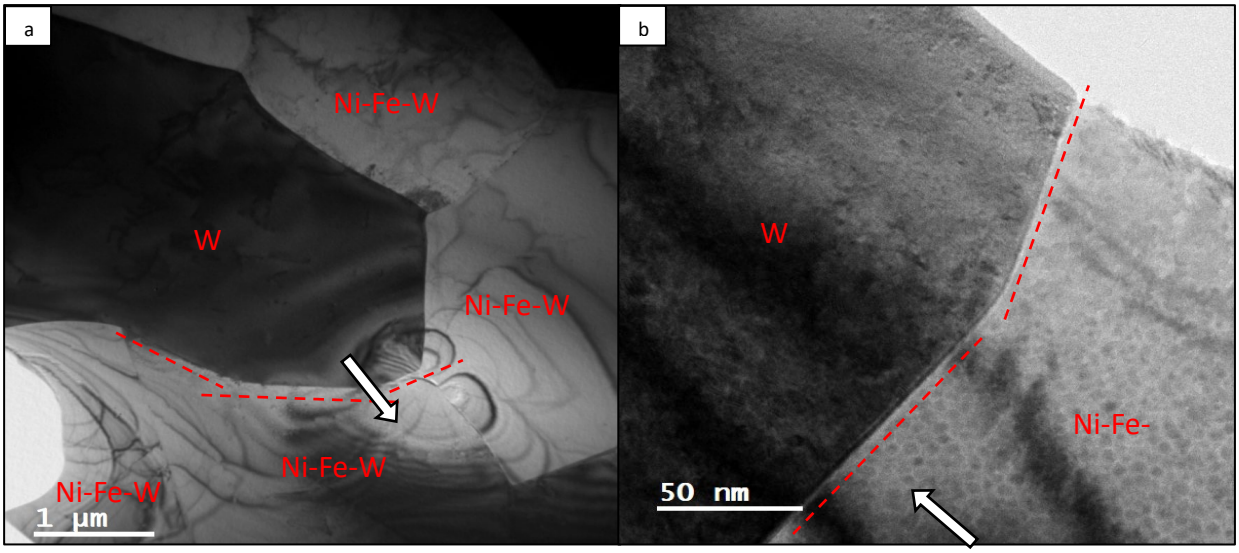

Figure 2. Bright field TEM images from two different interphase boundaries. Apparent facets at the phase boundary plane are marked by red dashed lines. White arrows indicate the faceted regions shown at a higher magnification in Figure 3a and b respectively.

The structural nature of these facets has been investigated in greater detail, and it has been found that these boundary regions exhibit features which are indicative of semi-coherency. High magnification phase contrast TEM images of the facets delineated by white arrows in Figures 2a and b have been displayed in Figures 3a and b respectively. Both these regions display periodic arrays of regularly spaced linear contrast features across the boundary plane, which are thought to be interfacial misfit dislocations. The inset of Figure 3a lends further evidence to this semi-coherency claim as there is obvious strain present with the Ni-Fe-W lattice approaching the boundary plane that allows for the periodic matching of 4× W <110> planes to 5× Ni-Fe-W <200> planes. This misfit strain also does not appear to be present in the W phase, with no apparent expansion or contraction of the W lattice.

One conflicting factor with this claim of semi-coherency is that these features may also be a result of a periodic interference pattern which arises from the overlapping of the two crystal structures, called Moiré fringes. To discuss this potential effect, the micrographs of Figure 3 have been displayed alongside their simulated Moiré fringe patterns. These simulated patterns were generated by creating a grating of parallel lines whose spacings match that of the crystallographic planes in question and whose orientation matches that of the planes in the micrograph. These gratings can then be superimposed to simulate the effect of the boundary being inclined with respect to the field of view, visualizing both lattices at once, and the resulting interference pattern. These simulations of the interference patterns slightly overlapping crystallographic planes on either side of the boundary can be compared to the features noted in the micrographs, and their spacing as well as orientations relative to one another can be used to aid in the assessment of the nature of these features. If the overlapping gratings produce a pattern perfectly mimicking that of the micrographs, then it is likely that these features are not interfacial dislocations and are instead the result Moiré fringes.

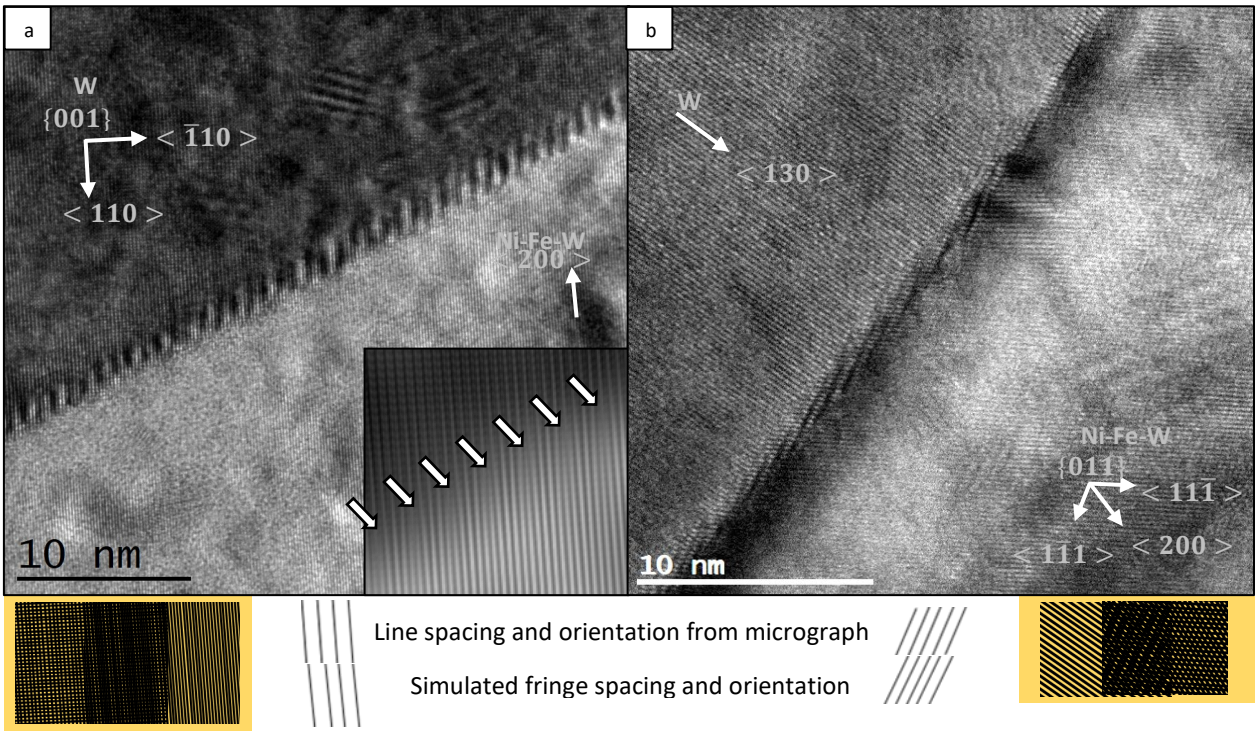

Figure 3. High magnification phase contrast TEM images of facets from Figures 2a and b respectively. Micrographs have been provided alongside their simulated Moiré fringe patterns, shown at 1:1 scale within the yellow boxes. For ease of observation the measured linear spacings and calculated fringe spacings have been displayed next to one another for both (a) and (b). The inset in (a) shows a higher magnification FFT filtered region from the larger region of (a) with white arrows delineating the extra half planes visible on the Ni-Fe-W side of the boundary.

Comparison of the micrographs and simulated fringe patterns in Figure 3 yields a very similar spacing and orientation, but not exact match between the simulated Moiré patterns and those of the micrograph. It is possible that the slight differences in fringe spacing and angle with respect to the micrographs are within the margin of error for the simulation. It cannot be entirely ruled out that these features may indeed be the result of Moiré fringe contrast instead of interfacial dislocations or vice versa. To definitively prove the true nature of these features, an emphasis will be placed upon conducting on-edge atomic column imaging of these regions using an aberration corrected scanning transmission electron microscope (STEM). A concerted effort will also be made towards indexing the boundary planes in a multi-faceted interphase boundary region to confirm if these facets trend towards certain low-index or low-energy crystallographic planes.

Understanding the structure of these boundaries is paramount in developing a working theory of phase boundary strength in these materials. Thus far, evidence seems to indicate that the system is attempting to reach an overall lower energy free energy through faceting at the interphase boundaries, and potentially establishing some form of edge-to-edge lattice matching or semi-coherency. One specific area that would greatly benefit this experimental work is complementary modelling study, like that done in [10] on these boundaries to determine if a faceted phase boundary presents a higher decohesion energy than a contoured boundary of similar geometry. The greater question raised by this research is if a lower interphase boundary energy corresponds to a stronger boundary. If this is the case, then the surprising strength of the interphase boundary region may come because of the WHA system attempting to achieve thermodynamic equilibrium by the lowering of interfacial energies through increasing lattice coherency and faceting along low-energy planes. While it remains unknown if these facets represent further interfacial energy reduction in the form of semi-coherent boundary structures in the faceted regions, it is important to note that these interphase boundary regions have been shown to exhibit a surprisingly strong bond. The direct link between the postulated decrease in interfacial energy and increase in decohesion energy of the boundary remains unknown, but the idea of the system achieving lower associated boundary energies is thought to be one of the determining factors in the interphase boundary strength expressed by this material.

Acknowledgement

This research has been supported by the U.S. Department of Energy, Office of Science, Office of Fusion Energy Sciences and performed at the Pacific Northwest National Laboratory under contract number DE-AC05-76RL01830

References

[1] R. Neu et al., “Investigations on tungsten heavy alloys for use as plasma facing material,” Fusion Engineering and Design, 124 (2017) 450.

[2] M. Li, D. Ruprecht, G. Kracker, T. Höschen, R. Neu, “Impact of heat treatment on tensile properties of 97W-2Ni-1Fe heavy alloy,” J. Nucl. Mater., 512 (2018) 1.

[3] C. H. Henager et al., “Ductile-Phase Toughened Tungsten For Plasma-Facing Materials In Fusion Reactors,” International Journal of Powder Metallurgy, 53 (2017) 18.

[4] J.V. Haag IV, M. Olszta, D. Edwards, M. Murayama, C.H. Henager Jr., W. Setyawan, “In-situ mechanical testing and interfacial characterization of ductile-phase toughened tungsten,” DOE0313/67 (2019) 78–85.

[5] J.V. Haag IV, M. Murayama, M. Olszta, D.J. Edwards, J. Wang, W. Setyawan, “Investigation of ductile phase toughening behavior in tungsten heavy alloys,” DOE fusion react, Mater. Progr. Semiannu. Prog. Rep. DOE0313/68 (2020) 91–95.

[6] J.V. Haag IV, M. Murayama, M. Olszta, D.J. Edwards, J. Wang, W. Setyawan, “Incorporating crystallographic orientation into the study of tungsten heavy alloy boundaries,” DOE fusion react, Mater. Progr. Semiannu. Prog. Rep. DOE0313/69 (2020) 106–111.

[7] M.E. Alam and G. R. Odette, “On the remarkable fracture toughness of 90 to 97W-NiFe alloys revealing powerful new ductile phase toughening mechanisms,” Acta Materialia, 186 (2020) 324.

[8] M.E. Alam, J. Wang, C.H. Henager Jr., W. Setyawan, G.R. Odette, “The effect of hot rolling on the strength and fracture toughness of 90W-7Ni3Fe tungsten heavy meal alloys,” Mat. Sci. Eng. A. https://doi.org/10.1016/j.msea.2021.141738.

[9] J. V. Haag, D. J. Edwards, C. H. Henager, W. Setyawan, J. Wang, and M. Murayama, “Characterization of ductile phase toughening mechanisms in a hot-rolled tungsten heavy alloy,” Acta Materialia, 204 (2021) 116523.

[10] W. Setyawan, “Density functional theory calculation of helium segregation and decohesion effect in W110/Ni111 interphase boundary,” Journal of Applied Physics, 128 (2020) 145101.

[11] J.M. Howe, W.T. Reynolds Jr., V.K. Vasudevan, “Static and in-situ high-resolution transmission electron microscopy investigations of the atomic structure and dynamics of massive transformation interfaces in a Ti-Al alloy,” Metallurgical and Materials Transactions A, 33A (2002).

[12] W.T. Reynolds Jr., J.F. Nie, W.Z. Zhang, J.M. Howe, H.I. Aaronson, G.R. Purdy, “Atomic structure of high-index α_2:γ_m boundaries in a Ti-46.54 at.%Al alloy,” Scripta Materialia, 49 (2003) 405.

4.9 QUANTIFYING MICROSTRUCTURE-MECHANICAL PROPERTY CORRELATION IN DUCTILE PHASE TOUGHENED W-NiFe HEAVY ALLOY

—Jing Wang, Ramprashad Prabhakaran, Wahyu Setyawan, Charles H. Henager (Pacific Northwest National Laboratory)

OBJECTIVE

The objective of the project is to understand the deformation behavior of ductile phase toughened tungsten heavy alloys, such as W-NiFe, for applications in fusion reactor divertor and plasma-facing components.

SUMMARY

This report summarizes the progress in investigating microstructure-mechanical property correlation in ductile phase toughened (DPT) W-NiFe alloys at PNNL. Previous studies have covered microstructure characterizations and tensile testing, in collaboration with finite element model development. The result of fracture surface characterizations of some of the failed tensile specimens is presented in this report. The measure microstructure and fracture surface characteristics are quantified, and their correlations with measured stress-strain curves are examined.

PROGRESS AND STATUS

Introduction

Ductile phase toughening (DPT) is a fracture toughness improvement concept being used to develop tungsten-based composites for fusion reactor divertor and plasma-facing materials. Tungsten is a promising candidate material for fusion reactor component applications due to its excellent high-temperature strength, low sputtering rate, and high melting temperature [1, 2]. However, the potential application of tungsten as a structural material is limited due to its low ductility, which could further degrade after irradiation [3]. Introducing a ductile phase for developing W composite could serve as an alternative route to overcome its limitations.

Previously, W-Cu composite materials have been investigated, and it is found that the ductile phase could form bridges near crack tips to enhance the fracture toughness of W-Cu composites [4, 5]. A finite element model was developed for understanding toughening mechanism (Dynamic Bridging Model) and for predicting load-displacement curves and crack propagation patterns (Finite Element Continuum Model) [6, 7]. Although W-Cu composites are a good starting model system for exploration, they are not suitable for the fusion reactor environment due to the low melting point of the ductile Cu phase. An alternative system of W-Ni-Fe composites was proposed and studied.

The 90W-NiFe as-received samples, in which W powders were embedded in a Ni-Fe matrix, were hot-rolled at PNNL to 62%, 74%, and 87% thickness reduction to attain a lamellar structure. In FY19 and FY20, efforts to collect experimental data to understand the effects of hot rolling and deformation behavior of DPT W-NiFe alloys are continued. This report focused on fracture surface characterization of the as-received 90W, and hot-rolled 90W to 87% thickness reduction, and examining microstructural characteristics correlations with measured stress-strain curves.

Experimental Procedure

The SEM examinations on DPT W-NiFe samples were carried out using a JEOL 7600 field emission SEM at PNNL. Samples for characterization were polished to a 0.05 μm colloidal silica finish. A low-angle backscatter electron (BSE) detector was utilized to examine the general microstructure at various locations. The results were processed and analyzed using the AZtec software package from the Oxford Instruments. Fractography was performed on selected samples as is without any tampering of the fracture surfaces. The specimen matrix in this report is listed in Table 1, and the corresponding specimen orientations are shown in Figure 1.

Table 1. Specimen matrix in this report

Specimen ID	Details
90W-0R	90 wt% W, as received, powder purchased from MiTech, sintered at PNNL
90W-87R-RD	90 wt% W, hot rolled to 87% thickness reduction, ND-RD orientation, along RD

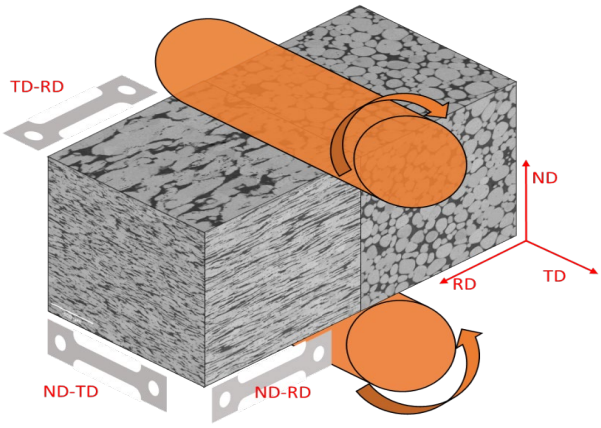

Figure 1. Tensile Specimen Orientations in 90W-87R [8]. The 90W-87R-Plan features the TD-RD orientation while the 90-87R-RD features the ND-RD direction. (RD = Rolling Direction, TD = Transverse Direction, ND = Normal Direction).

Preliminary Results

More detailed overviews of the general microstructure of W-NiFe alloy samples have been presented in previous reports [9-11]. Figure 2 shows the microstructure of the surface of as-sintered W-NiFe (90W-0R) specimens, surfaces of rolled W-NiFe (TD-RD for 90W-87R-Plan and ND-RD for 90W-87R-RD, as illustrated in Figure 1). The microstructure resembles two typical phases in this set of materials: a NiFe phase, which serves as the ductile matrix; and a W phase, which provides strength and high-temperature mechanical performance. It shows that along the rolling direction, the W phase deforms significantly into a plate-like structure. In the as-sintered 90W-0R, the W-phase is mostly spherical-like and some W-W grain boundaries exist, while in the hot-rolled W-NiFe samples, the W-phase deformed into plate-like morphology. The NiFe ductile phase shows significant grain refinement in the hot-rolled samples compared to as-sintered ones.

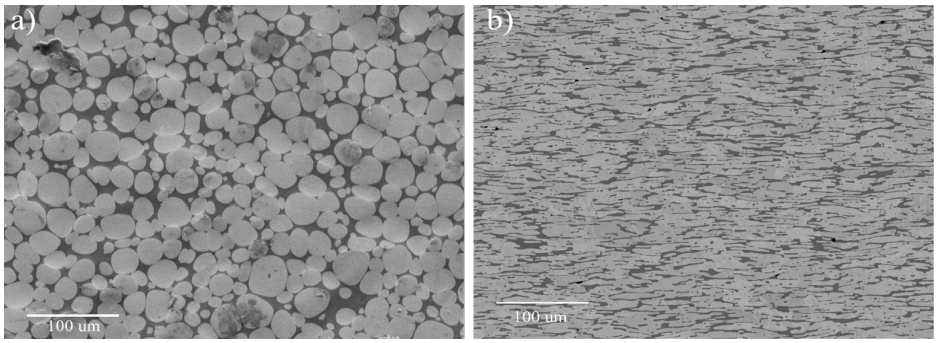

Figure 2. Band contrast (BC) images with marked grain boundary (GB, black), and phase boundary (PB, red, between W and NiFe phases) of 90W-0R, 90W-87R-Plan, and 90W-87R-RD in a), d) and g). The rest of band contrast images show W-phase and NiFe phases separately.

The images of the tensile specimen surface, though being representative for as-received 90W-0R specimens, only reflect one dimension of the story for hot-rolled specimens 90W-87R. Due to the highly anisotropic W phase, the surface image only provided a side view. The fracture surface would be useful to find out the area fraction of the NiFe phase along the crack propagation paths. Figure 3 shows examples of fracture surface images acquired with secondary and back-scattered electrons imaging. The BSE is used since in SE mode is difficult to distinguish W and NiFe phase. Combine the rich morphology information from SE and compositional information from BSE, the determination of fracture type is more accurate. In the as-received 90W-0R, four distinct fracture modes can be seen: the W phase cleavage; the W-W inter grain boundary (GB) fail; the NiFe matrix fail; and the W-NiFe interface fail. The first two are likely brittle while the latter two are likely ductile. In hot-rolled specimens, we have even observed brittle intergranular failure of NiFe matrix, likely due to the severe grain refinement during the process. The W phase cleavage is determined by its clear cleavage type fracture surface, while the inter grain boundary fail can be spotted with the typical ellipsoid-shaped flat surface. The W-NiFe interface fail can be a bit difficult to determine. On one side, the exposed spherical surface of the W phase is highly likely due to the W-NiFe interface failure. However, it is hard to determine from the NiFe phase side whether it is from NiFe matrix fracture or W-NiFe interface fracture.

Though fracture surface examination was almost routinely performed in investigating materials' mechanical properties, most of those studies follow a qualitative analysis approach. Instead, we are wondering whether a more precise, quantitative analysis would help on this already complicated structured composite or not. It is not very practical to manually label and measure all fracture modes since more than dozens of images were acquired from each specimen and we are interested in surveying significant areas of the fractured surface from failed tensile specimens. Machine learning, specifically deep learning models, comes in handy for this segmentation task.

Interestingly, a quick search online yielded a similar work by Tsopanidis et al., where a UNet convolutional neural network model was chosen to detect whether local microstructure is ductile or brittle fracture [12]. A schematic of the UNet model is shown in Figure 4. The Tsopanidis UNet model was trained using the $MgAl_2O_4$, to perform semantic segmentation on brittle and ductile fracture regions. The result from using their trained weights is presented in Figure 5, where green corresponds to ductile, and blue corresponds to brittle fracture. A couple of apparent issues can be seen immediately. First there are significant regions not segmented, which means the model doesn’t know which label to apply; Secondly the result seems to change with different magnifications; the third issue is that the classification is mostly based on textures, where smooth regions were classified as brittle, and uneven surfaces were classified as ductile.

Therefore, it is more reasonable to train the model with our DPT W-NiFe specimens and labels of 4 fracture modes. An example of manually labeled images is displayed in Figure 6. Since it is difficult to distinguish NiFe matrix failure and W-NiFe interface failure for the NiFe phase, all NiFe phase regions in BSE are assigned NiFe matrix fails. Thus, the labeled NiFe matrix fail area fraction is at the upper bound, while the W-NiFe interface failure is at the lower bound, of reality. Table 2 and Table 3 listed the area fractions of fracture modes, and the tensile testing characteristics for corresponding samples. First, in 90W-0R samples, the dominant failure modes are the NiFe matrix fail and the W-NiFe interface fail, while in 90W-87R-RD samples, the dominant shifted to W cleavage and the W-W intergranular failures. Due to the plate-like geometry of the W-phase aligned with the tension direction, we are not able to observe many W-NiFe interface failures. The lowered elongation is likely attributed to the plate-like W phase failure, either intergranular or intragranular. The corresponding microstructure change is the increased W phase area fraction in the specimen cross-sectional surface, compared to as-received 90W-0R. Between 90W-0R-03 and 90W-0R-06, the yield and ultimate strengths seem not affected by the ratio between W cleavage and W-W intergranular much. The 5% increase in elongation may be due to lower proportions of W-W grain boundary fail. Note these analyses are based on a limited number of manually labeled images so may not be representative of the specimen. The next step is to continue to label more images and use them to train the UNet model for semantic segmentation.

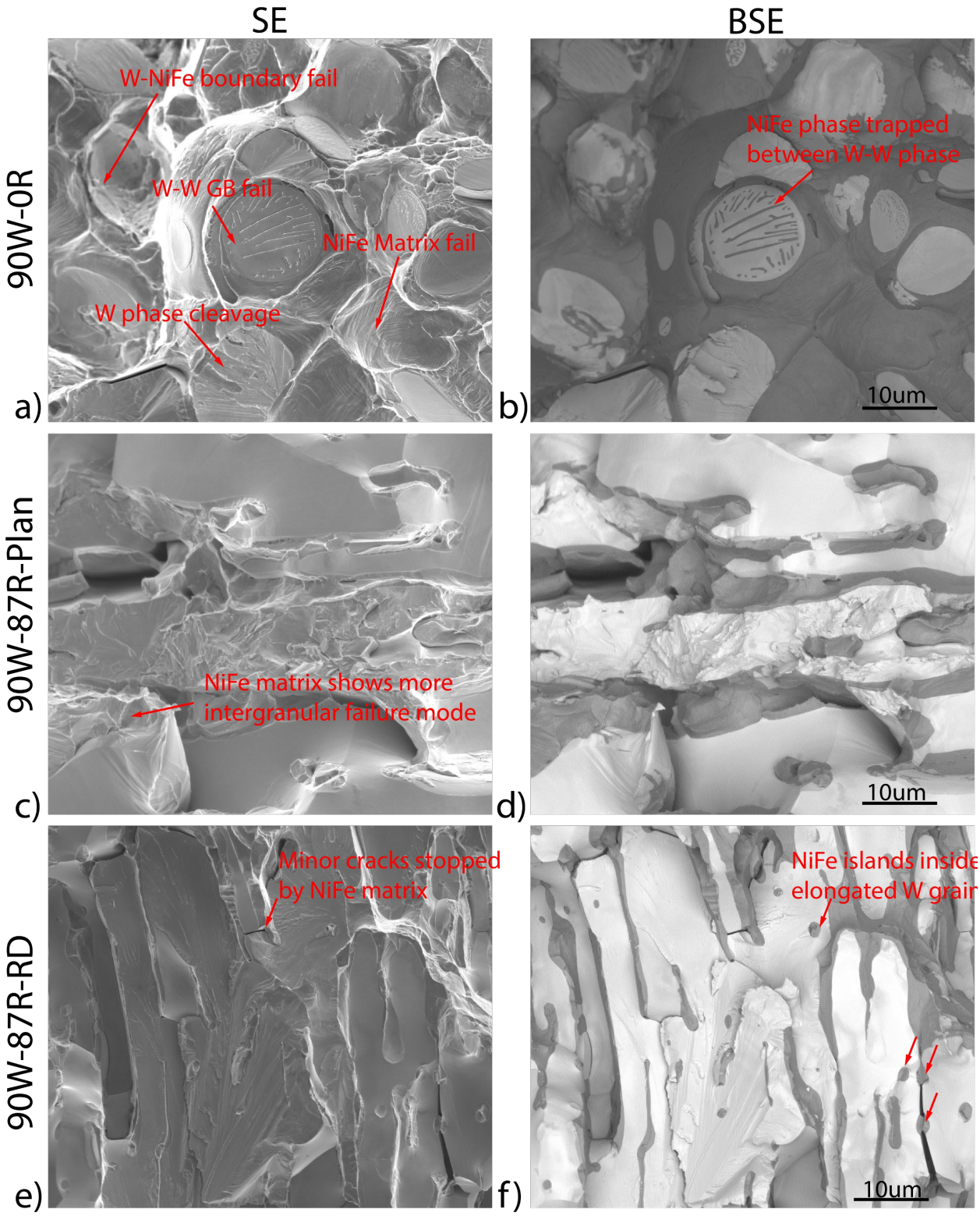

Figure 3. SEM secondary electron (SE) and back-scattered electron (BSE) images of the fractured surface of as-sintered (90W-0R) and hot-rolled (90W-87R-Plan and 90W-87R-RD) samples.

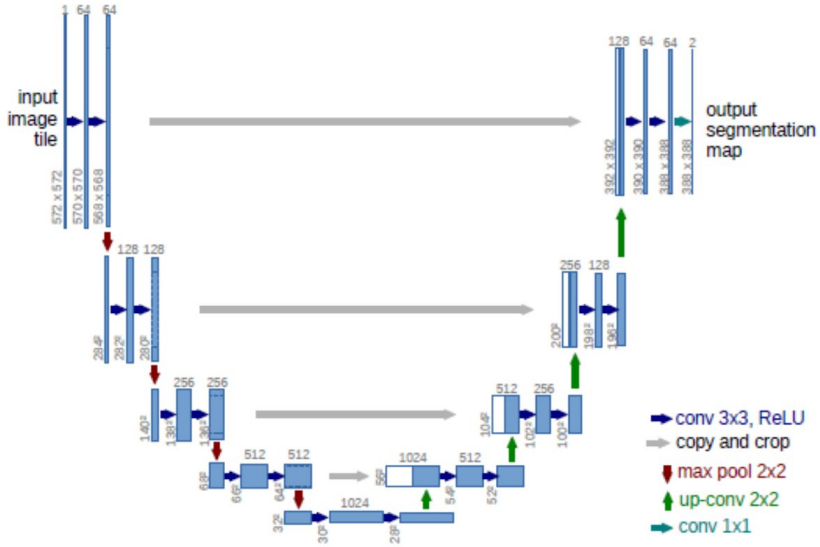

Figure 4. Schematics of UNet model [13].

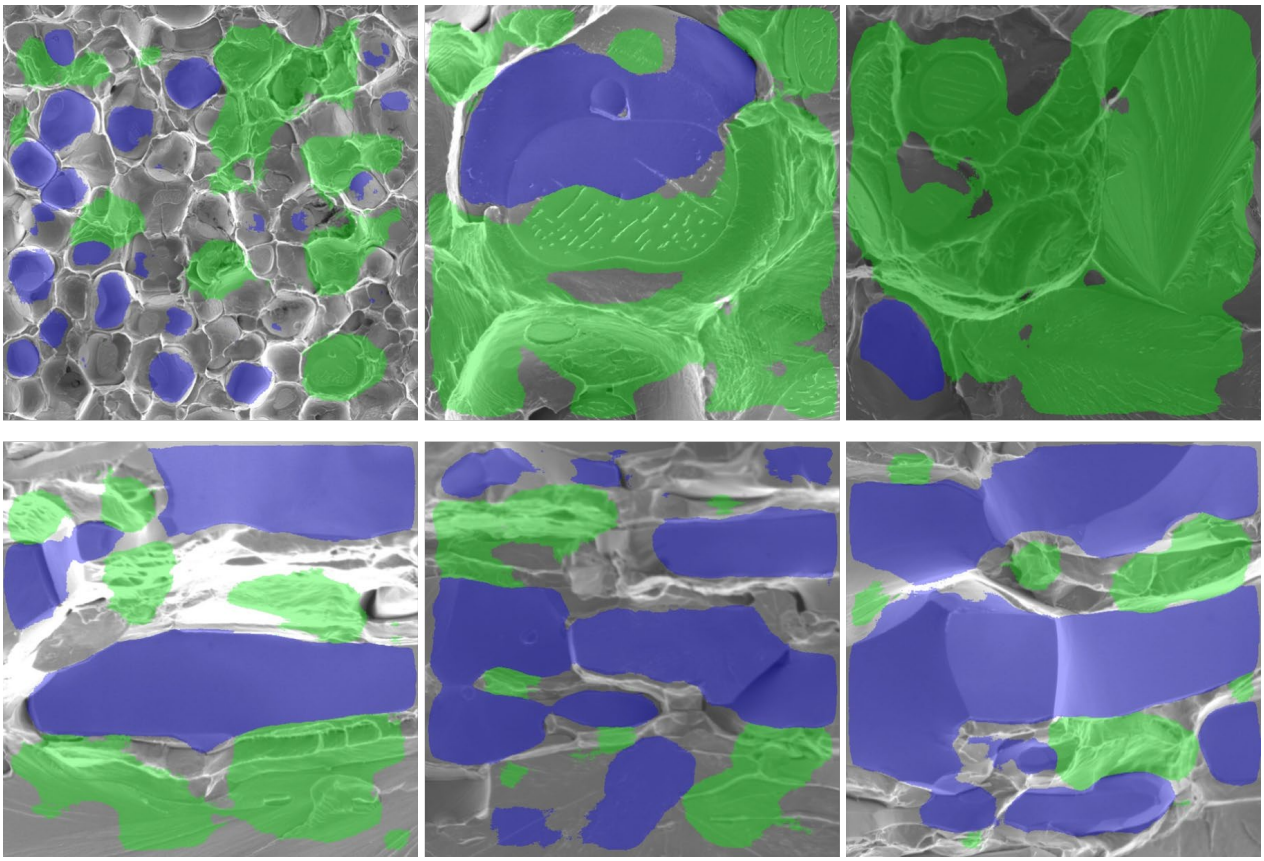

Figure 3. Examples of segmented fracture surface secondary electron micrographs at various magnifications: upper 90W-0R; lower 90W-87R-RD.

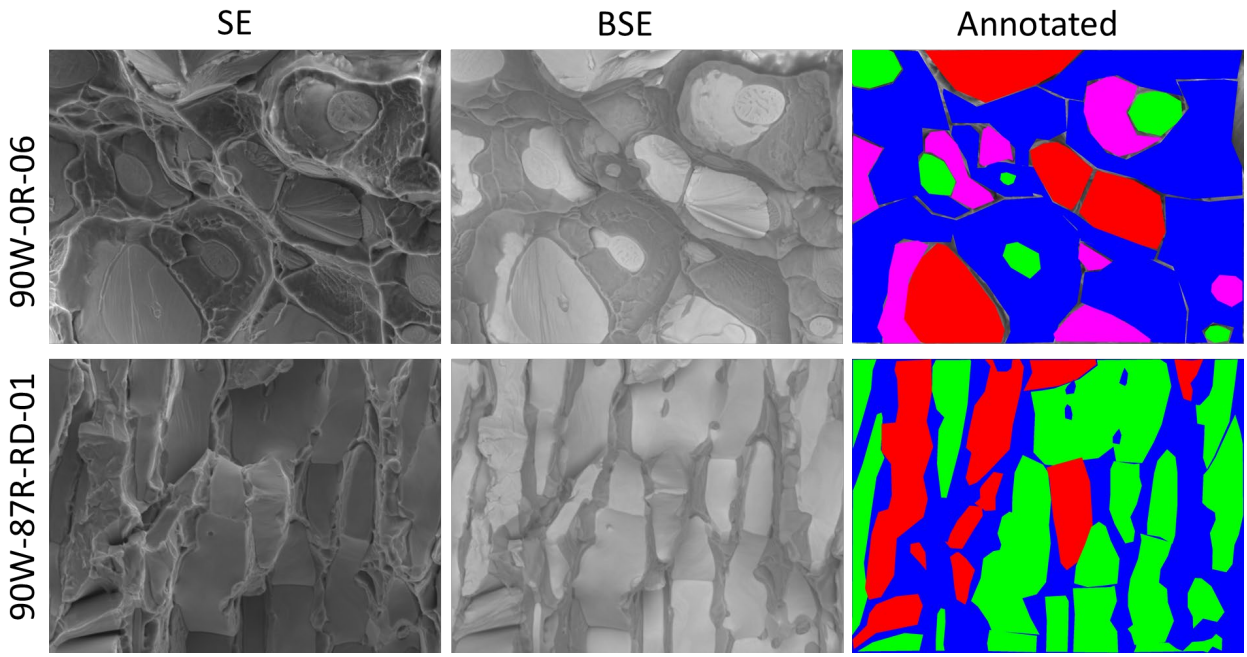

Figure 4. SE and BSE images of the fractured surfaces, and the manually annotated labels: Red-W cleavage; Green-W-W boundary failure; Blue-NiFe matrix failure; Magenta-W-NiFe boundary failure.

Table 2. Summary of area fractions for each fracture surface mode

Specimen-ID	W cleavage (%)		W-W GB fail (%)		NiFe Matrix fail (%)		W-NiFe boundary fail (%)	
	Ave	Std	Ave	Std	Ave	Std	Ave	Std
90W-0R-03	5.1	7.9	14.8	5.1	55.1	7.6	25.0	6.0
90W-0R-06	16.6	11.0	10.5	3.6	54.1	6.7	18.8	6.7
90W-0R-11	2.8	4.9	15.2	6.0	52.9	6.7	29.1	7.8
90W-87R-RD-01	22.9	10.2	40.7	10.0	36.4	4.5	0	0
90W-87R-RD-02	33.1	9.7	36.9	8.3	30.0	4.9	0	0

Table 3. Summary of stress-strain curve characteristics of DPT W-NiFe specimens

Specimen-ID	crosshead speed (um/s)	Yield (MPa)	Ultimate (MPa)	Elongation (%)
90W-0R-03	0.1	550	831	22.6
90W-0R-06	0.1	545	827	27.4
90W-0R-11	10	665	914	17.6
90W-87R-RD-01	0.1	572	758	11.3
90W-87R-RD-02	1	610	825	10.7

Other Progress

High-Temperature Furnace Installation for Tensile Testing

The PNNL has a Materials Research Furnace (MRF; Model M-4x6-M-1600-V&G) front loading, mechanical testing type furnace, with a usable work zone of 3.5" dia. x 4.0" high, and a maximum operating temperature of 1600°C. The furnace chamber has the following features:

- Ports to accommodate the temperature thermocouples, vacuum sensors, vacuum system, and others.
- Two 1/2"x2" slotted sight windows on the front and rear center to the hot zone.
- The hot zone is a 180° split design with tungsten mesh heating elements for operation in vacuum (50-100 milliTORR) and inert gas.
- Four water-cooled copper power feedthroughs that supply power to the heating elements.
- Ar, N_2, or Ar/O_2 gas mixture.

This furnace was not used for a while. It needs to be relocated and reconfigured to our lab space for Fusion materials research. This FY's primary effort is to restore and install this furnace to a compatible state with an existing testing frame in the lab. Due to the COVID-19 pandemic, ordering components and work with building support staff have been greatly hampered. So far, we have finished checking electrical safety, re-configured cooling water, gas, electrical wires, repaired heating elements, etc. Currently, we are waiting for replacement components for the lift. After that, we will test the furnace at medium (400-600 °C) with an existing tensile fracture for initial verification. Figure 7 shows pictures of the high-temperature furnace located in the new lab space.

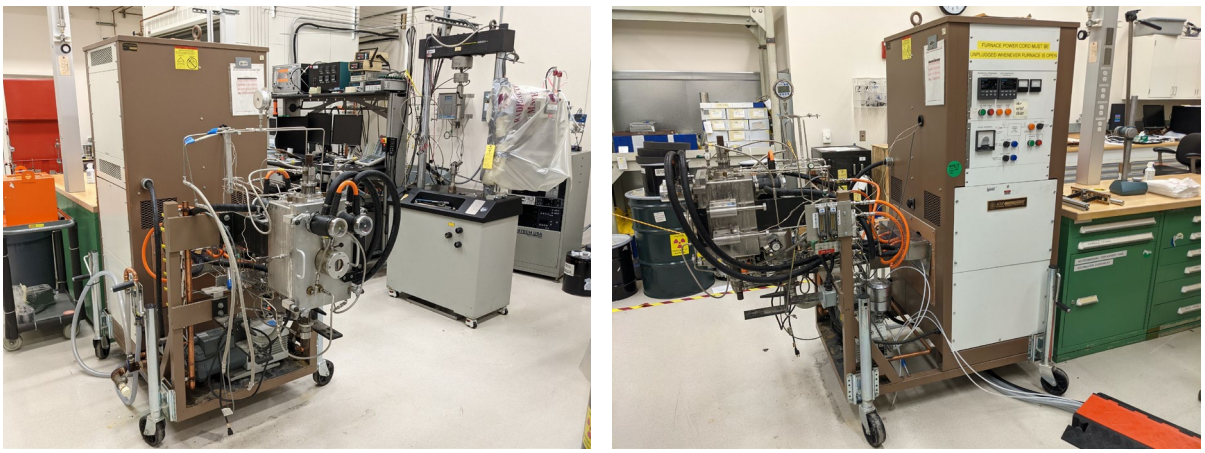

Figure 7. Materials Research Furnace (1600C) along with Instron 8801 mechanical test frame.

Re-initiated Hot-rolling DPT W-NiFe

Hot rolling of DPT W-NiFe specimens activities restarted in FY21. However, due to the downtime of instruments, COVID-19 pandemic, heat waves in the region, the progress is delayed. Several as-received 90W-0R specimens were cut into strips with ~0.25 inches in thickness. Before rolling, the sample was pre-heated to around 1150 °C in the furnace. After 2 passes, the sample was then annealed with H_2/Ar 50/50 mix to 1200 °C for 3 hours. Figure 8 shows pictures taken during hot rolling and after annealing. Thickness reduction was targeted at ~10% each pass, with a goal at ~87%.

Acknowledgments

This research was supported by the Office of Fusion Energy Sciences, U.S. Department of Energy (DOE) under Contract DE-AC05-76RL01830.

a) 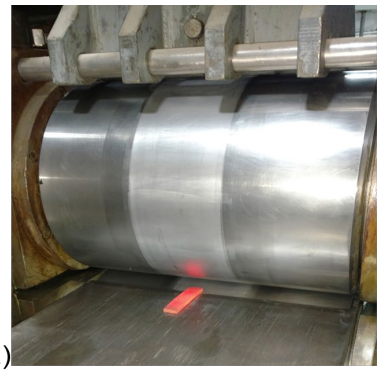 b) 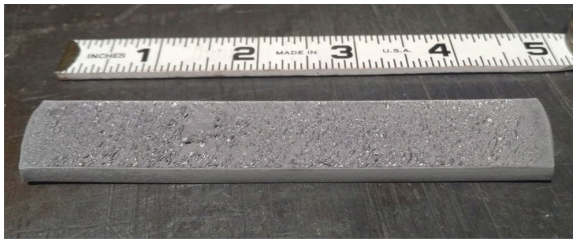

Figure 8. Pictures of a) hot-rolling mill; b) rolled specimen after 2 passes with 10% thickness reduction each.

References

[1.] Wurster, S., et al., *Recent progress in R&D on tungsten alloys for divertor structural and plasma facing materials.* Journal of Nuclear Materials, 2013. **442**: p. S181-S189.

[2.] Stork, D., et al., *Developing structural, high-heat flux and plasma facing materials for a near-term DEMO fusion power plant: the EU assessment.* Journal of nuclear materials, 2014. **455**: p. 277-291.

[3.] Hasegawa, A., et al., *Neutron irradiation effects on the microstructural development of tungsten and tungsten alloys.* Journal of Nuclear Materials, 2016. **471**: p. 175-183.

[4.] Henager, C.H., et al., *Recent Progress in the Development of Ductile-Phase Toughened Tungsten for Plasma-Facing Materials.* 2014.

[5.] Henager, C.H., et al., *Recent Progress In The Development Of Ductile-Phase Toughened Tungsten For Plasma-Facing Materials: W-Ni-Fe Composites.* 2015.

[6.] Henager, C.H., B.N. Nguyen, and R.J. Kurtz, *Preliminary Progress In The Development Of Ductile-Phase Toughened Tungsten For Plasma-Facing Materials: Dual-Phase Finite Element Damage Models*. 2016.

[7.] Nguyen, B.N., C.H. Henager, and R.J. Kurtz, *Modeling Ductile-Phase Toughened Tungsten for Plasma-Facing Materials: Progress in Damage Finite Element Analysis of the Tungsten-Copper Bend Bar Tests*. 2017.

[8.] James V. Haag IV, et al., *In-situ mechanical testing and interfacial characterization of ductile-phase toughened tungsten*, in *Fusion Materials Semiannual Progress Report For the Period Ending December 31, 2019*. p. 78-85.

[9.] Wang, J., et al., *Tensile Testing And Microstructural Characterization Of Ductile Phase Toughened W-NiFe Alloys*, In *Fusion Materials Semiannual Progress Report For The Period Ending June 30, 2020*.

[10.] Wang, J., et al., *Microstructural Characterization And Mechanical Testing Of Ductile-Phase Toughened Tungsten*, In *Fusion Materials Semiannual Progress Report For The Period Ending December 31, 2019*.

[11.] Wang, J., et al., *Microstructure-Mechanical Property Correlation in Ductile Phase Toughened W-NiFe Heavy Alloy*, in *Fusion Materials Semiannual Progress Report for the Period Ending December 31 2020*.

[12.] Tsopanidis, S., R.H. Moreno, and S. Osovski, *Toward quantitative fractography using convolutional neural networks.* Engineering Fracture Mechanics, 2020. **231**: p. 106992.

[13.] Ronneberger, O., P. Fischer, and T. Brox, *U-Net: Convolutional Networks for Biomedical Image Segmentation.* arXiv pre-print server, 2015.

5. ADVANCED MANUFACTURING

5.1 FABRICATION OF CERAMIC AND METAL MATRIX ENHANCED SHIELD THROUGH DIRECT CURRENT SINTERING—J.M. Gentile, B. Cheng, D.J. Sprouster, J. R. Trelewicz, L.L. Snead (Stony Brook University)

OBJECTIVE

In this report, we discuss progress made toward developing ceramic and metal matrix entrained hydride shields for enabling compact superconducting Tokamaks. Using direct current sintering (DCS), we show that a combination of sintering aids suppresses the consolidation temperature of ceramic and metal matrices, which can be brought down to suitable levels for entraining metal hydrides that are historically beneficial for neutron absorption and moderation applications.

SUMMARY

Tokamaks require shielding to minimize neutron damage and heat deposition to the delicate superconducting magnets necessary for sustaining fusion [1-5]. Current generation shields employ a combination of light or heavy elements and neutron absorbers such as W, H_2O, and ^{10}B. However, H_2O is effectively ruled out for compact reactors, and B-based compounds suffer from inherent irradiation instability and burnout. Due to the limitations of conventional shields, enhanced shields are necessary to drive the efficiency, reliability, and cost-effectiveness of next generation fusion reactors. Our proposed solution involves the use of radiation stable ceramic and metal matrices to entrain otherwise irradiation unstable metal hydrides, which ironically exhibit high performance for neutron moderating and absorption applications. In essence, these composite materials will combine the benefits of low activation, radiation stable matrices with the superior neutron stopping performance of the entrained hydride phase [6], in turn mitigating the risk associated with their radiation instability.

PROGRESS AND STATUS

For the metal matrix, pure Ni powder was selected for its low hydrogen diffusivity [7] and acquired from Alfa Aesar in course (-45μm) and fine (3-7μm) particle size configurations. The powders were portioned out at 20g, loaded into a 25mm graphite die, and into a DCS system (Sinterland LABOX-3010KF, Japan) placed under vacuum. For all experiments, only the maximum sintering temperature was varied from 500-1100°C and the heating rate, pressure, and hold time was left invariable at 100°C/min, 50MPa, and 5min, respectively. A second set of experiments was conducted with the addition of 40V% GdH_{2-3} speed-mixed into the Ni powder, and a cold compaction of this mixture was performed at 100MPa prior to loading into the DCS. Whereas sintering of the pure Ni matrix was performed in vacuum, the sintering of the Ni-GdH_{2-3} samples were performed under hydrogen partial pressure.

For the ceramic matrix, two distinct MgO feedstock powders were employed. Following baking, ethanol solution containing an binder-agent and sintering-additive was then introduced to the powders at 70°C. The mixed MgO slurry was baked in a forced air oven at 100°C for over 12 hours, and after grinding and sieving using -120 Mesh, the processed MgO powder was then ready for green forming. To form the MgO greenbody, the powder was loaded into a 25mm hardened steel pressing die and heated to 80°C for 30min in a force air oven. Then heated die was then compressed in a hydraulic press at 100MPa pressure prior to cooling down to room temperature. The unloaded greenbody displayed good strength and density (~52%~54%) and was ready for DCS using a 25mm graphite die. The sintering temperature, heating rate, sintering pressure, and peak holding time varied for each experiment and will be discussed in detail in the results section.

Following synthesis, synchrotron x-ray diffraction (XRD) was performed on all samples at the National Synchrotron Light Source II Pair Distribution Function (PDF) beamline to determine the phase structure of the compacts, where the phase fraction was quantified through Rietveld refinement in Maud.

Metal Matrix Results

To acquire an optimized set of process parameters for DCS consolidation of the Ni matrix, sintering temperature was mapped to relative density, calculated as the measured Archimedes density normalized by the theoretical density of Ni, and plotted in Figure 1 for both powder size distributions. A fully dense compact is signaled by the convergence achieved at 1100°C, while the -45µm powder shows marginally higher density relative to the 3-7µm for equivalent temperatures below 1100°C. In seeking to entrain metal hydrides within the Ni matrix, it is advantageous to sinter at reduced temperature to prevent decomposition of the hydride resulting in the loss of hydrogen. Therefore, slightly reduced compact density is acceptable to retain more hydrogen during consolidation and thus, during sintering with metal hydride inclusions, we target the temperature range of 700-900°C.

Using these optimized parameters, samples were then sintered with the inclusion of 40V% GdH_{2-3} within the Ni matrix and corresponding synchrotron XRD results for the sample sintered at 700°C are shown in Figure 2. The pattern illustrates phase separation between the Ni matrix and GdH_2 where we retained an encouraging 25V% GdH_2, while the minor presence of $GdNi_5$ and GdO observed within the compact is expected given the composition gradient at unlike particle interfaces during sintering, and their effects on shield performance will be investigated.

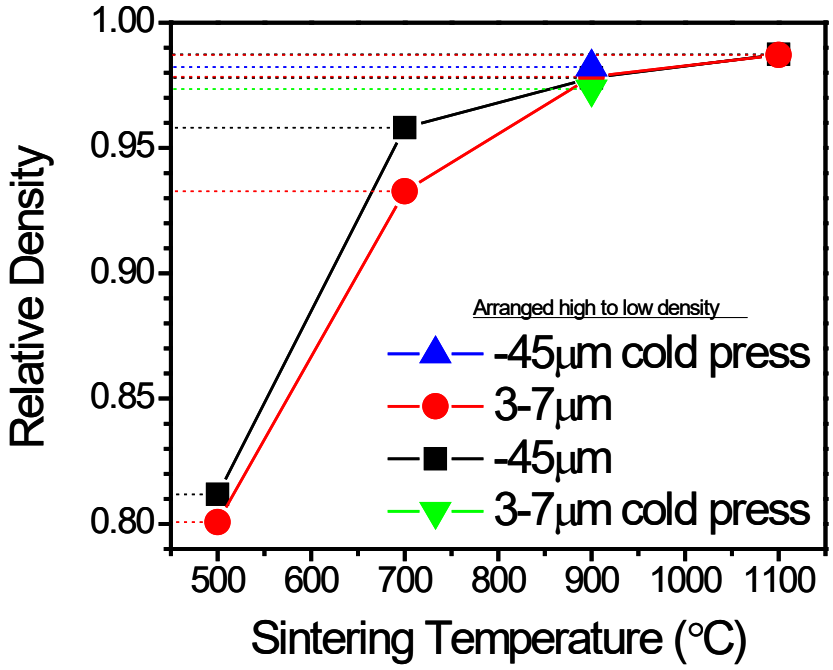

Figure 1. Relative density plotted against sintering temperature for the pure Ni powder with particle size distributions of 3-7 and -45µm. Full density is achieved at 1100°C and coincides with convergence of the two powder size distributions.

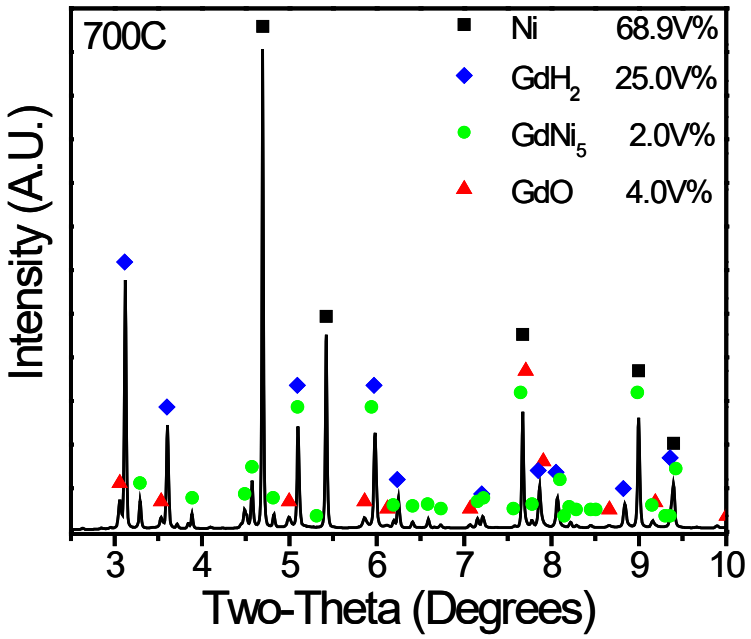

Figure 2. Synchrotron XRD results plotted as intensity against two-theta for the Ni matrix with 40V% GdH_{2-3} addition sintered at 700°C. Rietveld refinement of the data illustrates the retention of 25V% GdH_2 with a minor presence of a $GdNi_5$ intermetallic and GdO.

Ceramic Matrix Results

The MgO powder is hygroscopic and thus, when exposed to the atmosphere, forms an $Mg(OH)_2$ layer on the particle surface. As shown in the XRD patterns in Figure 3, both MgO powders show a $Mg(OH)_2$ phase. Inconveniently, the $Mg(OH)_2$ phase will decompose into MgO and water vapor when heated to 350°C, which is detrimental to metal hydrides as water vapor causes oxidization during sintering. Therefore, to remove the $Mg(OH)_2$ layer, the feedstock MgO powders were baked in a vacuum furnace at 500 °C for 1hr. The XRD patterns of the baked MgO powders in Figure 3(a) shows the complete removal of $Mg(OH)_2$ phase, but trace amounts of the $Mg(OH)_2$ phase is still present in the baked second MgO powder as shown in Figure 3(b).

In previous work our team demonstrated a reduction in sintering temperature of MgO using metal halide salts and in particular LiF. This reduced sintering temperature from well above 1000°C to nominally 700°C. In the present work that sintering onset temperature has been further reduced. Figure 5 demonstrates a series of sintering parameters optimization aiming to limit the peak temperature within 800°C. Starting with a heating rate of 50°C/min, hold time of 10min, and pressure of 10MPa, a density above 99% was achieved for the sintering of MgO with 1wt% LiF at 850°C as shown in Figure 5(a). However, at 800°C, a relative density above 95 was also obtained, suggesting a potential further peak sintering temperature reduction. Then, we varied the heating rating from 25°C/min to 100°C/min and show in Figure 5(b) that the relative density increased with an increase in heating rate. At 100°C/min, a density above 98% was acquired after sintering to 800°C. To achieve over 99% density, we increased the sintering pressure from 10MPa to 30MPa. Figure 5(c) shows that the density achieved 99% after pressure increased above 20MPa. Peak holding time also affected the final density as depicted in Figure 5(d), which increased from 95% for peak holding of 2.5min to >99% for peak holding of 5min. In summary, optimized low-temperature sintering parameters are obtained in this work: a peak sintering temperature of 800°C; heating rate of 100°C/min; sintering pressure of 20MPa; and peak holding time of 5min. These optimized sintering parameters ensure a high density (>99%) of the MgO matrix.

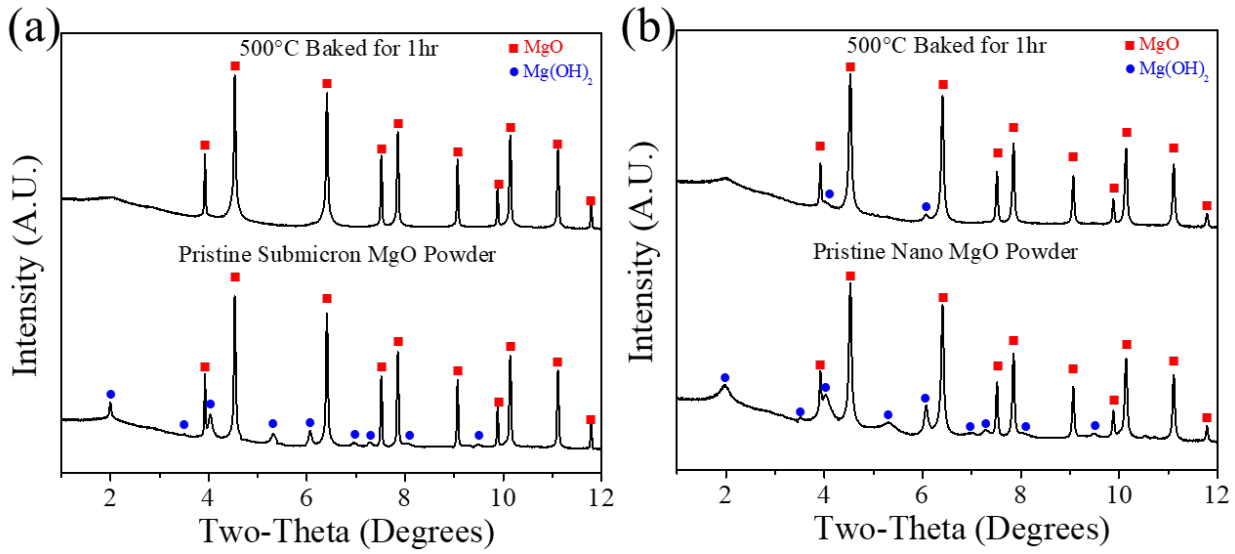

Figure 3. The XRD patterns of the pristine and baked (a) first MgO and (b) second MgO powders illustrating the removal of $Mg(OH)_2$ upon baking.

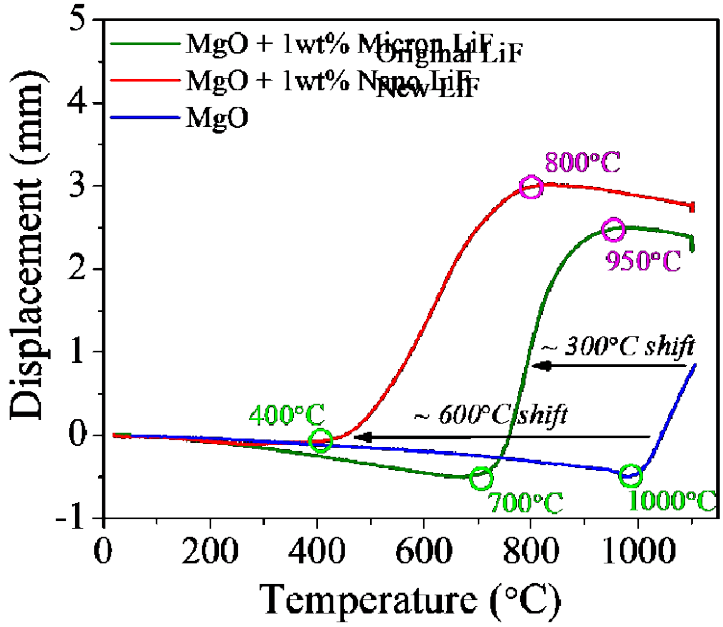

Figure 4. The displacement-temperature curves of pure MgO, MgO with original 1wt% LiF, and MgO with new 1wt% LiF sintered under at 1100°C under 10MPa pressure for 10min.

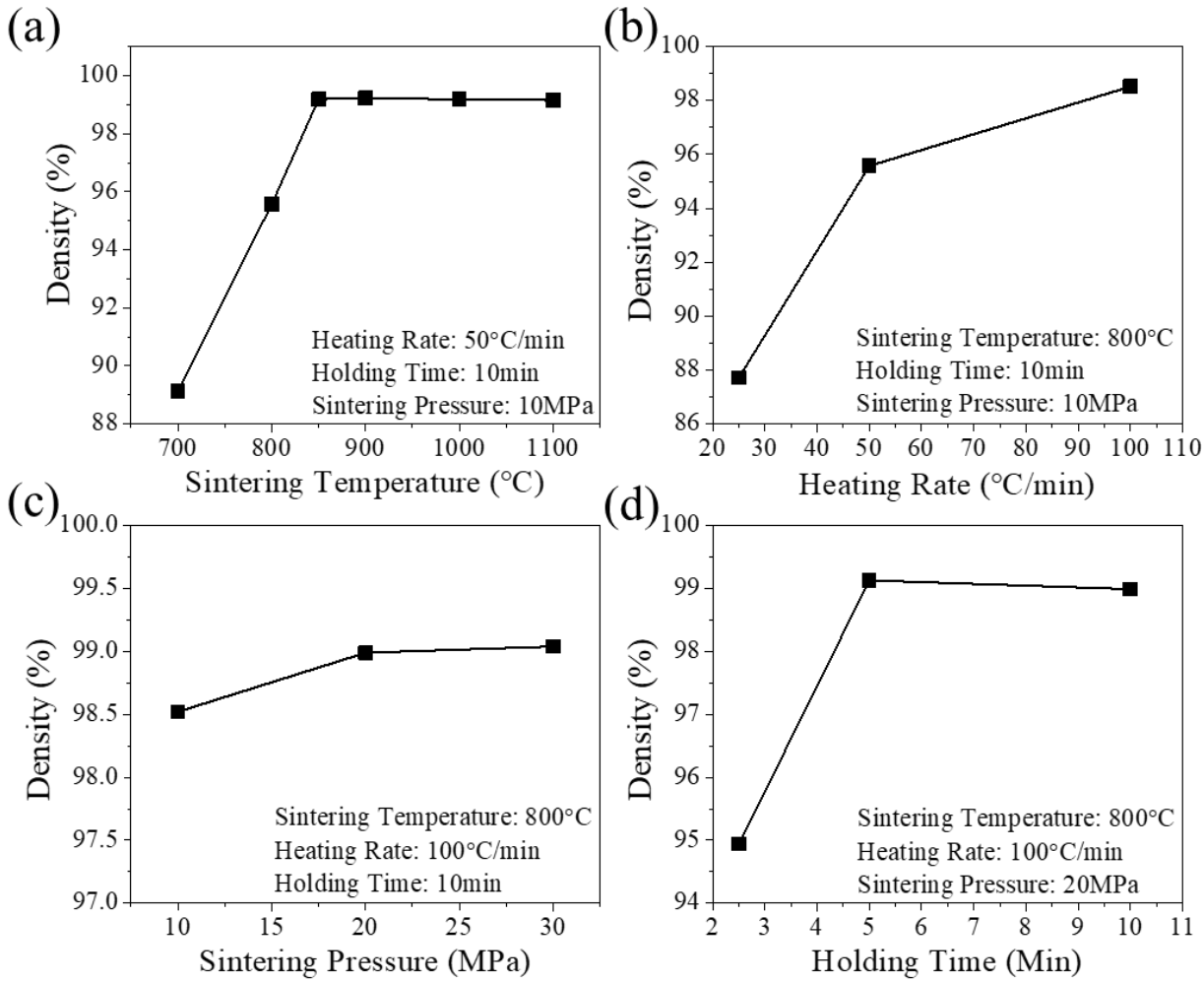

Figure 5. The effects of (a) sintering temperature, (b) heating rate, (c) sintering pressure, and (d) holding time on the density of final sintered MgO compacts.

Future Work

The preliminary results shown here suggest that metal hydrides can be entrained within metal and ceramic matrices to produce a composite, potentially enabling the development of enhanced shields for compact superconducting Tokamaks that combine low activation, radiation stable matrix materials with inclusions that have high neutron stopping power. Beyond optimization of the Ni-GdH composite structure through alloying to suppress the sintering temperature required for densification and in turn, improve H retention, future work involves systematic investigation of other candidate metal matrix materials, such as RAFM steel, and inclusions, such as WC/B, to produce a high-performance enhanced shield. Future work for the ceramic matrix will be focused on the co-sintering of MgO with various metals hydrides using the optimized sintering parameters developed here and followed by microstructural characterization of sintered composites.

Acknowledgements

This work was supported by the Advanced Research Projects Agency-Energy (ARPA-E) Galvanizing Advances in Market-Aligned Fusion for an Overabundance of Watts (GAMOW) program under contract

DE-AR0001381. The authors gratefully acknowledge the use of instrumentation at the Center for Functional Nanomaterials, and the X-ray Powder Diffraction (XPD) beamline of the National Synchrotron Light Source-II, which are U.S. Department of Energy (DOE) Office of Science User Facilities operated for the DOE Office of Science by Brookhaven National Laboratory under Contract No. DE-SC0012704.

References

[1] P. Pereslavtsev, F. Cismondi, F.A. Hernández, Analyses of the shielding options for HCPB DEMO blanket, Fusion Eng. Des. 156 (2020) 111605.
[2] C. Windsor, J. Marshall, J. Morgan, J. Fair, G. Smith, A. Rajczyk-Wryk, J. Tarragó, Design of cemented tungsten carbide and boride-containing shields for a fusion power plant, Nuclear Fusion 58(7) (2018) 076014.
[3] A. Sykes, A. Costley, C. Windsor, O. Asunta, G. Brittles, P. Buxton, V. Chuyanov, J. Connor, M. Gryaznevich, B. Huang, Compact fusion energy based on the spherical tokamak, Nuclear Fusion 58(1) (2017) 016039.
[4] M. Gryaznevich, O. Asunta, T.E.L. Team, Overview and status of construction of ST40, Fusion Eng. Des. 123 (2017) 177-180.
[5] U. Fischer, C. Bachmann, J.-C. Jaboulay, F. Moro, I. Palermo, P. Pereslavtsev, R. Villari, Neutronic performance issues of the breeding blanket options for the European DEMO fusion power plant, Fusion Eng. Des. 109 (2016) 1458-1463.
[6] L. Snead, N. Brown, J. Trelewicz, C. Ang, B. Cheng, X. Hu, D. Sprouster, Fabrication of Two-Phase Composite Moderators as Potential Lifetime Reactor Components, Transactions 121(1) (2019) 1445-1447.
[7] A. Turnbull, Hydrogen diffusion and trapping in metals, Gaseous hydrogen embrittlement of materials in energy technologies, Elsevier2012, pp. 89-128.

5.2 SYNCHROTRON ANALYSIS OF WIRE ARC ADDITIVE MANUFACTURING G-91 STEEL - PRINT-DIRECTION MICROSTRUCTURAL ANISOTROPY—I.K. Robin, S.J. Zinkle (University of Tennessee), D.J. Sprouster, L.L. Snead (Stony Brook University)

OBJECTIVE

This work is a direct follow on from our previous FY20 synchrotron characterization analysis, of wire arc additive manufacturing G-91 steel. In the present work, high energy x-ray diffraction patterns and mechanical properties were quantitively determined both the Z-directional (build direction) and X-direction (transverse direction). The amount of carbon within different phases, and lattice parameters for the BCC, FCC and BCT phases are correlated to the mechanical properties, to aid determining any print-dependent microstructural anisotropy.

SUMMARY

Wire arc additive manufacturing (WAAM) was employed to produce ferritic martensitic steel at the Manufacturing Demonstration Facility (MDF) at Oak Ridge National Laboratory. Four additional specimens cut parallel and perpendicular to the print direction (pre-, and post-heat treatment) were measured and analyzed at the PDF beamline at the NSLS-II. These specimens were investigated to determine any build-dependent asymmetry in lattice parameters and microstructure in and out of the print plane. More details of the specimens and heat treatment are discussed in the 2020 Fusion Materials Semiannual Progress Report [1].

PROGRESS AND STATUS

The XRD measurements were performed at the National Synchrotron Light Source-II (NSLS-II) using the high-energy X-rays available at The Pair Distribution Function beamline (PDF). All measurements were performed in transmission mode with an amorphous Silicon-based flat panel detector (Perken-Elmer) mounted orthogonal to and centered on the beam path. The sample-to-detector distances and tilts of the detector relative to the beam were refined using a LaB6 powder standard (NIST standard reference material 660c). The wavelength of the incident X-rays was 0.1665 Å (74.465 keV). The sample-to-detector distance was calculated to be 1399.79 mm. 300 individual patterns with detector exposures of 0.2s were collected for each specimen. All raw two-dimensional patterns were background corrected by subtracting the dark current image and the air scattering and Kapton background within IgorPro (Wavemetrics). Noticeable artefact regions of the detector (like the beam stop, dead pixels) were masked. The corrected and masked two-dimensional detector images were then radially integrated to obtain one-dimensional powder diffraction patterns.

The background subtracted XRD patterns were Rietveld refined with the MAUD software package. The peak profiles were modeled by a modified pseudo-Voigt function. The instrument contribution to the broadening of the measured profiles was quantified by fitting the LaB_6 NIST powder standard, with a known coherent grain size and negligible microstrain contribution. The Gaussian and Lorentzian-based broadening parameters were subsequently fixed during the analysis of the alloys under investigation to quantify the microstructure (coherent grain size and microstrain components). The phase fraction, lattice parameter, microstrain and coherent grain size components could vary for the different crystal phases present. The microstrain components for the $M_{23}C_6$ phase (in HT-G91) was not included in the refinements. Therefore, the refined coherent grain size parameters of the M23C6 phase are lower limits.

Results

The XRD patterns for the as prepared parallel and perpendicular print directions are shown in Figure 1(a). The XRD pattern for the as-deposited specimen show reflections from BCC Fe and a minor retained FCC austenite phase. The BCC peaks (like in [1, 2]) are appreciably broad and asymmetric, indicative that a martensite phase is present (i.e., buried under the BCC peaks). A slight orientation dependence in some

hkl peaks (intensities are away from the ideal powder average), indicating preferred orientation in the FCC and BCC matrix. The heat-treated specimens, both parallel and perpendicular builds are shown in Figure 1 (b). The XRD patterns for the HT specimens show that heating results in the removal of the retained FCC austenite phase, sharper (less broad and asymmetric) BCC peaks, and the formation of a minor $M_{23}C_6$ phase. Both patterns, regardless of orientation are comparable.

The quantitative XRD refinement results are given in Table 1, along with nanohardness data collected on the same specimens. Minor differences in the lattice parameters and microstructure are apparent for the as built specimens, with subtle variations in the lattice parameters weight fractions of the BCT and BCC phases. The slight anisotropic microstructure leads to minor anisotropic mechanical properties in the as-built state. Note, not including the BCT phase resulted in large residuals and failure to effectively capture intensity under and around the BCC reflections. After heat treatment, the microstructure clearly changes, with a larger coherent grain size and lower microstrain parameter. The similarity in the microstructures from the two directions indicates that the annealing leads to a more homogeneous morphology. The lower hardness values indicate that the heat treatment removes microstructural features (presumably martensite phase, FCC phase and dislocations in the BCC host) that lead to higher hardness values in the as printed state.

Conclusion

The anisotropic microstructure in 9 Cr AM build G-91 FM steel was characterized by measuring XRD patterns for both the Z-directional (build direction) and X-direction (transverse direction). Specimens from both build directions, pre and post heat treatment were examined. The as-built structures have ferrite, martensite and retained austenite phases present in the microstructure. The amount of microstructural anisotropy was correlated to the nanohardness. The microstructures in the as-built state show that the hardness is attributable to the large microstrain (from dislocations in the BCC host), FCC austenite component and martensite components. Heat treatment effectively improves the microstructure and leads to lower hardness values, directly resulting from a reduction in the martensite phase, and removal of microstrain (dislocations) in the ferrite phase. Anisotropy in the heat-treated specimens was negligible.

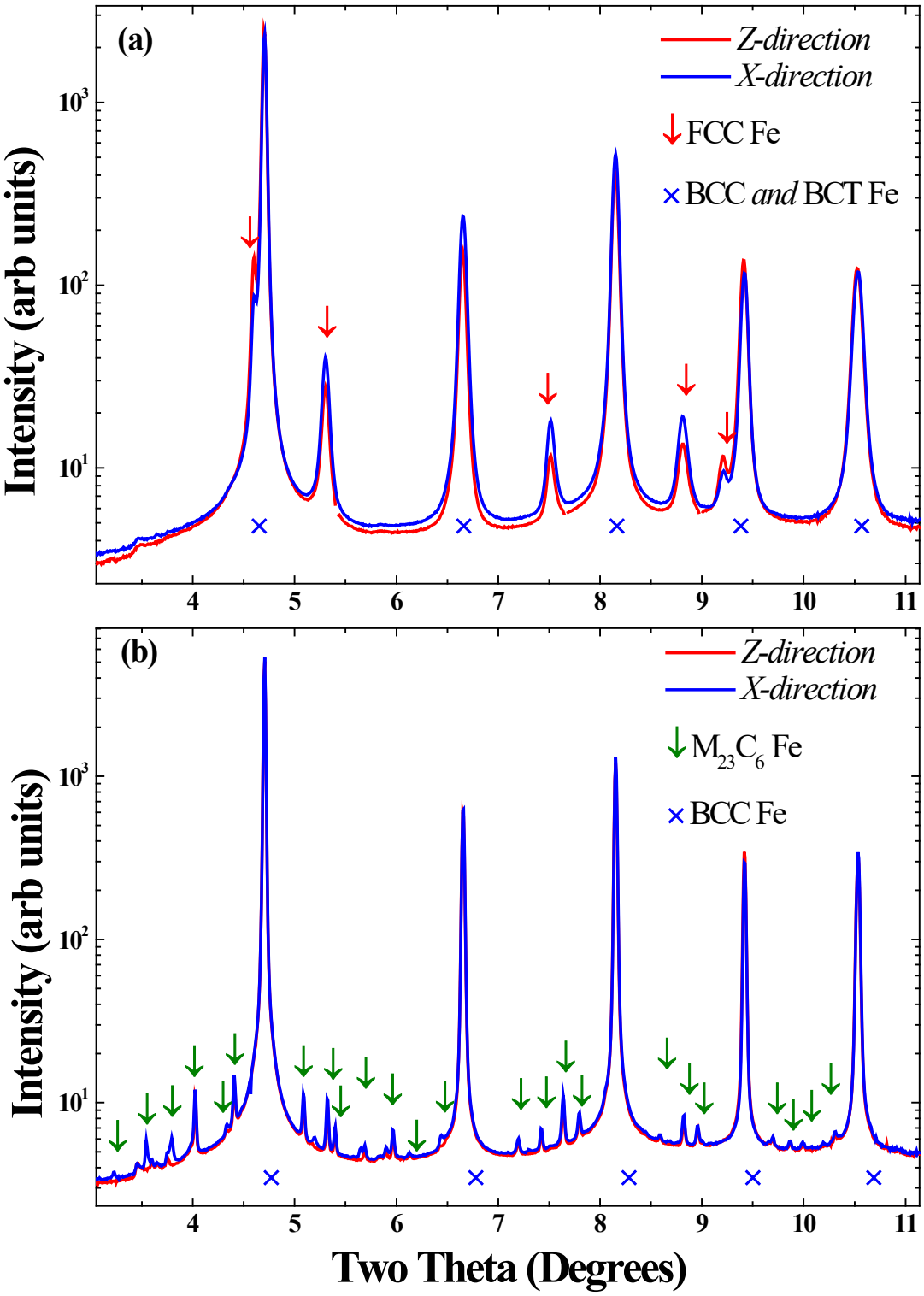

Figure 1. XRD patterns for (a) as fabricated and (b) heat treated G91. The XRD refinements and phases are overlaid for reference.

Table 1. Quantitative XRD results for AMG91 specimens; cgs is the coherent (XRD) grain size and μs is microstrain

Sample	Phase	*a*	c	cgs	μs	wt.	Carbon	RWP	Hardness
		(Å)	(Å)	(nm)	(10^{-3})	(%)	(at.%)	(%)	(GPa)
As-built									
Z-direction	FCC	3.59422 (0.00036)		47.1 (5.2)	3.15 (0.2)	4.9± (0.3)		7.7	5.8
	BCC	2.87013 (0.00005)		299.3 (47.3)	2.44 (0.03)	64.5± (1.0)			
	BCT	2.86199 (0.00049)	2.89509 (0.00094)	51.8 (4.5)	4.40 (0.2)	32.5± (1.1)	1.20		
X-direction	FCC	3.59398 (0.00047)		52.7 (6.4)	3.87 (0.14)	4.4 (0.2)		6.9	5.8
	BCC	2.86874 (0.00007)		312.5 (86)	2.48 (0.03)	57.3 (2.3)			
	BCT	2.85859 (0.00044)	2.89153 (0.00081)	53.4 (3.7)	3.2 (0.005)	38.4 (2.4)	1.19		
As-annealed									
Z-direction	BCC	2.86739 (0.00005)		682.8 (32.4)	0.77 (0.01)	98.7 (0.3)		7.5	3.2
	$M_{23}C_6$	10.60150 (0.00182)		47.5 (1.5)	-	1.3 (0.1)			
X-direction	BCC	2.86711 (0.00005)		665.8 (36.0)	0.73 (0.01)	98.6 (0.3)		7.5	3.4
	$M_{23}C_6$	10.60665 (0.00013)		48.0 (2.0)	-	1.1 (0.1)			

Acknowledgements

These experiments and analysis were supported by the DOE Office of Fusion Energy Sciences under contract DE-SC0018322 with the Research Foundation for the State University of New York at Stony Brook. This research used The X-ray Powder Diffraction and Pair Distribution Function beamlines of the National Synchrotron Light Source II, a U.S. Department of Energy (DOE) Office of Science User Facility operated for the DOE Office of Science by Brookhaven National Laboratory under Contract No. DE-SC0012704.

References

[1.] Parish, C., Y. Kato, and S. Melton, *Fusion Materials Semiannual Progress Report for the Period Ending December 31, 2020*. 2021, ; Oak Ridge National Lab. (ORNL), Oak Ridge, TN (United States). p. Medium: ED.

[2.] Eftink, B.P., et al., *Tensile properties and microstructure of additively manufactured Grade 91 steel for nuclear applications.* Journal of Nuclear Materials, 2021. **544**: p. 152723.

6. EFFECTS OF IRRADIATION

6.1 X-RAY DIFFRACTION STUDY OF BASELINE AND NEUTRON IRRADIATED RAFM AND CNA STEELS—D.J. Sprouster, L.L. Snead (Stony Brook University), W. Zhong, T. Koyanagi, L. Tan, Y. Kato (Oak Ridge National Laboratory)

OBJECTIVE

This work is a direct follow on from our previous FY20 synchrotron characterization analysis. In this report, we extent and demonstrate the utility of high-energy x-ray diffraction to identify and capture minor phases in a series of baseline annealed, and neutron irradiated reduced activation ferritic martensitic alloys and castable nanostructured alloys. Additional phases introduced during annealing include the Laves ($FeMo_2$) phase (quantified in aged baseline G92 specimens). Elevated temperature neutron irradiation induces the formation of an FCC phase, observed in two G92 irradiated specimens. Changes in the MX and $M_{23}C_6$ precipitates was also apparent from the XRD results. Changes in the XRD peak shape position, height, and full-width-at-half-maximum (FWHM), indicate changes in the atomic structure (lattice parameters) and microstructure (dislocation density, coherent grain size, weight fraction of minor phases). These results highlight that synchrotron-based XRD is appreciably sensitive to the irradiation-induced phase transformations and can quantitatively extract changes in the atomic and microstructural features for both the BCC host and minor precipitate populations.

SUMMARY

Strategies to improve the radiation performance of structural materials for fusion energy applications have led to the realization of engineered microstructures [1]. Current strategies for designing alloys for fusion energy applications include intentionally engineering high non-cavity sink strengths via incorporating precipitates within the BCC host matrix. Two classes of such materials include (i) Castable nanostructures alloys (CNA) [2, 3] , and (ii) Reduced Activation Ferritic Martensitic (RAFM) alloys [3]. Both CNA and RAFM microstructures are heterogeneous with several nanometer-sized precipitate phases purposely introduced through the fabrication process. Quantification of the different nm-scale precipitates and BCC host matrix with processing and irradiation is needed to optimize material builds and develop microstructural insights that can be compared to thermodynamic modelling [4]. Quantitative and qualitative XRD methods were employed here to examine the different atomic and microstructural properties of the BCC host and nm-scale precipitates.

PROGRESS AND STATUS

The XRD measurements were performed at the National Synchrotron Light Source-II (NSLS-II) using the high-energy X-rays available at The Pair Distribution Function (PDF) beamline. All measurements were performed in transmission mode with an amorphous Silicon-based flat panel detector (Perkin-Elmer) mounted orthogonal to and centered on the beam path. The sample-to-detector distances and tilts of the detector relative to the beam were refined using a LaB_6 powder standard (NIST standard reference material 660c). The wavelength of the incident X-rays was 0.1665 Å (74.46 keV). The sample-to-detector distance was calculated to be 1235.20 mm. 600 individual patterns with detector exposures of 0.1s were collected for each specimen and repeated at 4-5 locations on each sample. All raw two-dimensional patterns were background corrected by subtracting a dark current image, and the air and Kapton scattering background within IgorPro (Wavemetrics). Noticeable artefact regions of the detector (like the beam stop, dead pixels) were masked. The corrected and masked two-dimensional detector images were then radially integrated to obtain one-dimensional powder diffraction patterns.

Phase identification was performed using Match3! (Crystal Impact, Bonn, Germany). The background subtracted XRD patterns were Rietveld refined (to include any texture) with the MAUD software package.

The peak profiles were modeled by a modified pseudo-Voigt function. The instrument contribution to the broadening of the measured profiles was quantified by fitting the LaB_6 NIST powder standard, with a known coherent grain size and negligible microstrain contribution. The Gaussian and Lorentzian-based broadening parameters were subsequently fixed during the analysis of the alloys under investigation to quantify the microstructure (coherent grain size and microstrain components). The phase fraction, lattice parameter, microstrain (MS) and coherent grain size (CGS) components could vary for the different crystal phases present. The microstrain components for the FCC Fe, MX and $M_{23}C_6$ phases were not included in the refinements. Therefore, the refined coherent grain size parameters of are lower limits.

Results

The XRD patterns for the baseline specimens are shown in Figure 1. The phases identified in the RAFM samples include MX (MN and MC), $M_{23}C_6$ and $FeMo_2$ Laves phase in the aged G92 specimens (700C1 and 700C3). For the G92 specimens, the MX peak locations are like a VN phase, while all MX peaks in the FTa-01 specimens look more closely matched a TaC phase. The quantitative phase analyses for the baseline specimens is given in Table 1. The XRD analysis resulted in residual weights parameters (RWPs) less than 10%. Additional microstructural features captured by the baseline XRD analysis included: (1) the need to include an additional nanocrystalline Fe phase to the FTA-01 490 specimen, likely due to a broad coherent grain size distribution, or the presence of a possible Martensite phase; (2) An $FeMo_2$ phase was present in the G92 specimens annealed at elevated temperatures. The microstructure, including lattice parameters, coherent grain size and microstrain appear to be sample-dependent. The microstrain parameter is directly attributable to two-dimensional defects (such as dislocations), and the coherent grain size is the amount of defect free material (and is thus usually smaller than the grain size from SEM). The lattice parameters appear to show subtle variations among the different specimens and is potentially related to the processing/alloy chemistry.

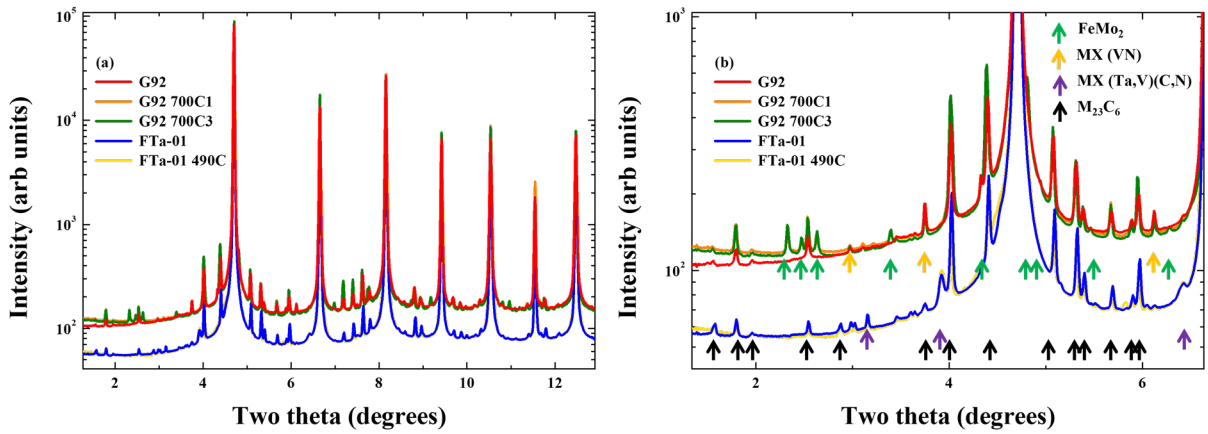

Figure 1. (a) Baseline XRD patterns with FTa-01 and G92 specimens offset vertically, (b) inset showing higher magnification in low angle two-theta region with the multiple phases identified for reference.

The XRD patterns for the neutron irradiated specimens are shown in Figure 2. The intensity and positions of the MX and $M_{23}C_6$ specimens in Figure 2 vary relative to their unirradiated counterparts, indicative of radiation-induced microstructural changes. Of note is the complete loss of the $M_{23}C_6$ peaks in the G92 GB11A specimen. The intensity of the low angle hkl's may also be an indication that the $M_{23}C_6$ chemistry is not the same pre- and post-irradiation. The MX precipitates appear to be radiation stable. For the irradiated G92 specimens, an additional (new) FCC phase is present with broad (nanocrystalline) peaks at ~4.5 and ~5.3 degrees. Changes in the position of the BCC peaks are also apparent from Figure 2 (position,

width, and asymmetry), indicating irradiation-induced microstructural changes. Table 1 lists the microstructural parameters for the irradiated specimens. The lattice parameters for the BCC host increase with irradiation for both FTA-01 and G92 specimens (relative to unirradiated baselines). There are subtle differences in the microstructural response, post-irradiation, with the irradiated FTA-01 specimen showing an increase in the coherent grain size and a decrease in the microstrain value. This could potentially be due to the specific irradiation conditions (temperature, flux, and fluence). Additionally, the microstrain values for the BCC phase in the irradiated G92 specimens decrease with irradiation, and the coherent grain sizes both decrease. An additional Martensite phase was needed to refine the GBA11 specimen, with an appreciable asymmetry observed in all BCC peaks. This specimen also contained the largest fraction of radiation-induced FCC phase. The origins of the irradiation-induced microstructural changes in the microstructure could pair with the electron microscopy investigations. The XRD results point to a potential change in the type and density of dislocations in both FTA-01 and G92 neutron irradiated specimens.

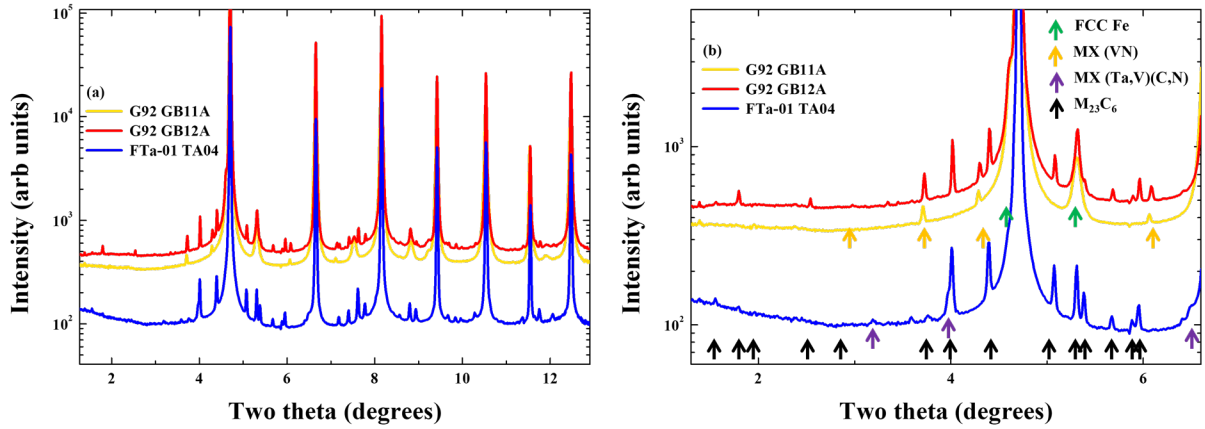

Figure 2. (a) XRD patterns for irradiated specimens with FTa-01 and G92 specimens offset vertically, (b) inset showing higher magnification in low-angle two-theta region with the multiple phases identified for reference.

Table 1. Quantitative XRD results for the RAFM and CNA specimens. CGS = Coherent grain size, us = microstrain.

sample	phase	a	±	c	±	cgs	±	us	±	wt	RWP
	id	Å		Å		nm		(1 ×10^{-3})		%	
G92	Fe	2.86808	0.00001			357.5	10.1	0.92	0.01	98.0 (0.2)	**6.0**
	$M_{23}C_6$	10.62040	0.00065			152.9	7.3			1.7 (0.1)	
	MX	4.41138	0.00437			43.8	2.1			0.2 (0.1)	
FTA-01	Fe	2.86656	0.00001			397.4	10.2	0.93	0.01	98.2 (0.2)	**6.0**
	$M_{23}C_6$	**10.60189**	0.00095			229.9	45.8			1.5 (0.1)	
	MX	4.21497	0.00606			33.0	6.6			0.3 (0.1)	
490	Fe	2.86578	0.00002			267.0	7.5	1.41	0.01	98.7 (0.4)	**7.9**
	$M_{23}C_6$	10.61850	0.00163			100.0	10.0			1.1 (0.1)	
	MX	4.20700	0.00679			15.0	5.0			0.13 (0.05)	
490*	Fe	2.86599	0.00003			500.0	*(fixed)*	1.42	0.01	85.1 (0.4)	**5.3**
	$M_{23}C_6$	10.61970	0.00122			100.4	19.2			0.94 (0.1)	
	MX	4.21540	0.00329			19.6	0.0			0.13 (0.1)	
	Fe nano	2.86487	0.00010			38.2	0.7			13.8 (0.4)	
700C1	Fe	2.86741	0.00001			540.6	13.1	0.41	0.01	96.4 (0.2)	**4.6**
	$M_{23}C_6$	10.63705	0.00067			69.9	4.8			2.6 (0.1)	
	MX	4.40219	0.00167			52.4	15.5			0.4 (0.1)	
	$FeMo_2$	4.73824	0.00141	7.71221	0.00381	180.0	85.0			0.5 (0.1)	
700C3	Fe	2.86738	0.00001			571.4	13.0	0.36	0.01	96.3 (0.1)	**4.2**
	$M_{23}C_6$	10.63769	0.00061			94.2	2.6			2.5 (0.1)	
	MX	4.40746	0.00010			85.2	16.6			0.4 (0.1)	
	$FeMo_2$	4.73459	0.00080	7.72436	0.00215	200.0	60.3			0.8 (0.1)	
	Irradiated										
TA04	Fe	2.86733	0.00001			435.6	11.7	0.51	0.01	97.7 (0.2)	**5.8**
	$M_{23}C_6$	10.63542	0.00088			153.6	2.7			2.0 (0.1)	
	MX	4.15783	0.00385			27.4	0.5			0.1 (0.1)	
GBA12	Fe	2.86775	0.00001			173.6	2.4	0.32	0.02	98.9 (0.2)	**6.2**
	$M_{23}C_6$	10.60711	0.00091			141.5	15.7			0.8 (0.1)	
	MX	4.43424	0.00267			35.0				0.4 (0.1)	
	FCC Fe	3.59333	0.00127			20.1	2.2			0.4 (0.01)	
GBA11	Fe	2.87074	0.00003			181.7	10.4	0.59	0.03	55.0 (0.7)	**6.1**
	MX	4.45467	0.00549			35.0	*(fixed)*			0.2 (0.1)	
	FCC Fe	3.58901	0.00091			52.6	23.0	3.56	0.66	1.9 (0.1)	
	Fe nano	2.86804	0.00077			228.8	24.7	3.31	0.04	42.8 (0.7)	
GBA11*	Fe	2.87069	0.00002			247.9	19.3	0.79	0.02	53.8 (0.7)	**5.5**
	MX	4.45376	0.00487			35.0	*(fixed)*			0.2 (0.1)	
	FCC Fe	3.58802	0.00083			30.8	5.6	2.93	0.61	2.0 (0.1)	
	Martensite	2.86091	0.00018	2.88277	0.00028	193.3	15.0	2.70	0.04	44.0 (0.7)	

Conclusions

The high energy XRD measurements were sensitive to the different minor nm-scale precipitates present in the CNA and RAFM alloys after heat treatment and after neutron irradiation. The phase identification and quantification were complete for all specimens, forming an extension to the existing database for understanding the effects of processing and neutron irradiation on the stability and phase. The XRD analysis yields quantitative atomic information for both the BCC host, precipitate phases and changes with processing and irradiation. Next steps include benchmarking the phase identification with those predicted from TEM or Thermo-Calc simulations, and comparison to electron microscopy results.

Acknowledgements

These experiments and analysis were supported by the DOE Office of Fusion Energy Sciences under contract DE-SC0018322 with the Research Foundation for the State University of New York at Stony Brook. This research used The Pair Distribution Function beamline of the National Synchrotron Light Source II, a U.S. Department of Energy (DOE) Office of Science User Facility operated for the DOE Office of Science by Brookhaven National Laboratory under Contract No. DE-SC0012704.

References

[1.] Zinkle, S.J. and L.L. Snead, *Designing Radiation Resistance in Materials for Fusion Energy.* Annual Review of Materials Research, Vol 44, 2014. **44**: p. 241-267.

[2.] Tan, L., Y. Katoh, and L.L. Snead, *Development of castable nanostructured alloys as a new generation RAFM steels.* Journal of Nuclear Materials, 2018. **511**: p. 598-604.

[3.] Tan, L., L.L. Snead, and Y. Katoh, *Development of new generation reduced activation ferritic-martensitic steels for advanced fusion reactors.* Journal of Nuclear Materials, 2016. **478**: p. 42-49.

[4.] Sprouster, D.J., et al., *Advanced synchrotron characterization techniques for fusion materials science.* Journal of Nuclear Materials, 2021. **543**: p. 152574.

6.2 HELIUM BUBBLES IN ISHI 14YWT AND ON-ZONE STEM IMAGING OF DISLOCATION LOOPS—D. Zhang, D.J. Edwards, M.J. Olszta, A. Schemer-Kohrn, Karen Kruska, Wahyu Setyawan (Pacific Northwest National Laboratory), T. Yamamoto, Y. Wu, G.R. Odette (University of California, Santa Barbara)

OBJECTIVE

The objective of this work is to characterize the distribution of helium bubbles in in-situ helium injected (ISHI) nanostructured ferric alloy 14YWT irradiated at 400 °C to ~21 dpa. While co-location of helium bubbles (diameter ~1 nm) and nano-particles (diameter ~10 nm) were occasionally observed, most bubbles were randomly distributed in the ferritic matrix. Larger bubbles were observed inside Cr-rich precipitates. In addition to helium bubbles, we report a recent study on the use of on-zone scanning transmission electron microscopy (on-zone STEM) technique in imaging dislocation loops in irradiated ferritic alloys. Flash polishing, adequate microscope beam current, and a good combination of convergence and collection angle are key to the successful application of this technique.

SUMMARY

Fresnel contrast under/over focus transmission electron microscopy (TEM) technique was used to characterize helium bubbles in ISHI 14YWT sample. A high density of very small helium bubbles (diameter ~1 nm) was observed. They appeared to be randomly distributed, and there were no sign of bubble clustering or growing into voids/cavities. Co-location of bubbles with nano-particles was occasionally observed, but no strong correlation could be established yet. It is possible that very small particles (≤ 1nm) are associated with helium bubbles, which is the topic of further investigation at higher resolution. In addition to helium bubble characterization, on-zone STEM technique has been successfully used to image dislocations loops in irradiated ferritic alloys. A flash polished PM2000 sample that has undergone ~21 dpa of neutron irradiation at 400 °C was used for preliminary study. The established on-zone STEM imaging condition(s) will be used to characterize dislocation loops in other irradiated alloys, including 14YWT, F82H.mod3+CW, and Eurofer97.

PROGRESS AND STATUS

Besides neutron-irradiation induced or enhanced defects, including dislocation loops and precipitates, metallic materials used in a fusion reactor are also faced with a high concentration of helium, leading to helium embrittlement [1, 2]. To understand helium effects, in-situ helium injection (ISHI) experiments were carried out on a family of fusion relevant materials, including F82H.mod3+CW, Eurofer97, 14YWT, MA957, PM2000, etc. in HFIR with varying neutron doses and irradiation temperatures [3-5]. Preliminary results on helium bubbles in ISHI 14YWT neutron irradiated at 400 °C to ~21 dpa is reported here.

In addition to helium bubbles, dislocation loops developed in these neutron irradiated materials are of great interest too due to their role in irradiation hardening and deformation mechanisms. Traditionally two-beam condition TEM technique has been used to image dislocations and dislocation loops. In recent years, diffraction contrast imaging in STEM mode (i.e., DCI-STEM) has also been used, which offers the potential benefits of reducing specimen contour, better contrast, and ease of coupling with other STEM-based techniques including energy dispersive X-ray spectroscopy (EDS) and electron energy loss spectroscopy (EELS) [6]. However, both TEM and DCI-STEM techniques rely on the two-beam visibility principle, in that a thorough characterization of all dislocations and loops requires laborious tilting, imaging, and pattern matching. With on-zone STEM technique, where dislocation contrast formation is more “relaxed”, it is possible to capture all dislocation loops in a single image, regardless of the types of loops, i.e., a<100> or a/2<111> [7]. Using a TEM specimen of neutron irradiated PM2000 prepared by a standard focused ion beam (FIB) procedure followed by in-house developed flash polishing, parametric on-zone STEM study was performed to establish optimal imaging condition(s) for dislocation loops.

Experimental Procedure

Ferritic 14YWT and PM2000 alloys (Plansee GmbH) were machined into discs of 3 mm diameter. The discs were coated with ~4 μm thickness of NiAl on one side, then irradiated in High Flux Isotope Reactor (HFIR) up to ~21 dpa at 573K, 673K, 773K, respectively. ~1230 appm of helium was injected on the NiAl coated side (i.e., ISHI side), whereas the uncoated side only experienced neutron irradiation ("neutron irradiated only", i.e., NIO side). Details regarding the ISHI technique have been reported elsewhere [3-5].

For studying helium bubbles, TEM specimen from ISHI side of 14YWT was prepared with a standard FIB procedure using an FEI (now Thermo Fisher Scientific) Quanta 3D FIB. As for on-zone STEM study on dislocation loops, FIB prepared TEM specimen from NIO side of PM2000 was further cleaned up with a flash polish (FP) procedure to remove artifacts caused by FIB milling [8]. On-zone STEM was performed on a cold field-emission JEOL ARM200CF microscope operated at 200 kV, equipped with a hexapole type probe CS-corrector (CESCOR, CEOS) for STEM mode. This was the same instrument where previous DCI-STEM characterization of dislocation and dislocation loops was done, so tangible comparison could be made [6, 8]. Meanwhile, helium bubble study for ISHI 14YWT was performed on a probe-corrected JEOL GrandARM-300F microscope operating at 300 kV. It is worth noting that GrandARM is "double corrected", namely for both STEM mode and TEM mode, which makes it quite suitable for Fresnel contrast TEM imaging of helium bubbles.

Future Work

Figure 1 shows Fresnel contrast imaging with ±500 nm defocus for helium bubbles in ISHI 14YWT. The bubbles are mostly ~1 nm in diameter, and randomly distributed in Fe matrix. There is no sign of bubble clustering or growing into voids/cavities. Co-location of bubbles and nano-particles can also be observed sometimes, but the correlation seems to be too weak to suggest sequestration of helium bubbles by nano-particles is happening here [9]. One reason could be the irradiation temperature 400 °C was much lower than that in Parish et al. (650 °C) [9], so the as nucleated smaller helium bubbles had very little mobility to "find" nano-particles and/or grow larger. Preliminary results for helium bubbles in ISHI PM2000 irradiated at 400 °C also show random distribution of bubbles without voids/cavities. Another possibility is much smaller nano-particles, e.g., 1-2 nm in diameter, sequestrated helium bubbles with comparable size, but these dual features are very challenging to capture. Future atomic-resolution S/TEM study is planned [10].

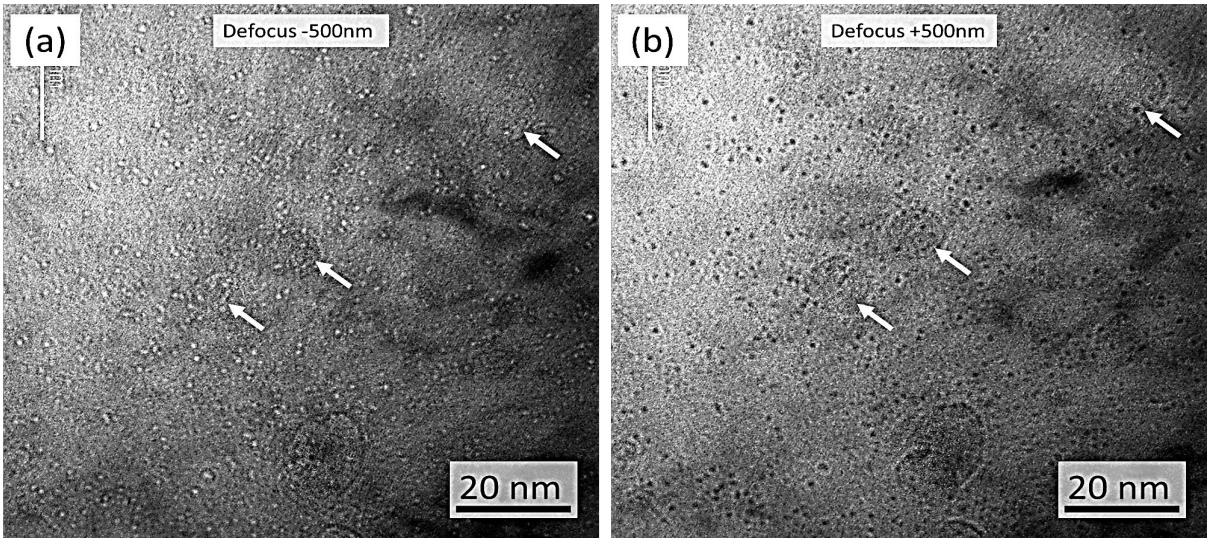

Figure 1. Fresnel contrast imaging with ±500 nm defocus for helium bubbles in ISHI 14YWT. Co-location of bubbles and nano-particles could be seen, like the selected nano-particles highlighted by the white arrows.

For the on-zone STEM study using a flash polished NIO PM2000 specimen, one guiding principle in setting up the STEM parameters is to have the bright field (BF) detector collect the direct beam and the dark field (DF) detector collect the diffracted beams. Within the hardware confinement of available condenser aperture (CA) sizes and camera lengths (CL) on a given microscope, compromises must be made in that BF detector might not be able to collect all direct beam, or maybe some low index diffracted beams would overlap with direct beam and get partially collected by BF detector. Similar practical consideration also applies for DF detector. Nevertheless, given the more "relaxed" contrast formation mechanism in on-zone STEM [11, 12], such compromises may not necessarily degrade the contrast of dislocations and loops.

Initial efforts were made to set up on-zone STEM with parameters resembling those for DCI-STEM [6], where a small convergence angle (6.9 mrad) was achieved using the smallest CA available, i.e., CA = 10 μm. A small convergence angle was chosen so that DCI-STEM would closely resemble the two-beam condition in conventional TEM, and there is minimal overlap between direct beam and diffracted beams. Accordingly, the CL of 40 cm was chosen for DCI-STEM so that the direct beam arrives at BF detector, whereas the DF detector would collect most of the major diffracted beams. These parameters (CA = 10 μm, CL = 40 cm) yielded clean, crisp dislocation contrast under the g = 011 "two-beam" condition near the ferritic 001 zone axis. However, in the case of on-zone STEM, such parameters led to fuzzy, low signal-to-noise ratio (SNR) images. One key factor is the smallest CA means a very small amount of probe current is allowed through the optical axis. This is not a significant problem for DCI-STEM since the current is shared by the direct beam and just one major diffracted beam, namely both BF and DF detectors could still collect abundant signals. However, in the case of on-zone STEM, whereby definition the probe current is divided among the directed beam and many diffracted beams, a small starting probe current means neither the BF detector nor the DF detector could get abundant signals.

To improve SNR for on-zone STEM, the largest probe current available was used, i.e., ~50% higher current than that used in DCI-STEM. Then a parametric study was performed by gradually increasing the CA from 20 μm to 40 μm while adjusting CLs accordingly to enable adequate collection of signals by both the BF and DF detectors. Table 1 summarizes the parameters used.

Table 1. Condenser aperture sizes, convergence angles, camera lengths (CLs), and corresponding collection angles in BF and DF used for on-zone STEM study

Condenser aperture size	Convergence angle	Camera length	Collection angle in BF	Collection angle in DF
**10 μm (DCI-STEM)*	*6.9 mrad*	*40 cm*	*9 mrad*	*14-55 mrad*
20 μm	**13.1 mrad**	**20 cm**	**18 mrad**	**27-110 mrad**
30 μm	20.6 mrad	20 cm	18 mrad	27-110 mrad
30 μm	20.6 mrad	12 cm	30 mrad	45-180 mrad
40 μm	27.5 mrad	12 cm	30 mrad	45-180 mrad

Figure 2 shows the same area of interest imaged with the four conditions listed above. In general, both line dislocations and dislocation loops can be identified. Moreover, as expected both <100> and <111> dislocation loops can be seen in one view on 001 zone axis, with <100> loops appear as thick-short lines, whereas <111> loops appear as ellipses [7]. Comparing the four conditions, the first two with CA 20/30 μm and the same CL 20 cm, the contrast in BF and DF is visibly better than the latter two with CA 30/40 μm and CL = 12 cm. This indicates that even though a larger CA offers a higher probe current, the more divergent beam leads to more overlapping between direct and diffracted beams, namely the signals on BF and DF detectors are more "contaminated". This is particularly true for the DF image in Figure 2(h). Therefore, further comparison will be made among the first two conditions, along with previously obtained DCI-STEM images using the same specimen.

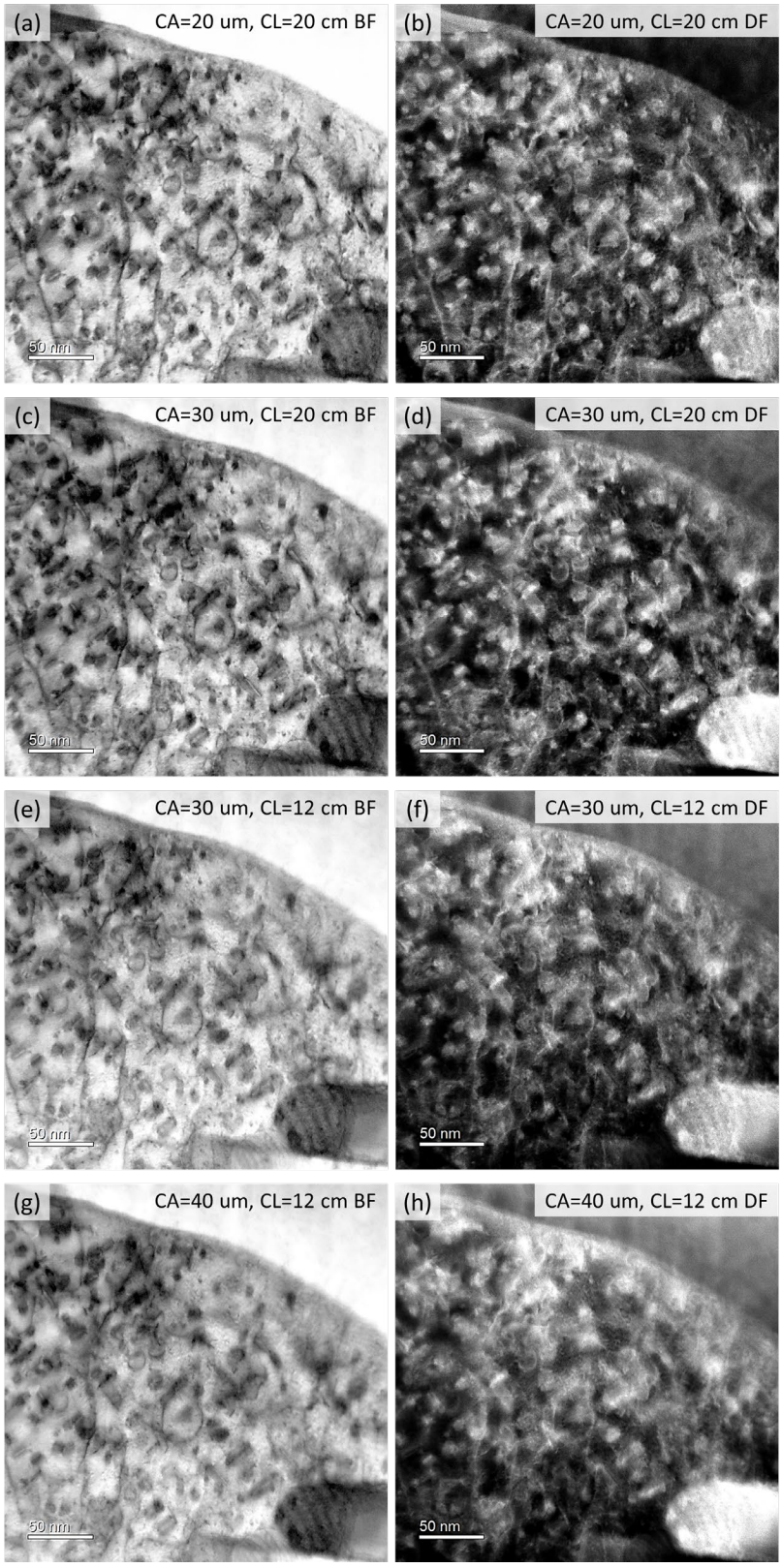

Figure 2. The same area of interest imaged with the four on-zone STEM conditions listed in Table 1.

Figure 3 shows a brief quasi-quantitative SNR analysis for loops and dislocations in the BF image of (a) on-zone STEM with CA = 20 μm, CL = 20 cm; (b) on-zone STEM with CA = 30 μm, CL = 20 cm; (c) DCI-STEM with CA = 10 μm, CL = 40 cm. An intensity profile line was drawn across a dislocation loop (or line dislocation), encompassing the signal intensity for dislocation/loop and that for the background. Then SNR was calculated according to the method reported by Zhu et al. [6]. It is interesting that on-zone STEM with CA = 20 μm, CL = 20 cm yields the highest SNR (28.1) for dislocation loops, with DCI-STEM getting the lowest. However, DCI-STEM gives the highest SNR (6.4) for line dislocations, slightly higher than that in (a). Overall, on-zone STEM with CA = 20 μm, CL = 20 cm seems to give the best SNR for all the line defects, even though one might consider that DCI-STEM gives a "cleaner" image.

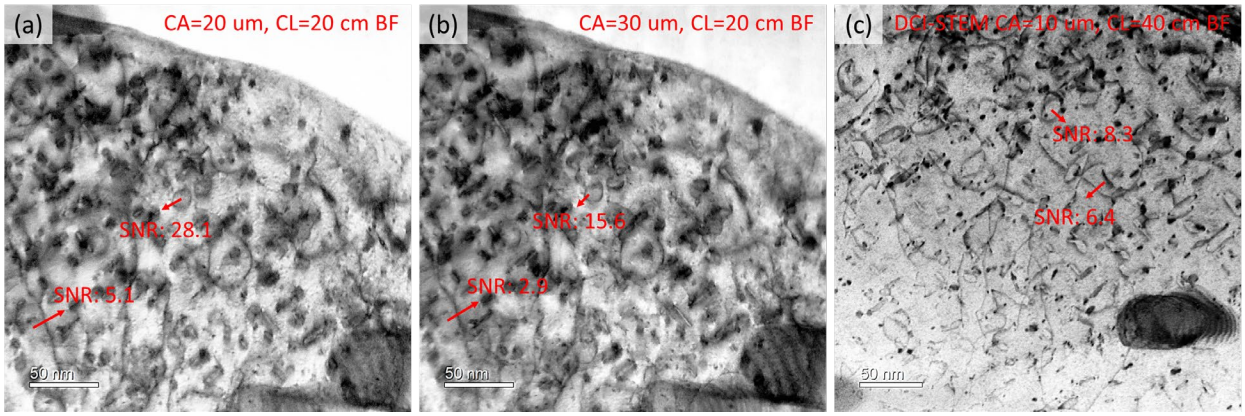

Figure 3. Brief quasi-quantitative SNR analysis for loops and dislocations in the BF image of (a) on-zone STEM with CA = 20 μm, CL = 20 cm; (b) on-zone STEM with CA = 30 μm, CL = 20 cm; (c) DCI-STEM with CA = 10 μm, CL = 40 cm.

Future work includes atomic resolution study of nano-particles and their potential effect on helium bubble sequestration in ISHI 14YWT. On-zone STEM technique will also be applied to the flash polished NIO 14YWT, and eventually to ISHI 14YWT to reveal the correlation between nano-particles, helium bubbles, and dislocation loops.

Acknowledgements

This research has been supported by the U.S. Department of Energy, Office of Science, Office of Fusion Energy Sciences and performed at the Pacific Northwest National Laboratory under contract number DE-AC05-76RL01830. Fruitful discussions with Dr. Kevin Field at University of Michigan, Ann Arbor and Dr. Chad Parish at Oak Ridge National Laboratory were highly appreciated.

References

[1] C. Cabet, F. Dalle, E. Gaganidze, J. Henry, H. Tanigawa, Ferritic-martensitic steels for fission and fusion applications, Journal of Nuclear Materials 523 (2019) 510-537.
[2] S.J. Zinkle, J.L. Boutard, D.T. Hoelzer, A. Kimura, R. Lindau, G.R. Odette, M. Rieth, L. Tan, H. Tanigawa, Development of next generation tempered and ODS reduced activation ferritic/martensitic steels for fusion energy applications, Nuclear Fusion 57(9) (2017) 092005.
[3] H.J. Jung, D.J. Edwards, R.J. Kurtz, T. Yamamoto, Y. Wu, G.R. Odette, Structural and chemical evolution in neutron irradiated and helium-injected ferritic ODS PM2000 alloy, Journal of Nuclear Materials 484 (2017) 68-80.
[4] T. Yamamoto, G.R. Odette, P. Miao, D.T. Hoelzer, J. Bentley, N. Hashimoto, H. Tanigawa, R.J. Kurtz, The transport and fate of helium in nanostructured ferritic alloys at fusion relevant He/dpa ratios and dpa rates, Journal of Nuclear Materials 367-370 (2007) 399-410.

[5] R.J. Kurtz, G.R. Odette, T. Yamamoto, D.S. Gelles, P. Miao, B.M. Oliver, The transport and fate of helium in martensitic steels at fusion relevant He/dpa ratios and dpa rates, Journal of Nuclear Materials 367-370 (2007) 417-422.
[6] Y. Zhu, C. Ophus, M.B. Toloczko, D.J. Edwards, Towards bend-contour-free dislocation imaging via diffraction contrast STEM, Ultramicroscopy 193 (2018) 12-23.
[7] C.M. Parish, K.G. Field, A.G. Certain, J.P. Wharry, Application of STEM characterization for investigating radiation effects in BCC Fe-based alloys, Journal of Materials Research 30(9) (2015) 1275-1289.
[8] A. Schemer-Kohrn, M.B. Toloczko, Y. Zhu, J. Wang, D.J. Edwards, Removal of FIB Damage using Flash Electropolishing for Artifact-free TEM Foils, Microscopy and Microanalysis 25(S2) (2019) 1606-1607.
[9] C.M. Parish, K.A. Unocic, L. Tan, S.J. Zinkle, S. Kondo, L.L. Snead, D.T. Hoelzer, Y. Katoh, Helium sequestration at nanoparticle-matrix interfaces in helium + heavy ion irradiated nanostructured ferritic alloys, Journal of Nuclear Materials 483 (2017) 21-34.
[10] T. Stan, Y. Wu, J. Ciston, T. Yamamoto, G.R. Odette, Characterization of polyhedral nano-oxides and helium bubbles in an annealed nanostructured ferritic alloy, Acta Materialia 183 (2020) 484-492.
[11] P.J. Phillips, M.J. Mills, M. De Graef, Systematic row and zone axis STEM defect image simulations, Philosophical Magazine 91(16) (2011) 2081-2101.
[12] P.J. Phillips, M.C. Brandes, M.J. Mills, M. De Graef, Diffraction contrast STEM of dislocations: Imaging and simulations, Ultramicroscopy 111(9) (2011) 1483-1487.

6.3 ON BIAS EVOLUTION DRIVEN VOID SWELLING IN TEMPERED MARTENSITIC STEELS—G. Robert Odette, Takuya Yamamoto (University of California, Santa Barbara)

OBJECTIVE

Purpose of the research is to develop a void-swelling model for fusion relevant condition based on the balance of cavity and dislocation sink strengths and biases that evolve under dpa and He irradiation.

SUMMARY

While conventional critical bubble models work reasonably well for void nucleation under neutron irradiations, they fail to predict the large critical bubble sizes (≈ 4 nm) needed for highly accelerated dual ion irradiations. The conventional models assume that dislocation sinks are initially biased (B) for self-interstitial atoms (SIA), as $k_{di} = K_{dv}(1+B_d)$, while bubbles and voids are neutral, unbiased cavity sinks with $k_{cv} = k_{ci}$, where the k are the defect sink strengths. As a result of dislocation bias for SIA, excess vacancies drive bubble to void conversion above a critical size and accumulate at growing voids. Low dpa rate neutron irradiations result in low effective vacancy supersaturations, which intrinsically require large critical bubble sizes to convert to voids. However, the vacancy supersaturations are nominally much higher for dual ion irradiations, resulting is conventional critical bubble model predictions of very small bubble sizes. Fortunately, recent studies by Kohnert [1] Haley [2] and Chang [3] rationalize the observed behavior. The initial bias of the dominant bcc lattice screw dislocations is for vacancies, rather than SIA [2], and the initial bias of bubbles is for SIA, rather than being neutral [1]. The dislocation bias for SIA increases as a population of edge dislocations, with a SIA bias evolves, partly due to climb of the screw dislocations into helical configurations and partly due to the formation of dislocation loops [2]. The cavities are initially bubbles, which have a vacancy bias that decreases sharply with their size. These evolutions lead to a condition where the SIA $B_d > B_c$, leading to void nucleation and growth. We show that for a reasonable set of parameters the quantitative models of Kohnert and Chang can predict the void incubation and post-incubation selling rates for dual ion irradiations of F82H tempered martensitic steels.

PROGRESS AND STATUS

Background

Previously we reported updates on the analyses of conventional TEM and scanning TEM (STEM) microstructures in F82H steel irradiated in a dual ion irradiation, nominally up to maximum values of 82 dpa and 3700 appm He [4]. The cavity microstructures were imaged by through-focus series bright field TEM, as well as by high angular annual dark field STEM, while dislocations were characterized using weak-beam dark field STEM. The void swelling (f_v) and swelling rates (f_v') were defined in terms of the volume fractions of cavities that are larger than 4 nm. The total dislocation density in the analyzed area was ≈ 2.5 x 10^{15} (m^{-2}). The corresponding sink-strengths of 1.6 x 10^{15} (m^{-2}) for both bubbles and voids, results in a predicted post incubation swelling rate, f_v' ≈ 0.08%/dpa, sinks assuming a small SIA dislocation bias, B_{di} ≈ 1-2%, which is in good agreement with the dual ion irradiation database trends. The key conclusion was that post incubation void swelling rates in the dual ion irradiations are consistent with simple defect partitioning between dislocation (k_d), bubble (k_b) and void (k_v) sinks. The TEM results suggested that the total dislocation line density increases under irradiation, mainly with added edge contributions from both loops and helical network dislocation evolution. The observed post incubation swelling rates were near the predicted maximum values due to the reasonably balanced void and dislocation sinks strengths ($k_v \approx k_d$). Note, however, a significant population of bubbles can reduce the peak f_v', by up to a factor of ≈ 2.

Here, we describe a swelling model, including incubation and growth of voids, based on the evolution of cavity and dislocation sink strengths and biases. We also discuss injected interstitial and high dose rate effects in DII. Swelling in local regions shielded from IIA effects, and more generally the upper bounds of observed f_v and f_v', provide the best estimate of unperturbed swelling rates. Further, it appears that defect recombination effects in the high dpa rate DII, in the range used in this study (< ≈ 3x10^{-3} dpa/s), are not

large, at least at 500°C. This is very important since it indicates that ion irradiations can reasonably emulate post incubation neutron swelling, again at sufficiently high temperature.

Dual ion irradiation void swelling

The dual ion irradiation data in this report do not directly emulate fusion neutron irradiation effects. For example, as shown in Figure 1c in reference [5], which was focused on developing a predictive fusion relevant swelling model, at the same He/dpa, the void incubation dpa_i in in situ helium injection (ISHI) neutron irradiations is much lower than for dual ion irradiation. The ISHI critical bubble sizes (r_c) are relatively large (≈ 5 nm at 500°C) due to the low effective vacancy supersaturations at neutron irradiation dpa rates. These low dpa rate ISHI r_c are reasonably consistent with conventional critical bubble models and experimental observations [6 and the references therein]. However, conventional models predict much smaller critical bubble sizes at high dual ion irradiation dpa rates, due to the correspondingly higher effective vacancy supersaturations.

Thus, rather than higher incubation dpa, the DII dpa_i are predicted to be negligible, even at 500°C. This conundrum may be partially resolved by the work of Kohnert et al. [1], who pointed out that small cavities are not neutral sinks, but rather they are SIA biased, due to attractive SIA image force interactions with cavity free surfaces. This effect is characterized by a larger SIA versus vacancy interaction distance. Further, recent work by Haley et al. [2] showed that the dominant population of screw dislocations in an unirradiated 9Cr bcc ferrite, are initially biased vacancy sinks, rather than for SIA [2]. The absorption of excess vacancies causes the screw dislocations to climb into helical configurations, with an edge component, which has a much larger SIA bias and capture efficiency. Further, the development of a population of loops increases the overall SIA biased edge dislocation sink strength. Hence, both bubbles and dislocation structures, including loops, also must evolve to the point where there is an overall system dislocation SIA sink bias, relative to bubbles and voids. This sink evolution requirement results in large dual ion irradiation critical bubble sizes, which are qualitatively consistent with the observations reported here. That is, even at high dual ion irradiation dpa rates, the overall system dislocation SIA bias is initially negative, with $B_b > B_d$. The $B_b < B_d$ bias must be achieved to yield an effective vacancy supersaturation driving void nucleation and growth. This occurs only when the bubbles and edge dislocation sinks have sufficiently evolved. Of course, the same physics applies to ISHI neutron irradiations. However, due to the lower vacancy supersaturations for neutron irradiations, bubble to void conversion naturally takes place at intrinsically larger bubble sizes, and at a corresponding dpa associated with extensive dislocation evolution and bubble growth. A detailed model reported by Chang et al. [3], confirms that screw and edge dislocations are vacancy and SIA biased, respectively. Thus, a combination of the Kohnert and Chang models can be used to treat bubble, void and dislocation evolution effects on the overall SIA bias and swelling.

Bias models

The SIA biases to cavities and dislocations are obtained using the bias models by Kohnert et al. [1] and Chang et al. [3]. Here we summarize key points of the bias models.

Cavity bias [1]

Cavity [bubble (b) or void (v)] bias to SIA, B_c (c = b or v), used here is based on the cavity bias model with He pressure and temperature dependence [1]. The bias B_c of a cavity with radius r_c is given by:

$$B_c = Z_{i,c}/Z_{i,c} - 1 \ (c = b, V) \quad (1)$$

The $Z_{j,c}$ (j = i and v) are the capture efficiencies for SIA (i) or vacancy (v) at the cavity given as:

$$Z_{j,c} = 4\pi\left\{r_j + r_c + \alpha_{j,c}(p)\left(\frac{T_m}{T}\right)^{1/3}\right\} \quad (j = i, v; c = b, V) \quad (2)$$

$$\alpha_{j,c}(p) = \max\left[\alpha_{oj,c}, \beta_{j,c}\ pa_o/2\gamma\right] \ (j = i, v; c = b, V) \quad (3)$$

Here, r_j is the radius of SIA or vacancy, and $\alpha_{j,c}(p)$ is the interaction distance for j (SIA or vacancy) to c (the void or bubble) as a function of the He pressure, p, in k. T and T_m is the system temperature and the melting point of the material [1]. Here, γ = 1.8 J/m^2 is used for the surface energy, which was found consistent with an electron energy loss spectrum (EELS) measurements of DII He bubbles in NFAs [7]. The BCC lattice related atomic sizes are $a_o = 0.2867\ (nm)$ and $r_i = r_v = (3{a_o}^3/8\pi)^{1/3}\ (nm)$. The bubble SIA $\alpha_{i,b}$ is approximately constant over the p range modeled, as

$$\alpha_{i,b} \approx 0.25 \text{ nm} \qquad (4)$$

For vacancies

$$\alpha_{v,b} = [0.083 + 4.9357\text{x}10^{-12}\ (p - p_m(\approx 16\ GPa))] \qquad (5)$$

Thus $\alpha_{v,b}$ has a minimum value of 0.083 for p < p_m, then linearly increase with p. Here, p_m is about 16 GPa. Thus except for the initial high p condition for very small bubbles, the term $\alpha_{i\ or\ v,b}(p)(T_m/T)^{1/3}$ is constant for each of SIA and V, and always $Z_{i,b} > Z_{v,b}$, but the ratio $Z_{i,b}/Z_{v,b}$ continuously decreases towards 1 (or bias towards 0) as r_b becomes larger.

Dislocation bias [3]

Chang et al. have carried out extensive calculations to establish the bias of edge and screw dislocations [3]. Detailed discussion of the models is beyond the scope of this report but can be found in [3]. As noted above, screw dislocations biased for vacancies, while edge dislocation have a stronger bias for SIA. The model considers of 1/2<1 1 1> screw dislocation (SD), 1/2<1 1 1> edge dislocations (ED) and <1 0 0> ED. Net dislocation SIA bias, B_d, is based on the density and temperature dependent dislocation capture efficiency (Z) for point defect j (= i for SIA or v for vacancy) of each type of dislocations, $Z_j^{SD}(\rho,T)$, $Z_j^{<111>}(\rho,T)$, and $Z_j^{<100>}(\rho,T)$, along with their fractional densities, a, b, and c, as:

$$B_d = \frac{aZ_{SIA}^{SD} + bZ_{SIA}^{\langle 111\rangle} + cZ_{SIA}^{\langle 100\rangle}}{aZ_{vac}^{SD} + bZ_{vac}^{\langle 111\rangle} + cZ_{vac}^{\langle 100\rangle}} - 1 \qquad (6)$$

Linear least square fits to the Z_j^k (k=SD, <111>, <100>) data as a function of dislocation density at 500°C are shown in Figure 1 as:

$$Z_j^k = a_j^k + b_j^k\ log(\rho^k) \qquad (7)$$

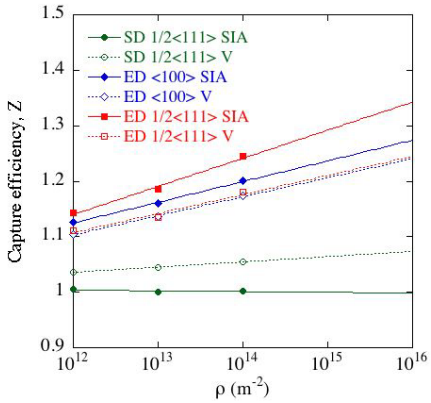

Figure 1. Point defects (SIA or. vacancy) capture efficiency, Z, of various types of dislocations. The values reported in [3] are least square fitted to equation (7) as shown by the lines.

The fitted coefficients $a_j^k and\ b_j^k$ are shown in Table 2.

Table 2. Fitted coefficients for equation (7), the capture efficiency of SIA or V at various types of dislocations

	SD<111> SIA	SD<111> V	ED 1/2<111> SIA	ED 1/2<111> V	ED 1/2<100> SIA	ED<100> V
a_j^k	-0.0013	0.0094	0.0507	0.03435	0.0373	0.0343
b_j^k	1.019366667	0.9232	0.532	0.69525	0.677533	0.691967

A microstructural and bias evolution swelling model

Cavity microstructures start with an assumed constant number density, N_c, of cavities, which initially are bubbles, each containing m_{He} He atoms, equally distributed from the total He concentration C_{He} = He/dpa x dpa as,

$$m_{He} = C_{He}\ N_a / N_b, = \text{He/dpa x dpa x } 10^{-6}\ N_a/N_b \quad (8)$$

Here, N_a is the number of atoms per unit volume. The ideal gas bubble radius, r_{bid} is,

$$r_{bid} = (3m_{He}kT/8\pi\ \gamma)^{1/2} \quad (9)$$

Here γ = 1.8 J/m^2. Then, the radius r_{bid} is converted to that for real gas hard sphere equation of state (HSEOS), r_b, using Stoller's master equation [8]. The bubble pressure, p_b, is obtained from the HSEOS as [8],

$$p_b = \left(\frac{1+y+y^2-y^3}{(1-y)^3}\right) m_{He}kT/(4\pi r_b^3/3) \quad (10)$$

$$y = \left(\frac{m_{He}\pi d_g^3}{6}\right)/(4\pi r_b^3/3) \quad (11)$$

$$d_g = 0.3135 * (0.8542 - 0.03996 * ln(T/9.16)) \quad (12)$$

The change in r_b as a function of dpa for He/dpa = 40 is shown in Figure 2.

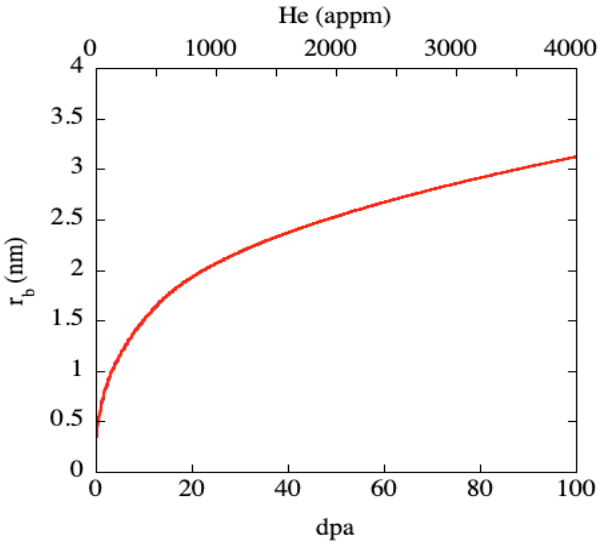

Figure 2. Evolution of He bubble radius as a function of dpa for He/dpa=40.

Voids convert from bubbles when m_{He} and r_b reach a critical size controlled by the evolution of bias and sink strengths to produce a net system dislocation SIA bias. To model the observed cavity microstructures, the number of bubbles and voids are fixed, after this conversion, at N_b and N_v, respectively. That is the bubble remain bubble, while the voids begin to grow. The additional He generated continues to be divided between bubbles and voids, where the bubble Δm_{Heb} is given by

$$\Delta m_{Heb} = [He/dpa]\Delta dpa_p (N_a/N_b)/(1+k_v/k_b) \quad (13)$$

The other Δm_{Hev} partitions to the voids. Here, Δdpa_p is the dose increment after void formation.

Dislocation evolution

Dislocation evolution is modeled assuming that most are screws before irradiation, and that only edge dislocations are produced during the irradiation. The radiation induced edge dislocation density evolves in a similar fashion to dislocation loop hardening, mostly at lower temperatures [9]. These are described in Equations (14) –(16).

$$\rho = \rho_{sd} + \rho_{ed} \quad (14)$$

$$\rho_{sd} = \rho_0 \quad (15)$$

$$\rho_{ed} = \rho_{es}\{1 - exp(-dpa/dpa_e)\} \quad (16)$$

Here, ρ_o is the initial screw dislocation density, ρ_{es} is the edge dislocation saturation density and dpa_e is the e-folding constant for the edge dislocation saturation. The 1/2<1 1 1 > and <1 0 0> edge dislocation ρ are assumed to be the same.

Bias evolution and swelling

We assess the effect of the bias evolution on both the void incubation dpa_i and the post incubation swelling rate, f_v', since while involving somewhat different physics much be consistent with the same set of model parameters. Here we use the dual ion irradiation dpa_i and f_v' data at a He/dpa = 40 to calibrate the model using observed parameters to the extent possible.

For simple partitioning between sinks f_v' is given by

$$f_v' = \eta k_v\{(k_d)(B_d - B_b)\}/(k_d + k_b + k_v)/\{k_d(1+B_d) + k_b(1+B_b) + k_v(1+B_b)\} \quad (17)$$

Here, the sink strengths are $k_d = \rho_d$, $k_b = 4\pi r_b N_b$, $k_v = 4\pi r_v N_v$ and η is the defect to displacement production ratio.

The key parameters are N_b, N_v, the initial screw dislocation ρ_{os}, the saturation edge dislocation ρ_{es}, and the e-folding dpa_o. Observed parameters (with standard deviations as available) are: $N_b = 0.9 \pm 1x10^{22}$ m^{-3}; $N_v = 2.1\pm 1x10^{22}$ m^{-3}; $\rho_o = 6\pm3x10^{14}$ m^{-2}. The edge saturated ρ_{es} is assumed to be $1.9x10^{15}$ m^{-2}, yielding a total saturation observed STEM value of $\rho = 2.5x10^{15}$. B_d is initially negative but increases with dpa due to an increasing edge fraction. B_b starts with large positive values but decreases with dpa due to the increasing r_b. For swelling to occur these curves must cross over with $B_d > B_b$. However, for the nominal SIA interaction distance, $\alpha_{ib} = 0.25$ nm, there is no early crossover, and $B_b > B_d$ up to 100 dpa. A fitted $\alpha_{ib} = 0.11$ and $dpa_e \approx 5$ was fitted to the He/dpa > 40 DII f_v' data as shown in Figure 3a.

Figure 3a shows that $B_d - B_b < 0$ at less than 7 dpa, thus swelling is not possible. $B_b - B_d > 0$ at higher dpa. Increasing to ≈ 1.5%. Integrating Equation (17) shows that f_v and f_v' increase with dpa, as seen in Figure 3b. Here it is assumed that the helium bubble void conversion radius is compatible with other critical radius

criteria. The good agreement between the model predictions and the DII f_v data for a reasonable set of parameters is very encouraging and establishes a foundation for developing models for fusion relevant irradiation conditions. Specifically, the bias evolution swelling dpa_i and f_v' model is believed to also be applicable to fusion neutron irradiations with high He/dpa ratios and lower dpa rates. Hence, we next evaluate the effect of recombination at high dual ion irradiation dpa rates.

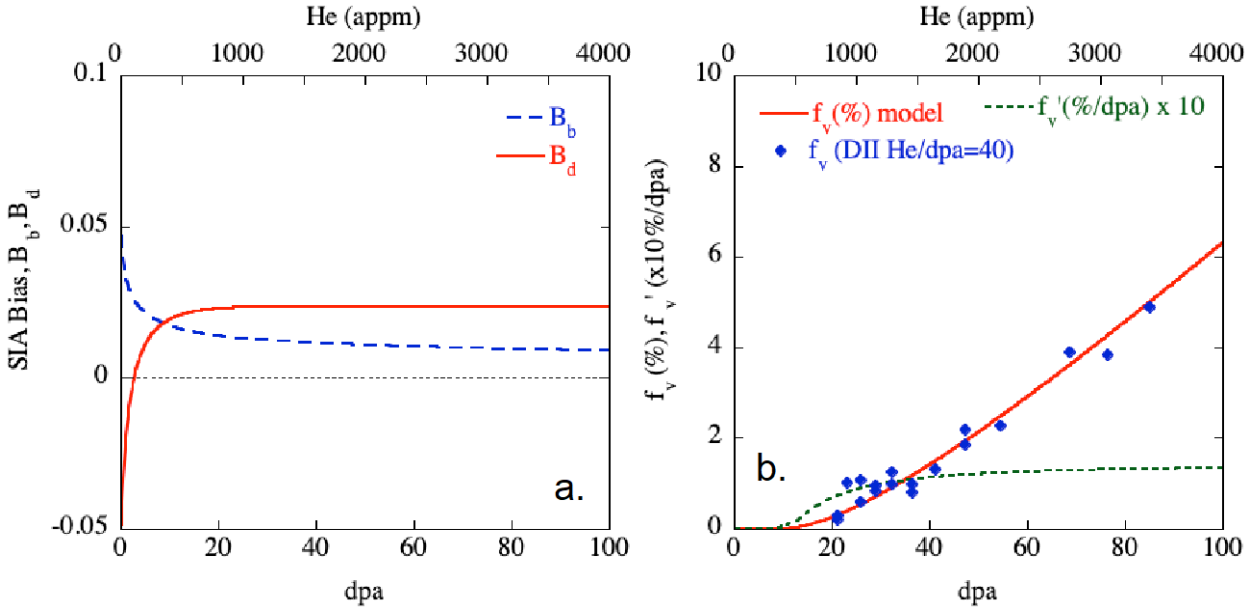

Figure 3. Evolution of bubble, B_b, and dislocation, B_d, biases and f_v and f_v' in a calibrated DII swelling model.

Recombination at high dual ion irradiation dpa rates

Simple rate theory models can be used to evaluate the effects of dual ion irradiation high dpa rates on vacancy-SIA recombination. In dilute alloys recombination is strongly promoted by vacancies trapped by solutes, with a binding energy E_b, as modeled in [10]. However, in more concentrated alloys, recombination can be treated by simply using an effective vacancy migration energy which is higher than that in pure Fe. Cascade defect cluster debris, like nanovoid-solute and small SIA-solute cluster complexes, which thermally dissolve under irradiation (or spatially saturate), also act as effective recombination centers [10]. These features have been called unstable matrix defects (UMDs) [11]. The overall recombination effect can be quantified as the fraction of point defects reaching permanent sinks (g_s), by escaping both matrix recombination and UMD sinks. The derivation of the matrix recombination model can be found in [10]. We use an effective vacancy migration energy of 0.9 eV (versus ≈ 0.6 eV in pure Fe), and a UMD production cross section (1.5×10^{-21} m^2), which is 1/3 of the nominal value, to account for the lower energy primary recoils produced in heavy ion versus neutron irradiations [12]. Figure 4a shows g_s at 500°C in a function of dpa rate for two sink densities. The effect of irradiation temperature on recombination from 425 to 500°C is shown in Figure 4b for the high sink density and dpa rate up to 4×10^{-3} dpa/s. At 500°C and a nominal ≈ 2×10^{-3} dpa/s, representative of this study, $g_s \approx 0.90 \pm 0.03$. For the high sink strength and dpa rate case, g_s decreases to ≈ 0.36 at 425°C. Figure 4a also shows $g_s = 1$ at a low neutron FRI dpa rate of 5×10^{-7} n/cm^2-s. While these values depend on the model parameters, they suggest that recombination effects are relatively modest for the dual ion irradiation in this study. Further, note that these results are also reasonably consistent with a nominal to 50-75°C temperature shift proposed to correct the ion irradiation data to lower peak neutron swelling temperature (430-450°C), as recently discussed in [13]. Notably, that DII study of the temperature dependence of swelling in 9Cr steels at a He/dpa = 0.1 [13] also show sharp reductions in the f_v below 500°C, which can largely be attributed to the effect of recombination on void nucleation.

Future Work

We have demonstrated that a simple microstructurally based bias evolution model is consistent with the observed void swelling behavior in dual ion irradiated F82H. More details are reported in a soon to be submitted paper [14]. The comprehensive dual ion irradiation database has also been integrated with in situ helium injection neutron irradiation results , as well as fission neutron and single ion irradiation data, in a companion fusion semiannual report [5] and soon to be submitted paper [15] aimed at developing a fusion relevent void swelling model. Of course, further experimental verification of the various model assumptions, and especially higher dpa in situ helium injection neutron irradiation data are critically needed. Further, the tremendous new insight on mechanisms mediating void swelling must be integrated in the master model of helium generation, transport, fate and consequences.

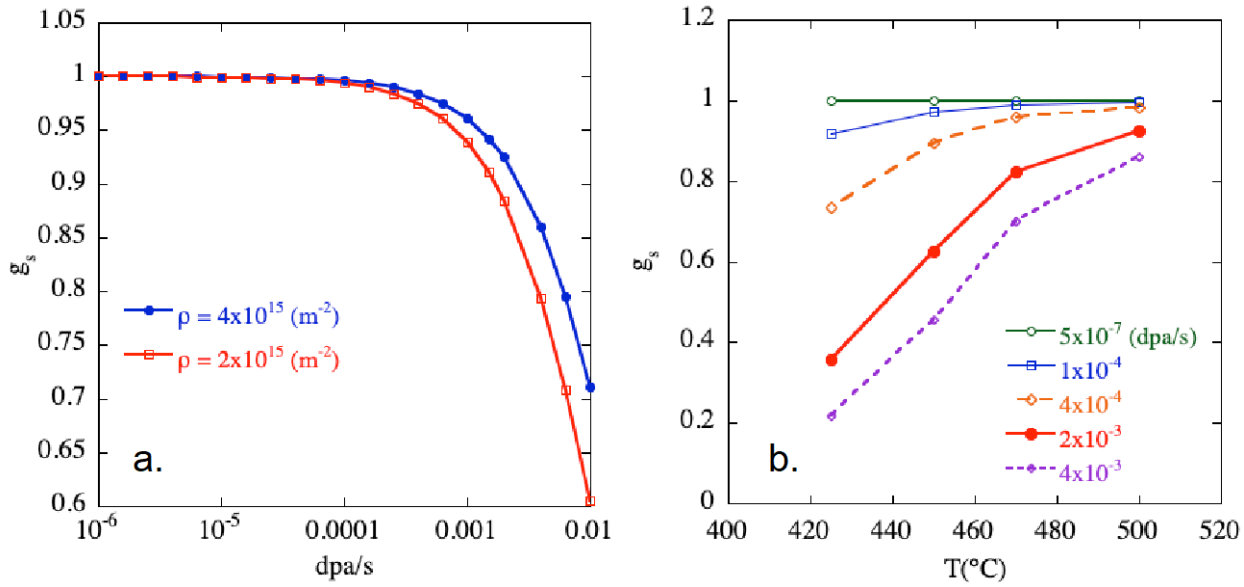

Figure 4. The a) dose rate and b) temperature dependence of the g_s, fraction of point defects reaching permanent sinks.

Acknowledgments

The authors gratefully acknowledge many collaborators who helped in carry out the irradiation experiments and PIE microstructural characterization studies. They include Drs. Y. Wu and P. Miao at UCSB (TEM); Drs. D.J. Edwards, R.J. Kurtz, D.S. Gelles, H.J. Jung at PNNL for PIE (specimen preparation and TEM); Professors K. Yabuuchi, S. Kondo, A. Kimura, and Mr. Hashitomi at the Kyoto University DuET facility (DII); Drs. R.E. Stoller and Y. Katoh at ORNL (ISHI HFIR irradiations and specimen recovery and shipping); Dr. J. Haley at Oxford University (DuET TEM PIE while visiting UCSB). This work was supported by the U.S. Department of Energy, Office of Fusion Energy Sciences, under the contract DE-FG03-94ER54275. The Joint Research Program on Zero-Emission Energy Research Institute of Advanced Energy, at Kyoto University, supported the DuET irradiation experiments. The TEM PIE microstructural characterizations were carried out in the NSF supported UCSB California Nanosystems Microstructural and Microanalysis and the DOE/INL supported National Scientific User CAES facility operated by Idaho State University.

References

[1] A.A. Kohnert, M.A. Cusentino, B.D. Wirth, J. Nucl. Mater. 499 (2018) 460.
[2] J.C. Haley, F. Liu, E. Tarleton, A.C.E. Cocks, G.R. Odette, S. Lozano-Perez, S.G. Roberts, Acta Mater. 181 (2019) 173.

[3] Z. Chang, D. Terenvyev, N. Sandberg, K. Samuelsson, P. Olsson, “Anomalous bias factors of dislocations in bcc iron,” J. Nucl. Mater. 461 (2015) 221.
[4] T. Yamamoto, G.R. Odette, K. Yoshida, K. Yabuuchi, “A Microstructurally Based Model for Post Incubation Void Swelling in Dual Ion Beam Irradiation Tempered Martensitic Steels,” *Fusion Materials Semiannual Report 7/1 to 12/31/2020* DOE/ER-313/69 (2021) 38.
[5] T. Yamamoto, G.R. Odette, “A Data Driven Fusion Relevanat Void Swelling Model Update,” *Fusion Materials Semiannual Report 1/1 to 6/30/2021* DOE/ER-313/70 (2021).
[6] Y. Dai, G.R. Odette, T. Yamamoto, *The Effects of helium on irradiated structural alloys, in Comprehensive Nuclear Materials, R. Konings, T. R. Allen, R. E. Stoller, S. Yamanaka Eds. (2012) Elsevier.*
[7] Y. Wu, G.R. Odette, T. Yamamoto, J. Ciston, P. Hosemann, “An Electron Energy Loss Spectroscopy Study of Helium Bubbles in Nanaostructured Ferritic Alloys,” *Fusion Materials Semiannual Report 6/30/2013* DOE/ER-0313/54 (2013) 173.
[8] R.E. Stoller and G. R. Odette, “Analytical Solutions for Helium Bubbles and Critical Radius Parameters using a Hard Sphere Equation of State,” J. Nucl. Mater. 131 (1985) 118.
[9] T. Yamamoto, G.R. Odette, H. Kishimoto, J-W. Rensman, P. Miao, *J. Nucl. Mater.* 356 (2006) 27.
[10] G.R. Odette, T. Yamamoto, D. Klingensmith, “On the effect of dose rate on irradiation hardening of RPV steels,” Phil. Mag. 85 (2005) 779.
[11] G.R. Odette, T. Yamamoto, T.J. Williams, R.K. Nanstad, C.A. English, “On the History and Status of Reactor Pressure Vessel Steel Ductile to Brittle Transition Temperature Shift Prediction Models,” J. Nucl. Mater. 526 (2019) 151863.
[12] Gary S. Was, *Fundamentals of Radiation Materials Science,* Springer New York, NY (2017).
[13] Y-R Lin, A. Bhattacharya, D. Chen, J-J Kai, J. Henry, S.J. Zinkle, “Temperature-dependent cavity swelling in dual-ion irradiated Fe and Fe-Cr ferritic alloys,” Acta Mater. 207 (2021) 116660.
[14] T. Yamamoto, Y. Wu, K. Yabuuchi, J. Haley, K. Yoshida, A. Kimura, G.R. Odette, “On Displacement Damage-Helium Interactions on Cavity Evolution and Void Swelling in Dual Ion Irradiated Martensitic Steels,” To be submitted to J. Nucl. Mater.
[15] T. Yamamoto, G.R. Odette, “A Fusion Relevant Data Driven Engineering Void Swelling Model for 9Cr Tempered Martensitic Steels,” To be submitted to J. Nucl. Mater.

6.4 EFFECT OF HELIUM ON CAVITY SWELLING IN DUAL-ION IRRADIATED HIGH PURITY IRON-CHROMIUM ALLOYS—Yan-Ru Lin, Steven John Zinkle (University of Tennessee), Arunodaya Bhattacharya (Oak Ridge National Laboratory)

OBJECTIVE

This task aims to study the He synergistic effect on cavity swelling in ion-irradiated high purity Fe and Fe-Cr alloys at 400-500°C. A fusion-relevant He production rate (10 appm He/dpa) was selected to compare with our previous study on the same materials but irradiated at a fission-relevant condition (0.1 appm He/dpa) [1].

SUMMARY

Simultaneous dual-beam irradiations on ultra-high purity Fe and Fe-Cr alloys (3-14 wt% Cr) at 400-550°C were performed to improve the understanding of cavity formation in ferritic alloys. 8 MeV Ni ions (relatively wide safe analysis zone with a midrange dose ~30 dpa) and helium production rates of 10 and 50 appm He/dpa were selected. Cavities were observed by TEM in all the 10 appm He/dpa irradiated samples. A bimodal cavity size distribution was observed. The peak swelling temperature was noticeably higher for the Fe-Cr alloys compared to pure Fe. Compared to the 0.1 He appm/dpa samples reported previously, the 10 appm He/dpa results showed a more considerable cavity swelling and higher peak swelling temperature.

PROGRESS AND STATUS

We performed simultaneous dual-ion (8 MeV Ni^{3+} and 3.4 MeV He^{2+}) irradiation on high purity Fe and Fe-Cr alloys (3-14 wt% Cr) at 400-550°C utilizing multiple ion accelerators at Michigan Ion Beam Laboratory (MIBL). The 20 investigated specimen/temperature conditions is a subset of the 30 material conditions previously investigated at 0.1 appm He/dpa [1]. With a total fluence of 9.68×10^{20} m^{-2} Ni ions, the mid-range damage (at depth ~1 μm) and dose rate were roughly 30 dpa and 1.4×10^{-3} dpa/s, respectively, based on SRIM simulation. He ions were degraded through a rotating Al foil to produce a graduated implanted helium concentration at constant 10 appm He/dpa at intermediate depths of 500 to 1250 μm. Plasma cleaner and cold trap was used to minimize contaminates. Infrared thermal imaging system was calibrated by thermocouples prior to the start of the irradiation. Using transmission electron microscopy (TEM), cavities were observed in all the twenty investigated irradiation conditions within the analysis depth range of 500-1250 nm (as shown in Figure 1).

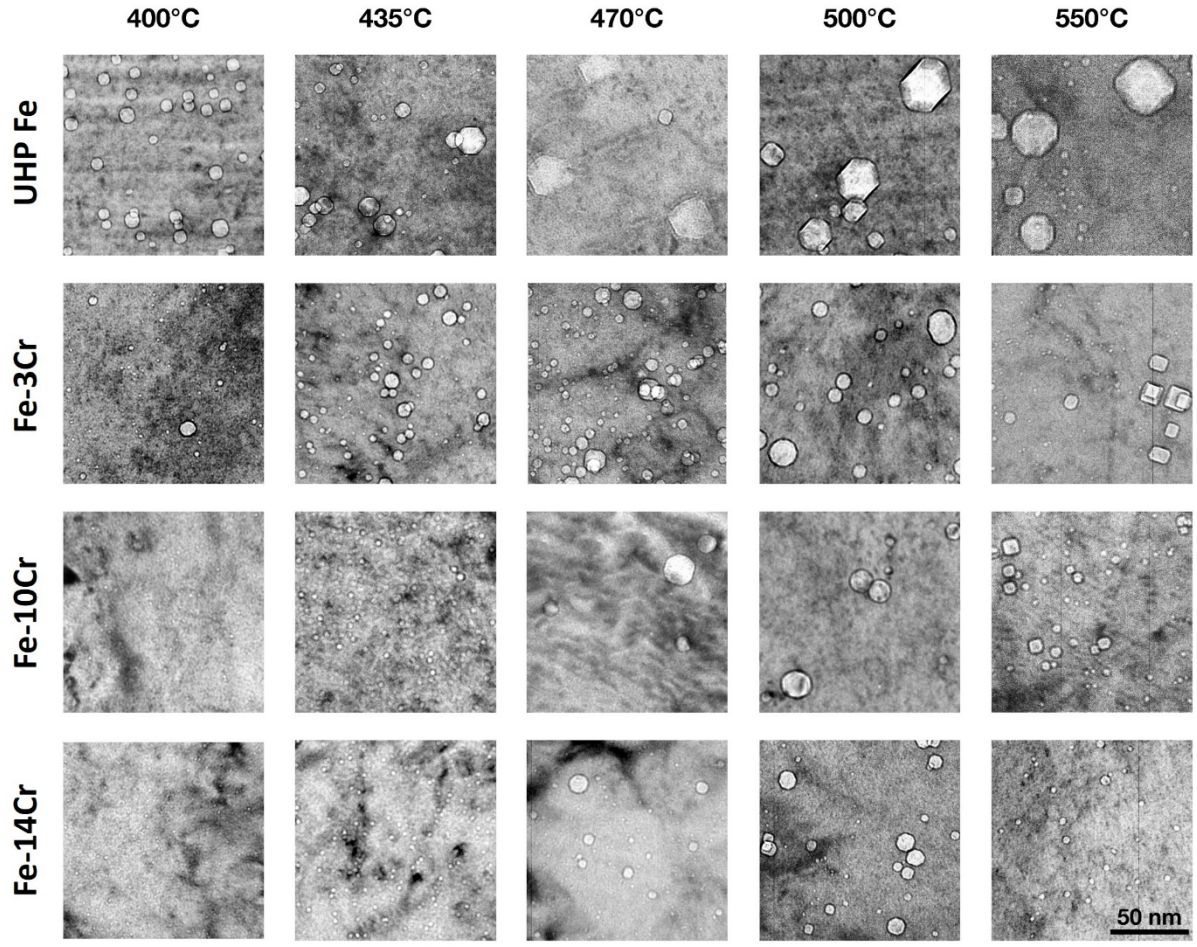

Figure 1. The TEM Images of cavities in dual-ion irradiated Fe and Fe-Cr alloys taken from the analysis depth range of 750-1250 nm (Midrange irradiation condition: 30 dpa, 10 appm He/dpa).

A bimodal cavity size distribution with an intermediate critical radius typically has a high density of bubble-like cavities at small sizes and a lower population of void-like cavities at larger sizes, with hardly any cavities between these two size groups. As shown in the cavity size distribution plots (Figure 2), a bimodal cavity size distribution was observed in most samples, but not in the Fe-10Cr and Fe-14Cr irradiated at 400°C. Because of the evident bimodal cavity size distribution observed in the 10 appm He/dpa irradiated samples, the size and density of the bubble-like ($r < 2$ nm) and the void-like ($r > 2$ nm) cavities were measured separately. The selection of 2 nm for the critical radius is in between the theoretical estimated value (1.7 nm) [2] and experimental results (2.5 nm) by Horton et al. [3] with irradiation conditions (30 dpa and 300 appm He) like the present study.

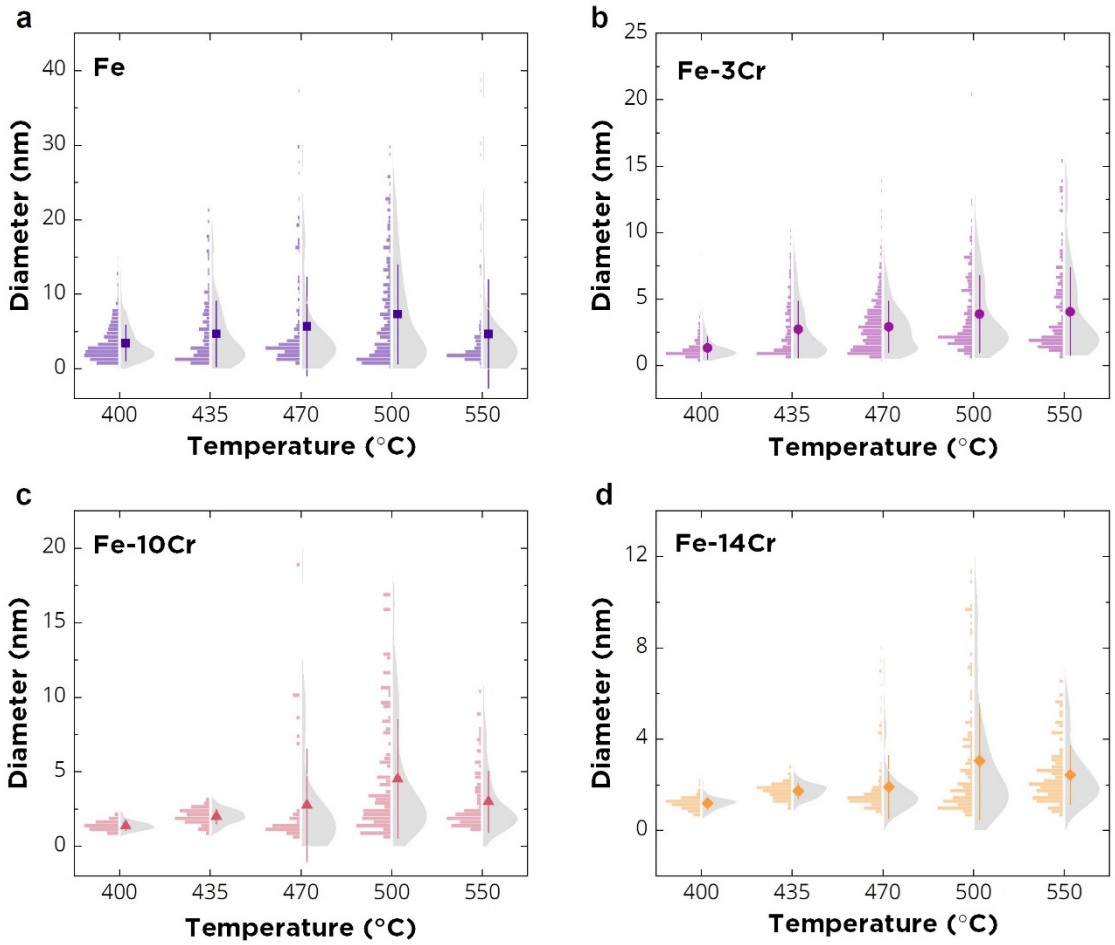

Figure 2. Cavity size distribution and average cavity diameter in dual beam irradiated (a) Fe, (b) Fe-3Cr, (c) Fe-10Cr, and (d) Fe-14Cr alloys at 400-550°C. (Midrange irradiation condition: 30 dpa, 10 appm He/dpa).

Following the size classification, larger voids with a diameter above 4 nm were not observed in Fe-3Cr and Fe-10Cr at 400 and 435°C. The void and bubble size increased with increasing temperature for temperatures below 500°C, as shown in Figure 3. However, for both the Fe and Fe-Cr alloys at 550°C, the void size either grew insignificantly or shrank by up to ~30%, likely due to the vacancy emission or diffusion of implanted Ni ions into the midrange analysis zone at high temperatures. The average void diameter in all the irradiation conditions is between 6-10 nm, while the average bubble diameter is ~2 nm.

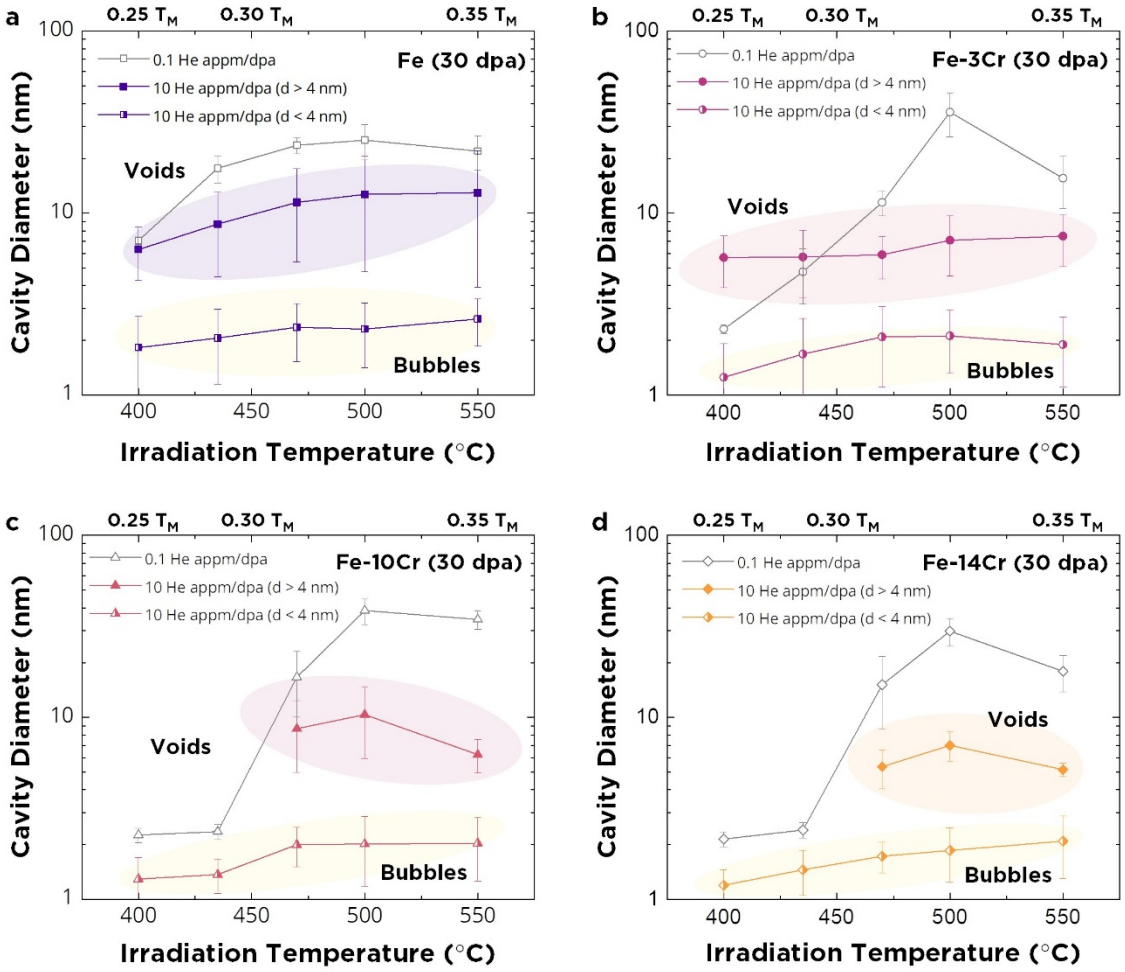

Figure 3. Average cavity diameter in dual beam irradiated (a) Fe, (b) Fe-3Cr, (c) Fe-10Cr, and (d) Fe-14Cr alloys at 400-550°C.

The cavity density is overall in the range of ~10^{22}-10^{23} m^{-3}. The bubble density is higher than the void density by a factor of 2-10. Both the void and bubble density for all materials irradiated at 10 appm He/dpa are much higher than the void density at 0.1 appm He/dpa at all temperatures. Regarding the temperature dependence of cavity density at 10 appm He/dpa (Figure 4), the void and bubble density in pure Fe decreased with increasing temperature as is typical for irradiated materials. However, for voids in the Fe-Cr alloys, the maximum density is at 470°C, and the void density is relatively low or not observed at lower and higher temperatures. In general, the variation of the cavity size and density as a function of temperature agrees with our previous 0.1 appm He/dpa results (colored in gray in Figures 3 and 4). The absence of voids at lower temperatures in Fe-Cr alloys could be caused by solute trapping of defects or the formation of α' precipitates that would lead to a higher sink strength which suppresses the formation of cavities.

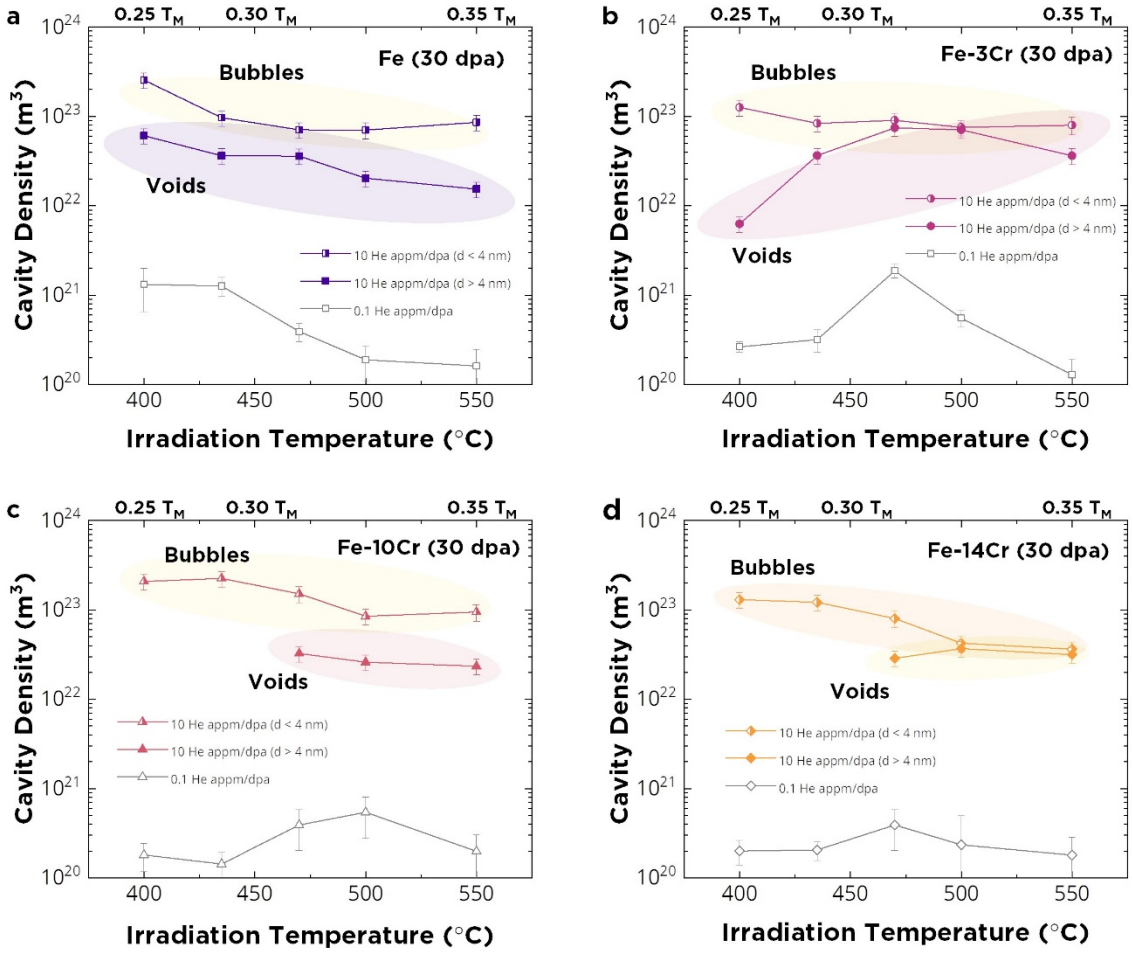

Figure 4. Cavity density in dual beam irradiated (a) Fe, (b) Fe-3Cr, (c) Fe-10Cr, and (d) Fe-14Cr alloys at 400-550°C.

Using the measured cavity size and density, the total volumetric swelling of cavities can be given by summing up the volume of each cavity (assumed spherical) with respect to the volume of the analyzed zone. As shown in Figure 5, compared to the 0.1 He appm/dpa samples irradiated previously, the increase of 100 times in the He/dpa content overall resulted in a higher cavity swelling value. The maximum swelling value of the 20 samples irradiated at 10 appm He/dpa was ~2.8% for Fe irradiated at 470°C. The peak swelling temperature was ~50-65°C higher for the Fe-Cr alloys than pure Fe. The higher He/dpa content resulted in a higher peak swelling temperature for pure Fe with a temperature difference of ~35°C compared to the 0.1 appm He/dpa case. The effect of He on the peak swelling temperature of Fe-Cr alloys is unclear. Extra data points with irradiated temperatures between 500-550°C or using higher ion irradiation energy to avoid implanted ion artifacts would be useful to confirm the He effects on peak swelling temperature shift in the Fe-Cr alloys.

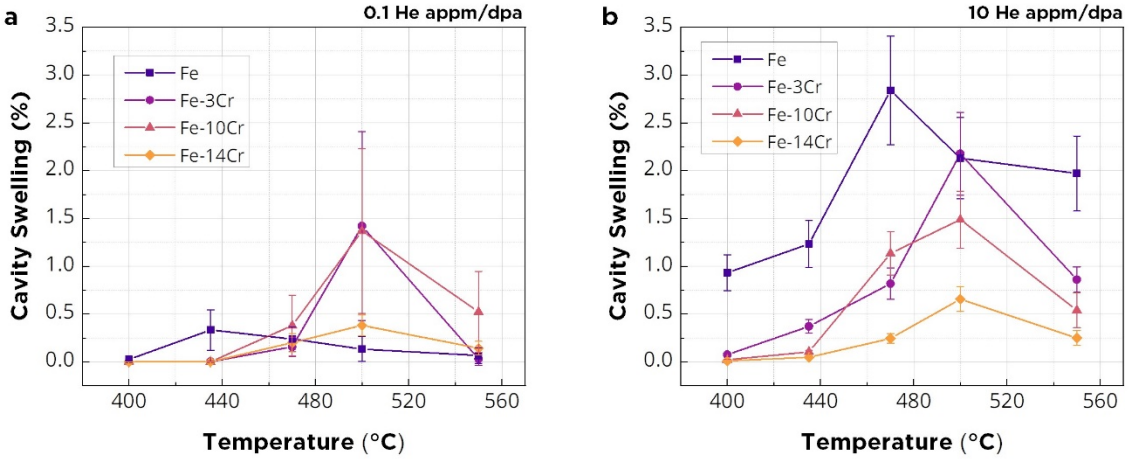

Figure 5. Cavity swelling in dual beam irradiated Fe and Fe-Cr alloys at 400-550°C: (a) 0.1 appm He/dpa and (b) 10 appm He/dpa.

Future Work

The TEM characterization of the 50 appm He/dpa irradiated samples is in progress. Investigation of the correlation between α' precipitates (by APT), dislocation loops, and cavities will be completed to understand the potential roles of solute trapping of defects and sink strength effects on cavity swelling.

References

[1] Y. Lin, A. Bhattacharya, D. Chen, J. Kai, J. Henry, S.J. Zinkle, "Temperature-dependent cavity swelling in dual-ion irradiated Fe and Fe-Cr ferritic alloys", Acta Mater., 207 (2021), 116660.

[2] A. Hishinuma, L.K. Mansur, "Critical radius for bias-driven swelling - a further analysis and its application to bimodal cavity size distributions", J. Nucl. Mater., 118 (1983), pp. 91-99.

[3] L.L. Horton, L.K. Mansur, "Experimental Determination of the Critical Cavity Radius in Fe-10Cr for Ion Irradiation", in: F.A. Garner, J.S. Perrin (Eds.), ASTM International, West Conshohocken, PA, 1985, pp. 344-362.

6.5 EFFECT OF ION IRRADIATION ON PHASE STABILITY IN Fe-12%Cr AND Fe-14%Cr—Y. Zhao, S.J. Zinkle (University of Tennessee), A. Bhattacharya (Oak Ridge National Laboratory)

OBJECTIVE

The objective of this work is to study the effect of bulk Cr content on the formation of α' phase and the possible modification of ballistic dissolution effect on the equilibrium phase diagram.

SUMMARY

Ultra-high purity Fe-Cr alloys with 10-18 wt.% Cr were irradiated with 8 MeV Fe ions to a midrange (~1 um) dose of 0.37 or 3.7 displacements per atom (dpa) between 300-450 °C at 10^{-3}, 10^{-4} and 10^{-5} dpa/s. Following irradiation, atom probe tomography (APT) was employed to characterize the Cr-rich clusters. Homogeneously distributed α' precipitates were revealed in Fe18Cr after ion irradiation at most conditions except for the 300 °C at 10^{-3} dpa/s, which were summarized in previous reports [1-3]. The main progress of the current report is using a cluster searching algorithm developed by the authors to analyze the distribution of α' precipitates in Fe(12-14%)Cr after ion irradiations.

PROGRESS AND STATUS

Several additional specimens were characterized with APT during this reporting period. Their Cr contents and irradiation conditions are summarized in Table 1.

Table1. The specimens characterized with APT during this reporting period

Cr concentration (wt. %)	Irradiation temperature (°C)	Dose rate (dpa/s)	Dose (dpa)
14	300	10^{-4}	0.37
14	350	10^{-3}	0.37
14	350	10^{-4}	3.7
14	450	10^{-4}	3.7
12	300	10^{-4}	0.37
12	450	10^{-5}	0.37

Experimental Procedures

The specimens' chemical compositions, sample preparation procedures, and details related to ion irradiation experiments can be found in the prior reports [1-3]. After ion irradiations, the precipitates in the samples were characterized by APT. The samples for APT analysis were prepared by focused ion beam (FIB). Cr-enriched α' precipitates were identified and quantified through a solute concentration-based cluster analysis algorithm written with Python codes. Details regarding this Python code will be documented in a separate publication.

Preliminary Results

α' precipitation in Fe-14Cr

A cluster searching algorithm using a threshold Cr content of 24 at. % was applied to the APT datasets of Fe-14Cr to identify the α' clusters. The results for the final dose of 0.37 dpa are presented in Figure 1. Large number density of α' precipitates could be observed after irradiations at dose rates of 10^{-5} to 10^{-3} dpa/s. In general, the number densities of precipitates are lower compared to that of Fe-18Cr after ion irradiation at

the same conditions. The radii and of precipitates are summarized in Figure 2. The radii are larger at higher temperatures and lower dose rates, while the number densities show an opposite trend.

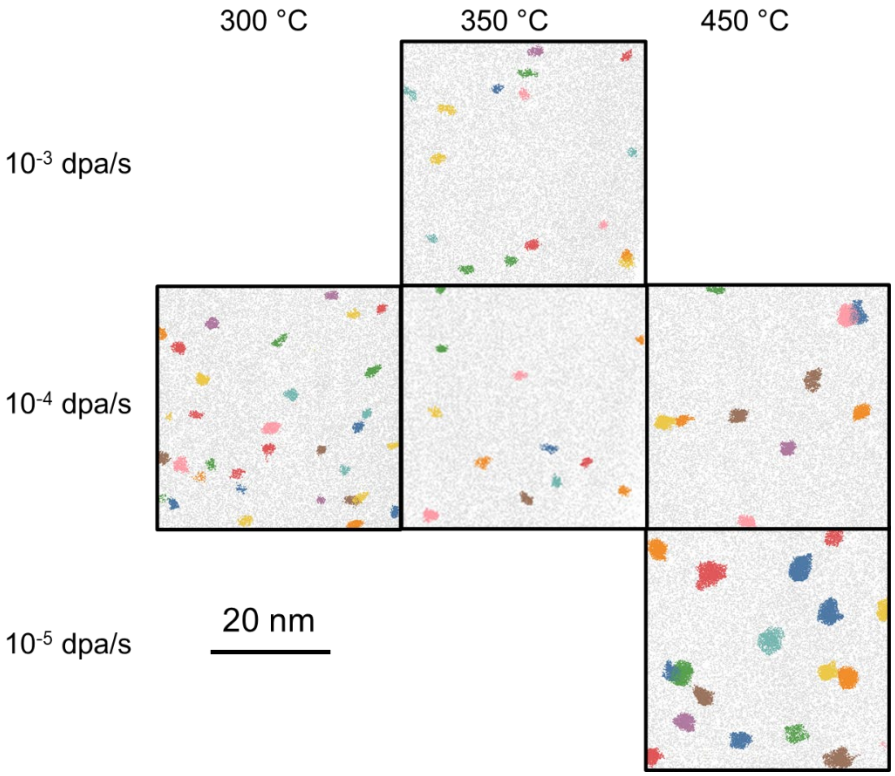

Figure 1. Cluster atom maps for Fe-14Cr irradiated to 0.37 dpa in a sampled volume of 40×40×10 nm^3. Clusters are indexed with different colors. All elements including both Fe and Cr atoms are included.

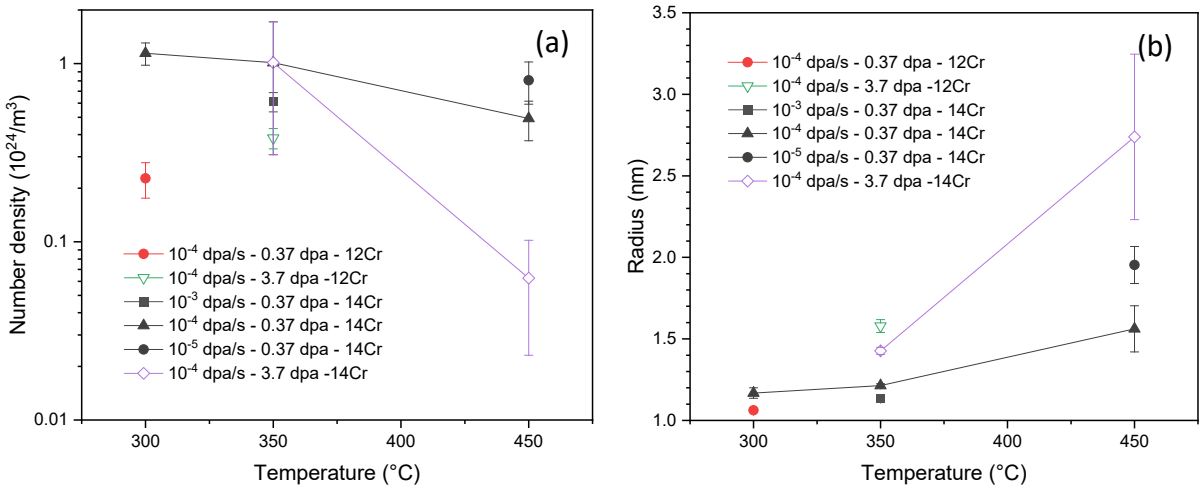

Figure 2. The evolution of the (a) radius and (b) number density of α' precipitates with irradiation dose rates, temperatures and doses in Fe-12Cr and Fe-14Cr.

The distributions of clusters after irradiation to 3.7 dpa at two temperatures are shown in Figure 3. At 350 °C, the number density of precipitates is high, and the sizes are very similar among each other. However, only a few very large precipitates are presented after ion irradiation at 450 °C to 3.7 dpa. The number density of clusters was largely decreased compared to that after irradiation to 0.37 dpa at the same temperature and dose rate, which indicates the coarsening of α' precipitates.

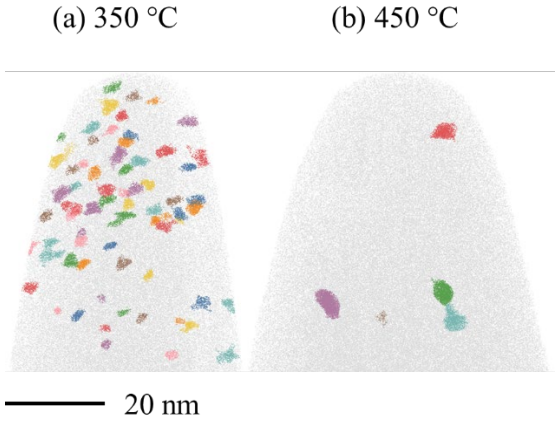

Figure 3. The APT reconstructions for Fe-14Cr irradiated at 10^{-4} dpa/s to 3.7 dpa at a) 350 °C and b) 450 °C. All particles indexed by different colors are α' precipitates.

α' precipitation in Fe-12Cr

Four specimens of ion irradiated Fe-12Cr have been characterized using APT. The irradiation conditions are shown above each APT reconstruction in Figure 4. α' precipitates were observed after irradiations at 300 or 350 °C and 10^{-4} dpa/s, and there are fewer precipitates at the lower temperature and dose. After irradiations at an equal or lower dose rate at 450 °C, no α' was detected, but a Cr-enriched carbide was observed. There are two possible explanations for the absence of α' at 450 °C: the Cr concentration of Fe-12Cr is too low to enter the two-phase region of the Fe-Cr phase diagram or the Cr supersaturation is so low that the driving force for phase separation is not strong enough to balance the ballistic dissolution of displacement cascades. Due to the uncertainty in the phase boundary between Fe solid solution and the two-phase region, further experimental studies to obtain a more precise solubility limit will be helpful.

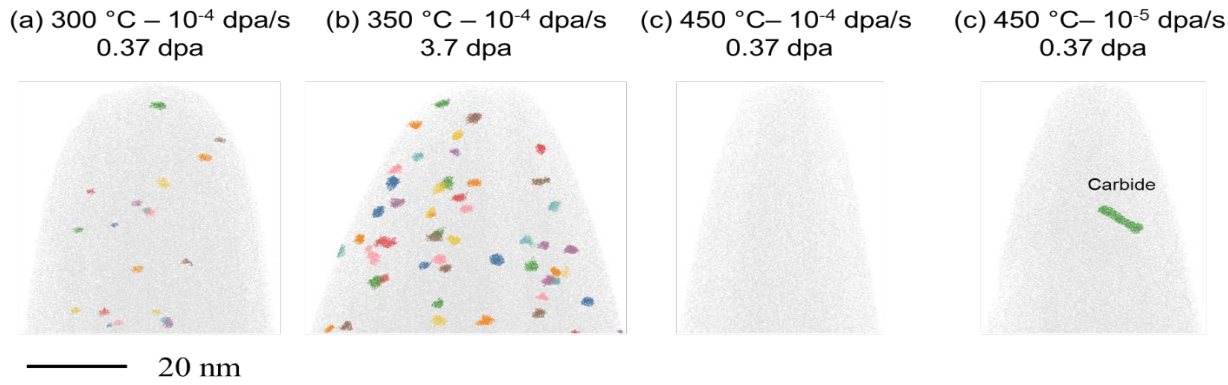

Figure 4. The APT reconstructions for Fe-12Cr after irradiation at 4 conditions. The irradiation temperature, dose rate and final dose are presented above each reconstruction. All the particles indexed by different colors are α' precipitates.

Conclusion

The formation and distribution of α' precipitates in Fe-12Cr and Fe-14Cr alloys are summarized in this report. α' precipitates were observed in Fe-14Cr at all investigated irradiation conditions, indicating that these irradiations were within the two-phase region of the Fe-Cr phase diagram. In Fe-12Cr, α' phase was identified after irradiation at 300 and 350 °C, but not at 450 °C. The presence or absence of α' at each irradiation dose rate and temperature are compared to the predicted phase boundaries available in the literature in Figure 5. The phase boundary from Bonny et al. was empirically fitted from neutron irradiation studies, which shows a large difference from the version calculated from the Calphad database. The data points are from the experimental observations of this work and the possible phase boundaries at 10^{-4} and 10^{-3} dpa/s are plotted with dashed lines. At 450 °C, the Calphad calculation gives a reasonable fit to the absence of α' in the Fe-12Cr specimens. At the two lower temperatures, large discrepancies from the equilibrium phase boundary were observed, within which the deviation is most pronounced at the higher dose rate. The deviation of α' precipitation behavior away from the thermal equilibrium state during ion irradiations is attributed to significant ballistic dissolution effects by the energetic displacement cascade, which dissolves the α' clusters more effectively at higher dose rates or lower temperatures relative to the precipitate renucleation and regrowth processes that increase with increasing temperature.

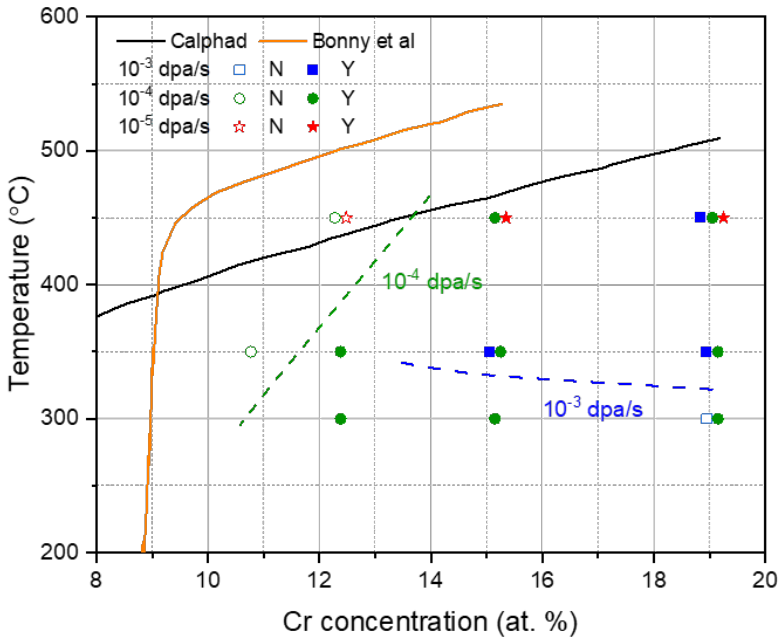

Figure 5. The comparison of experimentally observed presence/absence of α' from the current study to the phase boundary estimated with Calphad simulations [4] and empirically estimated from neutron irradiation studies [5].

Future Work

1. Proton irradiations are planned for the high purity FeCr alloys with a wide range of Cr concentrations to determine the phase boundary between α and α+α' at low PKA energy conditions (minimal ballistic dissolution).
2. APT characterization will be performed on a Fe-12Cr specimen irradiated at 350 °C, 10^{-3} dpa/s to 0.37 dpa.

3. The APT datasets from different depths of 2 selected ion irradiated samples will be analyzed and summarized.
4. TEM characterization of the dislocation loops at different depths will be performed, so their potential “sink strength” influence on radiation enhanced diffusion coefficient can be calculated.
5. APT characterization will be performed on the specimens irradiated with pre-existing α’ precipitates.

References

[1] Zhao Yajie et al. "Alpha-prime (α’) precipitate formation in ion irradiated Fe14Cr and Fe18Cr alloys” Fusion materials semiannual progress report for the period ending June. 30, 2019, DOE-ER-0313/66, p. 3.
[2] Zhao Yajie et al. "A study on the stability of Alpha-prime (α’) precipitates in high purity Fe-18Cr alloys after ion irradiation” Fusion materials semiannual progress report for the period ending Dec. 31, 2019, DOE/ER-0313/67, p. 33.
[3] Zhao Yajie et al. "The evolution of Alpha-prime (α’) precipitates in high purity Fe-(10-18)Cr alloys after thermal aging and ion irradiations” Fusion materials semiannual progress report for the period ending Dec. 31, 2020, DOE-ER-0313/69, p.12.
[4] J.-O. Andersson, B. Sundman, Thermodynamic properties of the Cr-Fe system, Calphad 11(1) (1987) 83-92.
[5] G. Bonny, D. Terentyev, L. Malerba, On the α–α′ miscibility gap of Fe–Cr alloys, Scr. Mater. 59(11) (2008) 1193-1196.

6.6 BUBBLE FORMATION IN HELIUM-IMPLANTED NANOSTRUCTURED FERRITIC ALLOYS AT ELEVATED TEMPERATURES—Yan-Ru Lin, Steven John Zinkle (University of Tennessee), Lizhen Tan, David T. Hoelzer (Oak Ridge National Laboratory)

Extended Abstract: Full manuscript published in Acta Materialia (2021) 117165
(https://doi.org/10.1016/j.actamat.2021.117165)

OBJECTIVE

This research aims to study the bubble size and density in two advanced nanostructured FM alloys (CNA3 and 14YWT) with different precipitate features and different initial dispersoid sink strengths. Coordinated ex-situ bulk material irradiation experiments with post-irradiation examinations and in-situ ion irradiation on transmission electron microscopy (TEM) samples were conducted to better understand the formation of He bubbles in nanostructured Fe-Cr alloys [Figure 1].

SUMMARY

Helium bubble formation was examined by scanning/transmission electron microscopy (S/TEM) in Fe-9/10Cr binary alloys and two dispersion strengthened nanostructured alloys (CNA3 and 14YWT containing 5-10 nm diameter carbide and oxide particles, respectively) after ex-situ and in-situ He implantation to ~10,000 appm at 500 to 900°C. The combination of high-resolution STEM images and electron energy loss spectroscopy (EELS) revealed that the Y-Ti-O nanoparticles in 14YWT were uniformly distributed and exhibited a one-to-one relationship for bubble attachment to the nanoclusters. In the in-situ experiment at 900°C, grain boundary cracking was severe in the Fe-10Cr model alloy, but not in the nanostructured alloys. From 500-900°C, the bubble size generally increased with increasing irradiation temperature, while the bubble density decreased with increasing temperature. At the same temperatures, the bubble size in the implanted materials was in the order of Fe-9/10Cr > CNA3 > 14YWT, while the bubble density showed the opposite order. The observed bubble number densities for the nanostructured alloys are comparable to the nanoparticle density, suggesting that the nanoparticles in both alloys were effective in trapping He. Our results indicate that very high He concentrations can be managed in nanostructured alloys by sequestering the helium into smaller bubbles (which leads to a lower volume swelling value) and to shield He from the grain boundaries. This can be attributed to the much higher sink strength associated with the nanoclusters or the He trapping ability between different types of nanoclusters.

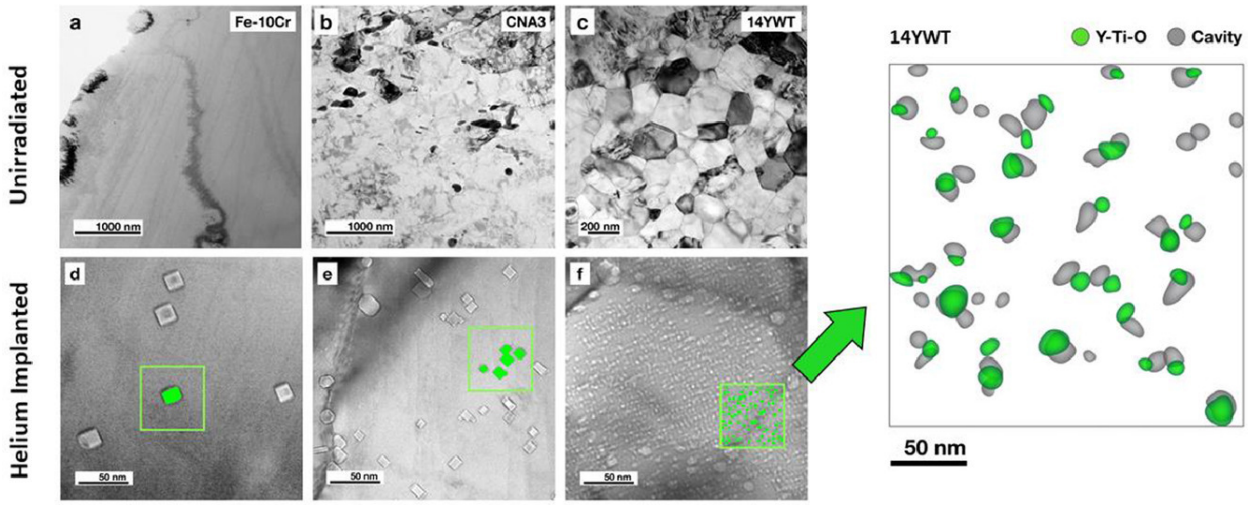

Figure 1. The TEM images of unirradiated and He implanted Fe-10Cr model alloy and nanostructured ferritic alloys.

Future Work

Small-angle neutron scattering experiments on the nanostructured ferritic alloys are in progress.

6.7 DOSE RATE EFFECTS ON DAMAGE ACCUMULATION AND VOID GROWTH IN SELF-ION IRRADIATED TUNGSTEN—Weilin Jiang, Yuanyuan Zhu (Pacific Northwest National Laboratory), Limin Zhang (Lanzhou University), Danny J. Edwards, Nicole R. Overman, Giridhar Nandipati, Wahyu Setyawan, Charles H. Henager Jr., Richard J. Kurtz (Pacific Northwest National Laboratory)

This extended abstract presents some of the major results in a paper recently published in the Journal of Nuclear Materials 550 (2021) 152905 [1]

OBJECTIVE

This study reports on the dose rate effects on damage accumulation and void growth in self-ion irradiated monocrystalline tungsten (mono-W) and polycrystalline tungsten (poly-W). Both mono-W and poly-W were irradiated at 900 K to 1 dpa at two dose rates, 10^{-4} and 10^{-3} dpa/s.

SUMMARY

In situ Rutherford backscattering spectrometry in channeling geometry (RBS/C) analysis was performed immediately after self-ion irradiation. The RBS/C spectra for a (111) oriented mono-W irradiated at 900 K to a peak dose of 1 dpa at the dose rates of 10^{-4} and 10^{-3} dpa/s are shown in Figure 1. The relative disorder at the depth (162 nm) of damage peak is estimated to be 0.19% and 1.1% at the dose rates of 10^{-4} and 10^{-3} dpa/s, respectively. Although the relative disorder is small in absolute values, there is a significant increase in the damage level, by ~6 times, at this low damage level because of the dose effects. In general, for the same dpa, a lower dose rate leads to a longer time for migrating point defects to interact. As a result, more point defects are either annihilated or clustered, leading to a decrease in the level of overall lattice disorder. In addition, the damage peak in W around the depth of 162 nm is completely absent, indicating that the self-interstitial atoms (SIAs) are extremely mobile in W at 900 K.

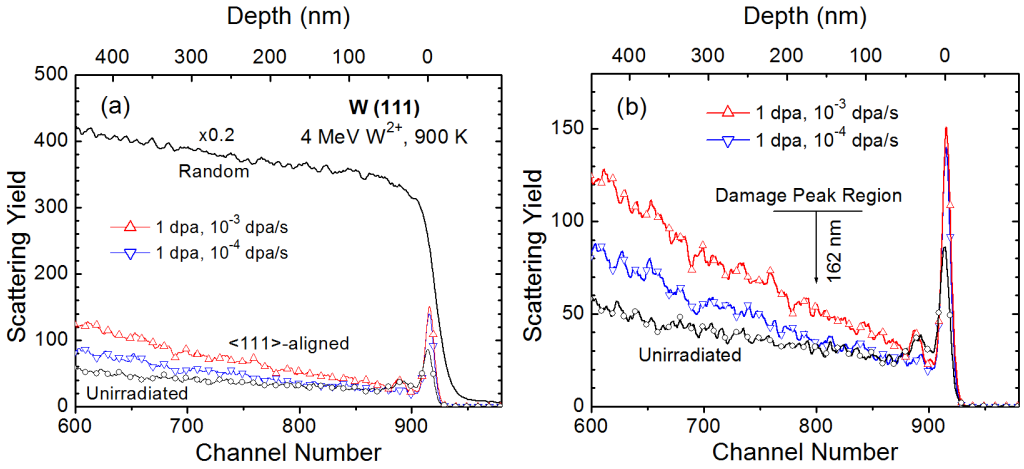

Figure 1. (a) 2 MeV He^+ RBS/C spectra along the ⟨111⟩ axis in mono-W irradiated with 4 MeV W^{2+} ions at 900 K to 1 dpa at 10^{-4} and 10^{-3} dpa/s. Also included are the ⟨111⟩-aligned and random spectra from an unirradiated area. (b) A zoomed view to better show the damage peak region.

Figures 2(a) and 2(b) shows bright-field (BF) images of mono-W irradiated at 900 K with self-ions to 1 dpa at 10^{-3} dpa/s. Under-focus and over-focus BF TEM conditions were applied to image voids in the specimen. Formation of the visible voids is attributed to self-ion irradiation at 900 K, where mono-vacancies are mobile in W. Based on counting and measuring the voids in the imaged area, a void diameter distribution is obtained, which is shown in Figure 2(c). The average diameter of the first dark Fresnel ring (D_{in}) is 2.1 nm and the actual void diameter D_0 is also 2.1 nm after defocus correction, as listed in Table 1. The void number density is deduced to be 2.0×10^{17} voids/cm^3, corresponding to an

average void spacing of ~17 nm. Table 1 summarizes the results of the void diameters in mono-W and poly-W under the irradiation conditions of this study. From Table 1, the void diameter ranges from 2.1 to 2.4 nm and the number density is on the order of 2×10^{17} voids/cm^3 in mono-W irradiated at 900 K to 1 dpa at 10^{-3} dpa/s. The average void diameter is ~60% larger at 10^{-4} than 10^{-3} dpa/s in mono-W. The void diameter (2.4 nm) at a large depth (820 nm) is the same as that (2.1 nm) at 400 nm within the experimental error (~0.2 nm). The void diameter in mono-W is ~40% larger than in poly-W under the same irradiation conditions. The grain boundary effect on the migrating defects is expected to play a role. For the same dpa, a lower dose rate allows more time for mono-vacancies to migrate and cluster between two consecutive damage cascades, leading to the formation of larger immobile vacancy clusters and dissociation of smaller ones at 900 K.

In addition, a simplified 3D model is proposed to provide criteria for irradiation conditions under which dose rate effects are expected to occur. The model also assesses the impact of free surface on dose rate effects. While model refinement is still needed, the 3D model has successfully predicted that occurrence of the dose rate effects under the irradiation conditions of this study.

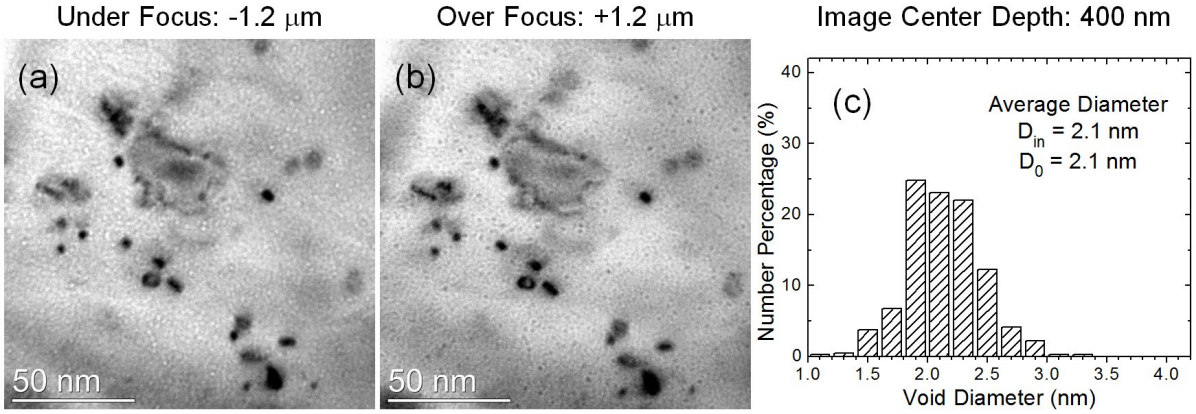

Figure 2. The BF TEM micrographs under (a) under-focus and (b) over-focus conditions showing a uniform distribution of voids in addition to black spots and dislocation loops around the depth of 400 nm in mono-W irradiated at 900 K with self-ions to 1 dpa at 10^{-3} dpa/s. (c) Void diameter distribution obtained from (a) and (b). D_{in}: the inner diameter of the first dark Fresnel ring; D_0: void diameter.

Table 1. Average inner diameter of the first dark Fresnel ring (D_{in}), average void diameter (D_0) and void number density in mono-W and poly-W irradiated with 4 MeV W^{2+} ions to 1 dpa at 900 K. Both D_{in} and D_0 have an uncertainty of ~0.2 nm

Specimen ID	Dose Rate (dpa/s)	Foil Thickness (nm)	Depth (nm)	Under-focus (μm)	Ring D_{in} (nm)	Correction Factor $f(D'_{in})$	Void D_0 (nm)	Number Density (voids/cm^3)
Mono-W-3a	10^{-3}	100	400	-1.2	2.1	0.98	2.1	2.0×10^{17}
Mono-W-3b	10^{-3}	120	820	-1.4	2.5	1.06	2.4	1.7×10^{17}
Mono-W-4	10^{-4}	---	300	-1.4	2.8	0.83	3.4	---
Poly-W-3	10^{-3}	---	150	-1.2	1.5	0.98	1.5	---
Poly-W-4a	10^{-4}	---	120	-1.0	1.9	0.90	2.1	---

References

[1] W. Jiang, Y. Zhu, L.M. Zhang, et al., Journal of Nuclear Materials, 550 (2021) 152905 10.1016/j.jnucmat.2021.152905.

6.8 MICROSTRUCTURES IN 87R DPT W IRRADIATED WITH Ni^+ AND He^+ IONS—Weilin Jiang, Dongsheng Li, Dalong Zhang, Bethany Matthews, Wahyu Setyawan (Pacific Northwest National Laboratory)

OBJECTIVE

This experimental research intends to emulate and characterize the microstructure of a hot-rolled (with 87% thickness reduction), ductile-phase toughened tungsten (87R DPT W) composite with the dose and He concentration comparable to those after the material is irradiated for five years in a conceptual fusion power plant.

SUMMARY

Following our previous characterizations of 87R DPT W irradiated sequentially with Ni^+ and He^+ ions, further effort has been devoted to the examination of the microstructures in two different regions of the same sample irradiated to 2.15×10^{16} Ni^+/cm^2 and 6.5×10^{15} He^+/cm^2 at 973 K, respectively. The STEM-EDS mapping data show that Ni^+ ion irradiation was done as intended. However, apparent voids in W or NiFeW and Ni precipitates in W are not observed in the Ni^+ ion irradiated region. In contrast, helium cavities are visible in both phases in the He^+ ion irradiated region. There is also a preferential cavity formation along the W/NiFeW interphase boundary. This behavior is like our previous report for the Ni^+ and He^+ ion co-irradiated region. The average cavity diameters are also comparable under the two irradiation conditions. One of the possible reasons for the similarity might be attributed to a significant recovery of point defects and/or formation of invisible defect clusters during Ni^+ ion irradiation at 973 K.

PROGRESS AND STATUS

Experimental Procedure

As previously reported in [1-3], the 87R DPT W (90W-7Ni-3Fe by weight) composite used in this study was determined to consist of 88 wt.% W and 12 wt.% NiFeW that contains 54.68 wt.% Ni, 22.57 wt.% Fe and 22.75 wt.% W. Sequential ion irradiation was performed with 1.2 MeV Ni^+ ions to a fluence of 2.15×10^{16} Ni^+/cm^2 and 90 keV He^+ ions to a fluence of 6.5×10^{15} He^+/cm^2 in different regions of an 87R DPT W composite at 973 K, creating 3 regions of irradiation with Ni^+ ions, He^+ ions, and Ni^+ and He^+ ions [3]. The corresponding dose of 31 dpa at the depth of 296 nm and He concentration of 0.39 at.% at 295 nm in the NiFeW phase within 87R DPT W is comparable to those after the material is irradiated for five years in a conceptual fusion power plant [2], assuming 50% retention of the implanted He atoms. Preliminary TEM study [3] of the Ni^+ and He^+ ion co-irradiated region shows that larger He cavities appear in NiFeW than W phase. There is a preferential distribution of cavities along the W/NiFeW interphase boundaries. To generate data for a better understanding of the vacancy and He processes in the composite during ion irradiation at 973 K, the defect microstructures in the two regions, irradiated individually with Ni^+ ions or He^+ ions, have been examined using both a Cs-aberration corrected JEOL ARM 200CF STEM at an operating voltage of 200 kV and a Thermofisher Tecnai F20 STEM also at 200 kV. Cavity diameters are determined based on under-focus images with assistance of the corresponding over-focus images. Statistical analysis of the cavity diameters and numbers was performed manually using the DT2000 General Image Analysis Software [4]. The inner diameter of the first dark Fresnel ring D_{in} is determined by a circle with diameter $D_{in} = \sqrt{4A_{in}/\pi}$, where A_{in} is the area of the circle. The actual cavity diameter D_0 was obtained from D_{in} using a correction factor from simulation [5]. Cavity volume was calculated based on an equivalent sphere with a diameter of D_0.

Results

Figure 1 shows the under- and over-focus images of 87R DPT W near an interphase boundary irradiated with 1.2 MeV Ni^+ to 2.15×10^{16} Ni^+/cm^2 at 973 K with the image center located at the depth of ~200 nm. Fresnel aperture diffraction theory suggests that small cavity-type defects should show central bright and

dark spots with under- and over-focus imaging, respectively. These features are not apparent in the Ni^+ ion irradiated W region shown in Figure 1, in a sharp contrast to a high density of small voids observed in polycrystalline W irradiated with self-ions to only 1 dpa at 900 K [4]. Possible reasons include a significant recovery of point defects produced in W during Ni^+ ion irradiation at 973 K. It is known that lighter ion irradiation produces a lower density of point defects within a single damage cascade, leading to a lower probability for formation of larger defect complexes during the defect relaxation process. The small defect clusters (~1 nm in size or smaller), if any, could not be visualized by TEM in this study. Also, from Figure 1, there are bright and dark lines along the boundary in the under-focus and over-focus images, respectively, as encapsulated in yellow. It is premature to claim its identity at this time, and further studies are needed to determine if the feature is associated with a misfit dislocation, a vacancy platelet that might form because of vacancy diffusion and clustering at the boundary, or simply an artifact. Figure 1 also shows dark spots in the under-focus image and the corresponding bright spots in the over-focus image in the NiFeW phase, as circled in red. These features, if not artifacts, show a reverse Fresnel diffraction effect, which are not related to cavity types of defects. Their identities are currently unknown and further investigations are needed for clarification.

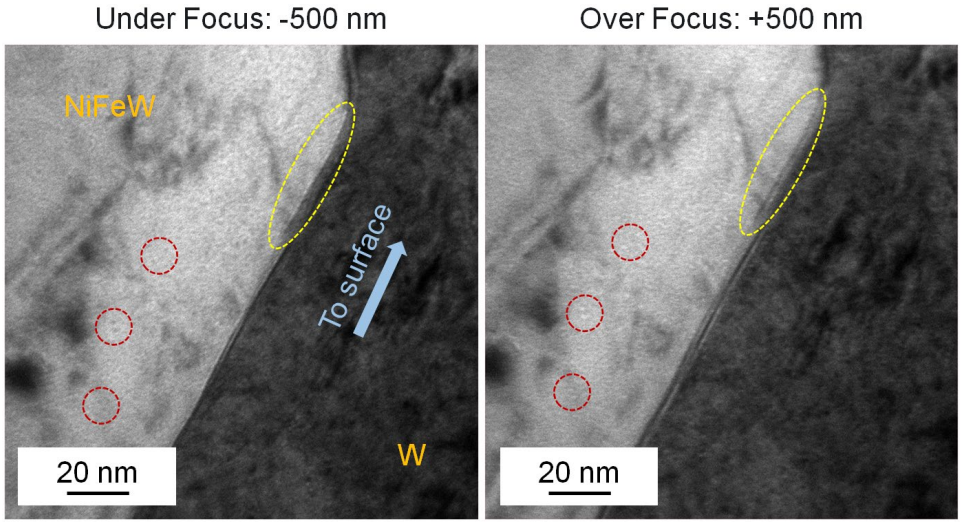

Figure 1. Microstructure of 87R DPT W irradiated with 1.2 MeV Ni^+ to 2.15×10^{16} Ni^+/cm^2 at 973 K, with the image center at the depth of ~200 nm.

In addition, the microstructure and composition in W within the Ni^+ ion irradiated 87R DPT W were carefully characterized using STEM and STEM-EDS mapping. The results are shown in Figure 2. The Ni map in Figure 2 does not provide any evidence for Ni particle precipitation in W under the irradiation conditions, where SRIM13 simulation predicts a maximum Ni concentration of 0.98 at.% in W at the depth of 294 nm [2].

To ensure Ni^+ ion irradiation was done as intended, STEM-EDS mapping with inclusion of an interphase boundary was performed in several locations for an extended time to improve data statistics. Figure 3 (left panel) shows the probe area with vertical and horizontal line scans indicated by yellow arrows. The bright contrast with a darker band (thicker region) on the left is the W phase. As noted above, the implanted Ni atomic concentration in W is predicted to peak to a concentration of 0.98 at.% at 294 nm. From the upper-right plot in Figure 3, the vertical line scan from the surface to a deeper region (~1.2 μm in depth) at a location far away from the W/NiFeW boundary shows that there is a Ni concentration peak (~1 at.%) in W at the depth of ~300 nm, which is consistent with SRIM simulation. The implanted Ni atoms tend to diffuse inward and outward, and some Ni atoms appear to accumulate at the surface. From lower-right plot in Figure 3, Ni diffusion from NiFeW to W extends to only a distance of ~400 nm from the interphase boundary, as shown by the horizontal line scans at the middle and bottom locations that show consistent

results as expected because both locations are well beyond the Ni^+ ion projected range. The horizontal line scan in the top location that includes the implanted Ni region shows a statistically higher Ni concentration at the distance larger than 500 nm from the boundary, confirming the presence of the implanted Ni atoms in the near-surface region.

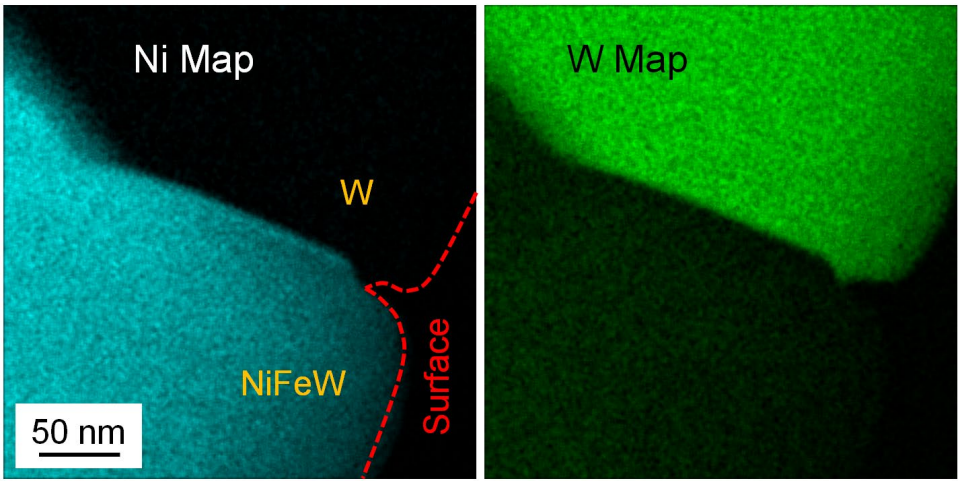

Figure 2. The STEM-EDS mapping of Ni and W in 87R DPT W irradiated sequentially to 2.15×10^{16} Ni^+/cm^2 at 973 K.

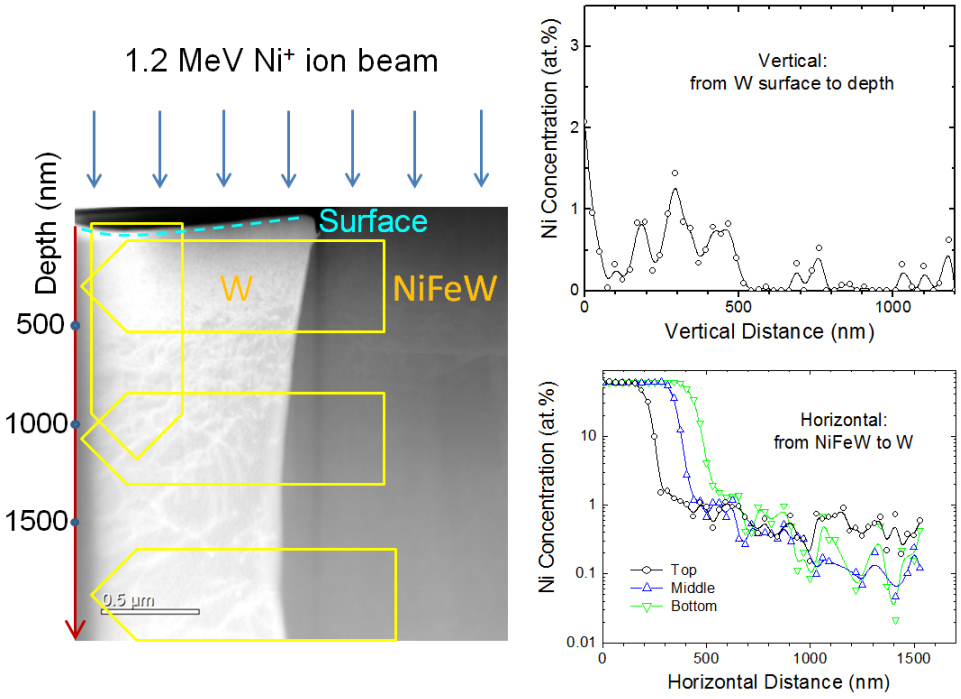

Figure 3. The STEM-EDS line scans for the depth profile of Ni concentration in W within 87R DPT W irradiated with 1.2 MeV Ni^+ to 2.15×10^{16} Ni^+/cm^2 at 973 K.

In contrast, He cavities are observed in W within 87R DPT W irradiated with He^+ ions, as shown in the left panel of Figure 4 where a spatial distribution of the cavities in the near the surface region is imaged with conventional TEM under a defocused (-500 nm) condition. The observed cavity diameter was corrected from simulation [5]. The corrected diameter and volume distributions of the He cavities are shown in the right panel of Figure 4, where the average diameter of 1.86 nm and the average volume (proportional to

the number of He atoms inside it) of 3.49 nm^3 are indicated. The dependence of the cavity diameter and number density on depth is weak, probably due to efficient diffusion of He atoms and mono-vacancies in W during irradiation at 973 K. Figure 5 shows a microstructure at the image center depth of ~160 nm in W within 87R DPT W irradiated sequentially with Ni^+ and He^+ ions. There is a similarity of the spatial distribution to the case of He^+ ion irradiation only (Figure 4). The average cavity diameter (1.62 nm) is consistent with each other within the analytical error (±0.2 nm). Again, the similarity might be attributed in part to a significant recovery of point defects produced during Ni^+ ion irradiation in W within 87R DPT W at 973 K. However, formation of small defect clusters that are invisible to TEM cannot be excluded.

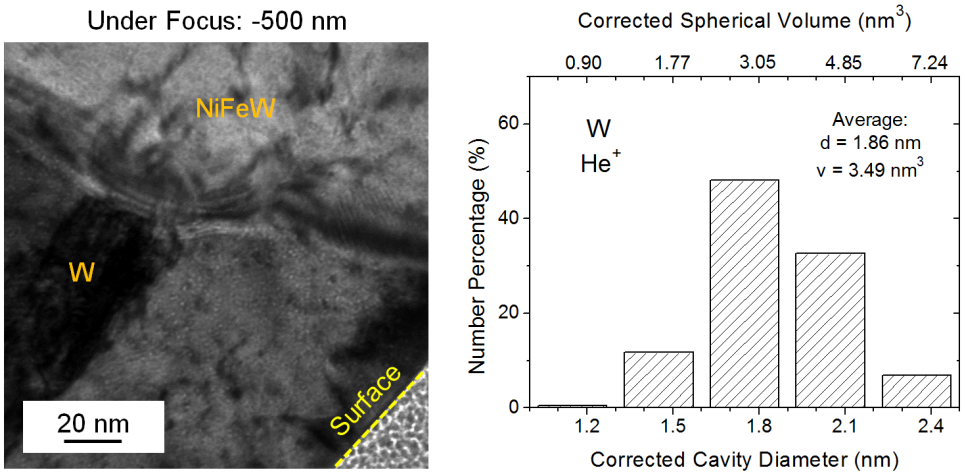

Figure 4. Cavity distribution in W within 87R DPT W irradiated with 90 keV He^+ to 6.5×10^{15} He^+/cm^2 at 973 K.

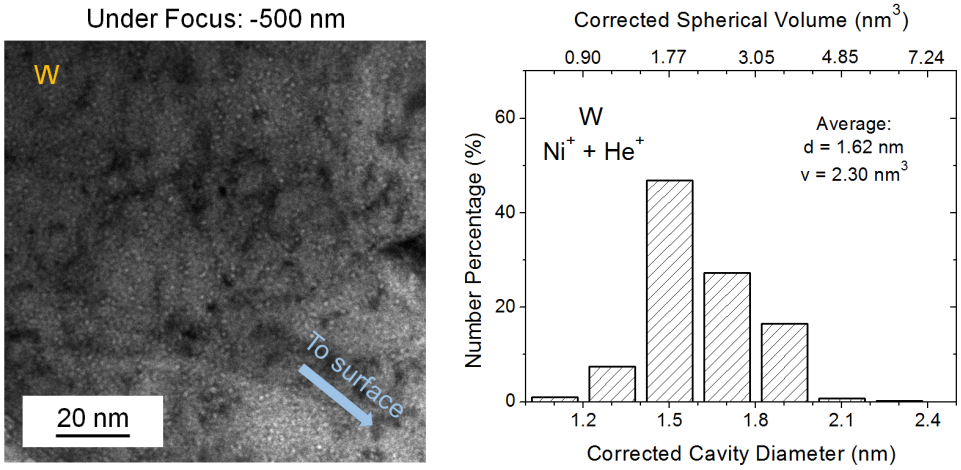

Figure 5. Cavity distribution in W within 87R DPT W irradiated sequentially with 1.2 MeV Ni^+ to 2.15×10^{16} Ni^+/cm^2 at 973 K and 90 keV He^+ to 6.5×10^{15} He^+/cm^2 at 973 K, with the image center at the depth of ~160 nm.

Figure 6 shows the microstructure of NiFeW within He^+ ion irradiated 87R DPT W. Apparently, the cavities in NiFeW are much larger than in W. The average cavity diameter is 8.18 nm in NiFeW as compared to 1.86 nm in W (Figure 4). There is a preferential distribution of cavities along the interphase boundary. These cavities have an average diameter of 5 nm with an average volume of 74.48 nm^3. The diameter is between the average cavity diameters in NiFeW and W. Similar cavity behavior is observed in NiFeW irradiated sequentially with Ni^+ and He^+ ions at 973 K, as shown in Figure 7, where the average cavity diameter and volume are 7.54 nm and 244.35 nm^3, respectively.

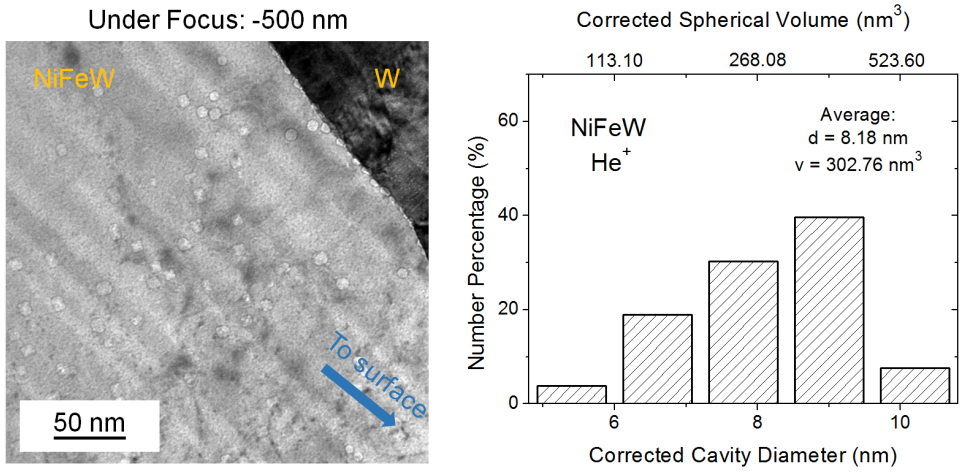

Figure 6. Cavity distribution in NiFeW within 87R DPT W irradiated with 90 keV He^+ to 6.5×10^{15} He^+/cm^2 at 973 K, with the image center at the depth of ~235 nm.

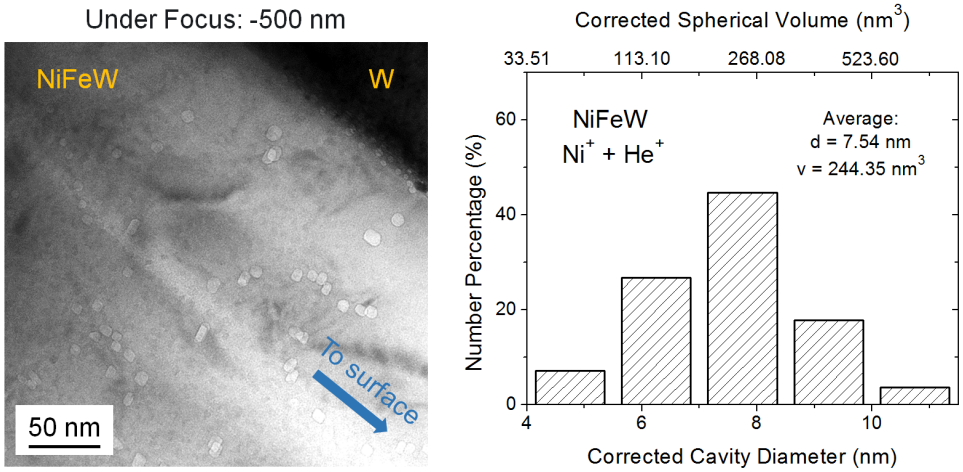

Figure 7. Cavity distribution in NiFeW within 87R DPT W irradiated sequentially with 1.2 MeV Ni^+ to 2.15×10^{16} Ni^+/cm^2 and 90 keV He^+ to 6.5×10^{15} He^+/cm^2 at 973 K, with the image center at the depth of ~290 nm.

Future Work

Detailed analysis of the data obtained from 87R DPT W irradiated with Ni^+ and He^+ ions at 973 K is currently being performed. It is our plan to prepare a manuscript for publication of the major findings from this and previous studies [1-3]. As reported previously [3] and in this study, a preferential distribution of He cavities is observed along the W/NiFeW interphase boundary in 87R DPT W irradiated with He^+ ions at 973 K. Obviously, this behavior is expected to weaken the interphase boundary cohesion. Further investigation of the cavity behavior dependence on irradiation temperature is warranted for a better understanding of the mechanisms responsible for the preferential formation of He cavities along the interphase boundary. We have started to investigate the He cavity behavior in 87R DPT W as a function of irradiation temperature. Similar sequential irradiation of 87R DPT W with Ni^+ and He^+ ions at room temperature and 1273 K has been performed in collaboration with University of Houston. The irradiated samples will be characterized for a comparison study. Progress reports are expected from the ongoing efforts in FY22.

Acknowledgements

This research was supported by the Office of Fusion Energy Sciences, U.S. Department of Energy and performed at PNNL under Contract DE-AC05-76RL01830. We are grateful to Charles Henager at PNNL for providing the 87R DPT W sample for this study, to Xuemei Wang and Zhihan Hu at Texas A&M University for ion irradiation at 973 K, to Di Chen at University of Houston for ion irradiation at room temperature and 1273 K, and to Zhiqiang Wang and Limin Zhang at Lanzhou University for analysis of cavity diameter distributions.

References

[1] W. Jiang, N. Overman, T. Varga, W. Setyawan, C.H. Henager Jr., Fusion Materials Semiannual Progress Report for Period Ending December 31, 2019, DOE/ER-0313/67, U.S. Department of Energy, 86.
[2] W. Jiang, W. Setyawan, K. Kruska, L. Kovarik, D. Zhang, Fusion Materials Semiannual Progress Report for Period Ending June 30, 2020, DOE/ER-0313/68, U.S. Department of Energy, 96.
[3] W. Jiang, D. Zhang, A. Schemer-Kohrn, B. Matthews, W. Setyawan, Fusion Materials Semiannual Progress Report for Period Ending December 31, 2020, DOE/ER-0313/69, U.S. Department of Energy, 112.
[4] W. Jiang, Y.Y. Zhu, L.M. Zhang, D.J. Edwards, N.R. Overman, G. Nandipati, W. Setyawan, C.H. Henager Jr., R.J. Kurtz, J. Nucl. Mater., 550 (2021) 152905.
[5] B. Yao, D.E. Edwards, R.J. Kurtz, G.R. Odette, T. Yamamoto, J. Electron Microsc., 61 (2012) 393.

7. PLASMA-MATERIAL INTERACTIONS

7.1 FLUX EFFECT ON HELIUM ACCUMULATION IN W{100} SUB-SURFACE—Giridhar Nandipati, Kenneth J. Roche, Richard J. Kurtz, Wahyu Setyawan (Pacific Northwest National Laboratory), Karl D. Hammond (University of Missouri), Dimitrios Maroudas (University of Massachusetts), Brian D. Wirth (University of Tennessee)

This is an extended abstract of a manuscript titled "Effect of Helium Flux on Near-Surface Helium Accumulation in Plasma-Exposed Tungsten" submitted to Journal of Physics Condensed Matter

OBJECTIVE

Tungsten is a candidate material for plasma-facing components (PFCs) in ITER because of its excellent thermomechanical properties and its ability to endure a harsh fusion reactor environment [1–3]. The PFCs are subjected to temperatures exceeding 800 K and a low-energy (≤ 100 eV), high-flux (on the order of 10^{24} He/m^{2}s) He$^+$ ion irradiation, resulting in subsurface He accumulation. To understand the accumulation as a function of flux, object kinetic Monte Carlo (OKMC) simulations of 100 eV He implantation of W surfaces were performed using KSOME [4-6]. These simulations were conducted at 933 K for fluxes ranging from 10^{22} to 4×10^{25} He m^{-2} s^{-1}. In the near-surface region, helium clusters interact elastically with the free surface. The interaction is attractive and stronger as the cluster approaches the surface, thereby lowering the activation energy barrier for cluster migration toward the surface. Furthermore, the average size of a cluster capable of displacing a W atom from its lattice (trap-mutation process) depends on the depth and decreases toward the surface. The reduction of the trap mutation barrier near the surface results in the kick-out of multiple tungsten atoms, which in some instances is followed by partial dissociation of the helium cluster itself. The above physical kinetic processes are considered in the OKMC simulations, and the associated kinetics and energetics are obtained from molecular dynamics simulations [7, 8].

SUMMARY

The OKMC simulations show that in pure (pristine) and intragranular-defect free tungsten, He accumulation depends on the flux and the diffusion and trap mutation characteristics of He clusters. With all other conditions remaining the same, the flux has a large effect on the fraction of retained helium and its depth profile. In general, the diffusion of He clusters toward the surface tends to lower the subsurface-He retention, whereas trap mutation reactions enhance it. With decreasing flux, helium retention decreases, and the minimum appearing in the retention curve as a function of fluence shifts to higher fluences (Figure 1).

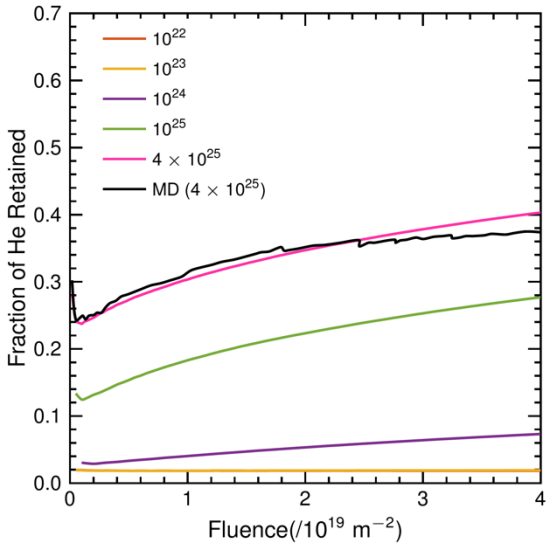

Figure 1. Fraction of retained He as a function of fluence at different fluxes (in He/m^{2}s). MD simulation data are from Ref. [9, 10].

At the lowest flux studied (10^{22} He/m^2 s), almost all the retained helium diffused into the bulk, resulting in no helium accumulation in the near-surface region. Decreasing flux reduces the average density of mobile He and effectively increases diffusion time. Therefore, He atoms implanted closer to the surface escape, while those implanted farther diffuse deeper. Accordingly, with decreasing flux, the helium accumulation shifts to deeper regions (Figure 2), and the fraction of retained helium diffusing into the bulk increases. Also, a lower density and an increased diffusion time result in a larger fraction of mobile helium being captured by previously formed immobile helium clusters or bubbles, thus decreasing the number density of immobile clusters while increasing their size (Figures 2, 3, 4).

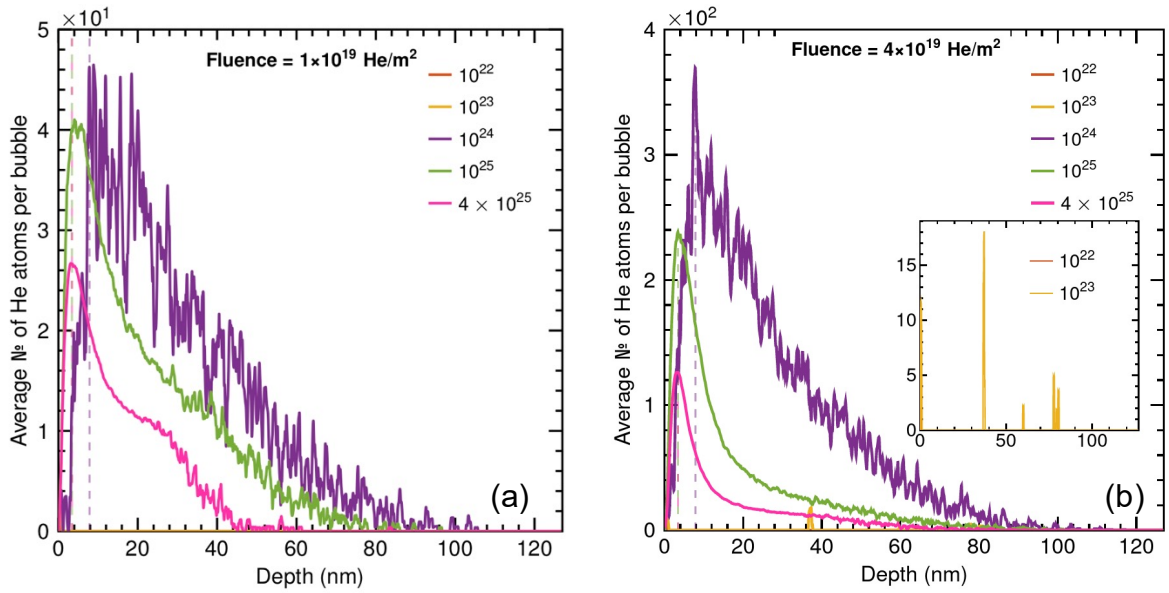

Figure 2. Depth profiles of the average number of helium atoms per bubble at (a) $\Phi = 1 \times 10^{19}$ He/m^2 and (b) $\Phi = 4 \times 10^{19}$ He/m^2, for $\Gamma = 10^{22} - 10^{25}$ and 4×10^{25} He/m^{2}s. In both (a) and (b), vertical dashed lines mark the depth of the profile peaks. The inset in (b) is a magnified view, showing He accumulation for 10^{22} and 10^{23} He/m^{2}s. Depth profiles are calculated with a bin size of $a_0/2$ (1.585 Å).

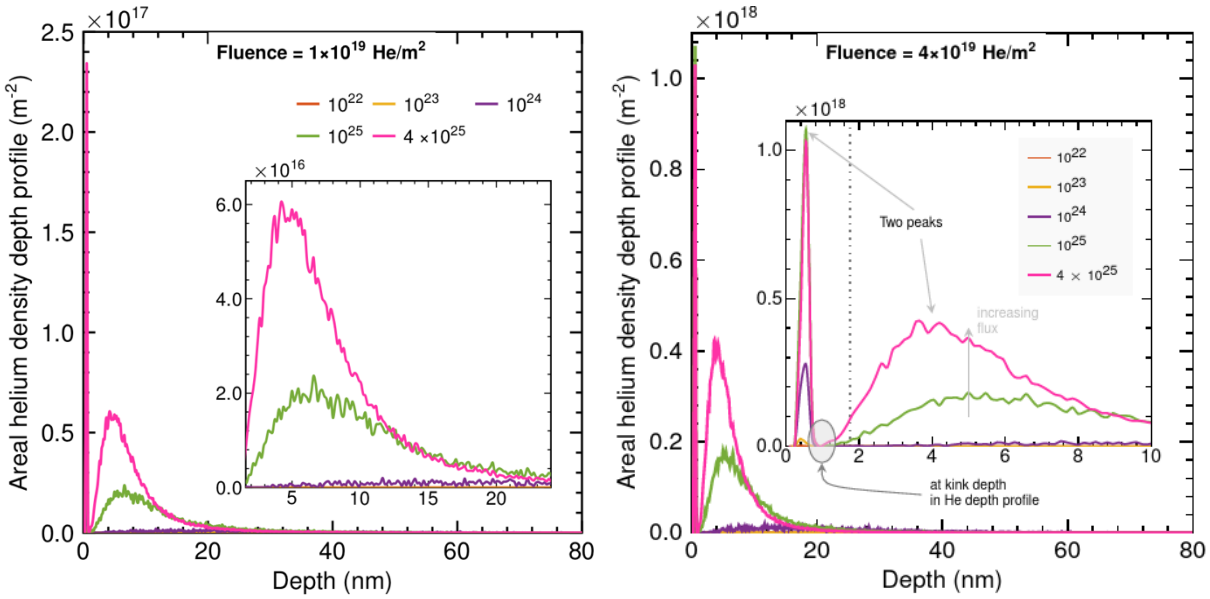

Figure 3. The depth profiles of the areal density of helium at flux values of $\Gamma = 10^{22} - 10^{25}$ and 4×10^{25} He/m²s, for (a) $\Phi = 10^{19}$ He/m² and (b) $\Phi = 4 \times 10^{19}$ He/m². Depth profiles are calculated with a bin size of $a_0/2$ (1.585 Å). In (a) and (b), the insets show the magnified view of the peaks.

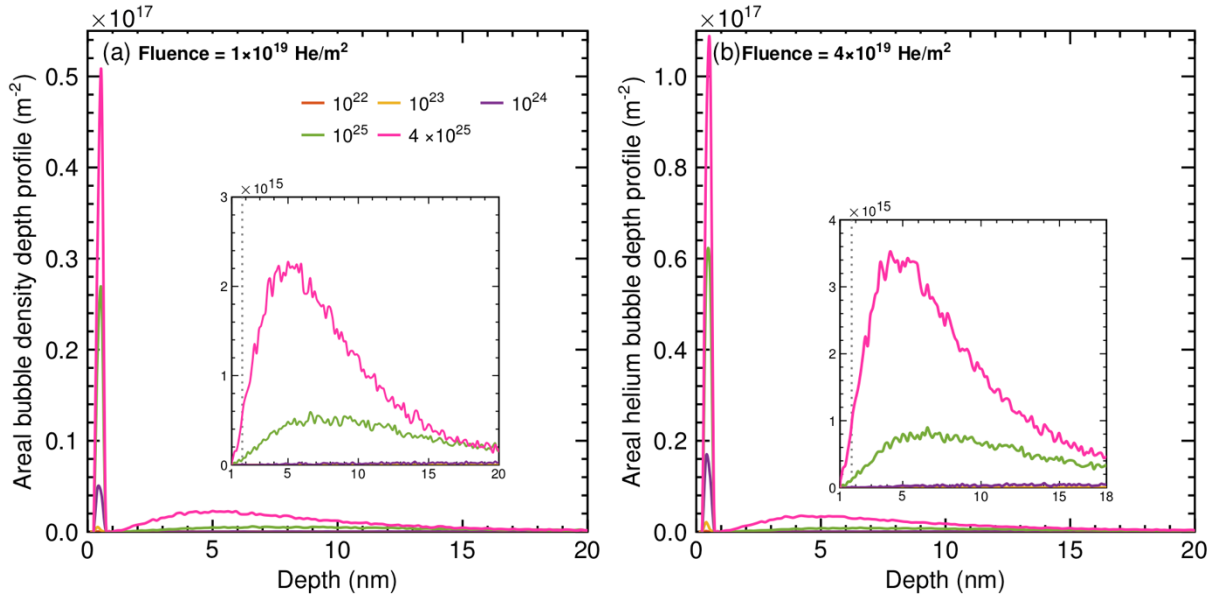

Figure 4. Depth profiles of the areal density of bubbles at flux values of $\Gamma = 10^{22} - 10^{25}$ and 4×10^{25} He/m²s, for (a) $\Phi = 10^{19}$ He/m² and (b) $\Phi = 4 \times 10^{19}$ He/m². Depth profiles are calculated with a bin size of $a_0/2$ (1.585 Å). In both cases, the insets show a magnified view of the corresponding second peaks.

With increasing fluence, helium retention first decreases (at low fluence) and then starts to increase after reaching a minimum (Figure 1), suggesting that a critical density of immobile helium clusters is required to retain a higher fraction of the implanted helium than it would be lost to the free surface. Also, with increasing fluence, newly implanted helium atoms are increasingly more likely to be captured by previously formed immobile clusters or bubbles in a region deeper than the implantation region. Thereby, they effectively

prevent implanted atoms from diffusing into the bulk and impeding mobile helium diffusion into the bulk. Accordingly, the cumulative depth profiles of retained helium tend to shift towards the free surface (Figure 5). The peak values of the average bubble size depth profiles increase linearly; however, the depths at which these peaks appear remain unchanged. This behavior suggests that the depth distribution of the bubbles does not change appreciably and that the bubbles grow only in size.

Future Work

Data obtained from KMC simulations at a flux of 4 x 10^{25} He/m^{2}s allow comparisons of the KMC predictions with results from MD simulations at the same flux and temperature (933 K). Under these conditions, the KMC-predicted He retention as a function of fluence up to about 1.8 x 10^{19} He/m^2 is in good agreement with MD. At higher fluences, the KMC results overestimate the retention, which is likely attributed to bubble-bursting events currently not included in the KMC simulations. Future research will implement bubble bursting events. In addition, interactions among helium clusters/bubbles will be considered to extend the simulations to fluences beyond the dilute limit. The current study serves as a reference study to elucidate the effects of flux on helium accumulation and distribution in the dilute limit of helium content in the PFC material, at fluences < 1.8x10^{19} He/m^2.

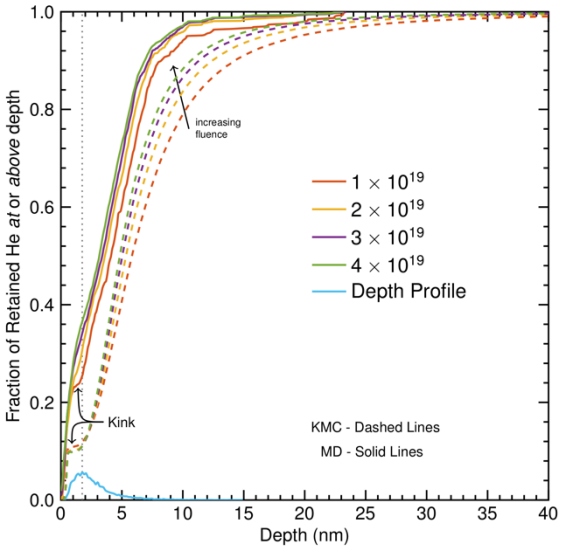

Figure 5. Cumulative depth profiles of the retained helium for a flux of 4×10^{25} He/m^{2}s and at various fluences over the range $(1-4) \times 10^{19}$ He/m^2 from the MD (solid curves) and KMC (dashed curves) simulations. The implantation depth profile (I) is superimposed for convenience, and the vertical dotted line at 1.75 nm corresponds to the peak in the implantation depth profile.

Acknowledgments

The work described in this article was carried out at Pacific Northwest National Laboratory, which is operated by Battelle for the United States Department of Energy (US DOE) under the contract DE-AC05-76RL01830. The U.S. Department of Energy, Office of Fusion Energy Sciences (FES), and Office of Advanced Scientific Computing Research (ASCR) supported this study through the SciDAC-4 program on Plasma-Surface Interactions [11].

References

[1] R.A. Pitts, S. Carpentier, F. Escourbiac, T. Hirai, V. Komarov, S. Lisgo, A.S. Kukushkin, A. Loarte, et. al., *J. Nucl. Mater.* 438 (2018) S48–S56.

[2] M. Merola, G. Vieider, M. Bet, L. Vastra, I.B. Briottet, P. Chappuis, K. Cheyne, et al., *Fusion Eng. Des.* 56 (2001) 173–178.
[3] V. Philipps, *J. Nucl. Mater.* 415 (2011) S2–S9.
[4] G. Nandipati, W. Setyawan, H. L. Heinisch, K. J. Roche, R. J. Kurtz, B. D. Wirth, *J. Nucl. Mater.* **462** (2015) 338.
[5] G. Nandipati, W. Setyawan, H. L. Heinisch, K. J. Roche, R. J. Kurtz, B. D. Wirth, *Semiannual Progress Report* DOE/ER-0313/54 (2013) 179.
[6] G. Nandipati, Kinetic Simulations of Microstructural Evolution, [Scientific Software, Ver.: 1.0] (Aug 26, 2020).
[7] L. Hu, K. D. Hammond, B. D. Wirth, and D. Maroudas, *J. Applied Physics* **118**, 163301 (2015).
[8] L. Hu, K.D. Hammond, B.D. Wirth, D. Maroudas, *Surface Science* **626** (2014) 21–25.
[9] K.D. Hammond, I.V. Naeger, W. Widanagamaachchi, L.T. Lo, D. Maroudas, B.D. Wirth, *Nucl. Fusion* **59** (2019) 066035.
[10] K.D. Hammond, S. Blondel, L. Hu, D. Maroudas, B.D. Wirth, *Acta Mater.* **144** (2018) 561.
[11] Plasma Surface Interactions: Predicting the Performance and Impact of Dynamic PFC Surfaces (https://tinyurl.com/ru8mwqt).

8. CORROSION AND COMPATIBILITY IN FUSION SYSTEMS

8.1 LIQUID METAL COMPATIBILITY OF PRE-OXIDIZED FeCrAl IN FLOWING Sn—B. A. Pint, J. Jun, M. Romedenne, Y.-F. Su (Oak Ridge National Laboratory)

OBJECTIVE

The goal of this research was to investigate the compatibility of liquid Sn with FeCrAl alloys and the viability of a thermally grown alumina scale to prevent dissolution and mass transfer. A thermal convection loop (TCL) was fabricated from a commercial FeCrAlMo alloy and pre-oxidized specimens of this alloy and two ODS FeCrAl alloys were exposed in the flow path with a peak temperature of 400°C.

SUMMARY

This first TCL experiment with liquid Sn completed 1000 h with a peak temperature of 400°C and initial characterization is reported from the FeCrAlMo (Kanthal alloy APMT) and ODS FeCrAl specimens exposed in APMT tubing. The mass losses in the hot leg were relatively high suggesting that compatibility remains a challenge with Sn in this temperature range. Characterization is still in progress.

PROGRESS AND STATUS

Introduction

An assessment of candidate liquid metals for plasma-facing components down selected Sn as an attractive candidate for further study because of its low vapor pressure [1]. However, Sn is very corrosive to most structural alloys [2]. To improve liquid metal compatibility, one strategy that has been used with Pb-17at.%Li is to form a stable, adherent surface oxide such as α-Al_2O_3 on FeCrAl alloys or using an Al-rich coating on steels [3-8] to prevent direct contact between the structural alloy and the liquid. This strategy has shown very promising results for Pb-Li and static testing was initiated in Sn. Initial screening used Sn in Mo capsules for 1000 h at 400°C [8]. As expected, a large mass loss (368 mg/cm^2) was observed for a reduced activation ferritic-martensitic (RAFM) F82H steel specimen. In contrast, the mass loss was much lower for APMT (composition in Table 1) specimens with almost no mass change for the specimen pre-oxidized for 2h at 1000°C to form an external alumina scale [7,8]. A similar small mass change was observed for pre-oxidized APMT specimens after capsule testing at 500°C for 1000 and 2000 h. To complete the Sn compatibility assessment, a thermal convection loop (TCL) made of APMT has been fabricated and coupon and tensile specimens of APMT and two ODS Fe-(10-12)Cr-6Al+Zr alloys were included in the hot and cold legs of the TCL in a ~55°C temperature gradient with a peak temperature of 400°C. The TCL experiment was completed, and initial characterization is presented as part of Task 3 in the Japan-US FRONTIER program.

Table 1. Alloy compositions measured using inductively coupled plasma and combustion analyses

Alloy	Fe	Cr	Al	Ni	Si	C	Other
APMT	69.0	21.6	4.9	0.12	0.53	0.03	2.8Mo,0.1Mn,0.2Hf,0.1Y,0.1Zr
APMT tube*	70.0	21.4	4.9		0.34	0.04	3.1Mo, 0.2Mn, 0.02Cu
ODS FeCrAl†	83.6	9.8	6.0			0.06	0.22Y,0.27Zr,0.10O,0.04N
ODS FeCrAl	80.8	11.6	6.2	0.03	0.02	0.03	0.39Zr, 0.38Y, 0.49Ti, 0.02Mn

* reported by manufacturer [6] † heat 4H795C

Experimental Procedure

This TCL experiment followed similar procedures as detailed previously [6-10]. Velocity measurements from hot spot experiments [6] varied between 0.9-1.1 cm/s during the experiment. Chains of 20 specimens were exposed in the hot leg (HL) and cold leg (CL) of the TCL for 1000 h with a peak hot leg temperature of 400°C. Coupon specimens were 15 x 25 x 2 mm and the tensile specimens were 25 mm long SS-3 type and alternated between APMT and two different ODS alloys [11,12] with low-Cr to avoid issues with α' embrittlement. Chemical compositions of the three alloys and APMT tubing are given in Table 1. All the specimens were pre-oxidized for 2 h at 1000°C in laboratory air [7,8]. The APMT loop was pre-oxidized for 8 h at 1050°C, as part of the standard heat treatment [6]. After the exposure, the Sn was dumped into a stainless-steel tank. However, significant liquid remained in the loop and the TCL had to be cut open to remove the specimens. Residual Sn was removed by dipping specimens in liquid Li at ~250°C in an Ar-filled glovebox. There was some concern that the Li would remove the alumina scale [13], therefore, a few specimens were characterized before Li cleaning. Residual Li was removed using ethanol. Specimens were weighed before exposure and after cleaning using a Mettler Toledo X205 balance with an accuracy of ±0.04 mg. X-ray diffraction could not detect a surface oxide on these specimens. Selected specimens are being metallographically sectioned for characterization of the reaction products and depth of attack. Focused ion beam (FIB) sections were taken from the two specimens from the top of the HL and CL using a Hitachi model NB5000 FIB to make scanning transmission electron microscopy (STEM) specimens. These were examined using an FEI Talos STEM operating at 200 kV and equipped with an extreme field emission gun (X-FEG) electron source and Super-X EDS (energy dispersive spectroscopy) system with 4 silicon drift detectors (SDD) for chemical analysis.

Results

Figure 1 shows a typical image of three coupon specimens after removal from the experiment with some Sn remaining on the specimens. After cleaning in Li, the specimen mass change of most of the specimens from the experiment is shown in Figure 2. Two specimens were not recovered, and two coupon specimens are still in line for FIB sectioning and await cleaning. Large mass losses were measured in the hot leg with the largest mass losses were measured for ODS FeCrAl specimens. In the cold leg, no mass gains were measured, which suggests there was no mass transfer, perhaps because the solubility of Fe is very high in Sn. However, the mass losses were much lower. The median mass loss was 0.4 mg/cm^2 with some of the largest losses for the ODS specimens with only 10%Cr. Figures 3 and 4 show example images of coupon specimens after cleaning in Li. Particularly the HL specimens appear deeply pitted. In most cases, the surfaces appear to be free of oxide and somewhat different than before cleaning, e.g., Figure 1. There is concern that the oxide may have been removed during the Li cleaning as Li_2O is more stable than Al_2O_3 [13].

Figure 1 also shows that residual Sn did not uniformly cover the specimens. In the capsule experiments, the pre-oxidized APMT specimens had no Sn on the surface after exposure suggesting that wetting did not

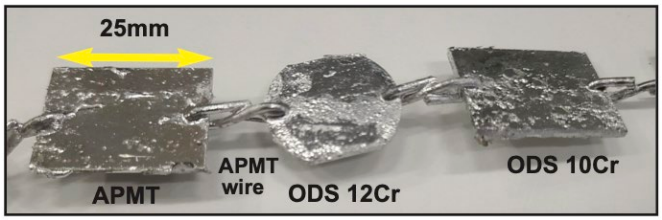

Figure 1. Three coupon specimens from the hot leg after removal from the loop with residual Sn.

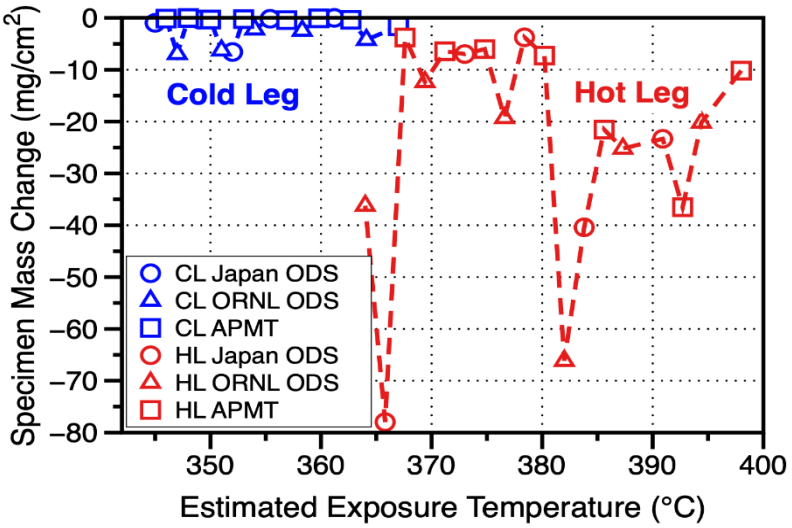

Figure 2. Specimen mass change of TCL specimens as a function of estimated temperature in the hot leg (HL) and cold leg (CL) of the Sn TCL experiment.

occur. The non-uniformly covered loop coupons suggested that the pre-formed alumina layer was not retained in all locations. To test this hypothesis, two specimens from the top of the HL and CL were taken for FIB sectioning before cleaning. Figures 5 and 6 show STEM/EDS analysis of the APMT specimen from

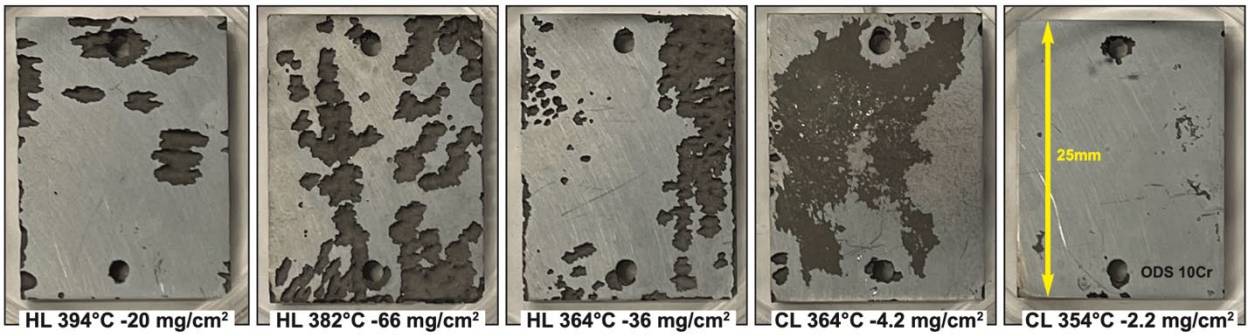

Figure 3. Images of five ODS 10Cr specimens after exposure and cleaning. The estimated temperature in the hot leg (HL) and cold leg (CL) and the mass change is shown for each.

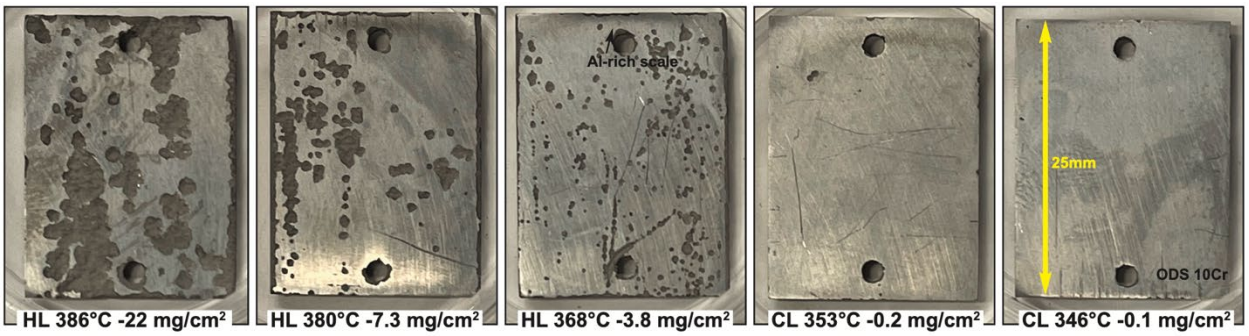

Figure 4. Images of five APMT specimens after exposure and cleaning. The estimated temperature in the hot leg (HL) and cold leg (CL) and the mass change is shown for each.

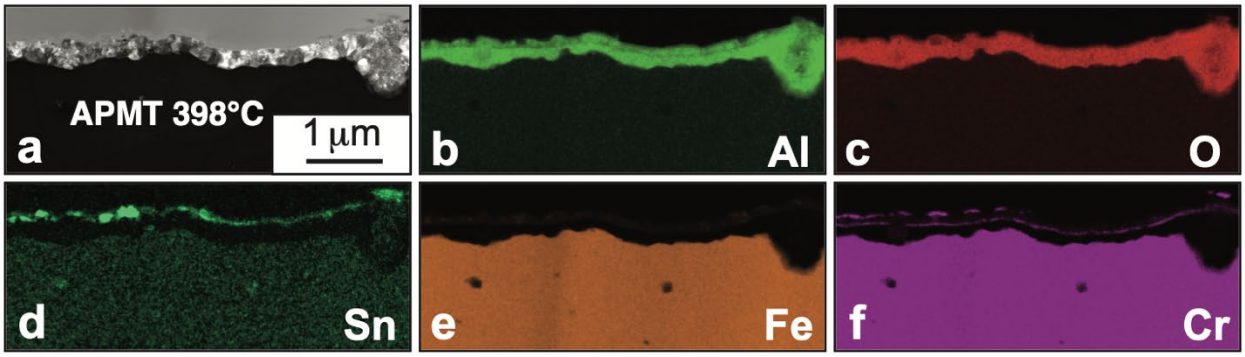

Figure 5. (a) TEM annular dark field image of the oxide on APMT after Sn exposure at 398°C and (b-f) EDS maps associated with (a).

the top of the HL, exposed at 398°C. Figure 5 shows an area without Sn on the surface. The surface alumina layer was intact, but some Sn was observed at the surface using EDS, Figure 5d. The sub-micron oxide thickness is consistent with the 2h/1000°C pre-oxidation for APMT [7]. The associated EDS maps show a small amount of Fe and Cr present in the outer portion of the oxide layer, which also is typical for APMT. Figure 6 shows a similar oxide thickness and structure in an area that was covered by Sn, Figure 6d. In this case, the alumina layer appeared very similar to the region not covered by Sn after exposure. For this specimen, there was no indication that the alumina layer was damaged by the Sn exposure prior to Li cleaning. However, only a small fraction of the surface was examined. Cross-sections from the other specimens remain to be examined.

Finally, the Sn was analyzed before and after the experiment using inductively coupled plasma and combustion analyses. Table 1 summarized the results with the as-received Sn being remarkably pure. The results from two samplings are shown. After the experiment, Sn samples were retrieved from the dump pot and from the top of the cold leg (TCL) and the bottom of the cold leg (BCL), i.e., Sn that did not drain out of the TCL and remained near the specimens. Both in the pot and at the BCL, only small quantities of Fe and Cr were measured in the Sn as well as increased levels of interstitials. The highest Sn impurities were measured at the TCL with 4.2%Fe. A fragment of metal may have inadvertently been incorporated into the Sn, the measured Fe/Cr ratio in Sn like the ratio in APMT, Table 1. Another possibility is that dissolved Fe increased the melting point and an Fe-Sn compound solidified in this region after Fe dissolved in the hot leg and the liquid cooled after leaving the hot leg. The Fe-Sn phase diagram is shown in Figure 7 with a steep increase in the liquidus temperature as Fe is added. At ~4%Fe, the liquidus may have increased to ~800°C while the top of the cold leg thermocouple averaged 367°C during the experiment.

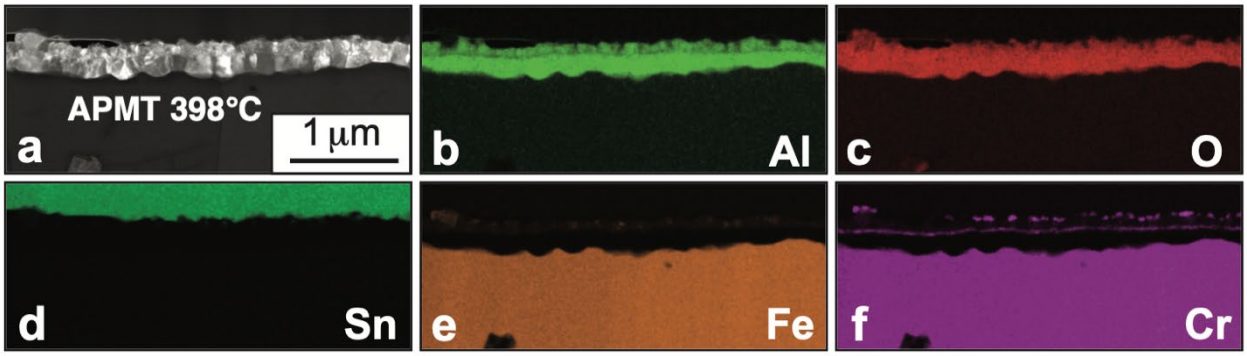

Figure 6. (a) TEM annular dark field image of the oxide on APMT where Sn covered the specimen after exposure at 398°C and (b-f) EDS maps associated with (a).

Table 2. Composition (mass%) of Sn measured using inductively coupled plasma and combustion analyses, O, C, S and N in wppm

Sample	Fe	Cr	Al	S	O	C	Other
As-rec	<0.002	<0.002	<0.002	<5	<2	6-8	<2 N, <0.002 P
Pot	0.012	0.004	<0.002	<5	2	13	<2 N, 0.002 P
BCL	0.010	0.002	<0.002	<5	45	35	2 N
TCL	4.2	0.8	0.3	6	83	26	0.05Mo, 0.007 Ni, 0.005 Mn, 0.002 P, <2 N

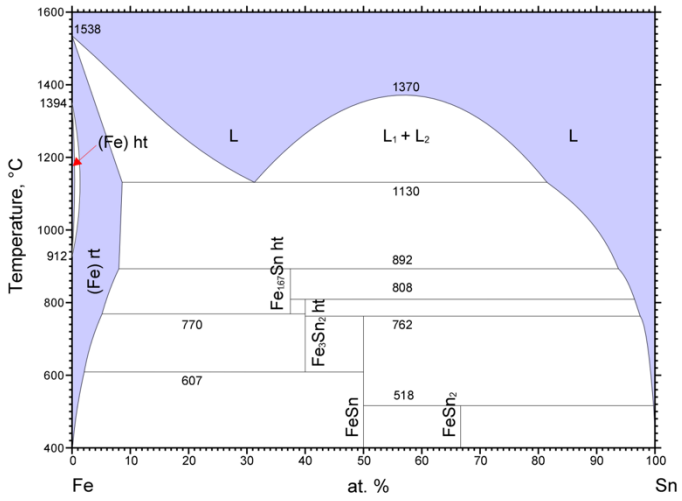

Figure 7. Fe-Sn phase diagram [ASM International, 2011]

No further compatibility experiments are planned for Task 3. Additional characterization and post-exposure tensile testing is in progress. The remaining experiment is to expose these three pre-oxidized materials with and without Sn in HFIR [14].

References

[1] M. Kondo, M. Ishii, and T. Muroga, Fus. Eng. Design 98–99 (2015) 2003.

[2] S. J. Zinkle and N. M. Ghoniem, Fus. Eng. Design, 51-52 (2000) 55.
[3] H. Glasbrenner, Z. Peric and H. U. Borgstedt, J. Nucl. Mater. 233-237 (1996) 1378.
[4] W. Krauss, J. Konys, N. Holstein and H. Zimmermann, J. Nucl. Mater. 417 (2011) 1233.
[5] W. Krauss, J. Konys, S.-E. Wulf, J. Nucl. Mater. 455 (2014) 522.
[6] S. J. Pawel and K. A. Unocic, J. Nucl. Mater. 492 (2017) 41.
[7] J. Jun, K. A. Unocic, M. J. Lance, H. M. Meyer and B. A. Pint, J. Nucl. Mater. 528 (2020) 151847.
[8] B. A. Pint and J. Jun, Oxid. Met. in press (2021).
[9] B. A. Pint, J. Jun, and M. Romedenne, Fus. Eng. Design 166 (2021) 112389.
[10] B. A. Pint, J. Jun, E. Cakmak, D. J. Sprouster, N. Olynik and L. L. Snead, Fus. Sci. Tech. in press (2021).
[11] B. A. Pint, S. Dryepondt, K. A. Unocic and D. T. Hoelzer, JOM 66 (2014) 2458.
[12] S. Dryepondt, K. A. Unocic, D. T. Hoelzer, C. P. Massey, B. A. Pint, J. Nucl. Mater. 501 (2018) 59.
[13] R. J. Lauf and J. H. DeVan, J. Electrochem. Soc., 139 (1992) 2087.
[14] M. Kondo, et al., Plasma Fus. Res. 16 (2021) 2405040.

9. MODELING AND COMPUTATIONAL STUDIES

9.1 MECHANICAL PROPERTIES AND RADIATION EFFECTS IN FUSION MATERIALS—Y. Osetskiy (Oak Ridge National Laboratory)

OBJECTIVE

The objective of this task is to obtain a better understanding of the atomic-scale mechanisms operating in fusion materials. Two main groups of effects are under consideration: mechanisms of radiation damage and properties of irradiated materials. Main materials studied are ferritic and tungsten-based alloys.

SUMMARY

An extensive atomic–scale study was carried out to investigate the detailed mechanisms of dislocation dynamics in the environment of radiation induced defects in tungsten. Molecular dynamics (MD) was used to model atomic scale dynamics of edge dislocation with the Burgers vector ***b*** = ½<111> gliding along the {110} plane. Spherical precipitates with 100% and 50% of Re and voids of diameter D_{prpt} =1-9 nm diameter were considered at temperatures from 100 K to 1600 K. Atomistic results were treated within the theoretical approach by Bacon-Kocks-Scattergood (BKS), and the conclusions include:

1. 100 at.% Re precipitates in W are strong obstacles interacting with an edge dislocation via "Orowan-like" mechanism, whereas 50 at.% Re precipitates are about two times weaker. Voids are intermediate obstacles.
2. All the studied obstacles follow the different side and obstacle density dependences, BKS model can consider these effects qualitatively.
3. Matrix-obstacle interface properties affect the ability of screw dislocation segments to glide over and cross-slip. Enhanced glide on the interface and cross-slip lead to earlier dipole recombination and thus decrease in CRSS. This is an atomic scale effect, and it is strong in W.
4. Obstacle size and density effects observed by atomistic modeling and treated within the BKS model can be used for estimating the obstacle strength parameter for the dispersed barrier hardening model. Temperature effects cannot be accounted for within the BKS model; atomistic modeling produces more accurate data on high temperature strengthening.

PROGRESS AND STATUS

The atomic scale approach developed in [1] and molecular dynamics (MD) modeling were used to study interactions between a ***b*** = ½<111> edge dislocation moving along the {110} plane and spherical obstacles in W. Obstacles were 100% Re precipitates, 50% Re precipitates, and voids. The model [1] considers a periodic array of dislocations and obstacles, where the main parameter, characterizing the obstacle number density, is the dislocation length, *L* (i.e., the distance between obstacles along the dislocation line direction <112>). This distance should be long enough to reproduce the correct dislocation line shape at the critical resolved shear stress (CRSS). For strong obstacles interacting with edge dislocations, the dislocation line shape corresponding to CRSS usually presents an extended dipole of screw dislocation segments formed in the obstacle's vicinity [1]. In this study, the same dislocation segment length, *L*=42 nm, was used for all obstacles.

The MD modeling results for CRSS at 300 K are presented in Figure 1. The CRSS is in $\frac{\mu b}{L}$ units (m is the bulk W shea modulus at 300K obtained by MD) and is presented as a function of harmonic mean of the dislocation length, *L,* and obstacle diameter, D_{prpt}, both in the dislocation Burgers vector length units $\boldsymbol{r_o}$ = 0.2724 nm. This presentation of CRSS was revealed in series of dislocation-obstacle continuum modeling by Bacon, Kocks, and Scattergood (BKS) [2, 3] where the realistic self-interaction between dislocation segments was considered:

$$\tau_c = A\frac{\mu b}{L}[ln(D^{-1} + L^{-1})^{-1} + B] \qquad (1)$$

were $A = 1/2\pi$ and $A = 1/2\pi(1-\nu)$ for edge and screw dislocations respectively, μ and ν are the shear modulus and Poisson ratio respectively. The *B* is a constant characterizing the interaction between the dislocation and matrix-obstacle interface and is related to the interface energy. In the original BKS model *B* was used to adjust the CRSS level to modeling results.

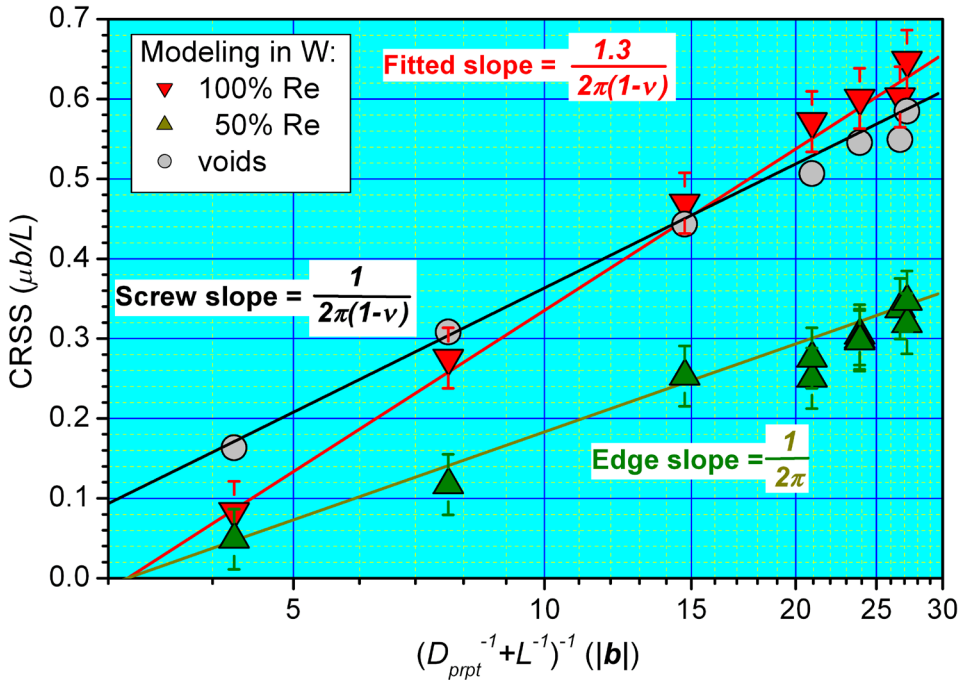

Figure 1. The MD derived CRSS as a function of the harmonic mean of D and L for Re-rich precipitates and voids in W at 300 K compared with the BKS model with fitted values of the surface energy parameter B.

For the case when yield stress is controlled by strong obstacles, like precipitates and voids considered here, the dispersed barrier hardening (DBH) model is often used to estimate the yield stress increase, $\Delta\sigma$, [13]:

$$\Delta\sigma = M\alpha\mu b(ND)^{1/2} \qquad (2)$$

where M is the Taylor factor and α is the obstacle strength parameter that is a measure of the barrier for a dislocation to bypass this obstacle. Estimation of α values is usually based either on a simplified theoretical approximation or/and treatment of experimental observations on the dislocation shape around obstacles. It is suggested here that atomic scale modeling and BKS approach can be used for estimating α values. The new technique for the first time allows estimation of size and temperature dependent α parameters. Examples of α parameter values for Re-rich precipitates and voids of different size at 300K are presented in Table 1.

Table 1. Obstacle strength parameters at 300K estimated for different obstacles size from MD data treated within BKS model. The r_0 = 0.2732nm is the value of ½<111> Burgers vector in W.

obstacle	α	2nm	5nm	10nm	20nm
50%Re	$0.159\left[ln\left(D_{prpt}/r_0\right) - 1.15\right]$	0.13	0.28	0.39	0.50
100%Re	$0.287\left[ln\left(D_{prpt}/r_0\right) - 1.15\right]$	0.24	0.50	0.70	0.90
void	$0.221\left[ln\left(D_{prpt}/r_0\right) - 0.68\right]$	0.29	0.49	0.65	0.80

Some of the results were published recently [5, 6].

Future Plans

This study will be continued to collect more data on the temperature dependence of CRSS for different obstacles to investigate this effect to the α parameter value. Contribution from thermally activated processes will be also studied by modeling dislocation-obstacle interactions at different strain rates applied. The final aim is to obtain a robust approach for estimation mechanical properties change in irradiated materials.

References

[1.] Y.N. Osetsky and D.J. Bacon, An atomic-level model for studying the dynamics of edge dislocations in metals. Modelling Simul. Mat. Sci. Eng. 11 (2003) 427.
[2.] D. J. Bacon, U. F. Kocks and R. O. Scattergood, The effect of dislocation self-interaction on the Orowan stress, Philos. Mag., 28 (1973) 1241-1263.
[3.] R.O. Scattergood and D.J. Bacon, The strengthening effect of voids, Acta. Metall., 30 (1982) 1665.
[4.] A.K. Seeger. Second UN Conference on Peaceful Uses of Atomic Energy, vol. 6, New York, 1958, p. 250.
[5.] Y.N. Osetsky, Atomic scale mechanisms of void strengthening in tungsten, Tungsten, 3 # 1 (2021) 65-71. DOI 10.1007/s42864-020-00070-6.
[6.] Y.N. Osetsky, Strengthening of tungsten by coherent rhenium precipitates formed during low fluence irradiation, Tungsten, (2021) in press.

9.2 A DATA DRIVEN FUSION RELEVANT VOID SWELLING MODEL UPDATE—Takuya Yamamoto, G. Robert Odette (University of California, Santa Barbara)

OBJECTIVE

The objective of this research is to develop an engineering model for void swelling (f_v) in 9Cr tempered martensitic steels (TMS) as a function of dpa for fusion service relevant effects of the dpa rate (dpa'), helium (He) and the He/dpa ratio.

SUMMARY

Here we update a void swelling model for tempered martensitic steels (TMS) under fusion relevant irradiation conditions at 500°C. The model has been, used in engineering analysis of the dimensional stability of fusion structures. The analysis focuses on the void volume fraction (f_v), recognizing that the actual swelling dimensional volume change is given by $S = f_v/(1-f_v)$, as reflected in the final model. The predicted S is 1.2+1.7/-0.9, 5.1+4.3/-3.1 and 16.5+14.5/-9.7 at 50, 100 and 200 dpa, respectively. The reliability of the f_v' model largely rests on the dual ion irradiation (DII) data, which is used, along with the in-situ helium injection (ISHI) neutron irradiation results, to estimate the void swelling incubation doses (dpa_i). Analysis of post incubation swelling rates (f_v'), also includes single ion and fission neutron data. Emphasis is on the dpa_i and f_v' He/dpa dependence. The model is far from the last word on the swelling of TMS in fusion environments, and much more research is needed for verification and refinement, including rigorous extension to lower temperatures. However, a qualitative assessment of the missing physics, including recent insights on the evolution of dislocations structures and sink biases, as well as injected interstitial and recombination effects, suggests that the model has a solid physical basis. Of course, ultimately the model must be validated by irradiations in a high energy neutron source.

PROGRESS AND STATUS

Fusion reactor designs must account for dimensional instabilities in structural components associated with void swelling and irradiation creep. It is well established that high He and He/dpa levels can cause severe degradation of both mechanical properties and acceleration of void swelling in TMS [1]. Thus, irradiation damage in a He-rich environment may greatly narrow the application window for the current candidate TMS for fusion reactor first wall and blanket structures. Here we analyze the DII, ISHI and literature databases to develop a predictive swelling model. We previously reported [2] that the UCSB database on cavity evolution, including the results of both dual ion irradiation (DII) and HFIR in situ helium injection (ISHI) neutron irradiation experiments, had been combined with data from the literature to develop a f_v(dpa, dpa', He/dpa) model for 500°C (400-500°C including literature data) irradiations of TMS F82H. The TMS cavity evolution 500°C DII database including 234 material-dpa-He-dpa' data sets, and the corresponding 500°C neutron ISHI irradiation observations including 16 material-dpa-He-dpa' data sets, were complemented by a large number of data sets on similar ion and neutron irradiated alloys found in the literature. In the case of the DII irradiations, f_v(dpa, dpa', He/dpa) is strongly affected by the He/dpa ratio, particularly regarding the incubation dpa (dpa_i) for the onset of void swelling. However, He/dpa also affects the post-incubation swelling rate (f_v'). The large "scatter" in the DII irradiation f_v is primarily due to local microstructural variations, and is mainly due to local effects on injected interstitial atoms (IIA) in single ion irradiations (SII) and DII. Local microstructures that shield regions at shallower depths from IIA provide the most accurate measures of dpa_i and f_v'; and, more generally, the highest f_v' is taken the best measure of void swelling rates. The incubation dpa_i is lower in the ISHI neutron irradiation experiments. The SII and neutron irradiation (NI) experiments, resulting in low He/dpa ratios, require a much larger dpa_i, which is again less in NI. The ion versus NI differences are likely due to the much lower dpa' in the latter case. The combined data set suggests that, after the initial incubation transient, f_v' can reach up to ≈ 0.3%/dpa, which is even higher than the canonical rate of 0.2%/dpa proposed by Garner [3]. This f_v' is also higher than the ≈ 0.1%/dpa found in the UCSB DII database, probably due to the lower post-incubation dpa increment, which is still in the transient regime. The post incubation f_v' can be qualitatively rationalized in terms of the void, bubble and dislocation sink ratios.

Here we report our recent updates on the model based on the recently updated DII analysis [4] as well as an updated literature database analysis.

Summary of DII updates and ISHI incubation dpa_i

An updated detailed mechanistic analysis of our DII database on the He/dpa dependence of dpa_i and the post incubation f_v' can be found in [4]. Figure 1 summarizes the key results found in [4]. Figures 1a and b show the high f_v DII data as a function of dpa and He/dpa. The incubation dpa_i is taken as the $f_v = 0$ intercept of fits of f_v(dpa) for various He/dpa. Clearly, dpa_i generally deceases with the increasing He/dpa. The dpa_i at He/dpa > 40 are roughly constant. The dpa_i as a function of He/dpa was estimated in two ways [4]: dpa = g(f_v) and f_v = h(dpa), where g and h are linear fit equations [4]. Figure 1c shows linear fits for both of the dpa_i estimates at He/dpa < 40. Thus, the dpa_i versus He/dpa is represented by a hockey stick form as:

$$dpa_i = [89 \pm 5.5] - [1.9 \pm 0.2]\ (He/dpa)\ (10 \leq He/dpa \leq 40) \quad (1a)$$

$$dpa_i = [18 \pm 2]\ (He/dpa > 40) \quad (1b)$$

Figure 1d shows f_v versus dpa at various He/dpa, with dpa_i normalized using Equation (1), to the fusion relevant He/dpa of 10. Here, the f_v' data are again from the two ways of fitting: dpa = g(f_v) and f_v = h(dpa) [4]. The f_v' data are scattered at some He/dpa, so we fit the average of the two f_v'(He/dpa) estimates as shown in Figure 1e, as

$$f_v' = [0.093 \pm 0.013] - [8.6 \pm 4.2]x10^{-4}\ He/dpa \quad (2)$$

Equations (1) and (2) constitute a model for DII f_v(dpa, He/dpa). The model allows normalization of all of the f_v data to a fusion relevant dpa_i. The normalized f_v data are shown in Figure 1f for a first wall He/dpa = 10. The normalized f_v data form a remarkably tight trend band.

The DII data cannot alone be a basis for a NI swelling model. For example, the dpa_i are clearly much lower for ISHI irradiations versus DII at the same He/dpa. The corresponding fusion relevant ISHI dpa_i(He/dpa) were estimated in three ways. The first, as shown by the dashed-dotted line in Figure 1c, is based on extrapolating from the dpa_i of ≈ 7 at ≈ 20, down to 5 dpa, assuming the DII/ISHI dpa_i ratio of ≈ 7.3 at 20 dpa can be used to scale the ISHI data. The dashed line in Figure 1c is based on a similar DII/ISHI scaling, but starting at 38 dpa_i. The dotted line assumes that the approximately constant dpa_i between 20 and 38 dpa can be extrapolated to 5 He/dpa. Thus, the bounds for dpa_i at He/dpa = 10 are estimated to be between ≈ 7 and 28.

Again, a more detailed and extended analysis of the DII data summarized here can be found in [4]. Note, the DII results showing an estimated f_v of ≈ 4% at ≈ 90 dpa is significant since this likely encompasses the dimensional instability limits for a fusion reactor structure. Evaluation of f_v at higher dpa must rely on literature NI and SII data.

The significance of the DII results to developing swelling models for FRI conditions

The UCSB swelling database covers a wide range of dpa rates, temperatures and He/dpa ratios for different Fe-9 to12Cr alloys. While the DII and ISHI results are for 500°C, the NI and SII data cover a range of lower temperatures. Swelling in TMS of more than f_v ≈ 5% is only observed in the very high dpa > 400 dpa SII data [5-7]. In spite of these differences, however, the FRI swelling model, represents well these diverse irradiation-alloy conditions. The FRI model is based on an empirical He/dpa sensitive dpa_i = f(He, dpa), derived from the DII results, as reported here, plus limited ISHI data, combined with a fitted linear post incubation f_v' that is also affected by the He/dpa ratio. Thus, key questions are: how applicable is FRI f_v' model, based on DII and ISHI $f_v \leq 5\%$ at 500°C, to lower FRI temperatures and dpa rates and higher dpa and corresponding swelling? Resolving these questions will require additional research, but it is useful to consider at least some qualitative answers.

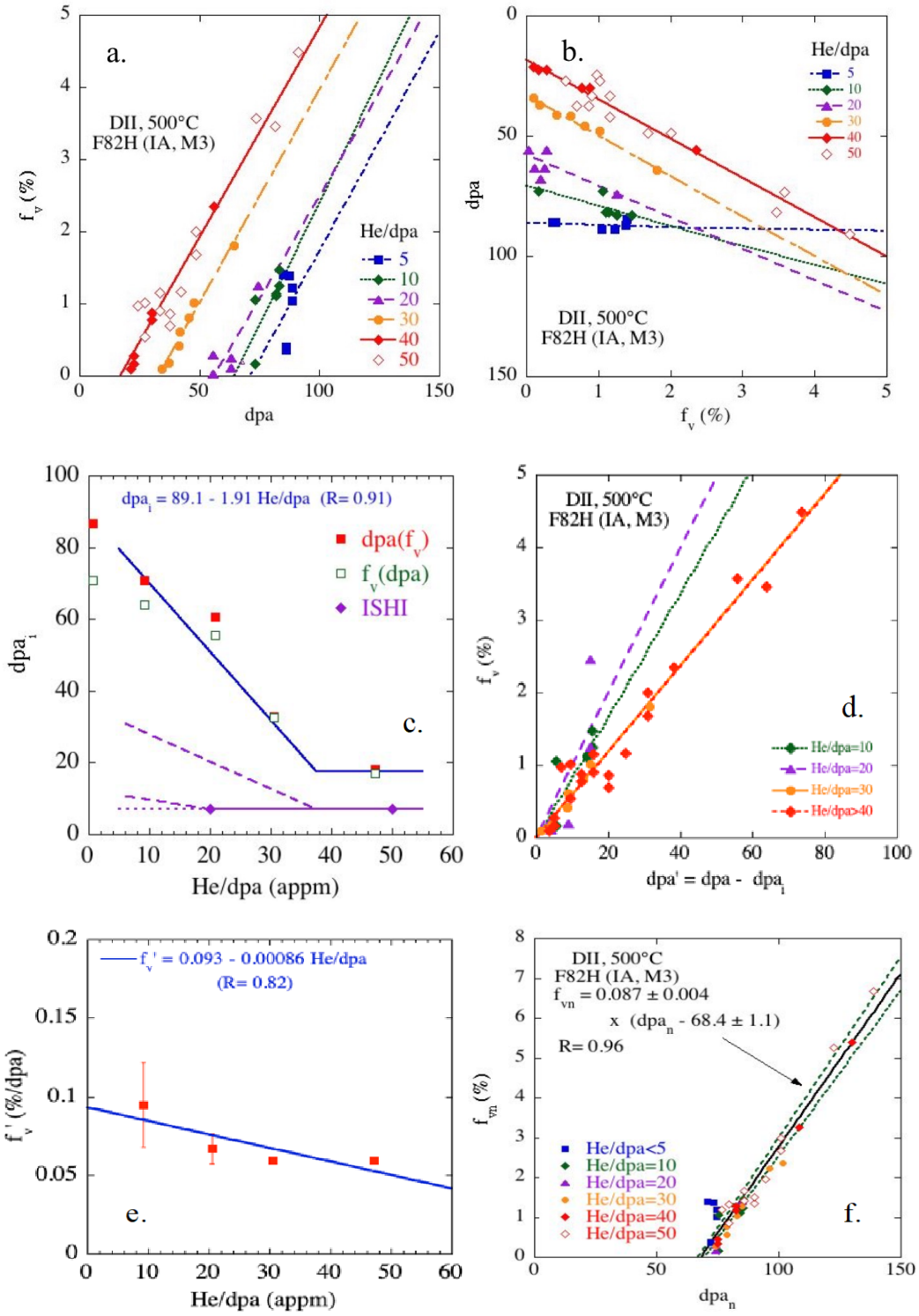

Figure 1. The high f_v data as a function of dpa fitted as: a) f_v(dpa); and, b) dpa(f_v); c) The dpa_i versus He/dpa for the two ways of fitting along with the solid fit line and the He_i scaled dpa_i dashed line for the ISHI; d) f_v as a function of dpa - dpa_i for various He/dpa ratios; e) the post incubation f_v' fitted in two ways as a function of He/dpa; and f) post-incubation f_{vn} data normalized to a common dpa_i and f_v for He/dpa = 10 appm/dpa.

a. One difference between DII and fusion relevant NI at high He/dpa is potentially significant recombination rates, with the fraction of point defects escaping recombination to reach permanent sinks, $g_s < 1$. The g_s can be estimated using simple rate theory models using effective vacancy migration energy for alloying effects and considering vacancy – SIA recombination at lattice as well as at cascade defect cluster debris, which is more significant at higher dose rates [8]. As shown in Figure 2, the g_s dependence on irradiation temperature and dose rate indicates that even at DII dpa rates of $4x10^{-4}$ to 4×10^{-3} dpa/s recombination rates are likely not large at 500°C. While the DII g_s decreases at lower temperatures, this is not the case for lower FRI dpa rates. Thus, with respect to recombination, the 500°C DII data is fully representative of FRI conditions.

b. Differences between the DII and FRI microstructures (loop, bubbles, voids and network dislocations) could also be significant, since they affect both dpa_i and f_v' by a variety of mechanisms [1]. An extensive body of data reported by Was and colleagues [9-12] shows that, at least for lower He/dpa conditions, DII irradiations emulate well the dislocation loop and cavity microstructures observed in fast reactor (BOR 60) irradiations. We can compare the DII microstructures to the ISHI results at ≈ 21 dpa in [13]. As shown in Figure 3a, the N, <d> and f_v for the ISHI and DII irradiations at 500°C to dpa' ≈ 15 dpa are similar. The dislocation density (network and loop) is somewhat lower for the ISHI condition compared to the specific STEM evaluation as shown in [4]. The ISHI irradiations swelling rate of ≈ 0.035%/dpa for the observed k_v/k_d and k_b/k_v, shown as the green unfilled diamond data points in Figure 3b, is reasonably consistent with the DII results and predicted f_v' curves. Thus, we conclude that the DII data are applicable to FRI conditions at least at 500°C.

c. The NI and SII results at lower temperature show a master curve type post incubation f_v', which is consistent with the lower DII and ISHI f_v and f_v' data at 500°C as shown below. A key question is: is the resulting f_v(dpa, He/dpa) model based on these merged data sources, applicable to a range of lower FRI temperatures? We have addressed the issue of dpa_i in our companion report [14], and believe that lower temperatures might somewhat reduce the FRI dpa_i. This hypothesis assumes that the larger contribution of loops at lower temperatures, increases the overall dislocation SIA bias. Further, lower temperature could result in smaller critical bubble sizes due self-diffusion effects on vacancy supersaturations [15], and the corresponding bias requirements for bubble to void conversion. However, dpa_i also depends on the initial bubble density, and N_b increases with decreasing temperature, reducing the helium in any individual bubbles. And the overall sink strength also increases with decreasing temperature, which could increase dpa_i. However, since the dpa_i is low for FRI dpa rates and He/dpa ratios shown above, the overall effects of temperature on swelling may still be modest, at least at higher dpa. Changes in the microstructure (bubbles voids, loops and network dislocations) might have a more profound effect on f_v', as reflected in the sink strengths and biases, and their corresponding effects of f_v' seen in Figure 3b. However, as long as the k_v/k_d and k_b/k_v ratios do not differ too much from 1, the effects of FRI sink strength variations with temperature on f_v' are expected to be less than a factor of ≈ ±50%.

Obviously, these speculations must be confirmed by well-designed experiments. The highest immediate priority to characterize dislocation evolutions. An important feature of future experimental studies of FRI experiments must be to comprehensively characterize microstructural evolutions, especially for the density and character of dislocations. Synchrotron x-ray studies will be particularly valuable in this regard [16]. The most immediate opportunity is to examine the TMS in the ISHI irradiations at 400°C. In the near future, a major focus should be placed on extending ISHI irradiations to higher dpa over a range of temperatures and He/dpa ratios. The US-Japan JP28-29 experiment in HFIR had that objective, but was not successful due to loss of temperature control [17-18]. However, as shown in Figure 4, re-irradiation of existing alloys in the ISHI 9 (JP26) and 22 (JP27) dpa irradiation conditions could reach up to at least 40-50 dpa in a relatively short time of several years (Figure 4b). There is also an opportunity to use ions to re-irradiate the ISHI alloys, to reach higher dpa (and He) in what has been described as the bootstrapping experiments [19] as illustrated in Figures 4a and c. This approach would compare the effects of ISHI irradiations, to a series of DII irradiation increments, to reach a common higher dpa. For example, ion re-irradiations of ISHI 9 dpa specimens, from the JP26 experiment, could be carried out to match the ISHI conditions in the JP27

experiment at 22 dpa. DII could subsequently be used to match the conditions for the ISHI re-irradiations of the 22 dpa irradiation to, say, 50 dpa. Special features of these experiments would be to exploit lab-on-a-chip miniaturization techniques and, ideally, the bootstrap irradiations could involve dedicated lower dpa rate, extended time ion irradiations, to avoid confounding dose rate factors.

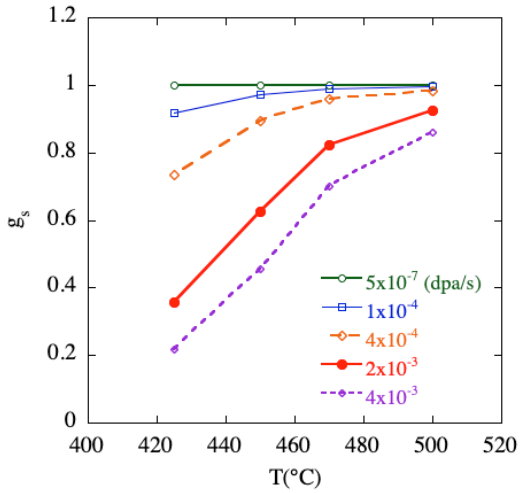

Figure 2. The fraction of point defects escaping recombination to reach permanent sinks, g_s, as a function of temperature and dose rate.

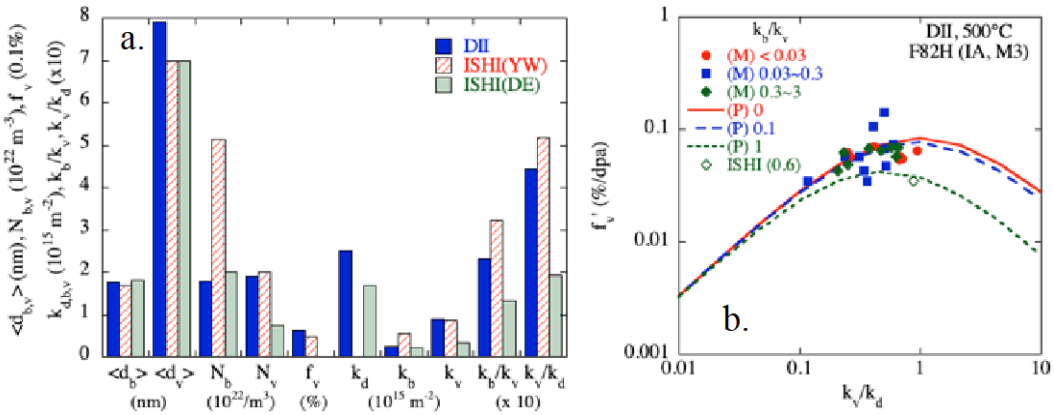

Figure 3. a) Comparisons of various microstructural properties after DII vs ISHI, b) observed swelling rate (f_v') in both DII (filled symbols) and ISHI (unfilled) compared to simple models based on point defect partitioning to the sinks as a function of sink densities of dislocations (k_d), bubbles (k_b) and voids (k_v) plotted versus k_v/k_d for various k_b/k_v.

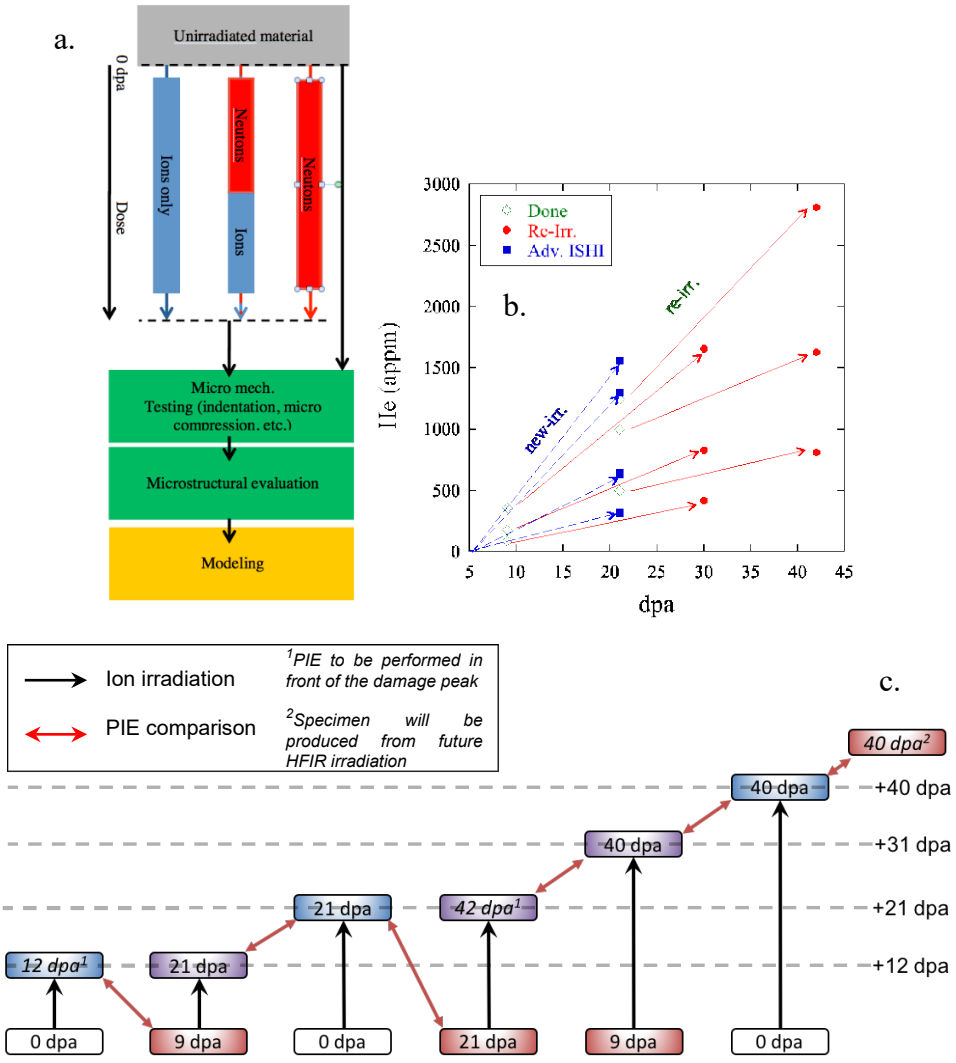

Figure 4. Schematic illustrations of a) neutron – ion irradiations boot-strapping approach to probe very high dose phenomena at a lower cost and in shorter time; b) expected He-dpa conditions in re-irradiation of ISHI JP26 and 27 specimens; c) an approach of NI-SII bootstrapping using ISHI JP26 and JP27 specimens.

Special mechanism experiments to gain insight on things like IIA, dpa rate recombination, cavity and dislocation evolutions and the effects on SIA bias would very useful as part of an overall roadmap for developing rigorous physical models of the effects of He-rich FRI. In the near future, the multiscale master model will be updated to reflect recent insights, especially those gained in this study.

Updated swelling models

Literature NI and SII Data based model

We have updated our literature swelling database [3,5-7,20-35] for various TMS and Fe-Cr model alloys for a range of irradiation conditions. This database currently consists of f_v (and usually N_v and $\langle d_v \rangle$) for 95 NI and 83 SII data sets for F82H, 9Cr-Mo (T91) and HT9 as well as Fe-3 to 15Cr binary model alloys. After examining all the data including the irradiation conditions and the details of materials including their sources,

we have identified several data subsets of f_v(dpa) that can be used in the analysis. The types and sources of those data are summarized in Table 1. Key observations in the analyses of database are summarized below for dpa_i, f_v and f_v'.

Table 1. The literature swelling data used in this study

Material	Irr. Type	Heat and/or Heat Treatment	T(°C)	dpa	Ref
T91	BOR60	30176, 1038°C/.5h 760°C/.5h	415	18.6	34
T91	HFIR	XA3590, 1040°C/.5h 760°C/1h	400	36	30
T91	FFTF	30176, 1040°C/.5h 760°C/.5h	400-420	35-208	28,31,32
F82H	HFIR	Std., 1040°C/.5h 760°C/2h	400	7.4-51	33
F82H	FFTF	Std., 1040°C/.5h 760°C/2h	430	67	33
HT9	FFTF	91353,1038/5m 760/.5h	400-420	30-165	29
T91	Ion	n/a, 1038°C/.5h 760°C/.5h	475	137-548	6
HT9	Ion	"fusion" heat, 760/.5h, 33%CW	480	200-600	5
Fe-9Cr	FFTF	1040°C/1h/AC 760°C/2h/AC	404-433	15 - 200	3,25-27
Fe-9Cr	EBRII	1040°C/1h/AC 760°C/2h/AC	400-450	13 - 49	3,25
Fe-12Cr	FFTF	1040°C/1h/AC 760°C/2h/AC	404-433	15 - 200	3,25-27
Fe-12Cr	EBRII	1040°C/1h/AC 760°C/2h/AC	400-450	13 - 49	3,25

Figure 5 plots the SII and NI f_v data, as a function of dpa for: (a) Fe-9 and 12Cr model alloys; (b-c) 9Cr TMS (F82H and T91); and (d-e) 12Cr HT9. Figure 5a shows NI Fe-9Cr and Fe-12Cr data from EBR-II and FFTF [3,25-27]. The nominal irradiation temperatures are from 400 to 480°C. Note, the DII was at 500°C, in part to provide a temperature adjustment to account for differences in the dpa rates [36-37]. In EBR-II, the dpa_i is very small for both binary alloys, while the $dpa_i \approx 78 \pm 25$ dpa in FFTF. Garner suggests that the difference may be due to different He generation rates: ≈ 0.17 versus ≈ 0.02 to 0.08 appm/dpa for EBR-II and FFTF, respectively [35]. However, the post incubation f_v' are similar, approaching ≈ 0.1%/dpa at $f_v \approx 10\%$. The fit lines in the 5a-c all have the same $f_v(dpa - dpa_i)$ shape, for NI of Fe-9-12Cr alloys (5a), NI of T91, F82H (5b) and HT9 (5c) TMS in different reactors (HFIR, FFTF and BOR60) [3,25-34], as well as for SII [5,6]. In all of these cases, the only differences between the various curves are the dpa_i. The fitted NI dpa_i is smallest in the mixed spectrum HFIR, larger in the fast reactors (BOR60 and FFTF) and largest for the SII. It is also notable that the dpa_i for T91 and F82H are the same for NI in the same reactor. This is also the case for the SII dpa_i for T91 and HT9. Figure 5d-e plots the f_v curves for SII HT9 on an expanded scale, showing that f_v' continuously increases with dpa, reaching ≈ 0.3%/dpa at a very high dose of ≈ 600 dpa.

The master $f_v(dpa\text{-}dpa_i)$ curve needs further confirmation, and is more approximate, especially with respect to some of the HT9 data at lower f_v and dpa. Further, the overlap of NI and SII data is limited to $f_v < \approx 3$ %. However, we consider the TMS master $f_v(dpa\text{-}dpa_i)$ curve to be a reasonable representation of swelling in both NI and SII.

Several studies have pre-implanted various amounts of He (generally at room temperature) followed by SII at different temperatures [7,22-23,38-39]. Figure 6 shows examples of observed the f_v vs. dpa trends. One notable result is that only small concentrations of ≈ 10 appm He are needed to promote void nucleation. However, compared to the dpa indexed master f_v curve shown as the solid line, 10 appm of pre-injected He greatly reduces f_v' in all cases. Pre-implantation of 100 appm He, leads to either f_v curves that flatten, or that are fully suppressed. Clearly, He pre-implantation is not a good way to simulate He effects.

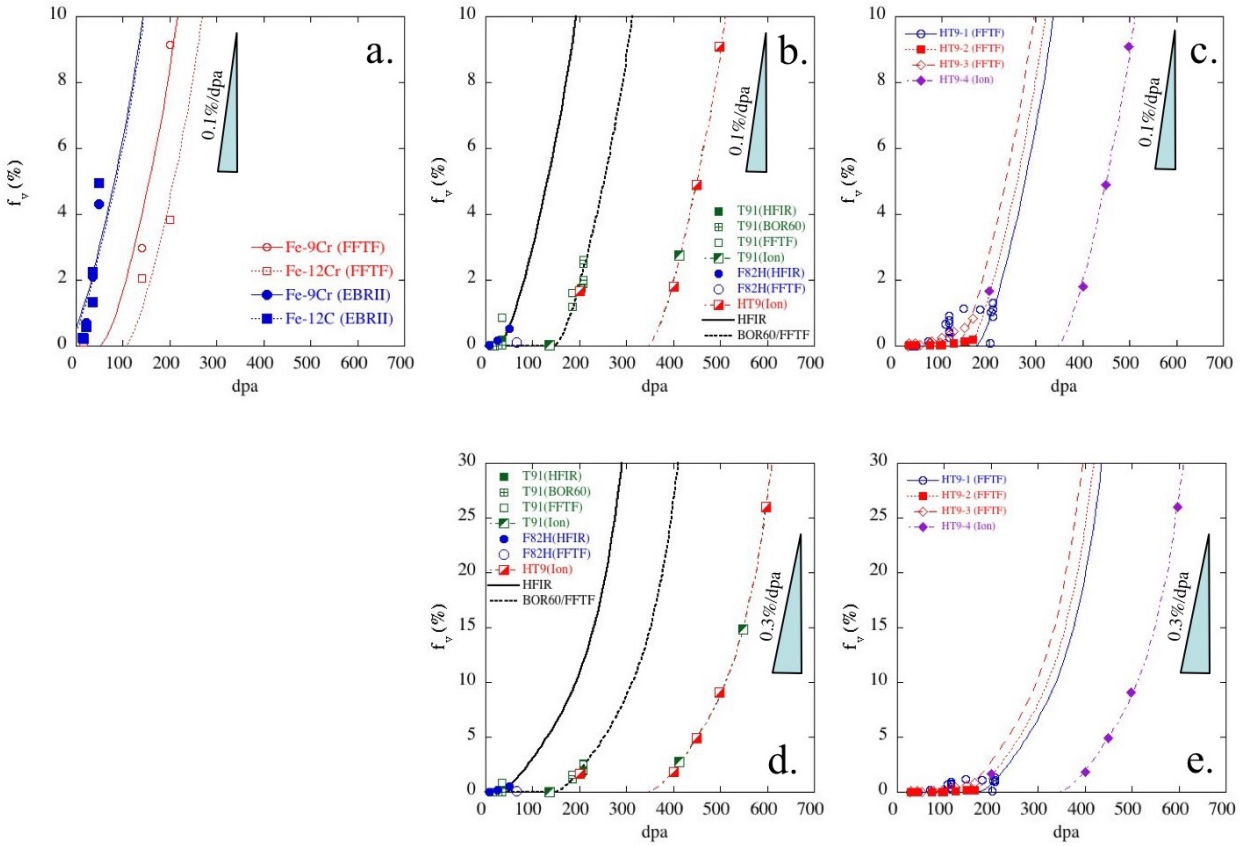

Figure 5. Swelling f_v vs dpa trends observed in the database for a) Fe-9,12Cr model alloys NI in EBRII and FFTF; b-c) ≈9Cr TMS (T91 and F82H) NI in HFIR, FFTF and BOR60 as well as SII; and d-e) various heats of HT-9 under NI (FFTF) and SII (Cr). Note the SII data has a common dpa_i ≈ 350 dpa.

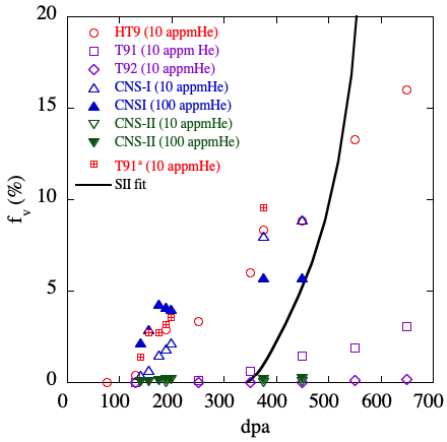

Figure 6. Swelling f_v – dpa trends in He pre-injection followed by SII irradiations compared to the fitted SII curve shown in Figures 5b-e.

Integrating the DII, ISHI, NI and SII f_v data to derive a fusion relevant f_v(dpa, He/dpa) model

A common f_v(dpa-dpa$_i$) master curve can be derived by fitting the data shown in Table 2 and Figure 7. Again, the dpa$_i$ strongly depend on the irradiation condition. In contrast, f_v vs. dpa (or f_v') trends are very similar for NI T91 and F82H, as well as for SII of T91 and HT9. Thus, all the data subsets were fit for a dpa$_i$, with a common f_v(dpa) fourth order polynomial master curve, shown in Figures 7a, and f_v (dpa – dpa$_i$) shown in Figure 7b. Again f_v' increases with dpa up to > 0.3%/dpa. The polynomial is:

$$f_v = 1.23\times10^{-2}(\text{dpa-dpa}_i)+6.15\times10^{-4}(\text{dpa-dpa}_i)^2-3.77\times10^{-6}(\text{dpa-dpa}_i)^3+1.10\times10^{-8}(\text{dpa-dpa}_i)^4 \quad (3)$$

to use with dpa$_i$ for the corresponding type of irradiation shown in Table 2.

Table 2. Incubation dpa$_i$ for various datasets in fitting to master f_v(dpa – dpa$_i$)

Master Curve Fitted Shape	HFIR	FFTF/BOR60	SII	DII	ISHI-22	ISHI-50
NI, SII	25	147	346	40	11	4.3

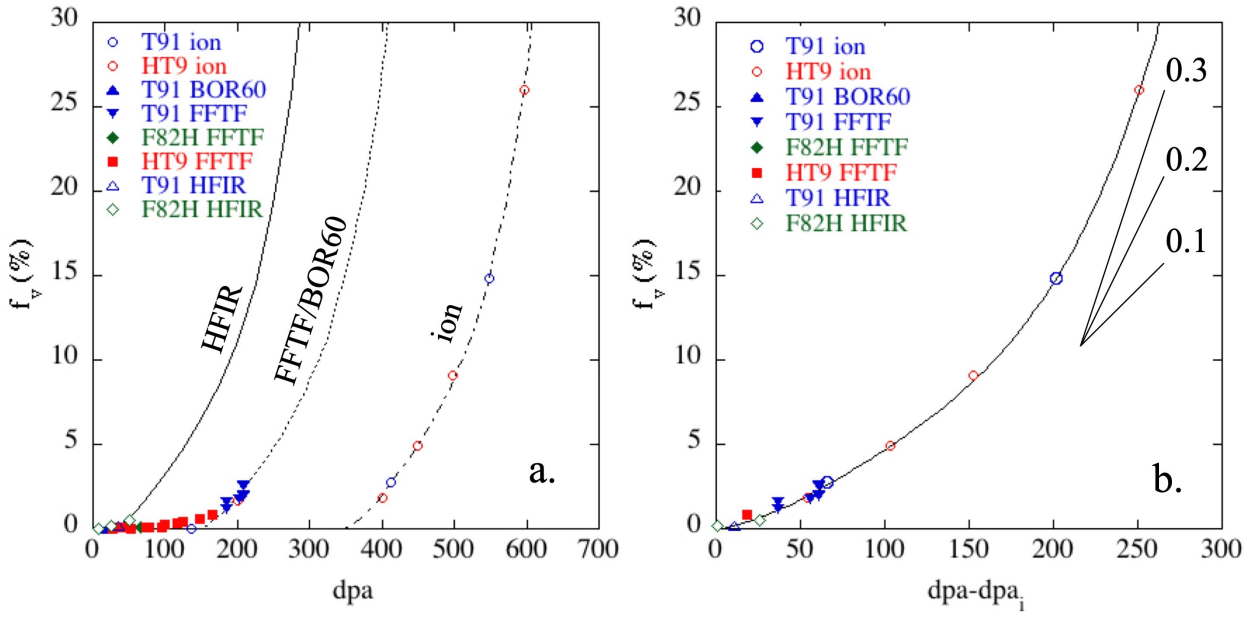

Figure 7. a) Literature f_v as a function of dpa for low He SII and neutron irradiations, fitted with a fourth order polynomial; and, b) the corresponding collapsed literature f_v as a function of dpa - dpa$_i$, along with the same fit curve.

Figure 8a shows a refitted master polynomial f_v(dpa – dpa$_i$) curve given by Equation (4), converted to more common expression of swelling, S, as defined in Equation (5), now including all the SII, NI, DII and ISHI data. The fitted parameters are dpa$_i$ and the polynomial coefficients. Table 3 summarizes the dpa$_i$ for the simultaneous least square fit of the polynomial coefficients. These effective refitted dpa$_i$ are affected by both the polynomial curve shape and the effects of the higher DII dpa rate.

$$f_v = 2.19\times10^{-3}(\text{dpa-dpa}_i) + 1.28\times10^{-3}(\text{dpa-dpa}_i)^2-9.17\times10^{-6}(\text{dpa-dpa}_i)^3+2.41\times10^{-8}(\text{dpa-dpa}_i)^4 \quad (4)$$

$$S(\%) = 100\, f_v(\%) /(100 - f_v(\%)) \quad (5)$$

Table 3. Incubation dpa_i for various datasets in fitting to master $f_v(dpa - dpa_i)$

Master Curve Fitted Shape	HFIR	FFTF/BOR60	SII	DII	ISHI-20	ISHI-50
All NI, SII, DII, ISHI	29	157	362	48	8.8	3.7

Figure 8b uses the $f_v(dpa - dpa_i)$ master curve shape in Equation (5), with an average $dpa_i \approx 18 \pm 11$ determined from the low dpa rate ISHI data, extrapolated to 10 He/dpa based on the procedures described above (see Figure 1f) and in [4]. This is again expressed in swelling S. Note that the literature f_v data is all at lower temperatures than the DII and ISHI results. The fact that, the wide range of alloys and irradiation conditions result in similar $f_v(dpa)$ curves, is remarkable, and provides a reasonable basis for the proposed swelling model. Note the very high f_v and dpa data are entirely based on low He, high dpa rate SII, which may not be representative of fusion relevant NI. However, at lower $f_v < \approx 10\%$ the model predictions are much more robust, and largely based on the DII results discussed in [4].

It is important to estimate the uncertainties of the nominal swelling curve in Figure 8b. An estimate of a higher swelling rate, shown as the dashed line, is based on a +50% higher post incubation f_v for $dpa_i = 7$. The lower swelling rate, shown by the dotted line, is based on a 50% lower post incubation f_v and a $dpa_i = 28$. Additional ISHI studies at higher dpa are critically needed to verify and refine these models.

A full and detailed discussion of the issues for dual ion versus high helium neutron irradiations is beyond the scope of this paper, but this is addressed further in [4]. However, by empirically accounting for the effect of ISHI and DII He/dpa on dpa_i and post incubation master curve $f_v(dpa - dpa_i)$ at 500°C, and lower temperature SII and NI with essentially the same f_v master curve, is a reasonable basis for proposing an $f_v(dpa, He/dpa)$ model for fusion relevant conditions. A major potential issue is dpa rate effects on recombination. However, as discussed in [4], this is unlikely to be a major issue for 500°C irradiations. If the only effect of lower temperatures is on recombination, the 500°C model could under-estimate f_v at 425°C by a factor of ≈ 2. Detailed modeling the effect of temperature on dpa_i and f_v' is work in progress. As has been discussed above, higher dpa and lower temperature ISHI data are clearly urgently needed to further refine the swelling model. A roadmap for acquiring such data including re-irradiation experiments has been developed [19] as briefly summarized above, but further discussion of these opportunities is also beyond the scope of this report.

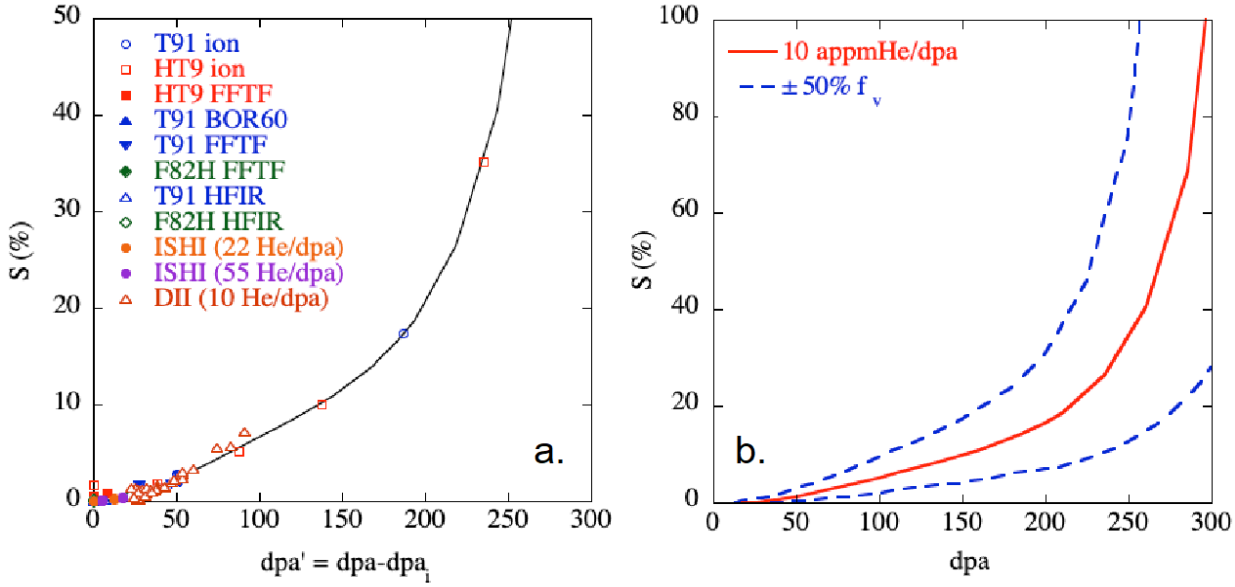

Figure 8. a) ISHI, DII and literature $S(dpa - dpa_i)$ along with the common fit curve; and, b) the S(dpa) model for He/dpa=10 appm He/dpa along with ±50% uncertainty estimates.

Acknowledgments

The authors gratefully acknowledge many collaborators who helped in carry out the irradiation experiments and microstructural characterization studies. They include Drs. Y. Wu and P. Miao at UCSB (TEM); Drs. D.J. Edwards, R.J. Kurtz, D.S. Gelles, H.J. Jung at PNNL for PIE (specimen preparation and TEM); Professors K. Yabuuchi, S. Kondo, A. Kimura, and Mr. Hashitomi at the Kyoto University DuET facility (DII This work was supported by the U.S. Department of Energy, Office of Fusion Energy Sciences, under the contract DE-FG03-94ER54275. The Joint Research Program on Zero-Emission Energy Research Institute of Advanced Energy, at Kyoto University, supported the DuET irradiation experiments. The TEM PIE microstructural characterizations were carried out in the NSF supported UCSB California Nanosystems Microstructural and Microanalysis and the DOE/INL supported National Scientific User CAES facility operated by Idaho State University.

References

[1] Y. Dai, G.R. Odette, T. Yamamoto, *The Effects of helium on irradiated structural alloys, in Comprehensive Nuclear Materials, R. Konings, T. R. Allen, R. E. Stoller, S. Yamanaka Eds. (2012) Elsevier.*

[2] T. Yamamoto, G.R. Odette, "A Fusion Relevant Engineering Void Swelling Model for 9Cr Tempered Martensitic Steels," *Fusion Materials Semiannual Report 7/1 to 12/31/2019* DOE/ER-313/67 (2020) 21.

[3] F.A. Garner, M.B. Toloczko, B.H. Sencer, "Comparison of swelling and irradiation creep behavior of fcc-austenitic and bcc-ferritic/martensitic alloys at high neutron exposure," J. Nucl. Mater. 376 (2000) 123.

[4] T. Yamamoto, Y. Wu, K. Yabuuchi, J. Haley, K. Yoshida, A. Kimura, G.R. Odette, submitted to J. Nucl. Mater. (2021).

[5] F.A. Garner, L. Shao, M.B. Toloczko, S.A. Malloy, V.N. Voyevodin, "Use of self-ion bombardment to study void swelling in advanced radiation-resistant alloys," Proc. 17th Int. Conf. on Environmental Degradation of Materials in Nuclear Power Systems Aug. 9-13, 2015, Ottawa, Ontario, Canada.

[6] J.G. Gigax, T. Chen, Hyosim Kim, J.Wang, L.M. Price, E. Aydogan, S.A. Maloy, D.K. Schreiber, M.B. Toloczko, F.A. Garner, Lin Shao, "Radiation response of alloys T91 at damage levels up to 1000 peak dpa," J. Nucl. Mater. 482 (2016) 257.

[7] E. Getto, K. Sun, S. Taller, A.M. Monterrosa, Z. Jiao, G.S. Was, "Methodology for determining void swelling at very high damage under ion irradiation," J. Nucl. Mater. 477 (2016) 273.

[8] G.R. Odette, T. Yamamoto, D. Klingensmith, "On the effect of dose rate on irradiation hardening of RPV steels," Phil. Mag. 85 (2005) 779.

[9] S. Taller, Z. Jiao, K. Field, G.S. Was, "Emulation of fast reactor irradiated T91 using dual ion beam irradiation," J. Nucl. Mater. 527 (2019) 151831. – DII T91 compared to BOR60.

[10] D. Woodley, S.Taller, Z. Jiao, K. Sun, G.S. Was, "The role of co-injected helium on swelling and cavity evolution at high damage levels in ferritic-martensitic steels," J. Nucl. Mater. 530 (2021) 152912.

[11] S. Taller and G.S. Was, "Understanding bubble and void nucleation in dual ion irradiated T91 steel using single parameter experiments," Acta Mater. 198 (2020) 47.

[12] S. Taller, G. VanCoevering, B.D. Wirth, G.S. Was, "Predicting structural material degradation in advanced nuclear reactors with ion irradiation," Sci. Rep. 11 (2021) 2949.

[13] Takuya Yamamoto, Yuan Wu, G. Robert Odette, Dan Edwards, Rick Kurtz, *Fusion Materials Semiannual Report 12/31/2015* DOE/ER-313/59 (2016)15.

[14] G.R. Odette and T. Yamamoto, in this issue of *Fusion Materials Semiannual Report 6/30/2021* DOE/ER-313/XX (2021).

[15] G.R. Odette, "On Mechanisms Controlling Swelling in Ferritic Alloy and Martensitic Alloys", *J. Nucl. Mat*. 155-157 (1988) 921.

[16] X. Zhang, M. Li, J-S Park, P. Kenesei, J. Almer, C. Xu, J.F. Stubbins, "In situ high-energy X-ray diffraction study of tensile deformation of neutron-irradiated polycrystalline Fe-9Cr alloys," Acta Mater. 126 (2017) 67.

[17] H. Sakasegawa, T. Hirose, X. Chen, J.W. Geringer, Y. Katoh, "Irradiation hardening behavior of F82H in JP28 and 29," *Fusion Materials Semiannual Report 6/30/2017* DOE/ER-313/62 (2017) 3.

[18] Takuya Yamamoto, Yuan Wu, G. Robert Odette, Dan Edwards, Rick Kurtz, *Fusion Materials Semiannual Report 12/31/2015* DOE/ER-313/59 (2016) 15.
[19] T. Yamamoto, G.R. Odette, P.B. Wells, D.J. Edwards, K. Kruska, R.J. Kurtz, S.J. Tumey, *Fusion Materials Semiannual Report 12/31/2018* DOE/ER-313/65 (2019) 139.
[20] J.G. Gigax, H. Kim, T. Chen, F.A. Garner, Lin Shao, "Radiation instability of equal channel angular extruded T91 at ultra high damage levels," Acta. Mater. 132 (2017) 395.
[21] Y. Li, T. Shen, X. Gao, C. Yao, K. Wei, J. Sun, B. Li, Y. Zhu, L. Pang, M. Cui, H. Chang, J. Wang, H. Zhu, B. Hu, Z. Wang, "Cavity swelling in three ferritic-martensitic steels irradiated by 196 MeV Kr ions," Chin. Phys. Lett. 30 (2013) 126101.
[22] Xu Wang, Qingzhi Yan, Gary S. Was, Lumin Wang, "Void swelling in ferritic-martensitic steels under high dose ion irradiation: Exploring possible contributions to swelling resistance," Scr. Mater. 112 (2016) 9.
[23] E. Getto, K. Sun, A.M. Monterrosa, Z. Jiao, M.J. Hackett, G.S. Was, "Void swelling and microstructure evolution at very high damage level in self-ion irradiated ferritic-martensitic steels," J. Nucl. Mater. 480 (2016) 159.
[24] D.S. Gelles, "Microstructural development in reduced activation ferritic alloys irradiated to 200 dpa at 420°C," J. Nucl. Mater. 212-215 (1994) 714.
[25] D.S. Gelles, "Microstructural examination of neutron-irradiated simple ferritic alloys," J. Nucl. Mater. 108&109 (1982) 515.
[26] Y. Katoh, A. Kohyama, D. Gelles, "Swelling and dislocation evolution in simple ferritic alloys irradiated to high fluence in FFTF/MOTA," JNM 225 (1995) 154-162.
[27] D.S. Gelles, "Void swelling in binary Fe-Cr alloys at 200 dpa," J. Nucl. Mater. 225 (1995).
[28] M.B. Toloczko, F.A. Garner, C.R. Eiholzer, "Irradiation creep and swelling of the US fusion heats of HT9 and 9Cr-1Mo to 208 dpa at ≈ 400°C," J. Nucl. Mater. 212-215 (1994) 604.
[29] M.B. Toloczko, F.A. Garner, "Irradiation creep and void swelling of two LMR heats of HT9 at ≈ 400°C and 165 dpa," J. Nucl. Mater. 233-237 (1996) 289.
[30] J.M. Vitek and R.L. Klueh, "Microstructure of 9Cr-1MoVNb steel irradiated to 36 dpa at elevated temperatures in HFIR," J. Nucl. Mater. 122&123 (1984) 254.
[31] J.J. Kai and R.L. Klueh, "Microstructural analysis of neutron -irradiated martensitic steels," J. Nucl. Mater. 230 (1996) 116.
[32] J. Van den Bosch, O. Anderoglu, R. Dickerson, M. Hartl, P. Dickerson, J.A. Aguiar, P. Hosemann, M.B. Toloczko, S.A. Maloy, "SANS and TEM of ferritic-martensitic steel T91 irradiated in FFTF up to 184 dpa at 413°C," J. Nucl. Mater. 440 (2013) 91.
[33] E. Wakai, N. Hashimoto, Y. Miwa, J.P. Robertson, R.L. Klueh, K. Shiba, S. Jistukawa, "Effect of helium production on swelling of F82H irradiated in HFIR," J. Nucl. Mater. 283-287 (2000) 799.
[34] Z. Jiao, S. Taller, K. Field, G. Yeli, M.P. Moody, G.S. Was, "Microstructure evolution of T91 irradiated in the BOR60 fast reactor," J. Nucl. Mater. 504 (2018) 122.
[35] F.A. Garner, D.S. Gelles, L.R. Greenwood, T. Okita, N. Sekimura, W.G. Wolfer, "Synergistic influence of displacement rate and helium/dpa ratio on swelling of Fe-(9,12)Cr binary alloys in FFTF at ~400°C," J. Nucl. Mater. 329-333 (2004) 1008.
[36] L.K. Mansur, "Theory and experimental background on dimensional changes in irradiated alloys," J. Nucl. Mater. 216 (1994) 97.
[37] L.K. Mansur, "Correlation of neutron and heavy ion damage," J. Nucl. Mater. 78 (1978) 156.
[38] Z. Jiao, N. Ham, G.S. Was, "Microstructure of helium-implanted and proton-irradiated T91 ferritic/martensitic steel," J. Nucl. Mater. 367-370 (2007) 440.
[39] Xu Wang, Anthony M. Monterrosa, Feifei Zhang, Hao Huang, Qingzhi Yan, Zhijie Jiao, Gary S. Was, Lumin Wang, "Void swelling in high dose ion-irradiated reduced activation ferritic-martensitic steels," J. Nucl. Mater. 463 (2015)119.

9.3 A MICROMECHANICAL MODEL FOR IRRADIATION EMBRITTLEMENT OF 9Cr TEMPERED MARTENSITIC STEELS UNDER FUSION SERVICE RELEVANT CONDITIONS—T. Yamamoto, M. Hribernik, G. R. Odette (University of California, Santa Barbara)

OBJECTIVE

The objective of this work is to develop a physically based, predictive model for irradiation embrittlement of tempered martensitic steels in terms of KJc(T) curves, which account for high for fusion relevant helium conditions with high He/dpa ratios.

SUMMARY

Defect tolerant fusion structures will require methods to predict severe embrittlement by establishing fracture toughness-structure temperature curves, $K_{Jc}(T)$, as a function of fusion relevant service conditions, including irradiation temperature (T), displacements per atom (dpa) and the helium (appm) to displacement ratio (He/dpa). Fission neutron embrittlement is primarily associated with irradiation hardening ($\Delta\sigma_y$) induced increases in the cleavage transition temperature regime (ΔT_o). This form of embrittlement is well treated by the so-called master curve method, described below, in terms of a shift in a reference temperature ΔT_o at 100 MPa$\sqrt{m}$, indexing a constant master cure $K_{Jc}(T-T_o)$ shape. However, at high fusion relevant He/dpa ratios, much more severe embrittlement is associates with the combination of helium induced: a) weakening of grain boundaries, leading to extremely brittle intergranular fracture; and b) contributions to larger $\Delta\sigma_y$. Here, we develop a physically based model of $K_{Jc}(T)$ for fusion relevant irradiation conditions.

PROGRESS AND STATUS

An important development in the evaluation of the cleavage fracture toughness of ferritic-martensitic steels is the ASTM Standard E 1921 [1]. This standard defines a reference fracture toughness $K_{Jc}(T)$ curve, known as the Master Curve (MC), in terms of a reference transition temperature, T_o, at 100 MPa$\sqrt{m}$. The MC is based on the observation that the $K_{Jc}(T)$ curves for ferritic steels have a constant, universal shape, shown in Figure 1, for various T_o. The T_o-indexed MC can be used to predict embrittlement based on a relatively small number of small specimens [2]. However, there are several fundamental questions concerning the MC, including the apparent existence of and basis for a universal MC shape [3]; and the effect of high fusion relevant He/dpa, leading to intergranular fracture, on the $K_{Jc}(T)$ and T_o.

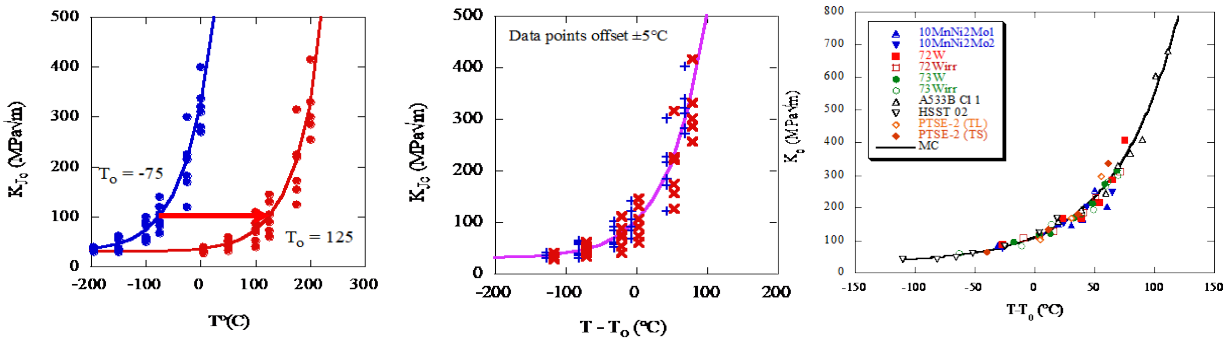

Figure 1. Illustration of the MC concept for the median unirradiated and irradiated $K_{Jc}(T)$ data.

As illustrated in Figure 2a, the normal stresses (σ_n) near the tip of a blunting fatigue crack can reach 3-5 times the steel's yield stress (σ_y). Such high σ_n are necessary for cleavage fracture. The condition for cleavage can be in terms of a specified crack tip stress contour $\sigma_n = \sigma^*$ (>> σ_y), encompassing a critical microstructural volume (V*) in a crack tip plastic process zone, which is needed to propagate a dynamic

cleavage microcrack formed at a broken brittle trigger particle, as illustrated in Figure 2b. If V is < V* a suitable brittle particle is not encountered and a propagating microcrack is not triggered. Thus, σ^* and V* are the steels local fracture properties. A deterministic description of the cleavage condition for cleavage fracture toughness is given by $V(\sigma^*, K_{Jc}) = V^*$. For plane strain small scale yielding conditions, V increases with the applied effective stress intensity K_J[4]. The $V(\sigma, K_J)$ can be modeled by finite element methods. Historically σ^* was assumed to be approximately independent of temperature. However, as shown in Figure 2c, large deviations between the K_{Jc} model predictions and MC shape at higher T_o occur for a constant σ^*. Irradiation hardening ($\Delta\sigma_y$) shifts T_o up in temperature at a typical rate of ≈ 0.7°C/MPa. For a constant σ^* this causes a large layover in the K_{Jc} curve. But it was shown that the observed MC shape can be rationalized by a σ^* which increases appropriately with temperature [4].

As illustrated in Figure 2d, the temperature dependence of σ^* is controlled by a microcrack arrest toughness, $K_\mu(T)$, which determines the local σ^* at which broken brittle particle microcracks propagate, rather than arrest, the tougher ferrite matrix at acritical, given by $\sigma^* = K_\mu/[g\sqrt{d}]$. Here g is a non-dimensional factor that depends on the geometry of the trigger particle microcrack. Thus $K_\mu(T)$, is a key valving property of a steel that mediates the much higher macroscopic K_{Jc}. $K_\mu(T)$ is controlled by dislocation interaction with the microcrack tip. If dislocation glide is sufficiently restricted the local microcrack stress intensity reaches to Griffith condition for fracture at k_μ, as shown in Figure 2e.

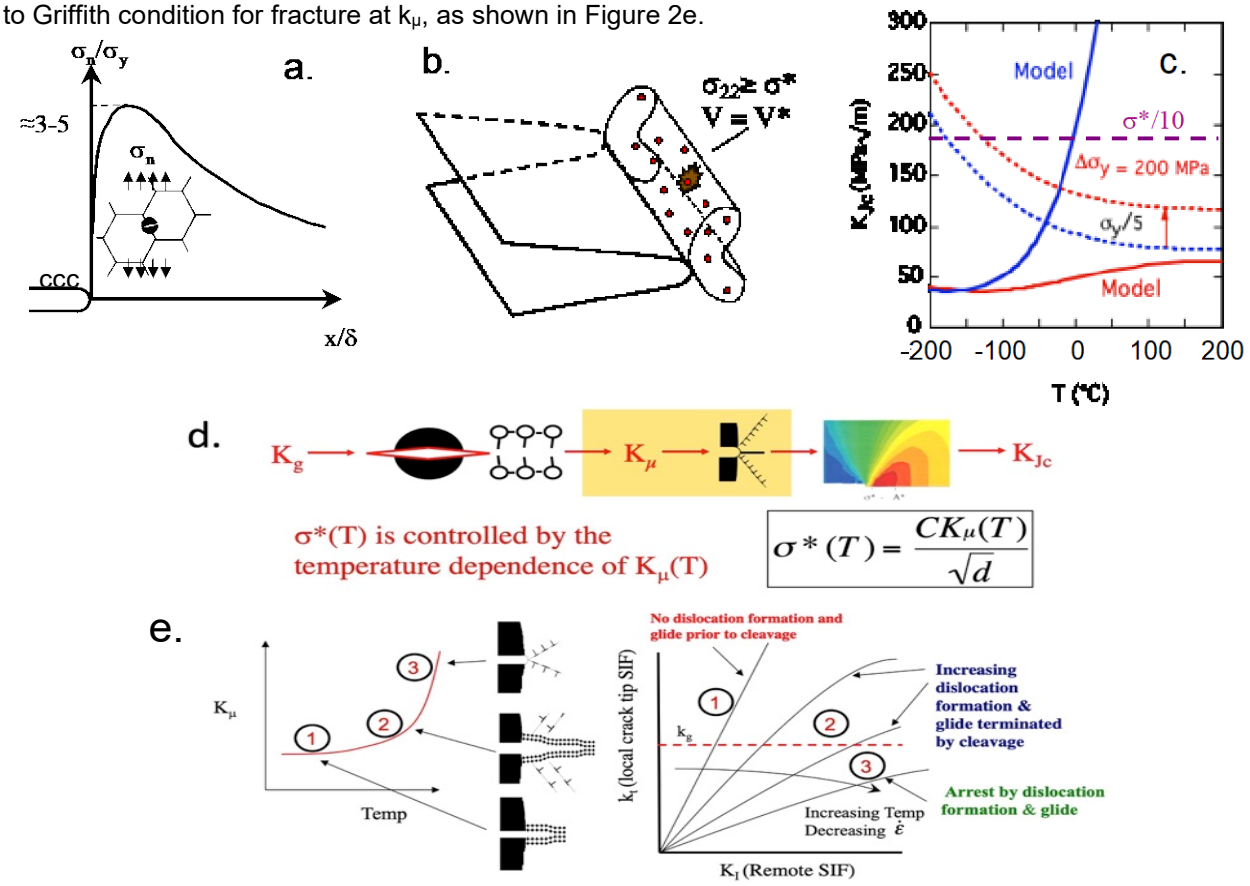

Figure 2. a) The stress (σ) concentration profile ahead of a crack tip; b) a critical volume, V*, bounding $\sigma \geq \sigma^*$, activations a brittle trigger particle; c) The predicted layover effect on $K_{Jc}(T)$ of an irradiation hardening $\Delta\sigma_y$ = 200MPa for constant $\sigma^* \approx$ 1900 MPa; d) a schematic illustration of how a semi-brittle crack arrest $K_\mu > K_g$ *(the purely elastic Griffith brittle fracture toughness) valves the macroscopic K_{Jc}; and, e) the relation between the nano-blunting at the broken particle dynamic microcrack tip dislocation activity and the local stress intensity factor leading to brittle fracture (1), semi-brittle fracture (2), or arrest (3).

V* is an extrinsic property that depends on the steel (mainly trigger particle) microstructure, like large grain boundary carbides. Thus, modeling $K_{Jc}(T)$ requires a) V* taken as being approximately temperature independent volume; b) the steel true stress (σ)-strain (ε), strain rate (ε') constitutive properties [$\sigma(\varepsilon,\varepsilon',T)$]; c) $K_{\mu}(T)$ and, d) the trigger particle d which govern $\sigma^*(T)$. The $\sigma(\varepsilon,\varepsilon',T)$ and d, can be measured independently, while σ^* and V* can be found by fitting K_{Jc} curves. However, historically $K_{\mu}(T)$ has not been independently well characterized. Fortunately, earlier work by Hribernik et al. [3,5-7] was the first to measure $K_{\mu}(T)$ in terms of the arrest $K_{Ia}(T)$ for cleavage-oriented Fe single crystals. The basis for the cleavage MC model is briefly outlined below.

Results

The underlying micro mechanisms of cleavage and a MC $K_{Jc}(T)$ shape and ΔT_o shift model

The unresolved key to understanding the cleavage MC shape and irradiation induced ΔT_o is the temperature dependence of $\sigma^*(T)$. As discussed above and in detail elsewhere [3], σ^* is controlled by the propagation of dynamic micro-cracks formed at broken brittle trigger particles. These atomistic scale mechanisms exert a powerful effect on the larger continuum K_{Jc} and reflect the critical underpinning of any multiscale model of cleavage fracture. Assuming a cleavage orientated penny-shaped particle crack with an effective diameter d_t

$$\sigma^*(T) \approx K_{\mu}(T)(\pi/2d_t)^{1/2} \qquad (1)$$

The micro-arrest toughness of the alloy, $K_{\mu}(T)$, is the underlying property that controls the temperature dependence of $\sigma^*(T)$. There are many potential trigger sites in a stressed volume, but only those with sizes, local stresses and orientations that can activate low toughness cleavage systems will produce propagating microcracks. Note the local stresses include the effects of strain incompatibilities between the matrix and trigger particle and internal stress fluctuations associated with crystal plasticity; hence, the local stresses are likely to be even larger than those produced by the blunting macro-crack itself. The preferred cleavage system in Fe and its alloys are {100} planes and <100> or <110> directions.

The K_{μ} can be expressed in terms of a modified Griffith fracture criteria that accounts for the combination of creation of new surfaces, a quasi-brittle process contributing < 1 MPa$\sqrt{m}$, and dislocation activity at or near the microcrack tip, contributing a few to several MPa$\sqrt{m}$ in the semi-brittle cleavage region (see Figure 2e). While the dislocation activity has been classically viewed as dislocation emission from the crack tip, and corresponding nano-blunting, other dissipative processes, due to crack interactions with and shielding by pre-existing dislocations, may also be important. Thus, cleavage in oriented Fe single crystals is semi-brittle, with low toughness values ($\leq \approx 5$ MPa$\sqrt{m}$ at low temperature); however, this single crystal toughness acts as a valve in controlling the much higher macroscopic toughness (>> than 20 MPa$\sqrt{m}$) in ferritic alloys again as shown in Figure 2e.

Several models have been proposed for static (K_{Ic}) and a fewer number for crack arrest toughness (K_{Ia}) in cleavage-oriented Fe single crystals, taken here to be a surrogate for K_{μ}. A common feature in the models is that they predict an increase in toughness with increasing temperature up to a brittle to ductile transition temperature (T_{BDT}), above which cleavage does not occur. The T_{BDT} increases with increasing loading rate, reflecting the thermally activated character of the underlying dislocation processes.

However, previously there were no reliable measurements of $K_{Ia}(T)$ and K_{Ic} (T) in unalloyed single crystal Fe, and only limited useful data on Fe-3Si [8]. Hribernik et al. carried out the first rigorous measurements of K_{Ia} and K_{Ic} over a wide range of loading rates for cleavage-oriented Fe-single crystals [3,5-7]. The composite specimens used are shown in Figure 3.

We summarize the implications of the work of Hribernik et al. and $K_{I\mu} \approx K_{Ia}$ to the MC shape.

- The average K_{Ia} gradually increases from about 3.5 MP$\sqrt{m}$, at -196°C, to about 9 MPa$\sqrt{m}$, at 0°C, and is similar in both the (100)[010] and (100)[011] cleavage orientations as shown in Figure 4a.

- Initiation, crack propagation, arrest and re-initiation produce complex slip step structures, river patterns and etch pits on the fracture and side surfaces of the Fe crystals, indicating significant dislocation activity, which is associated with {110}<111> and {112}<111> slip systems. The dislocation activity is qualitatively consistent with observation of the semi-brittle single crystal K_{Ic} and K_{Ia}.

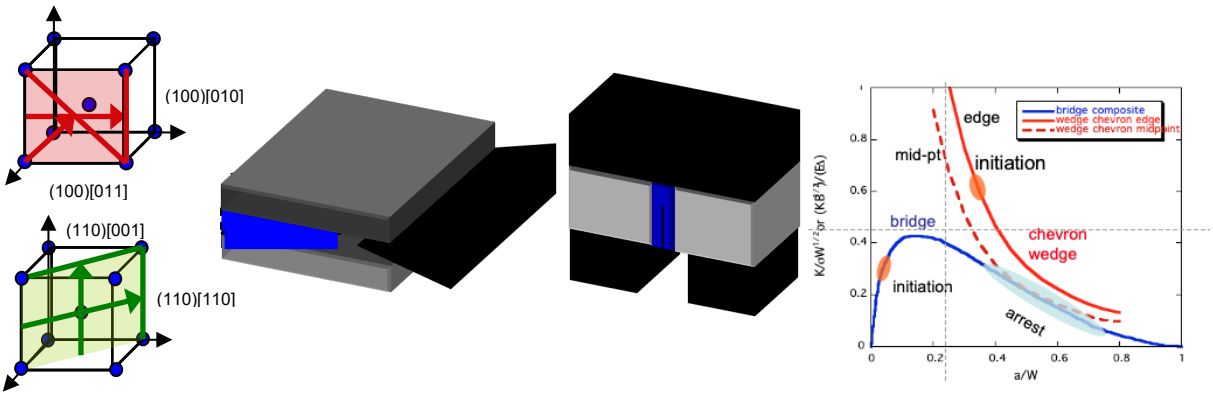

Figure 3. Composite specimens used to measure arrest (K_a) and initiation (KIc) toughness in cleavage-oriented Fe single crystals.

- Measurements of initiation toughness also show that K_{Ic} also increases with temperature and decreases with higher loading rates, which were from < 1 to $2x10^4$ MPa√m/s, as shown in Figure 4b, again reflecting thermally activated dislocation slip processes.
- The initiation cleavage dynamics (loading rate and temperature dependence) are controlled by, and indeed are identical to, thermally activated dislocation dynamics that mediate the corresponding yield stress of Fe based alloys as shown in Figures 5a to c.
- At lower temperatures the fracture and yield dynamics are dominated by double-kink nucleation on screw dislocations. Both fracture and yield dynamics are governed by a stress-dependent activation energy with a maximum value of ≈ 0.69 eV.
- This activation energy can be used to adjust the $\sigma_{yt}(T)$, $K_{Ic}(T)$ and $K_{Ia}(T)$ data to form a single MC on a strain rate compensated temperature scale (T') for a specified reference strain rate as shown in Figure 5c. The T' results assume an effective dynamic strain rate of $5x10^3$/s.

$$T' = T\,[1+ (1/\alpha)\ln(\varepsilon'/\varepsilon_r')),$$
$$\text{where } \alpha = 23.8$$

- The increase in $K_{Ia}(T')$ with temperature, in the unalloyed Fe single crystal, is too large to rationalize the shape of the macro-$K_{I/Jc}(T)$ MC and is inconsistent with the corresponding measured K_{Ia} in Fe-Si with a higher BDT shown in Figure 5d [8].
- The low BDT for the $K_{Ia}(T')$ and $K_{Ic}(T')$ single crystal curves are associated with the low strength of unalloyed Fe. The σ_y of the Fe-Si alloy is significantly larger than for Fe, which shifts the corresponding $K_{Ia}(T)$ curve up in temperature as shown in Figure 5d [3,5]. The $K_{Ia}(T')$ is shifted to even higher temperatures in stronger ferritic-martensitic steels.
- The BDT of the K_{Ia} curves for Fe, Fe-3Si and higher strength steels approximately scale with the inverse of their corresponding dynamic yield stress [$\sigma_{yd}(T')$] as

$$K_{Ia}(T) = C_a/\sigma_{yd}(T')$$

- Here, $C_a \approx 4000$ is a normalization factor fit to the Fe single crystal K_{Ia}(-196°C) data.
- These results indicate that K_{Ia} and K_{Ic} are controlled by the total strength of an alloy including both thermal (t) and athermal (a) components: $\sigma_y = \sigma_a + \sigma_t(T,\varepsilon')$.

- Thus, the $K_{Ia}(T)$ increases with decreasing $\sigma_{yd}(T)$ at higher temperatures. However, in polycrystalline steels the minimum K_{Ia} is found to be ≈ 3.25 MPa√m because of boundaries and grain misorientations on cleavage crack propagation. The resulting $K_{Ia}(T)$ curves an unirradiated alloy with a static σ_y = 475 MPa and $\Delta\sigma_y$ from 100 to 300 MPa are shown in Figure 6a.
- The K_{Ia} data can be converted to $\sigma^*(T)$ and used along with $\sigma = \sigma_a(\varepsilon) + \sigma_t(T, \varepsilon')$ to predict $K_\mu(T)$.
- The corresponding $K_{Jc}(T)$ MC predictions are shown in Figure 6b. The $K_{Jc}(T)$ are slightly too steep at low T_o but are in better agreement with the MC shape at higher T_o. Likewise, the ΔT_o versus $\Delta\sigma_y$ results in Figure 6c show a curvature that has not yet experimentally proven. A least square fit to the model prediction, shown as the solid line, has a slope of 0.73°C/MPa, which is reasonably consistent with the typical measured values of ≈ 0.7±0.1°C/MPa.

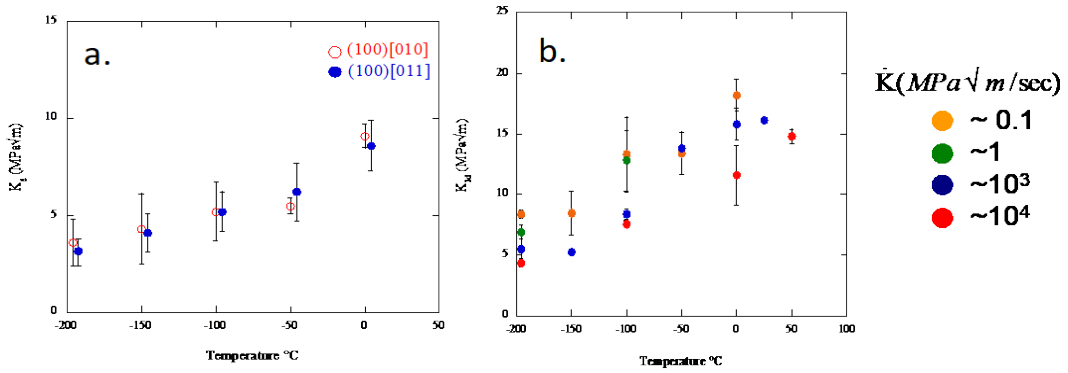

Figure 4. Cleavage oriented Fe single crystal: a) $K_a(T)$; and $K_{Ic}(T)$ for a range of loading rates.

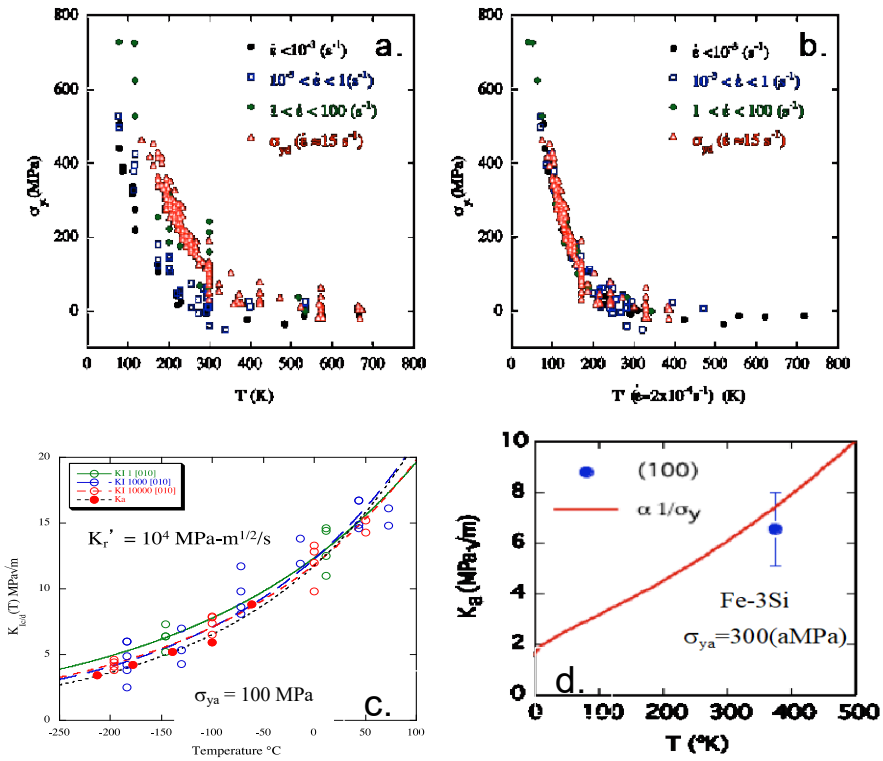

Figure 5. a) The thermally activated $\sigma_{yt}(T)$ at different strain rates; b) the corresponding thermally activated $\sigma_{yt}(T')$ plotted on a strain rate compensated T' scale; c) the master curve for the cleavage oriented single crystal Fe K_a and K_{Ic} data versus T, adjusted to a common dynamic K' loading rate $K_{Ia}(T')$ with the same dynamics as for $\sigma_{yt}(T')$; $K_a(T)$ for F-3Si [8].

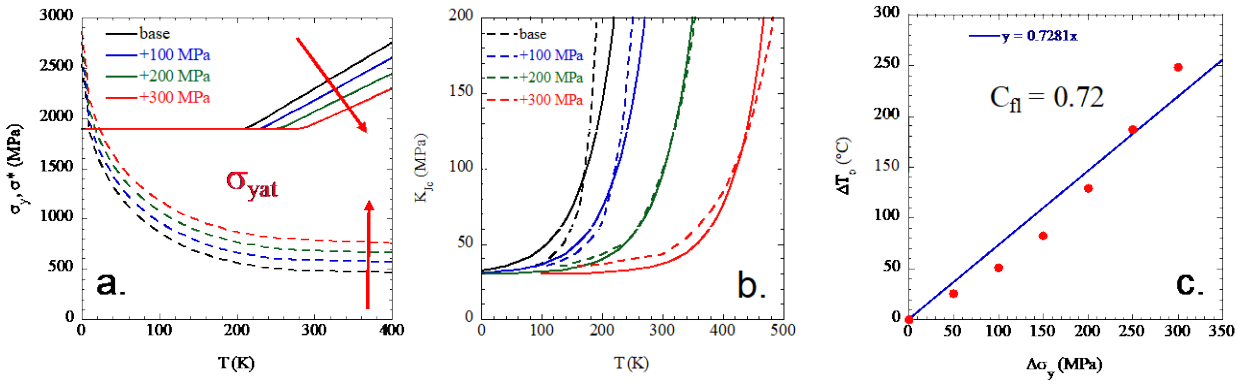

Figure 6. a). σ_y(T) contributions due to irradiation hardening from 0 to 300 MPa, and the corresponding σ^*(T) based on the dislocation confinement model; b) the predicted and nominal K_{Jc}(T) MCs as a function of $\Delta\sigma_y$, with the shaded band showing the range of most experimental data; and c) the corresponding predicted ΔT_o vs. $\Delta\sigma_y$ with a linear best fit slope of 0.72°C/MPa.

- Again, the basic physics underlying the K_{Ia} model was illustrated in Figure 2d. Locally semi-brittle cleavage occurs when the slip of dislocations in the ferrite matrix, at the tip of the microcrack propagating from the broken trigger particle, is blocked, such that further nano-blunting and stress field shielding is exhausted. Since dislocation slip ceases, the local microcrack stress intensity faction (k_t), and associated elastic stress field and Griffith energy release rate balance are sufficient for the microcrack to propagate by breaking atomic bonds, at $k_t = K_\mu$, without further plastic energy dissipation, again as schematically illustrated in Figure 2d and e. The high velocity of the microcrack, and correspondingly high strain rates, contribute to the cessation of slip and the corresponding high local k_t and elastic stresses.
- If this condition is not met, at temperatures above the BDT, the microcrack simply arrests.
- Such dislocation confinement increases with the total alloy σ_{yd}, hence, the corresponding K_μ is expected to vary with $1/\sigma_{yd}$. Thus, K_μ is not an intrinsic property of the ferrite lattice.
- While it generally cannot be directly measured, the cleavage oriented single crystal K_{Ia}(T) is a reasonable surrogate measure of K_μ(T).
- As expected, the K_{Ia}(T) curves are shifted to higher temperatures with increasing alloy strength.
- The increasing BDT with σ_{yd} and the resulting increased temperature dependence of K_μ are approximately sufficient to compensate for the reduced temperature dependence of σ_y(T). This prevents the layover in the K_{Jc}(T)
- The interplay of these dislocation mediated mechanisms results in an approximately constant MC shape and ΔT_o values that are close to experimental observations.

Clearly, this dislocation confinement model is oversimplified. For example, it assumes that the macroscopic K_{Ia}(T) is a surrogate for the micro K_μ(T), which may not be entirely valid. Nevertheless, given its physical underpinning, the K_{Ia}(T) model provides a good basis for predicting MC shapes and ΔT_o shifts due to irradiation hardening.

Irradiation Hardening and Helium Embrittlement

The irradiation induced ΔT_o shifts in the MC are typically associated with irradiation hardening ($\Delta\sigma_y$) as outlined in the previous section. However, there are also several non-hardening embrittlement mechanisms that can occur in neutron irradiated steels. These mechanisms include temper embrittlement, due to P segregation to grain boundaries, as well as the precipitation or coarsening of brittle trigger particle phases [9]. These mechanisms are accelerated in time, and occur at lower temperatures, due to radiation enhanced diffusion (RED) and, perhaps, radiation induced segregation (RIS). While temper embrittlement and intergranular fracture, is not observed in 9Cr TMS, modest levels of non-hardening embrittlement occur at

temperatures around 400°C and above, even in cases where the steel softens under irradiation. These non-hardening embrittlement mechanisms are not included in the model described below.

However, as shown in Figure 7, high concentrations of helium, primarily produced in spallation proto-neutron irradiations, results in severe embrittlement, with ΔT_o much greater than due to irradiation hardening alone. The helium synergistically both weakens grain boundaries, leading to brittle intergranular fracture, and increases $\Delta\sigma_y$. Helium induced $\Delta\sigma_y$ is also relatively athermal and extends the hardening temperature regime to more than 500°C [10].

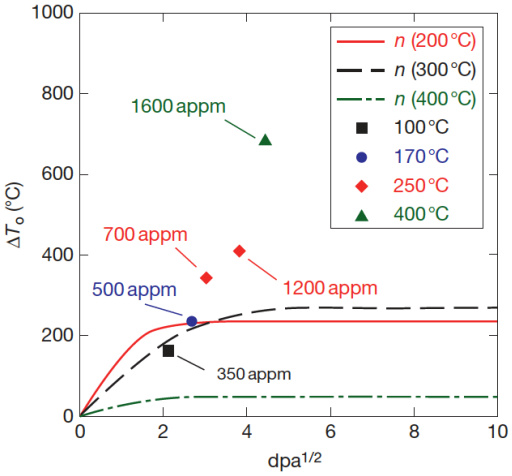

Figure 7. The severe embrittling effect of high SPI He on ΔT_o [10].

Figure 8 summarizes the results of a model of $\Delta\sigma_y$(dpa, He/dpa, T) for a He/dpa = 10 in units of appm/dpa, where T is the irradiation and test temperature from 300 to 550°C. This hardening model can be used to predict the ΔT_o for cleavage as outlined above. However, as previously noted, helium also weakens grain boundaries, reducing the intergranular fracture stress (σ_{IG}). When σ_{IG} is < σ^* hardening and non-hardening He mechanisms synergistically interact to produce enormous ΔT_o as illustrated in Figure 8.

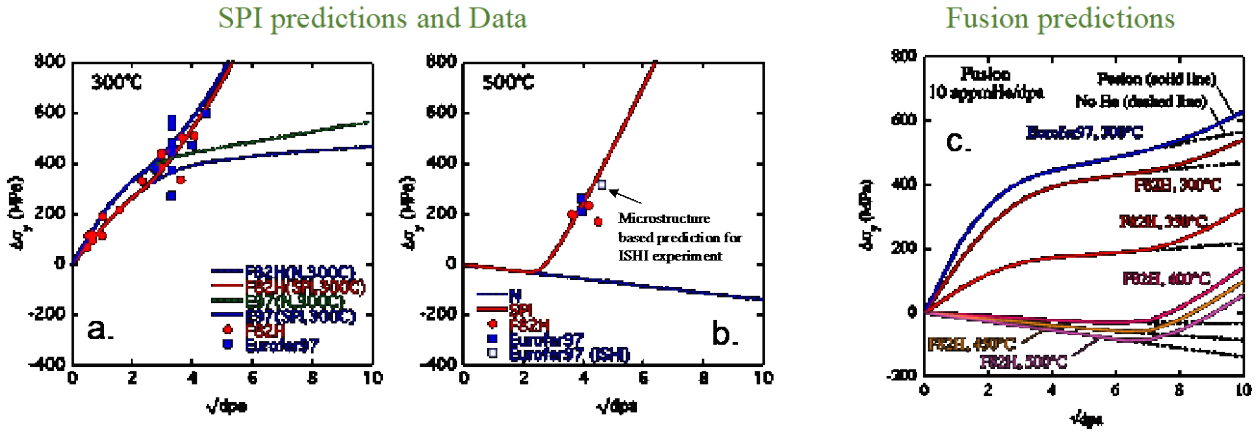

Figure 8. In a) and b) Fitted SPI $\Delta\sigma_y$ vs. √dpa at 300 and 500°C, respectively, including SPI high He contributions; and c) models of as a function of temperature with and without He hardening.

While several modeling studies have explored the effect of helium on grain boundary strength, we have adopted a simple empirical approach treating the effect of He on σ_{IG}. We know that σ^* for cleavage is less

that σ_{IG} without He; and that the maximum σ^* is ≥ 3GPa. We also use literature data [11-13] to estimate σ_{IG}(He). The resulting σ_{IG} model is simply

$$\sigma_{IG} = 3\ \text{GPa} - \text{He}[0.9\text{MPa/He}]. \quad (2)$$

Of course, this simple model can be refined later.

The base irradiation hardening - cleavage fracture MC models for RPV steels shown in Figure 6 was refitted to the F82H steels properties including the typical baseline $\sigma_y \approx 538$ MPa and $T_o \approx -103$°C [14]. The key fitted local fracture criteria were minimum $K_{Ia} \approx 3$ MPa$\sqrt{m}$; $A^* \approx 0.5 \times 10^{-6}$ m^2; $\sigma^* \approx 2000$MPa.

Results

Figure 9 shows predicted K_{Jc}(T) curves: the green curve is for cleavage with dpa and He hardening; the red solid curve includes the effect of reductions in σ_{IG} by He. The predictions are compared to measured toughness of spallation proton irradiated (SPI) F82H steels [10,15]. The irradiation conditions are a) 9.1 dpa and 532 appm He at 250°C; b) 14.7 dpa and 1176 appm He at 250°C; and c) 19.5 dpa and 1560 appm He at 400°C. The reported K_{Jq} 108, 53 and 31 MPa$\sqrt{m}$ values were adjusted for the specimen size effects due to statistical thickness and constraint loss. The data points represent the average of the statistically adjusted K_{JB} and statistical and constraint loss adjusted K_{Jr}, toughness values. The error bars show the range of those values. The K_{Jc}(T) considering σ_{IG} in equation (2) show significantly lower toughness, and hence larger temperature shifts in all cases, due to the σ_{IG} decreases below the cleavage stress as shown in Figure 10. In the case of 532 appm He, $\sigma_{IG} < \sigma_c$ only at T > ≈ 200°C. is reflected by the corresponding toughness curve shape change. For higher He concentration, $\sigma_{IG} < \sigma_c$ at all T, so that the K_{Jc}(T) curves are monotonic, and much lower compared to the K_{Jc}(T) for only hardening. The T shifts are underpredicted by the model at 532 appm He and fall on the lower shelf at higher He. Clearly the K_{Jc}(T) prediction for the highest He case with only moderate hardening is consistent with a transition to intergranular fracture as illustrated in Figure 10b. Unfortunately, there is no data at higher K_{Jc}(T).

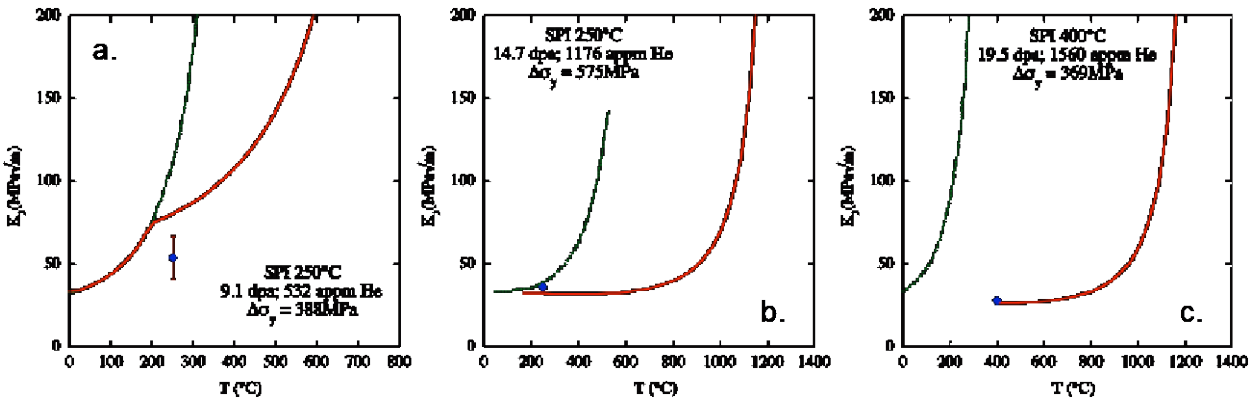

Figure 9. Predicted K_{Jc}(T) curves at different temperatures, dpa and He compared to data from SPI. The green curve shows the effect of hardening, including he contributions, while the red curve shows the synergistic effect of He on IG fracture.

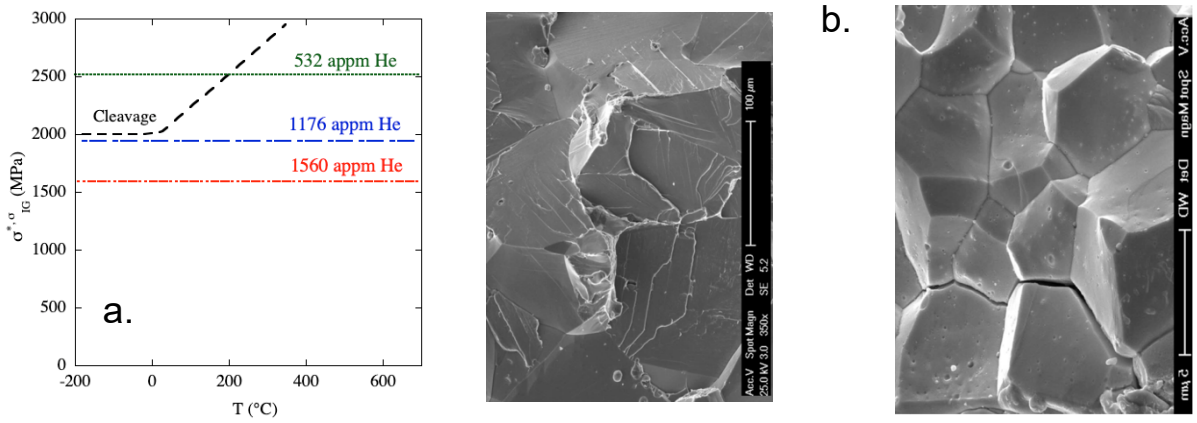

Figure 10. In a) $\sigma^*(T)$ and $\sigma_{IG}(T, He)$ for the models shown in Figures 9a-c along with $\Delta\sigma_y$ = 388, 575 and 369 MPa, respectively; and b) examples of cleavage and IG fracture.

The model was used to predict $K_{Jc}(T)$ curves for fusion relevant irradiation conditions at He/dpa = 10 for irradiation temperatures from 300 to 500°C, as shown in Figures 11 and 12. Figure 11 shows $K_{Jc}(T)$ curves shifting for a 300°C FRI irradiation to 4 to 36 (a), 64 (b) and 100(c) dpa. The solid black curve is the unirradiated $K_{Jc}(T)$. Figure 11a shows the shifts for the 4 and 16 dpa are only due to neutron dpa hardening and are not affected by 40 and 160 appm He. The dashed green curve at 36 dpa reflects hardening contributions to the shift from both dpa and 360 appm He, while the corresponding red curve shows the additional effect of He induced intergranular fracture at higher T, increasing the shift and changing the shape of the $K_{Jc}(T)$ curve. Figure 11b shows similar, but even more pronounced, IG fracture effects at higher 640 appm He, with the shape change occurring at lower T and KJc. The $K_{Jc}(T)$ curve Figure 11c at the highest 1000 appm. Is for IG fracture at all temperatures.

Figure 12 shows summary of the reference temperature shift, ΔT_o, at K_{Jc} = 100 MPa√m, as a function of dpa, for irradiation temperatures from 300 to 500°C. The black diamonds show the ΔT_o due to dpa hardening only, the blue unfilled squares show that additional ΔT_o because He contributions to hardening, and red circles show the overall effects of dpa and He on hardening and IG fracture. ΔT_o due to all the effects. Clearly, the synergistic effects of He on $\Delta\sigma_y$(dpa, He) and σ_{IG}(He) are enormous.

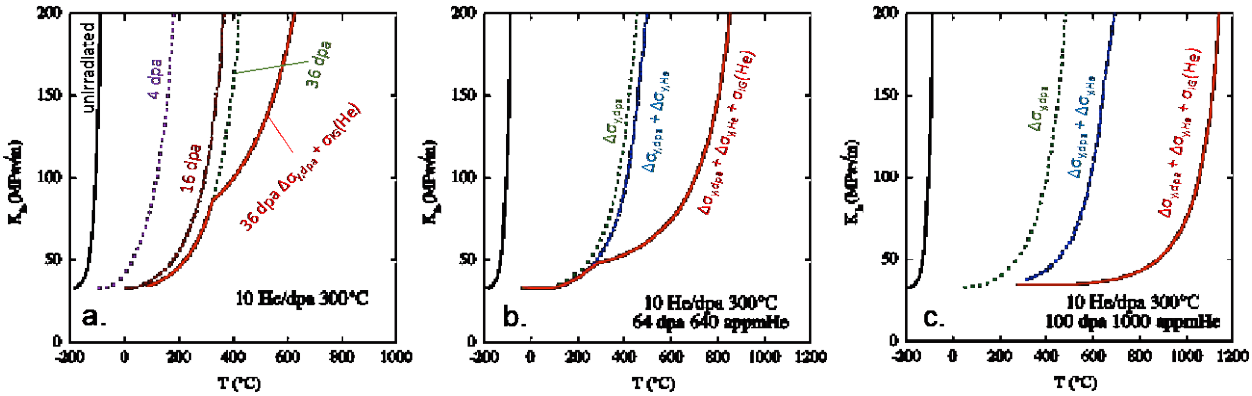

Figure 11. Predicted $K_{Jc}(T)$ at various He and dpa at 300°C: a) 0 to 36 dpa and 40, 160 and 360 appm He; b) 64 dpa and 640 appm He; c) 100 dpa and 1000 appm He. The black curve if for the unirradiated condition and the dashed and dotted curves are for irradiation hardening only. The shape change in the solid red curve at 35 and 64 dpa are due to the transition to IG fracture at higher temperatures. For 100 dpa IG fracture occurs at all temperatures.

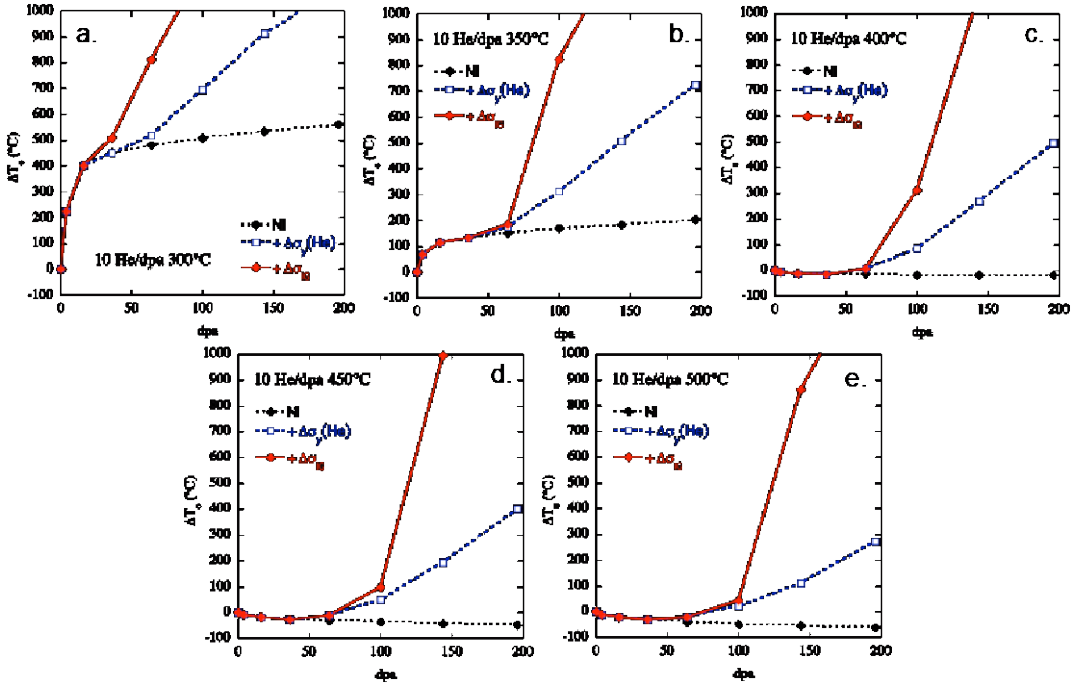

Figure 12. In a - e) Predicted DTo for 300 to 500°C showing low He, dpa and He hardening and dpa and He hardening with IG fracture.

As noted above, we are not aware of K_{Jc} data for steels with high He contends that are further up in the brittle fracture transition, which could be used to validate the results shown in Figures 11 and 12. However, there are Charpy data that support the predicted trends. In a previous publication we used both Charpy and disk bend test data to characterize the severe effects of hardening-He intergranular fracture synergisms. We showed that the effect of He on IG fracture is reflected in an increase in the ratio of Charpy shifts (ΔTc) to yields stress changes ($\Delta\sigma_y$): $C_c(He) = \Delta T_c/\Delta\sigma_y$ (°C/MPa). Figure 13 plots observed C_c and the predicted $C_o = \Delta T_o/\Delta\sigma_y$, as a function of He. It is well known that C_c is less than C_o so the absolute values are expected. However, what is significant is that both show very similar trends in C_c and C_o as a function of He up to ≈700 appm. This lends strong support the fusion relevant embrittlement model, which we have proposed. Future efforts will focus on obtaining additional K_{Jc} and other relevant data.

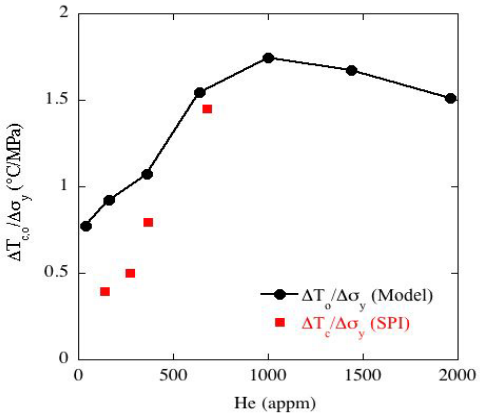

Figure 13. Predicted $\Delta T_o/\Delta\sigma_y$ and measured Charpy $\Delta T_c/\Delta\sigma_y$ vs. He, showing similar increasing embrittlement trends.

Future Work

The model results in Figure 12 can be used to assess the temperature-dpa window of TMS fusion first wall service. As an example, if the ΔT_o = 300°C is specified as an embrittlement limit the corresponding dpa versus temperature are shown in Figure 14. This suggests that there is a significant embrittlement advantage to service at temperatures around 400°C, However, higher temperatures provide little or no additional embrittlement advantage. Of course, there are large uncertainties in the model which will require additional spallation proton irradiation data to address.

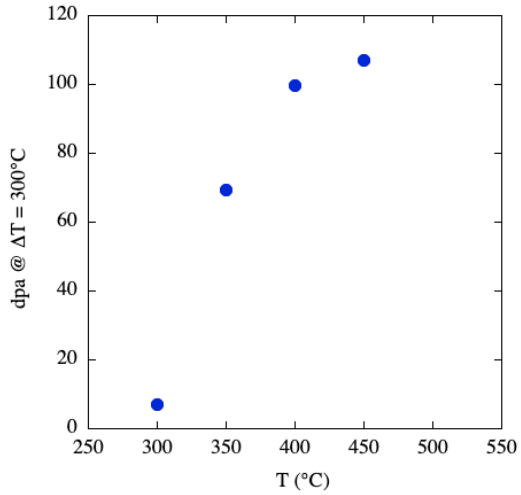

Figure 14. Dpa at ΔT_o = 300°C vs. temperature.

Acknowledgments

This work was supported by the U.S. Department of Energy, Office of Fusion Energy Sciences, under the contract DE-FG03-94ER54275.

References

[1] ASTM standard E 1921-20, ASTM International (2020).
[2] G.R. Odette, T. Yamamoto, H.J. Rathbun, M.L. Hribernik, J.W. Rensman, J. Nucl. Mater. 323 (2003) 313.
[3] G.R. Odette, H.J. Rathbun, M. Hribernik, T. Yamamoto, M. He, P. Spatig, "A Multiscale Approach to Measureing and Modeling Cleavage Fracture Toughness in Structural Steels," In: V. Ghetta, D. Gorse, D. Maziere, V. Pontikis eds. *Materials Issues for Generation IV Systems*, Springer, Dordrecht (2008).
[4] G.R. Odette, M.Y. He, "A Cleavage Toughness Master Curve Model," J. Nucl. Mater. 283-287 (2000) 120.
[5] M.L. Hribernik, *Cleavage Oriented Iron Single Crystal Fracture Toughness*, Ph. D Thesis, University of California Santa Barbara (2006).
[6] M.L. Hribernik, G.R. Odette, M.Y. He, "On the Intrinsic Initiation and Arrest Cleavage Fracture Toughness of Ferrite," *Fusion Materials Semiannual Report 7/1 to 6/30/2005* DOE/ER-313/38 (2005) 109.
[7] M.L. Hribernik, G.R. Odette, M.Y. He, "On the Intrinsic Initiation and Arrest Cleavage Fracture Toughness of Ferrite," *Fusion Materials Semiannual Report 7/1 to 6/30/2006* DOE/ER-313/40 (2006) 74.
[8] Y. Qiao and A.S. Argon, Mech. Mater. 35 (2003) 903.
[9] T. Yamamoto, G.R. Odette, H. Kishimoto, J-W. Rensman, P. Miao, *J. Nucl. Mater.* 356 (2006) 27.
[10] Y. Dai, G.R. Odette, T. Yamamoto, *The Effects of helium on irradiated structural alloys, in Comprehensive Nuclear Materials, R. Konings, T. R. Allen, R. E. Stoller, S. Yamanaka Eds. (2012) Elsevier.*

[11] J. Henry, L. Vincent, X. Averty, B. Marini, P. Jung, J. Nucl. Mater. 356 (2006) 78.
[12] J. Malaplate, L. Vincent, X. Averty, J. Henry, B. Marini, Eng. Fract. Mech. 75 (2008) 3570.
[13] J. Henry, X. Averty, Y. Dai, J.P. Pizzanelli, J. Nucl. Mater. 377 (2008) 80.
[14] G.R. Odette, T. Yamamoto, H. Kishimoto, M. Sokolov, P. Spatig, W.J. Yang, J.-W. Rensman, G.E. Lucas, "A Master Curve Analysis of F82H using Statistical and Constraint Loss Size Adjustments of Small Specimen Data," J. Nucl. Materl 329-333 (2004) 1247.
[15] X.Jia, Y. Dai, "The Change of Fracture Toughness of Martensitic Steels after Irradiation in SINQ Target-3," J. Nucl. Mater. 356 (2006) 50.

9.4 MODELING MICROSTRUCTURAL EFFECTS ON THE MECHANICAL BEHAVIOR AND DAMAGE DEVELOPMENT IN DUCTILE-PHASE TOUGHENED TUNGSTEN COMPOSITES—Ba Nghiep Nguyen, Jing Wang, Charles H. Henager Jr., James V. Haag IV, Wahyu Setyawan (Pacific Northwest National Laboratory)

OBJECTIVE

The objective of this research is to investigate the effects of the microstructure obtained from processing and forming of ductile phase toughened (DPT) tungsten (W) composites on the mechanical behavior and damage development in these materials. This investigation aims to elucidate the microstructural factors that control strength, ductility, and toughness of DPT-W composites. Two W composites have been studied: the as-formed 90 wt%-W/nickel-iron (Ni-Fe) composite (90W) and the 87% thickness-reduction material (90W-87R) hot-rolled from the as-formed one.

SUMMARY

The finite-element microstructural approach previously developed [1-2] was applied to analyze and compare the as-formed 90W to hot-rolled 90W-87R composites. The 90W consists of mostly spheroidal W particles while the 90W-87R possesses a lamellar-like microstructure. Under ideal rolling conditions where the 90W-87R composite was modeled to contain highly elongated W lamellae with no defects, its behavior was predicted to exhibit significantly higher strength and fracture strain than the 90W material. However, processing defects such as weak W-W boundary regions present in the hot-rolled composite have significantly reduced its mechanical performance. In this study different microstructural representations for both composites, that captures microstructural features such as W-W boundaries, W subdomains, and W regions completely separated by Ni-Fe phases, were investigated using this microstructural approach to elucidate factors that govern the mechanical performance of these composites.

PROGRESS AND STATUS

Introduction

The W-alloys and W-composites are being studied as potential structural materials for plasma-facing components (PFCs) of future fusion reactors due to their high melting point, strength at high temperatures, high thermal conductivity, low coefficient of thermal expansion, and low sputtering yield [3-6]. Tough composites are particularly needed since pure W exhibits little ductility and becomes brittle in the neutron irradiation environment [4,7]. To engineer a tough material, an approach is to make a composite in which W is embedded in a ductile phase to improve the ductility and fracture toughness. Previously, a finite-element (FE) multiscale microstructural approach was developed to investigate the deformation and fracture behavior of ductile-phase toughened (DPT) W materials such as W/copper (W/Cu) [1] and W/Ni-Fe composites [2]. This approach models the elastic-plastic deformation that is coupled to damage of individual phases discretized in finite elements in a microstructural domain. The microstructural domain reflects an actual microstructure from an SEM image. The approach allows to effectively describe various mechanisms, including ductile-phase toughening, responsible for increased strength and ductility of the composites. In addition, it was employed to explore artificially designed hierarchical lamellar-like and brick-and-mortar (BAM) microstructures. We showed that strength and ductility of BAM microstructures can be tailored by adjusting the brick aspect ratio [2].

In the previous semiannual report [8], we presented preliminary results based on this microstructural approach to compare the 90W to 90W-87R composites. Reference [8] discussed microdefects caused by processing such as weak W-W boundary regions present in the hot-rolled 90W-87R composite that significantly lowered the strength and failure strain of this composite. During the current reporting period, the microstructural effects were further investigated. Different microstructural domain representations for both 90W and 90W-87R composites were generated using the OOF2 software [9] and analyzed by the ABAQUS FE code to elucidate factors that govern the mechanical performance of these composites. This

work was presented at 18th International Conference on Plasma-Facing Materials and Components for Fusion Applications [10].

Model Development

A domain (Figure 1a) located on the symmetry axes and covering a half of a tensile specimen width was modeled and discretized in two-dimensional finite elements based on an SEM image using the OOF2 software [9]. The SEM image captures different phases (regions) and their distributions inside the domain. Figure 1b illustrates the FE plane-stress model of a microstructural domain (0.584 mm x 0.584 mm) from a 90W specimen with boundary conditions applied to simulate the tensile test. Fixed displacements in the *x*- and *y*-directions are respectively applied along the vertical left and bottom boundaries while uniform displacements in the *x*-direction are applied incrementally on the vertical right boundary until a complete failure of the domain occurs. Figure 1c presents a magnified view of a local region showing the detailed mesh inside the domain. The method used to develop a microstructural FE model for the simulation of tensile tests was also applied to the 90W-87R material as it was previously reported [2,8]. In the present report, we illustrate different FE models created by the same method that can capture some key microstructural features or microdefects present in the actual composites (90W or 90W-87R) such as W-W boundaries, W subdomains, and W regions or particles completely separated by Ni-Fe phases. Figures 2 to 4 show the typical microstructural FE models developed for the 90W. The models for the 90W-87R are given in Figures 5 to 7.

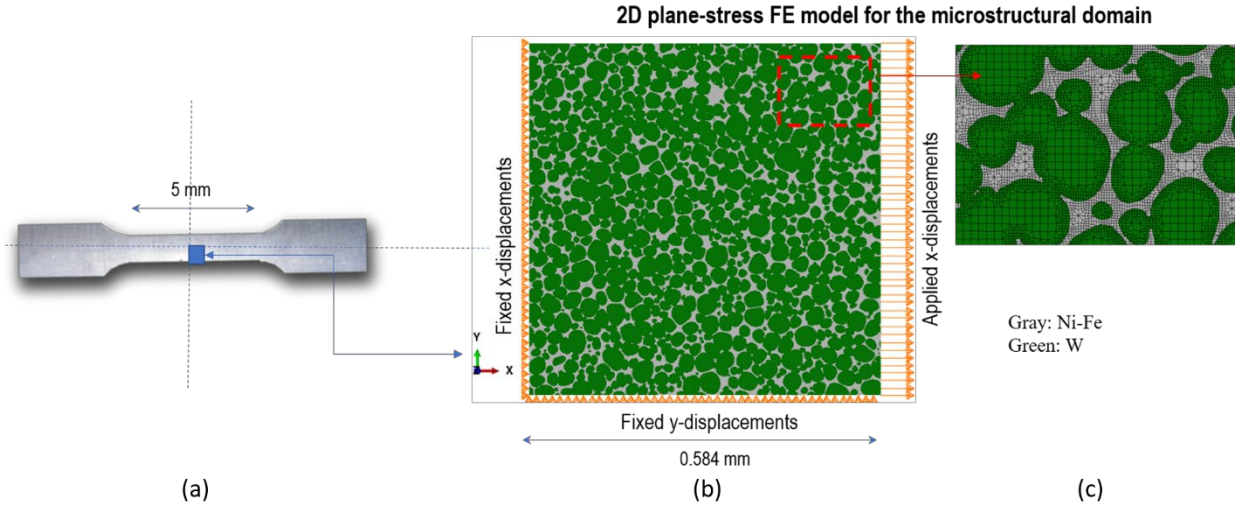

Figure 1. (a) The SEM image from a 0.584 mm x 0.584 mm domain (blue square) of a tensile 90W specimen is used to obtain a digital image for (b) developing a microstructural FE model, and (c) a magnified view showing the local mesh details.

A rate-independent elastic-plastic ductile damage model with isotropic damage and hardening from ABAQUS was used for the simulations. In this model, damage affects the elastic modulus as $E = E_0(1 - D)$ where D is the phenomenological damage variable and E_0 is the elastic modulus of the undamaged material. Failure occurs if the failure criterion (indicator) $\int \frac{d\bar{\varepsilon}_p}{\bar{\varepsilon}_p^D} = 1$ where $\bar{\varepsilon}_p^D$ is the equivalent plastic strain at fracture initiation. We used the same elastic properties previously determined for W and Ni-Fe reported in References [2, 8]. In addition, this elastic-plastic model requires the yield stress versus equivalent plastic strain and fracture energy input data for the constituent phases. The fracture energy was defined as the strain energy at complete fracture. As discussed in our previous report [8], initial guesses for yield stress versus equivalent plastic strain for W and Ni-Fe were obtained using the Ramberg-Osgood's relation. A simple elastic-plastic behavior for W-W boundaries was assumed in the analyses that included these boundaries. Numerical analysis trials using a FE microstructural model (that contains W-W boundaries) for

90W and another for 90W-87R were conducted to match the corresponding stress-strain data and crack pattern to adjust the model parameters for each composite. Subsequently, the same set of model parameters were used in the analyses of all the other microstructural models for each composite, respectively.

Tables 1 and 2 gather the model parameters for the 90W and 90W-87R used in the analyses. Figure 8 shows the yield stress versus equivalent plastic strain data determined for the constituent materials in these composites.

Table 1. Model parameters for the constituent materials in 90W

Constituent Material	Elastic Modulus (MPa)	Poisson Ratio	Strength (MPa)	Fracture Strain	Fracture Energy (MPa)
Ni-Fe	203570	0.304	880	0.9	4
W	383000	0.28	1170	0.35	5
W-W Boundary	203570	0.304	950	0.3	5

Table 2. Model parameters for the constituent materials in 90W-87R

Constituent Material	Elastic Modulus (MPa)	Poisson Ratio	Strength (MPa)	Fracture Strain	Fracture Energy (MPa)
Ni-Fe	203570	0.304	806	0.65	4
W	383000	0.28	1125	0.35	10
W-W Boundary	203570	0.304	756	0.3	5

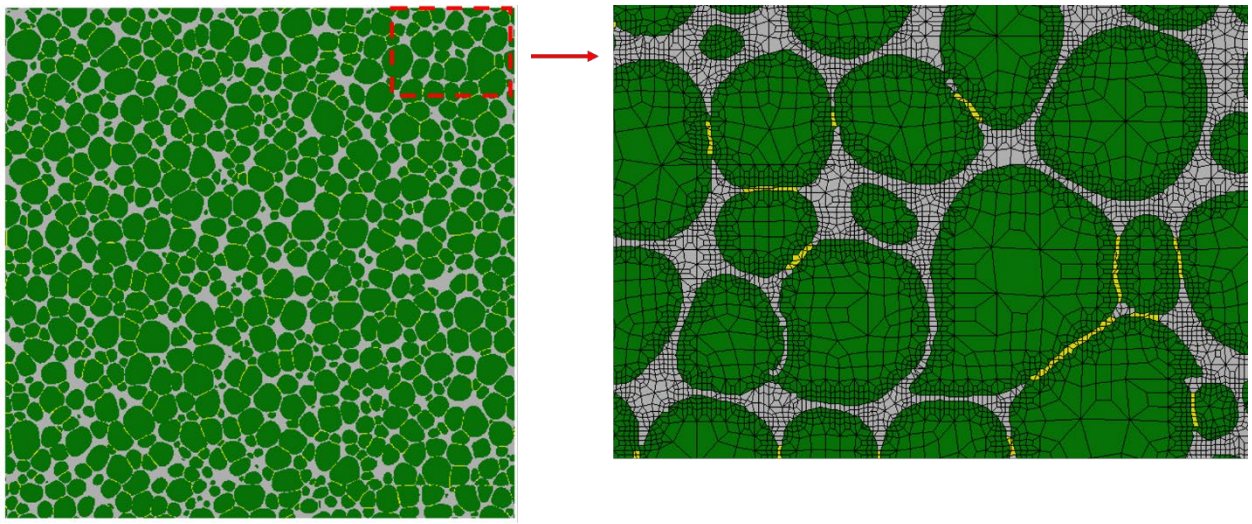

Figure 2. (a) A microstructural FE model for 90W with W-W boundaries, and (b) a magnified view showing the local mesh details (green: W; gray: Ni-Fe; yellow: W-W boundaries).

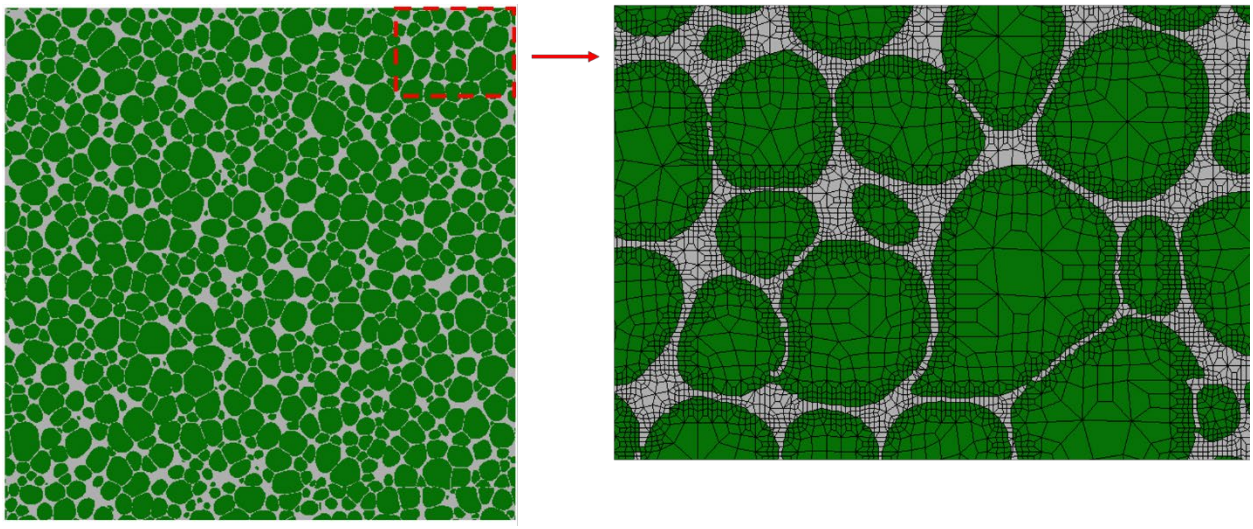

Figure 3. (a) A microstructural FE model for 90W with W particles completely separated by the Ni-Fe phase, and (b) a magnified view showing the local mesh details (green: W; gray: Ni-Fe).

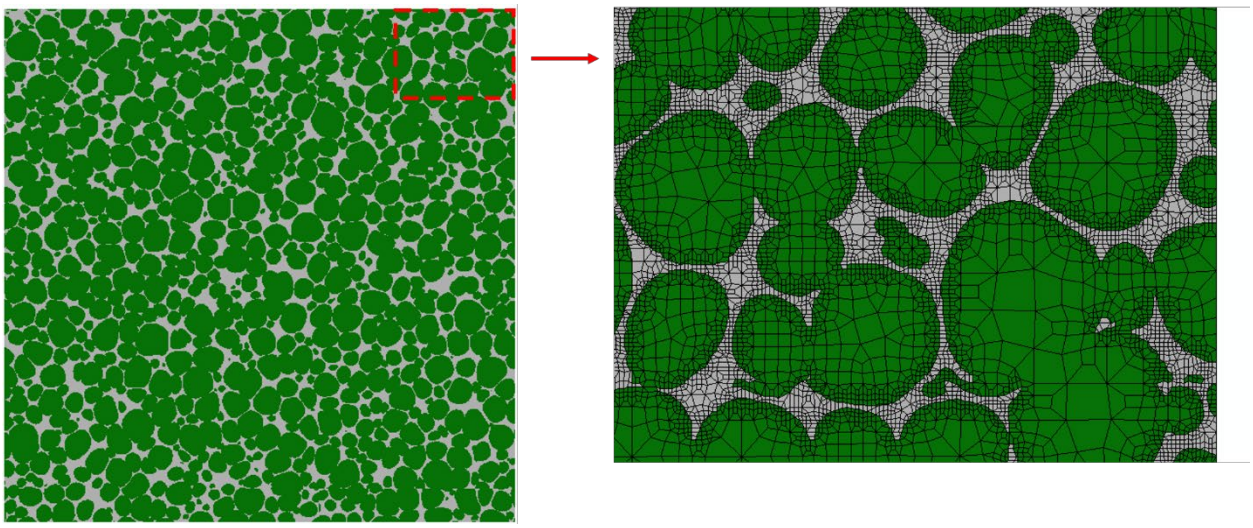

Figure 4. (a) A microstructural FE model for 90W with W sub-domains, and (b) A magnified view showing the local mesh details (green: W; gray: Ni-Fe).

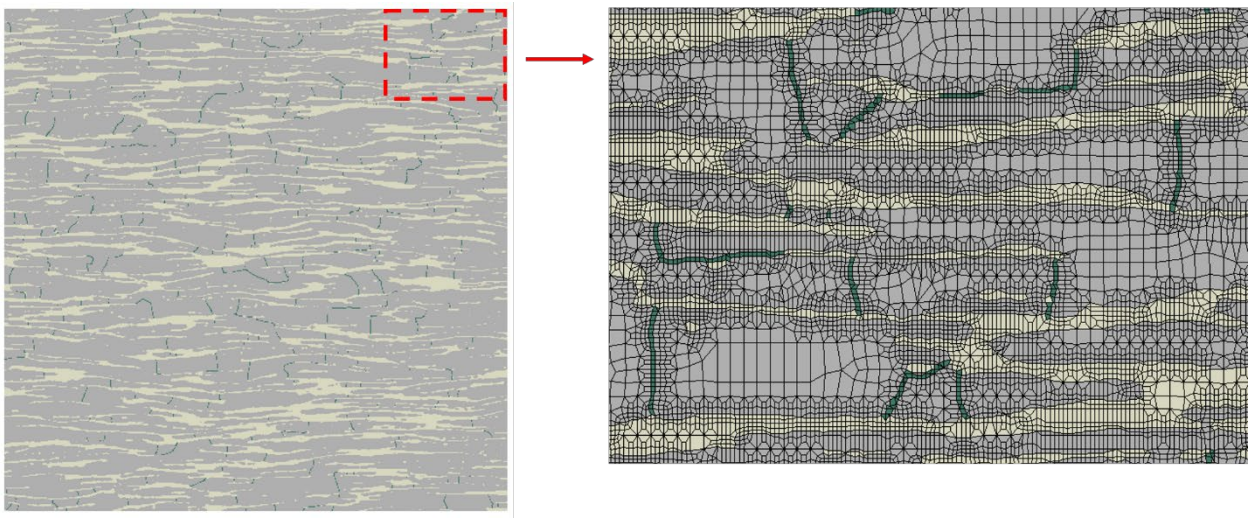

Figure 5. (a) A microstructural FE model for 90W-87R with W-W boundaries, and (b) a magnified view showing the local mesh details (gray: W; light brown: Ni-Fe; green: W-W boundaries).

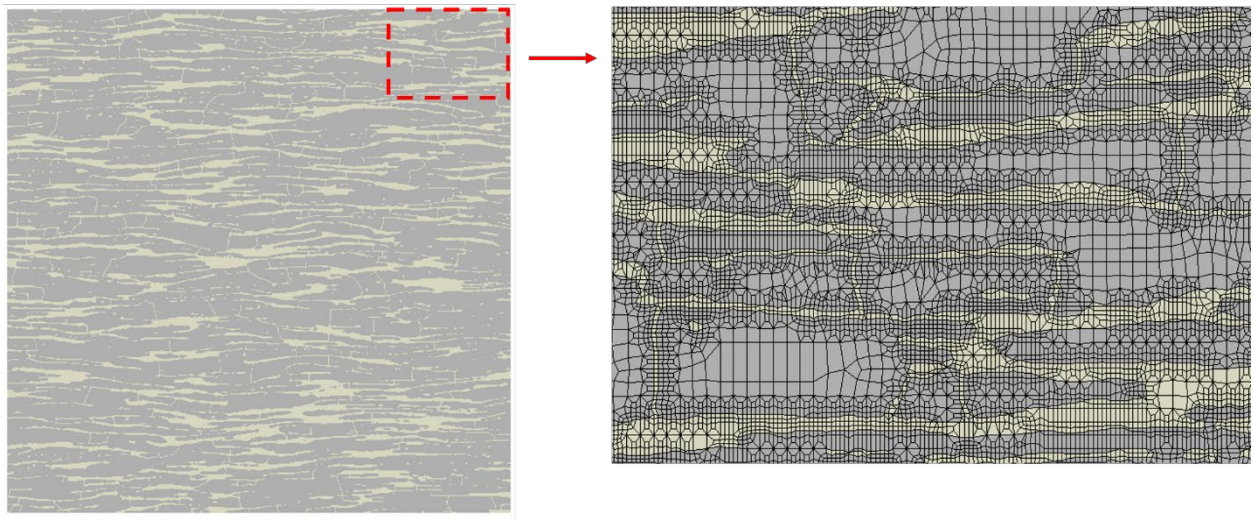

Figure 6. (a) A microstructural FE model for 90W-87R with nearly vertical W-W boundaries replaced by Ni-Fe, and (b) a magnified view showing the local mesh details (gray: W; light brown: Ni-Fe).

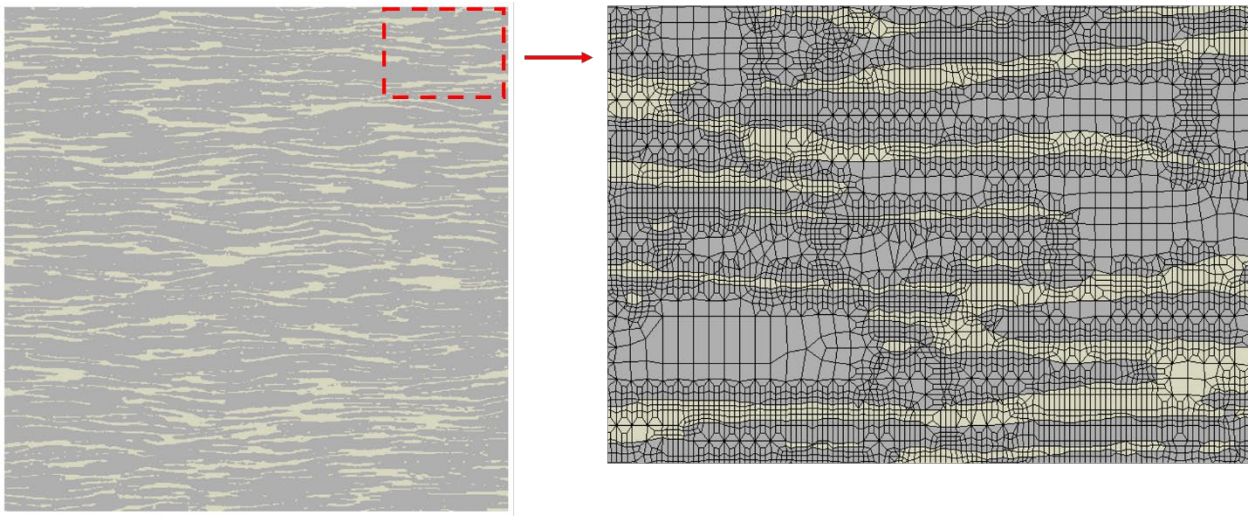

Figure 7. (a) A microstructural FE model for 90W-87R containing highly elongated W lamellae without W-W boundaries, and (b) a magnified view showing the local mesh details (gray: W; light brown: Ni-Fe).

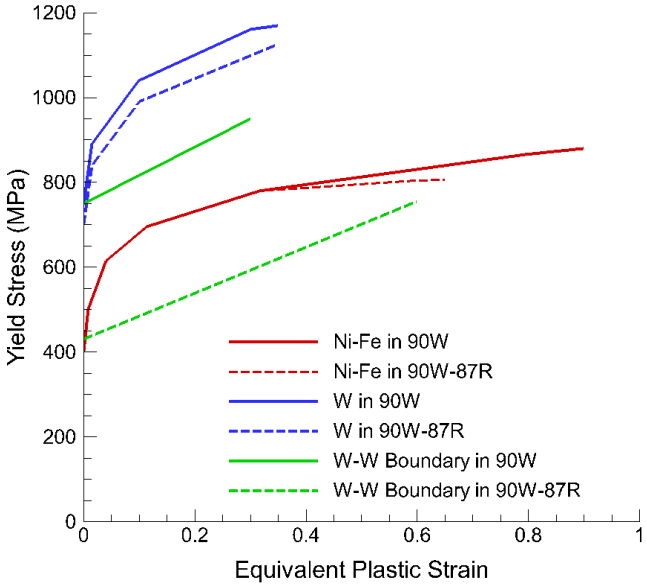

Figure 8. The yield stress versus equivalent plastic strain inputs determined for the constituent materials in the 90W and 90W-87R composites.

Results

Representative microstructural domains for each composite (90W or 90W-87R) were analyzed with ABAQUS. Each domain model captures selected key microstructural features such as W-W boundaries, W subdomains, W particles completely separated by Ni-Fe phases, etc. summarized as follows:

90W microstructure models incorporating

- W-W boundaries between several W particles (Figure 2),

- W particles completely separated by Ni-Fe (Figure 3), and
- W subdomains formed among several W particles (Figure 4).

90W-87R microstructure models incorporating

- W-W boundaries between several W lamellar-type regions (Figure 5),
- W-W boundaries filled with Ni-Fe (Figure 6), and
- Highly elongated W lamellae without W-W boundaries (Figure 7).

Figure 9 shows the damage distributions and crack patterns predicted for the 90W domain models at 13% applied strain. In the model with W-W boundaries (Figure 9a), microcracks initiate from Ni-Fe regions and propagate in these regions and along W-W boundaries. Figure 10a gives a magnified view of the damage mechanisms predicted for this case. The model with W particles completely separated by Ni-Fe exhibits similar mechanisms (Figure 9b), but in the absence of W-W boundaries, microcracks initiate and propagate only in Ni-Fe regions. In both models, no microcracks propagate across W particles. The damage and fracture patterns for model with W subdomains (Figure 9c) show microcracks initiate and first propagate in the Ni-Fe regions, but at higher applied strains, microcracks could penetrate W subdomains as illustrated in a magnified view on Figure 10b. A cracked region (Figure 10c) of an SEM image from a 90W tensile specimen tested to failure at about 13% strain reveals most microcracks forming along W-W boundaries. The SEM image given in Figure 10c was taken near the fractured zone from a polished surface.

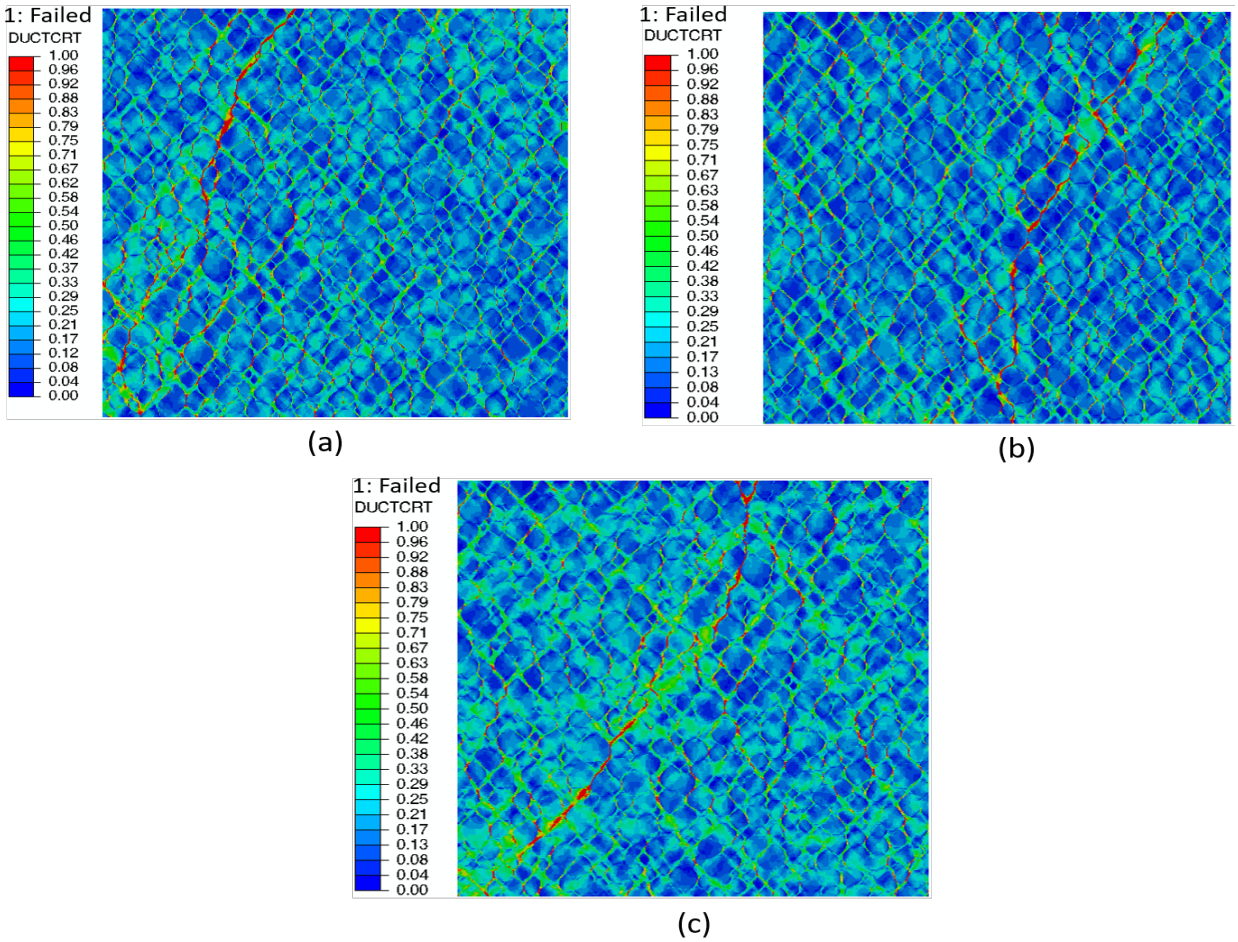

Figure 9. Predicted damage and fracture patterns at 13% applied strain for the 90W microstructural models with (a) W-W boundaries, (b) W particles completely separated by Ni-Fe, and (c) W subdomains.

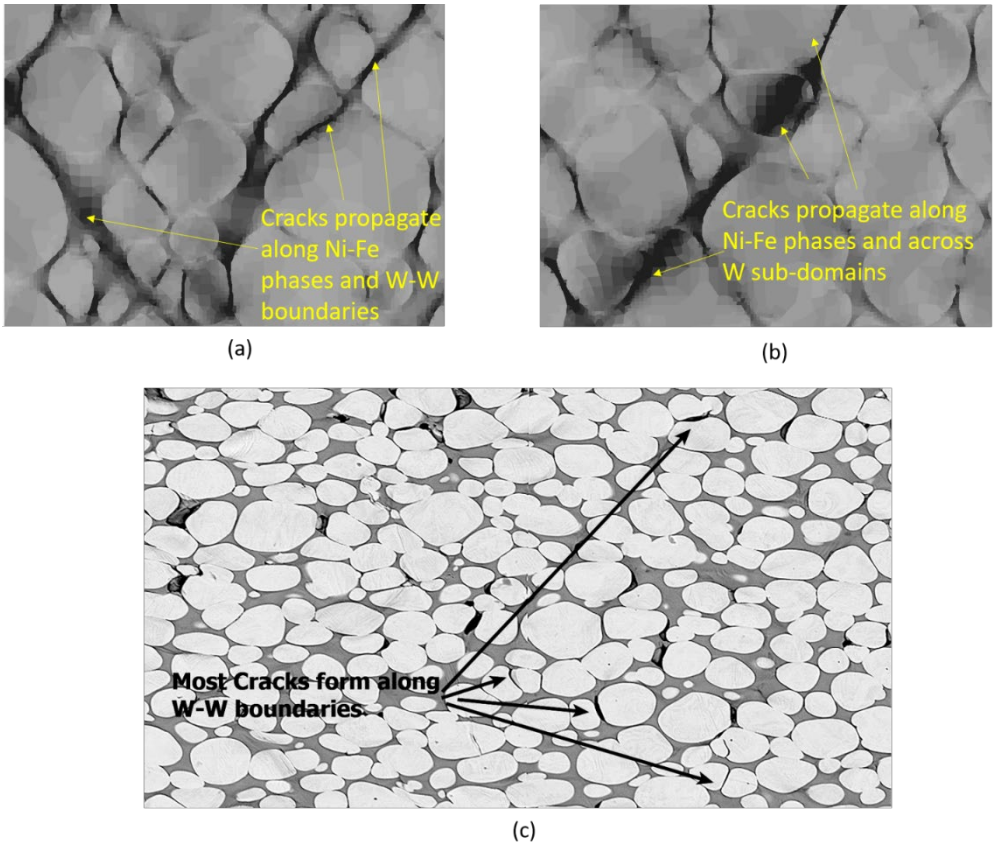

Figure 10. Magnified views of the damage mechanisms predicted at 13% applied strain for the 90W models with (a) W-W boundaries and (b) W subdomains. (c) An SEM image from a 90W tensile specimen tested to failure at about this strain level.

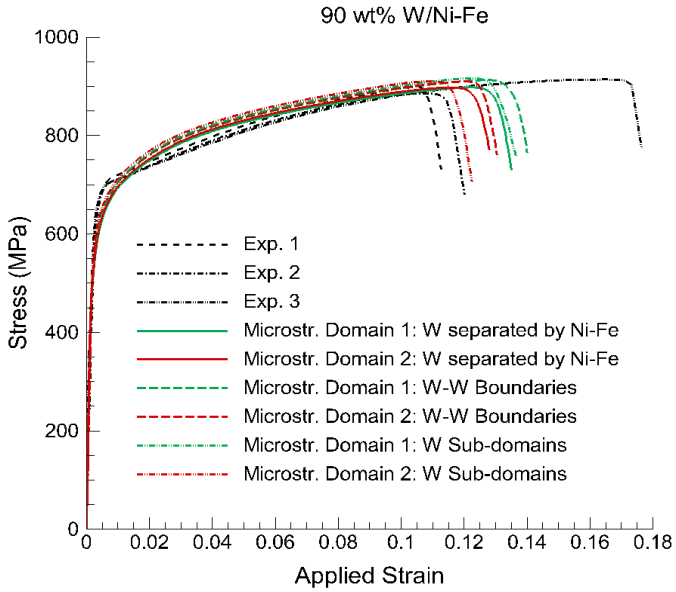

Figure 11. Predicted stress-strain responses for the 90W models compared to the experimental results.

The predicted stress-strain responses for the 90W microstructural models compared to the experimental results are given in Figure 11. The analysis results from the models based on two microstructural domains (numbered 1 and 2) of this composite are illustrated in this figure. Each model from a given domain includes a key microstructural feature discussed above. The predictions agree reasonably well with the measured data and capture not only the microstructural effects in terms of the difference in microstructural features, but also in terms of the microstructural variance reflected in the experimental curves.

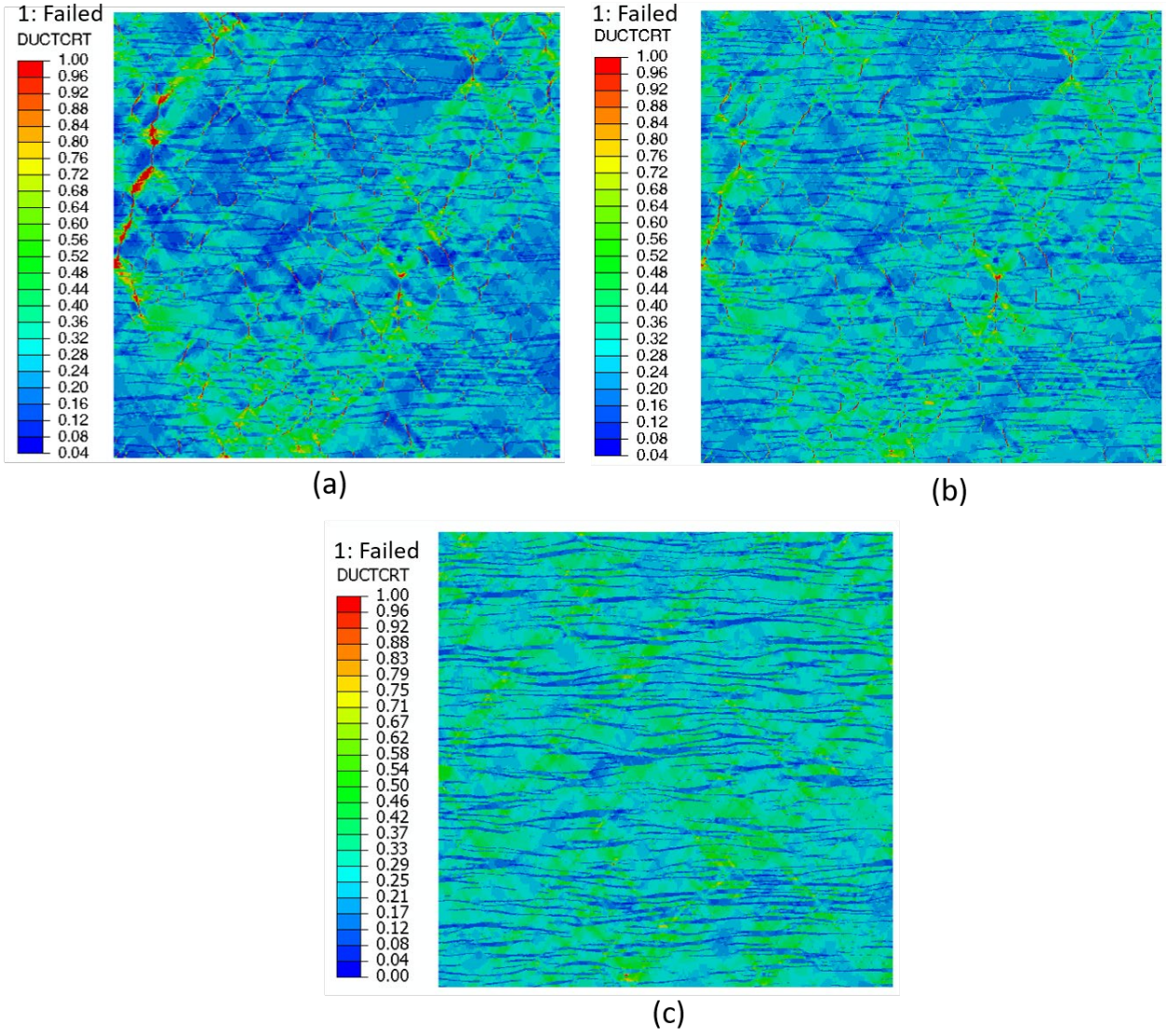

Figure 12. Predicted damage and fracture patterns at 12% applied strain for the 90W-87R microstructural models with (a) W-W boundaries, (b) Ni-Fe filling the W-W boundaries, and (c) Highly elongated lamellar-type W embedded in Ni-Fe without W-W boundaries.

The damage distributions and crack patterns predicted for the 90W-87R microstructural domain models at 12% applied strain are presented in Figures 12(a-c). In the model with W-W boundaries (Figure 12a), microcracks were predicted to initiate from the W-W boundaries nearly perpendicular to the loading direction and propagate first mainly along these boundaries. At higher loading levels, the microcracks linked up and were able to propagate across the W and Ni-Fe regions, as shown in Figure 13a that gives a magnified view of the damage mechanisms predicted for this case. A cracked region (Figure 13b) of an

SEM image from a 90W-87R tensile specimen tested to failure at about 12% strain shows the microcrack linkup and propagating along the W-W boundaries and through the Ni-Fe phase. The SEM image given in Figure 13b was taken near the fractured zone from a polished surface. Assigning the Ni-Fe constitutive properties to the W-W boundaries produced the damage and crack pattern given in Figure 12b. The same damage mechanisms were found in this case, but the extents of microcracking and crack linkup are less pronounced at the same applied strain (12%). Finally, removing the W-W boundaries produced a highly elongated lamellar-type microstructure leading to the damage and crack patterns in Figure 12c that contain only a few isolated microcracks at this applied strain level.

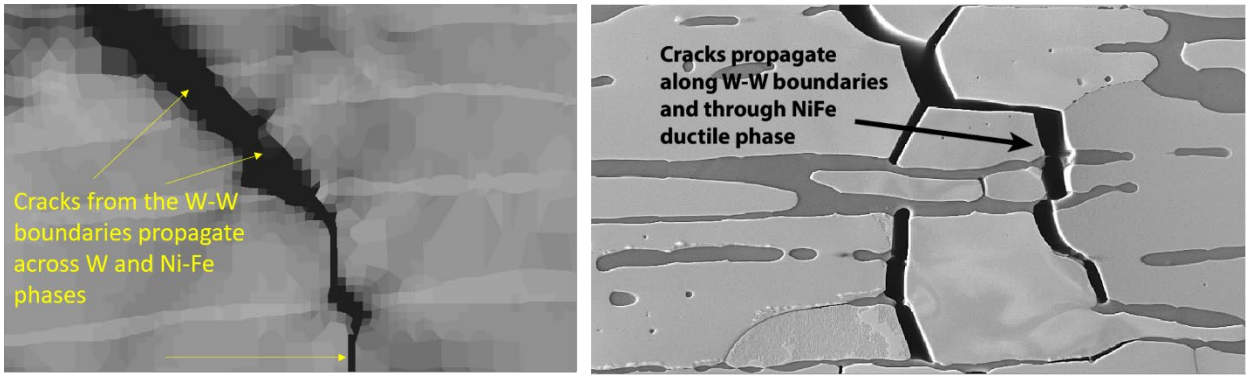

Figure 13. (a) A Magnified view illustrating the damage mechanisms predicted at 12% applied strain for the 90W-87R models with W-W boundaries, and (b) a cracked region of an SEM image from a 90W-87R tensile specimen tested to failure at about this strain level.

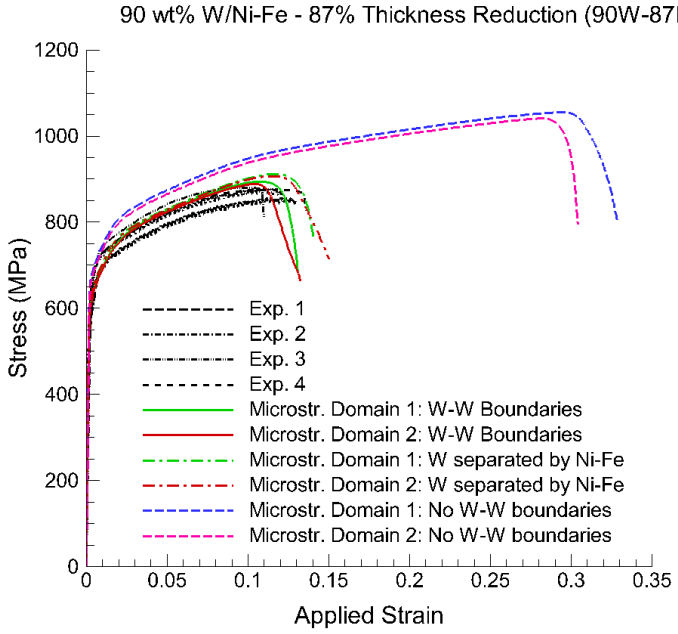

Figure 14. Predicted stress-strain responses for the 90W-87R models compared to the experimental results.

The predicted stress-strain responses for the 90W-87R microstructural models compared to the experimental results are given in Figure 14. As for the 90W cases, the analysis results from the models based on two microstructural domains (numbered 1 and 2) of the 90W-87R composite are illustrated in this figure. Each model from a given domain includes a key microstructural feature discussed above. The

predictions using the models with W-W boundaries agree well with the measured data and well capture the microstructural effects in terms of the difference in microstructural features. For the data used, the microstructural variance observed on the experimental curves appears less pronounced for the 90W-87R material than the variance observed in the 90W composite. The model predictions did capture these observations. For the model without W-W boundaries (ideal composite), the mechanical behavior largely exceeds those for the composites with W-W boundaries that appear as processing defects. As shown in Figure 12, at 12% strain level, negligible damage was predicted in the ideal composite while the other composites already suffered from cracking at many W-W boundaries that also caused damage in the neighboring W and Ni-Fe. When the loading increased, these microcracks grew and linked up and could propagate through the W and Ni-Fe regions leading the actual composite or the composite models with W-W boundaries to fail at substantially lower strength and fracture strain.

Conclusions

The FE microstructural approach [1-2] has successfully predicted damage, fracture, and stress-strain responses of 90W and 90W-87R composites. The following conclusions are drawn from this study:

- For the 90W composite, the microstructural effects in terms of the difference in microstructural features, or in terms of the microstructural variance are equally important and influence on the damage development and composite stress-strain response. The W-W boundaries and W subdomains in some cases can arrest and redirect crack propagations and can lead to increased strength and ductility compared to a composite with W particles completely separated by Ni-Fe.
- For the 90W-87R composite, W-W boundaries close to one to another strongly affect the composite strength and ductility compared to the ideal composite without these boundaries. A microstructural model without W-W boundaries exhibits very high strength and ductility due to its highly elongated W-lamellar-like hierarchical microstructure.

Acknowledgements

This research has been supported by U.S. Department of Energy (DOE), Office of Science, Office of Fusion Energy Sciences under Contract DE-AC05-76RL01830. PNNL is a multi-program national laboratory operated by Battelle Memorial Institute for the US DOE under DE-AC05-76RL01830.

References

[1.] Nguyen, B.N., C.H. Henager, Jr, N.R. Overman, R.J. Kurtz, J. Nucl. Mater., 508 (2018) 371.
[2.] Nguyen, B.N., C.H. Henager Jr., J. Wang, W. Setyawan, J. Nucl. Mater. 540 (2020) 152382.
[3.] Sigl, L.S., P.A. Mataga, B.J. Dalgleish, R.M. McMeeking, and A.G. Evans, Acta Metall., 36 (1988) 945.
[4.] Rieth, M. et al., J. Nucl. Mater., 417 (2011) 463.
[5.] Pitts, R.A., A. Kukushkin, A. Loarte, A. Martin, M. Merola, C.E. Kessel, V. Komarov, and M. Shimada, Physica Scripta, T138 (2009) 014001.
[6.] Mertens, P., T. Hirai, M. Knaup, O. Neubauer, V. Philipps, J. Rapp, V. Riccardo, S. Sadakov, B. Schweer, A. Terra, I. Uytdenhouwen, and U. Samm, Fusion Eng. Des., 84 (2009) 1289.
[7.] Mertens, P., V. Philipps, G. Pintsuk, V. Riccardo, U. Samm, V. Thompson, and I. Uytdenhouwen, Physica Scripta, T138 (2009) 014032.
[8.] Nguyen, B.N., J. Wang, C.H. Henager, Jr., L. Paw, W. Setyawan, “Investigation of The Microstructural Effects on the Mechanical Behavior and Damage Development in Ductile-Phase Toughened-Tungsten Composites”. In Fusion Materials Semiannual Progress Report for the Period Ending December 31, 2020, DOE-ER-0313/69, Vol. 69, pp. 224-234.
[9.] OOF2 Software, Finite Element Analysis of Microstructures, https://www.ctcms.nist.gov/oof/oof2/.
[10.] Nguyen, B.N., J. Wang, C.H. Henager, W. Setyawan, “Modeling Microstructural Effects on the Mechanical Behavior and Damage Development in Ductile-Phase Toughened Tungsten Composites.“ PFMC-18 (https://www.fz-juelich.de/conferences/PFMC-18/EN/Home/home_node.html), Poster # 268.

9.5 MOLECULAR DYNAMICS STUDY OF INTERPHASE BOUNDARIES IN W-Ni-Fe TUNGSTEN HEAVY ALLOYS—S. P. Edwards, N. Chen, W. Setyawan (Pacific Northwest National Laboratory)

OBJECTIVE

To generate an atomistic database of irradiation effects on the structure and mechanical property of interphase boundaries in W-Ni-Fe heavy alloys as a structural material in a divertor.

SUMMARY

Molecular dynamics simulations are performed to obtain a relaxed structure of W{110}<100>//Ni{111}<110> interphase boundary at 1000 °C. Subsequently, the cohesion of the boundary is explored as a function of W concentration in Ni. Increasing W concentration up to ~6 at.% of W increases fracture energy. However, further increasing the W concentration, up to the solubility limit of W in Ni at 1000 C of ~16 at.%, decreases the fracture energy. The observed trend is presumably caused by an interplay between attractive interaction between W and Ni atoms which strengthens atomic bonding across the boundary and the increase in stress in the ductile phase as the W concentration is increased. In all cases, the boundary is stronger than the cleavage fracture of the Ni{111} planes, partly corroborating the excellent toughness of W-Ni-Fe heavy alloys. Other relaxed structures as a function of W concentration will be explored to gain more understanding of the effect of W concentration.

PROGRESS AND STATUS

Tungsten Heavy Alloys (WHAs) made of W, Ni, and Fe are promising as a structural material for fusion reactor divertors, exhibiting higher fracture toughness (69-107 MPa/√m compared to 5-8 MPa/√m of pure W) and improved ductility compared to pure tungsten [1-4]. A strong interphase boundary cohesion between the W phase and the ductile phase is one of important characteristics that governs the high fracture toughness of WHAs. A neutronics analysis of WHAs if used in the divertor dome of the US ARIES-ACT2 concept [5, 6] for 10 years shows the feasibility of employing up to ~4.5 wt.% Ni to qualify for the Class C low-level-waste (LLW) classification based on the NRC's specific activity limits for terrestrial waste disposal, and up to ~9.5 wt.% Ni based on the Fetter's activity limits. While the neutronics analysis is encouraging, the irradiation effects on the interphase boundaries need to be understood. Nickel is known to produce He and H gases more than Fe and W. Our first focus is then understanding the He and H effects on the boundary cohesion.

Molecular dynamics is well-suited to study the boundary cohesion. Accurate interatomic potentials to fully model W, Ni, Fe, He, and H are currently unavailable. Developing such potentials is in our future plan. In the meantime, potentials to describe W-Ni systems are available [7, 8]. We employ these potentials to obtain different boundary structures and to understand the cohesion as a function of the composition of the ductile phase. In this report, we describe the results on W{110}<100>//Ni{111}<110> boundary. The detailed orientation relationship is W[100] // Ni[1-10] (taken as the *x*-axis), W[01-1] // Ni[11-2] (*y*-axis), and W(011) // Ni(111) (*z*-axis, also the normal of the boundary plane).

Table 1. Calculated lattice parameter (*a* in Å) of bcc W, fcc Ni, and ductile phase Ni-W fcc solid solution as a function of temperature. Atomic percentages represent the concentration of W in the solid solution. For each concentration, 10 random configurations are simulated to obtain an average value shown here.

T (°C)	W	Ni	3 at.%	6 at.%	9 at.%	12 at.%	15 at.%
-273.2	3.157243	3.519056	3.531715	3.544498	3.557590	3.570777	3.584505
-263	3.157274	3.519420	3.532103	3.544879	3.557969	3.571155	3.584885
25	3.158694	3.531178	3.543723	3.556403	3.569492	3.582738	3.596594
100	3.159089	3.534546	3.546931	3.559607	3.572727	3.585967	3.599891
200	3.159684	3.539028	3.551429	3.564095	3.577203	3.590545	3.604486
300	3.160344	3.543895	3.556252	3.568905	3.581988	3.595397	3.609365
400	3.160962	3.548781	3.561368	3.573965	3.587111	3.600486	3.614486
500	3.161627	3.554387	3.566690	3.579183	3.592456	3.605829	3.619807
600	3.162335	3.560088	3.572386	3.584957	3.597972	3.611347	3.625408
700	3.163177	3.566471	3.578532	3.591149	3.604103	3.617529	3.631269
800	3.163993	3.573262	3.585182	3.597545	3.610428	3.623721	3.637500
900	3.164702	3.580397	3.592347	3.604597	3.617372	3.630393	3.644117
1000	3.165613	3.589164	3.600059	3.612002	3.624736	3.637630	3.650938
1100	3.166646	3.597577	3.608771	3.620205	3.632565	3.645160	3.658282
1200	3.167782	3.606937	3.618140	3.629151	3.640944	3.653215	3.665741
1300	3.168696	3.617904	3.628241	3.638643	3.650074	3.661896	3.674074

Based on the lattice parameters (Table 1), supercells of W{110} and Ni{111} slabs (grains) along *x* and *y* are searched that have minimum lattice mismatches (mismatch strains). Here, the mismatch strain of an interphase boundary is defined as the strain experienced by the ductile-phase slab with respect to the dimensions of the W slab. Table 2 summarizes the supercells with the five smallest strains for several temperatures.

Table 2. Calculated supercells of W{110} and Ni{111} slabs along *x* and *y* which give the five smallest mismatch strains on the Ni slab with respect to the W slab. Supercells are searched up to 50 repeat units.

	along *x*			along *y*		
T (°C)	W	Ni	Mismatch Strain (%)	W	Ni	Mismatch Strain (%)
-263	26	33	0.0424	27	28	0.1113
-263	37	47	0.1242	29	30	0.1353
-263	15	19	0.1599	28	29	0.0163
-263	34	43	0.3152	30	31	0.2467
-263	30	38	0.1599	26	27	0.2483
25	19	24	0.1487	29	30	0.1532
25	34	43	0.0261	32	33	0.1598
25	30	38	0.1287	31	32	0.062
25	15	19	0.1287	30	31	0.0422
25	38	48	0.1487	33	34	0.2518
700	24	30	0.3436	42	43	0.0311
700	35	44	0.2265	41	42	0.0256
700	39	49	0.1683	40	41	0.0851
700	31	39	0.2996	43	44	0.0852
700	12	15	0.3436	44	45	0.137
1000	32	40	0.214	47	48	0.2781
1000	**4**	**5**	**0.214**	**48**	**49**	**0.2348**
1000	28	35	0.214	49	50	0.1933
1000	16	20	0.214	46	47	0.3233
1000	8	10	0.214	45	46	0.3704
1200	21	26	0.3177	47	48	0.7015
1200	29	36	0.0523	48	49	0.6584
1200	33	41	0.0318	49	50	0.617

1200	37	46	0.0977	46	47	0.7464
1200	25	31	0.1636	45	46	0.7933

As expected, the optimum supercells vary with temperature due to the different thermal expansion coefficient ($\frac{1}{a}\frac{da}{dT}$) of W and Ni. We select 1000 °C as a working temperature. This temperature represents the middle of a typical operating temperature window of tungsten-based divertors [9], ~700-800 °C in the lower limit and ~1200-1300 °C in the upper limit. The lower limit is dictated by the ductile-to-brittle transition temperature (DBTT), while the upper limit is imposed by the recrystallization temperature. Base on Table 2, we select supercells that give < 0.25% mismatch strain, i.e., 4x48 supercells for W along *x* and *y* respectively, and 5x49 supercells for Ni. Interphase boundary structures are constructed with W{110} and Ni{111} slabs, each with 36 layers, where the Ni slab is shifted along *x* and *y* relative to the W slab in a 11x11 grids. Molecular dynamics simulations are performed in constant pressure (zero Pa) and temperature (1000 °C) for 30 ps to relax each structure using Nose-Hoover thermostat with a damping factor of 0.5 ps. The structure with the minimum total energy, corresponding to grid (10, 10), is taken as the most stable structure of the boundary, as shown in Figure 1. Note that snapshot shown in Figure 1 is obtained after an additional static minimization (with a fixed box) to eliminate thermal fluctuations in atomic positions. In a static minimization, atom velocities are set to zero, and atoms are moved based on the gradient of energy towards a minimum-energy configuration.

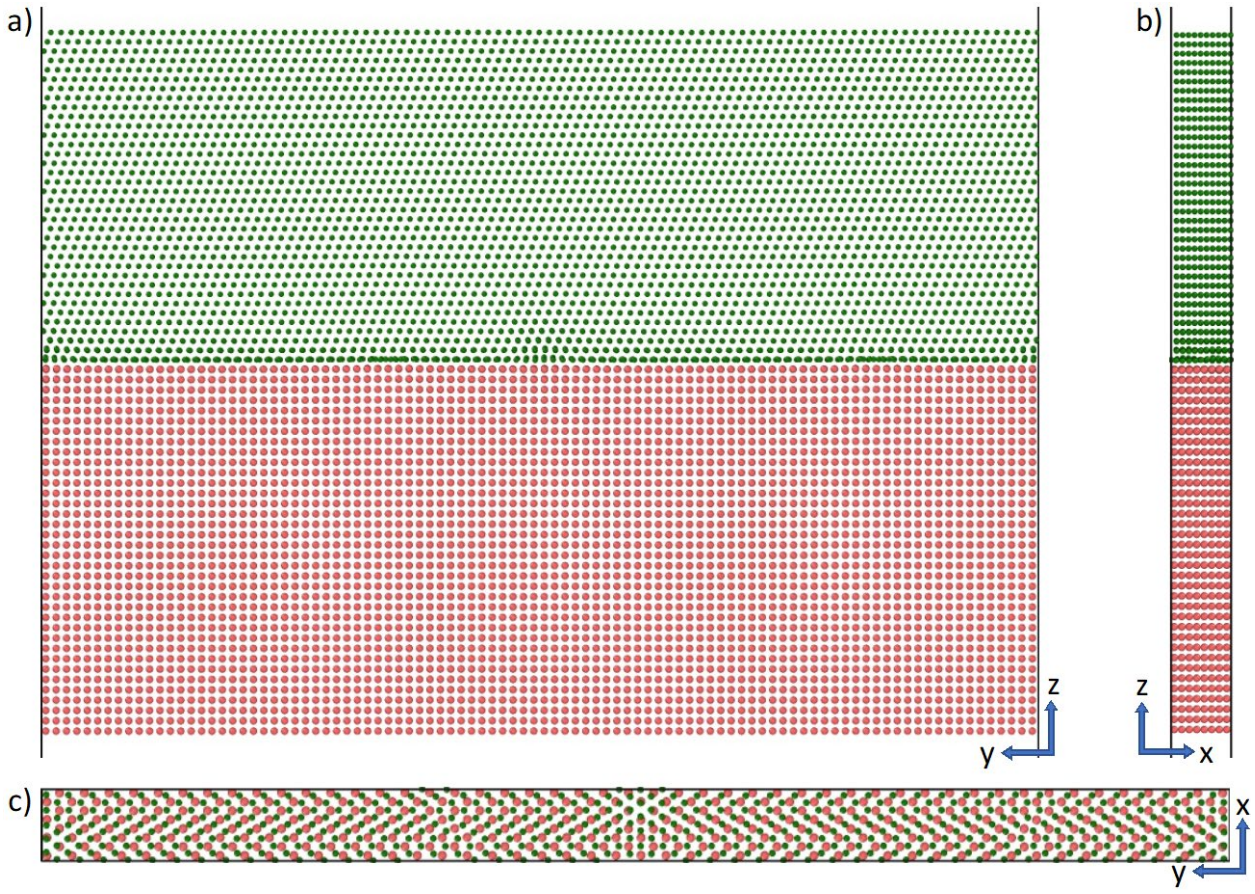

Figure 1. Structure of W{110}<100>//Ni{111}<110> interphase boundary at 1000 °C. The snapshot shown is after static minimization (with a fixed box) of the MD-relaxed structure to eliminate thermal fluctuations of atom positions for clarity. Panel c) shows the incoherency of the W and Ni layers closest to the boundary.

Subsequently, solid solutions are created by randomly substituting Ni atoms with W atoms. As in the case of lattice parameter calculations, 10 random configurations are generated for each solid solution concentration. Fracture energy (E_{fract}) of an interphase boundary (IB) is calculated using the following formula,

$$E_{fract}\{IB\} = (E\{slab_1\} + E\{slab_2\} - E\{IB\})/A\{IB\}$$

where $E\{slab_1\}$, $E\{slab_2\}$, and E{IB} are the total energy of the ductile-phase slab, the W slab, and the IB, respectively, and A{IB} is the area of the IB. The fracture energy of the W{110} and Ni{111} planes, known as cleavage energy (E_{cleav}), is calculated from the surface energy (E_s) of the corresponding planes (surfaces),

$$E_{cleav} = 2E_s$$

$$E_s = (E\{slab\} - E\{bulk\})/(2A\{slab\})$$

where E{bulk} is the total energy of a bulk single crystal containing the same number of atoms as the slab. Table 3 summarizes the fracture energy as a function of W concentration of the ductile phase, as well as the mismatch strain, along *x* and *y*, experienced by the ductile phase after relaxation.

Table 3. Cleavage energy of W{110}, Ni{111}, and fracture energy of interphase boundary where the ductile phase is made of Ni or solid solution with various W concentration (given in at.%). Also shown are the mismatch strain, along *x* and *y*, experienced by the ductile phase. Data is calculated from simulations at 1000 °C.

T (°C)	W	Ni	3 at.%	6 at.%	9 at.%	12 at.%	15 at.%
E_{cleav} (J/m^2)	5.29	3.11					
E_{fract}{IB} (J/m^2)		4.84	4.89	4.92	4.86	4.80	4.59
ε_x (%)		-0.24	-0.47	-0.64	-0.84	-0.96	-1.23
ε_y (%)		-0.03	-0.24	-0.50	-0.70	-0.90	-1.35

As can be seen from Table 3, the fracture energy increases with W concentration up to ~6 at.%, then decreases with further increase of W concentration. Attractive interaction between W and Ni strengthens the bonds between atoms across the boundary. However, as W expands the ductile phase and induces more compressive strain in both *x* and *y* directions, further increasing W concentration weakens the boundary. In all cases, the fracture energy of the IB remain larger than the cleavage energy of Ni{111}. The excellent cohesion of the IB partly elucidates the excellent ductile-phase toughening in this alloy.

Acknowledgement

This research has been supported by the U.S. Department of Energy, Office of Science, Office of Fusion Energy Sciences and performed at the Pacific Northwest National Laboratory under contract number DE-AC05-76RL01830 and by the U.S. Department of Energy, Science Undergraduate Laboratory Internship (SULI) program (PNNL project #45260).

References

[1.] C.H. Henager, W. Setyawan, T.J. Roosendaal, N.R. Overman, B.A. Borlaug, E.L. Stevens, K.B. Wagner, R.J. Kurtz, G.R. Odette, B.N. Nguyen, K. Cunningham, Ductile-Phase Toughened Tungsten for Plasma-Facing Materials in Fusion Reactors, International Journal of Powder Metallurgy, 53 (2017) 53-69.

[2.] M.E. Alam, G.R. Odette, On the remarkable fracture toughness of 90 to 97W-NiFe alloys revealing powerful new ductile phase toughening mechanisms, Acta Materialia, 186 (2020) 324-340.

[3.] J.V. Haag, D.J. Edwards, C.H. Henager, W. Setyawan, J. Wang, M. Murayama, Characterization of ductile phase toughening mechanisms in a hot-rolled tungsten heavy alloy, Acta Materialia, 204 (2021) 116523.

[4.] M.E. Alam, J. Wang, C.H. Henager, W. Setyawan, G.R. Odette, The effect of hot rolling on the strength and fracture toughness of 90W–7Ni3Fe tungsten heavy metal alloys, Materials Science and Engineering: A, DOI https://doi.org/10.1016/j.msea.2021.141738 (2021) 141738.

[5.] L. El-Guebaly, L. Mynsberge, A. Davis, C. D'Angelo, A. Rowcliffe, B. Pint, Design and Evaluation of Nuclear System for ARIES-ACT2 Power Plant with DCLL Blanket, Fusion Science and Technology, 72 (2017) 17-40.

[6.] The ARIES Project, http://aries.ucsd.edu/ARIES/.

[7.] Q.-N. Fan, C.-Y. Wang, T. Yu, J.-P. Du, A ternary Ni–Al–W EAM potential for Ni-based single crystal superalloys, Physica B: Condensed Matter, 456 (2015) 283-292.

[8.] J. P. Du, C. Y. Wang, T. Yu, Construction and application of multi-element EAM potential (Ni–Al–Re) inγ/γ′ Ni-based single crystal superalloys, Modelling and Simulation in Materials Science and Engineering, 21 (2013) 015007.

[9.] P. Norajitra, L. V. Boccaccini, E. Diegele, V. Filatov, A. Gervash, et al., Development of a helium-cooled divertor concept: design-related requirements on materials and fabrication technology, Journal of Nuclear Materials, 329 (2004) 1594.

10. IRRADIATION & TESTING ANALYSIS, METHODS, EXPERIMENTS, AND SCHEDULES

10.1 IAEA SMALL SPECIMEN TEST TECHNIQUE DEVELOPMENT: MASTER CURVE FRACTURE TOUGHNESS TESTING UPDATE AT ORNL—X. Chen, J. Reed, E. Manneschmidt, M. Sokolov (Oak Ridge National Laboratory)

OBJECTIVE

This task aims to develop reliable fracture toughness testing and analysis method for small size specimens. Under the framework of the International Atomic Energy Agency (IAEA) Coordinated Research Projects (CRP), the work aims for evaluating specimen size effects on fracture toughness characterization for fusion structural materials.

SUMMARY

Under the auspices of International Atomic Energy Agency (IAEA), a Coordinated Research Project (CRP) entitled “Towards the Standardization of Small Specimen Test Techniques for Fusion Applications” has started in 2017. The overall objective of the project is to provide a set of guidelines for small specimen test techniques (SSTT) based on commonly agreed best practices on main test techniques including tensile, creep, low cycle fatigue, fracture toughness, and fatigue crack growth rate. This will act as the first step of a full standardization of the SSTT. Fusion structural materials, i.e., reduced activation ferritic/martensitic (RAFM) steels, are used for testing. In addition, the project will create a comprehensive mechanical property database of RAFM steels tested by SSTT.

PROGRESS AND STATUS

For the fracture toughness task of the CRP, three testing methods including Master Curve, local approach, and ductile approach are evaluated. This project focuses on the Master Curve method based on the ASTM standard E1921-19b “Standard Test Method for Determination of Reference Temperature, T_0, for Ferritic Steels in the Transition Range” [1] and commonly agreed best practice from researchers at Oak Ridge National Laboratory (ORNL).

The materials used in the testing were Eurofer 97 batch-3 and F82H-BA12. Table 1 summarizes the test matrix adopted. The specimen machining plan is highlighted in Figure 1 with individual specimen drawings given in Figures 2-4. The testing and data recording strictly followed the testing guidelines and data reporting template in Reference [2].

Table 1. Master Curve round-robin testing matrix

Materials	Specimen configuration	# of specimens	Orientation	Size of raw material*
Eurofer97 batch-3	miniature bend bar (Fig.2)	16	LT	460mm(L) x 125mm(T) x 33mm (S)
	miniCT (Fig.3)	10		
	0.5TCT (Fig.4)	7		
F82H-BA12	miniature bend bar (Fig.2)	16	LT	100mm(L) x 300mm(T) x 26mm (S)
	miniCT (Fig.3)	11		
	0.5TCT (Fig.4)	6		

* L: longitudinal, T: transverse, and S: short transverse based on the plate orientation

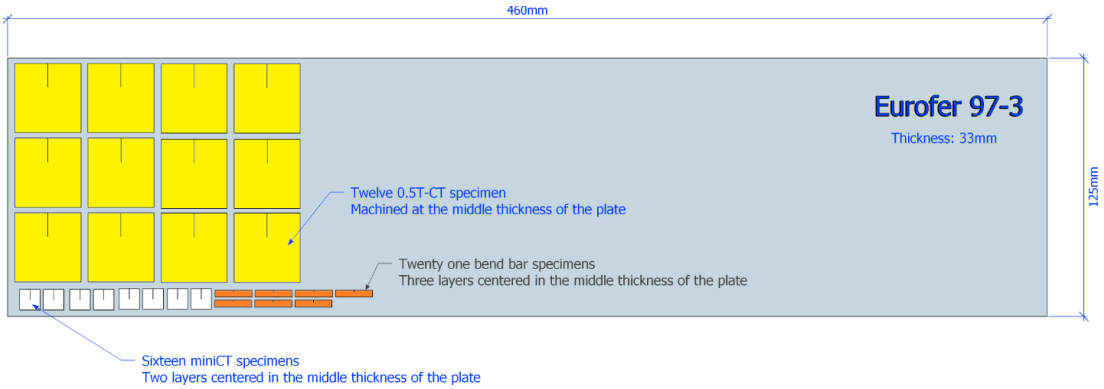

(a)

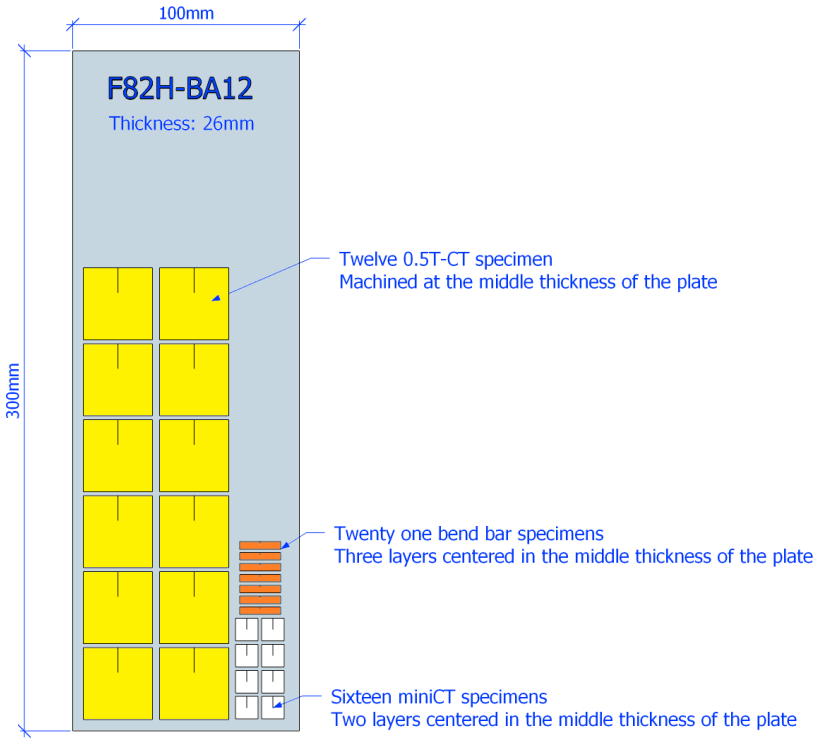

(b)

Figure 1. Specimen machining plans in (a) and (b).

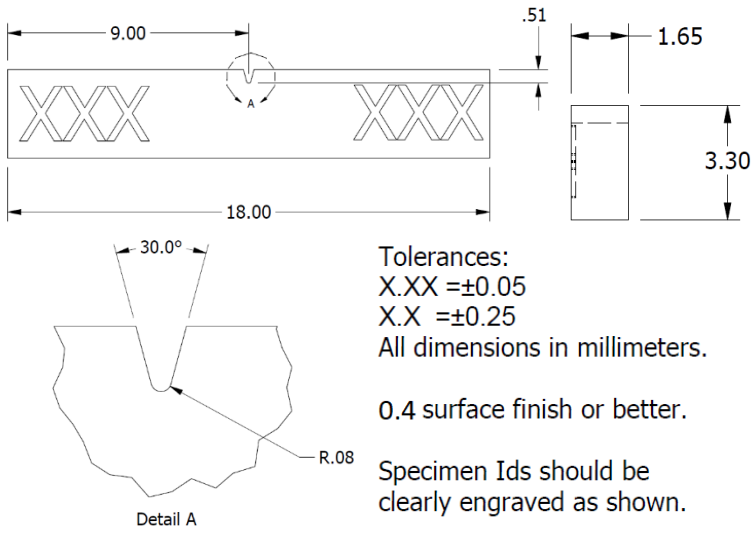

Figure 2. Miniature bend bar specimen drawing.

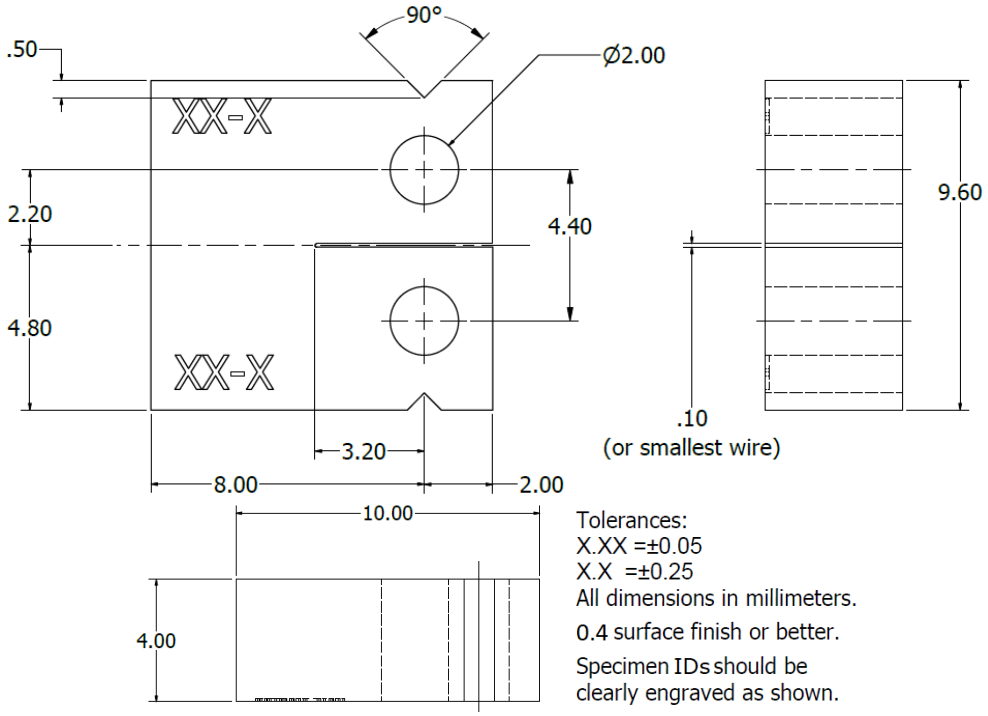

Figure 3. MiniCT specimen drawing.

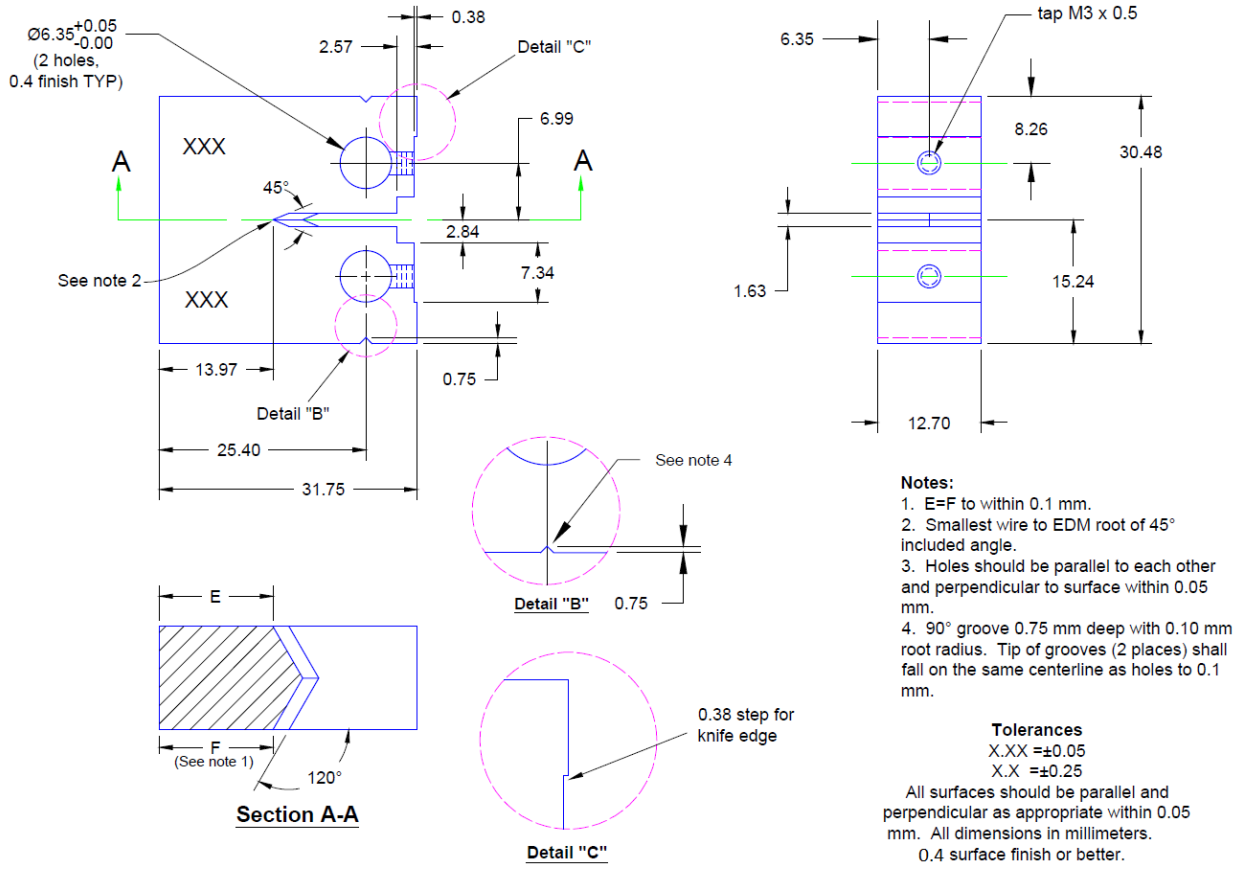

Figure 4. 0.5TCT specimen drawing.

The Master Curve fracture toughness testing consists of two parts: fatigue precracking and fracture toughness testing. Fatigue precracking was performed on a 44.5 kN capacity servo-hydraulic frame with calibrated load cells as shown in Figure 5. Depending on the specimen geometry, dedicated fixtures, grips, and deflection gauges were used for each specimen type. A commercial automated fatigue crack growth testing software was used with real-time compliance-based crack length measurements to control the fatigue precrack process.

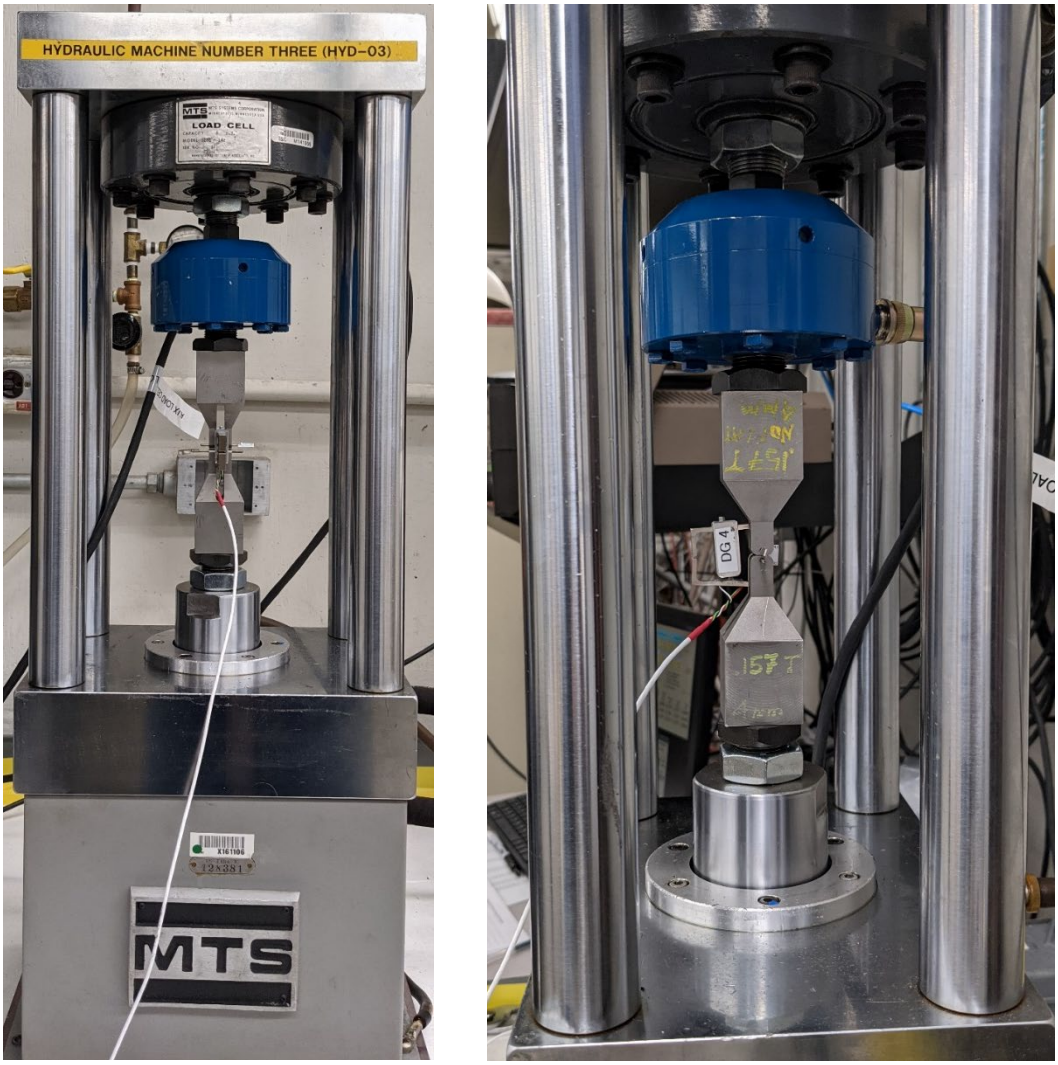

Figure 5. Servo-hydraulic fatigue precrack frame with a 4mm miniCT specimen loaded.

Fracture toughness testing was performed on a 97.87 kN capacity servo-hydraulic frame with calibrated load cells. Figure 6 illustrates the general layout of the experimental setup. Depending on the specimen geometry, dedicated fixtures, grips, and deflection gauges were used for each specimen type. Liquid nitrogen was used to control the testing temperatures which were measured directly from type-T thermocouples spot welded to specimens. The environment chamber enclosing specimens and the test fixture maintained a relatively stable temperature (±2°C from the target temperature) during testing.

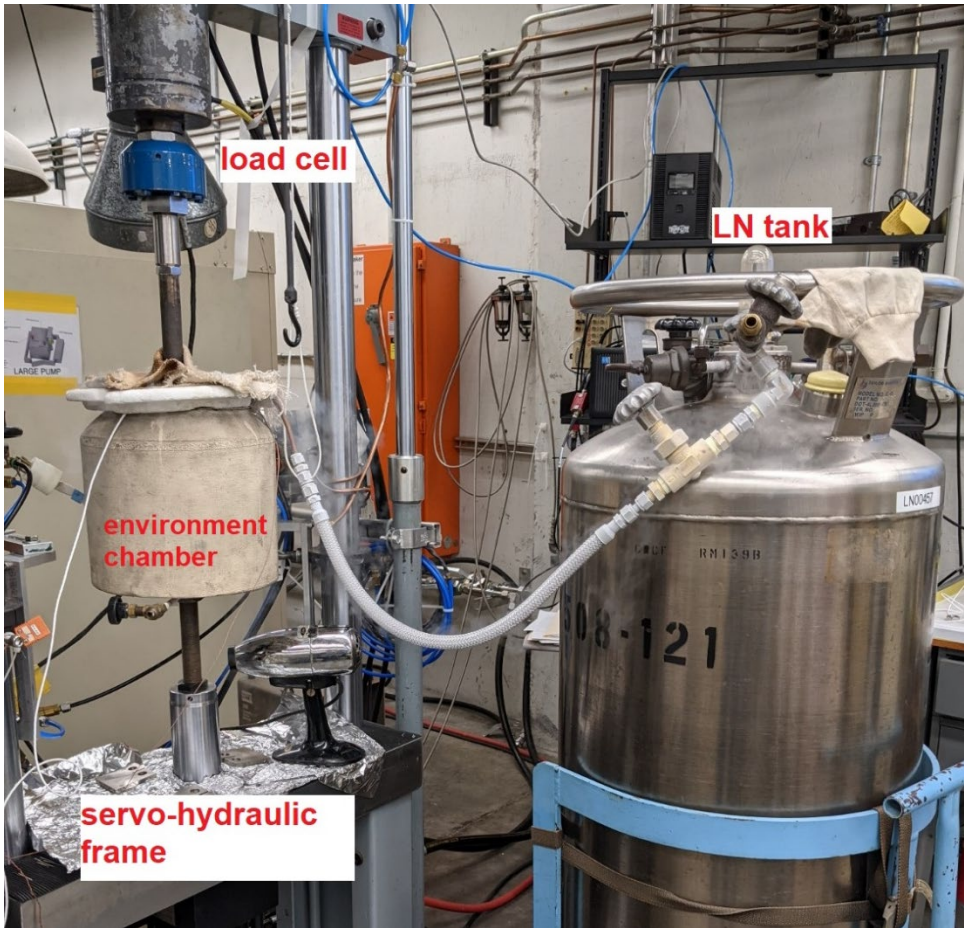

(a)

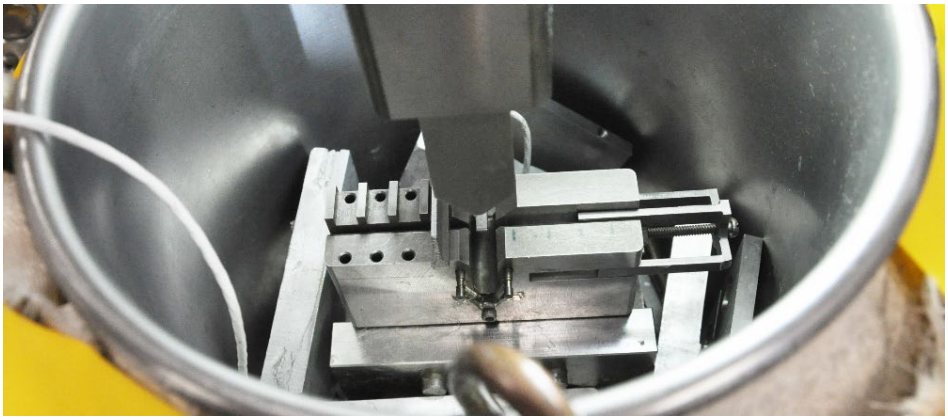

(b)

Figure 6. General layout of the fracture toughness test setup in (a) and close-up view of the miniature bend bar test fixture in (b).

Specimens were first fatigue precracked to the target crack length and then tested based on the Master Curve method in the ASTM E1921 standard without side-grooving. Testing was performed using a quasi-static loading rate such that dK/dt during the initial elastic portion between 0.1 and 2 MPa√m/s shall be used. Testing temperatures should be chosen such that the medium stress intensity factor $K_{JCc(med)}$ at the test temperature will be about 100 MPa√m for the specimen size selected. For small size specimens, this

may not be achievable due to the maximum K_{Jc} capacity limit ($K_{Jclimit}$). Hence, lower testing temperatures are necessary. Special attention is warranted during the initial working-in crack size estimation where the last three consecutive estimated crack sizes should be all within 10% of the final precrack size. Pop-in evaluation, if applicable, should also be performed based on the procedures in the ASTM E1921 standard. Fatigue precrack results are summarized in Table 2. Fatigue cycling was conducted using a sinusoidal waveform under stress intensity K control. Either a constant K or a decreasing K was used. Per ASTM E1921, the following requirements were evaluated and met during all fatigue precracking:

- The applied stress intensity was within the envelope of allowable K_{max}
- The initial maximum fatigue force P_{max} was less than the control force P_m
- Crack extension and final crack length requirements were met

Table 2. Summary of fatigue precrack results

Specimen types	Materials	Frequency (Hz)	Initial K_{max} (MPa√m)	Final K_{max} (MPa√m)	Initial P_{max} (N)	R ratio	a_0/W	Cycles
Miniature bend bar	Eurofer97-3	55-60	10.99-11.54	10.99-11.54	250.9-264.7	0.1	0.49-0.52	201k-344k
	F82H-BA12	60	12.64	12.64	276.2-288.7	0.1	0.49-0.51	201k-230k
4mm miniCT	Eurofer97-3	48-50	15.05	15.05	700.2-735.3	0.1	0.5-0.51	85-118k
	F82H-BA12	47-50	15.05	15.05	709.9-733.1	0.1	0.48-0.51	85-121k
0.5TCT	Eurofer97-3	30	22.24-22.68	13.68-13.78	6248-6659	0.1	0.45-0.48	160k-205k
	F82H-BA12	30	22.09-22.83	13.70-13.72	6494-6730	0.1	0.45-0.49	156k-202k

Albeit the compliance, it was later discovered that the fatigue precrack front straightness had significant issues for both 0.5TCT and 4mm miniCT specimens as shown in Figures 7 and 8. In contrast, all miniature bend bar specimens (e.g., Figure 9) exhibited straight fatigue precrack front which was within the ASTM E1921 requirement. The skewed fatigue precrack front for 0.5TCT and 4mm miniCT specimens likely resulted from the non-perfect alignment of the fatigue frame load train. Its impact on the measured Master Curve reference temperature, T_0/T_{0Q}, will be discussed in the latter part of this report.

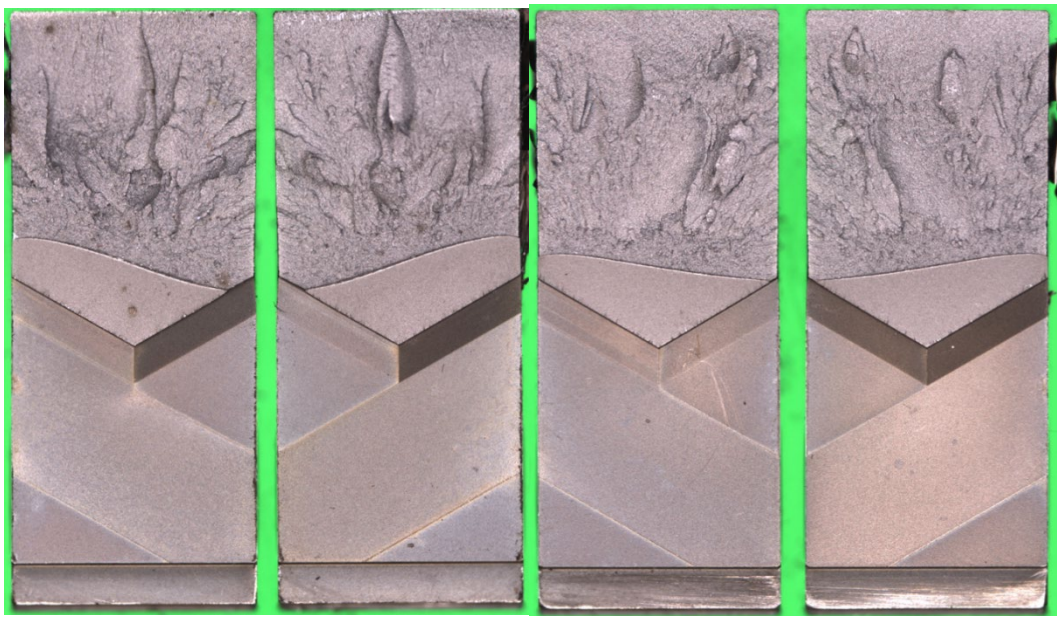

Figure 7. Sample fracture surface images for 0.5TCT specimens. Both samples had skewed fatigue precrack front although the sample on the right met the requirements in ASTM E1921 section 8.9.1.

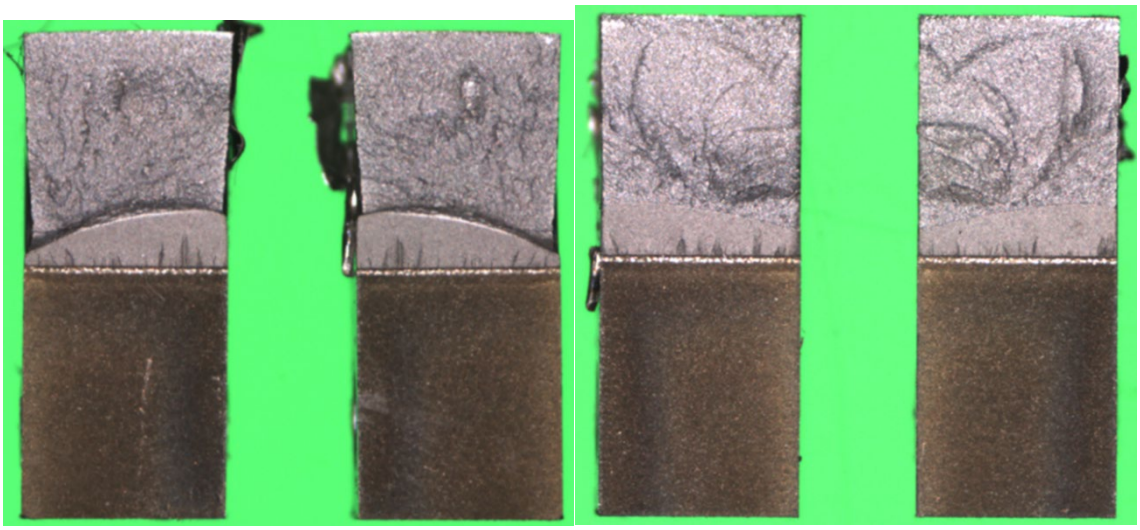

Figure 8. Sample fracture surface images for 4mm miniCT specimens. Both samples had skewed fatigue precrack front although the sample on the right met the requirements in ASTM E1921 section 8.9.1.

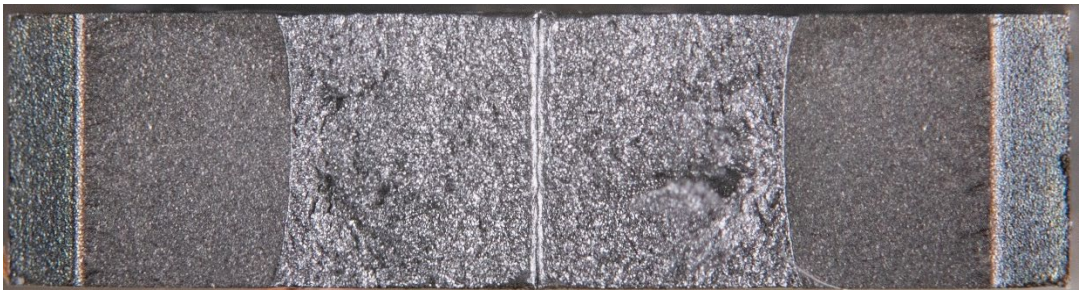

Figure 9. Sample fracture surface images for miniature bend bar specimens with straight fatigue precrack front.

Fracture toughness results are summarized with Master Curve plots shown in Figures 10-12 for three different specimen types tested at ORNL. Each test was censored against both $K_{Jclimit}$ and slow stable crack growth limit ($K_{JC\Delta a}$). It appears that for both Eurofer97-3 and F82H-BA12, the Master Curve can predict the median fracture toughness for each specimen type and the 2%/98% tolerance bounds can bound most valid tests with few valid tests showing very low toughness values. In addition, for 0.5TCT specimens very limited slow stable crack growth was observed before cleavage fracture even though the specimens were not side grooved after fatigue precracking.

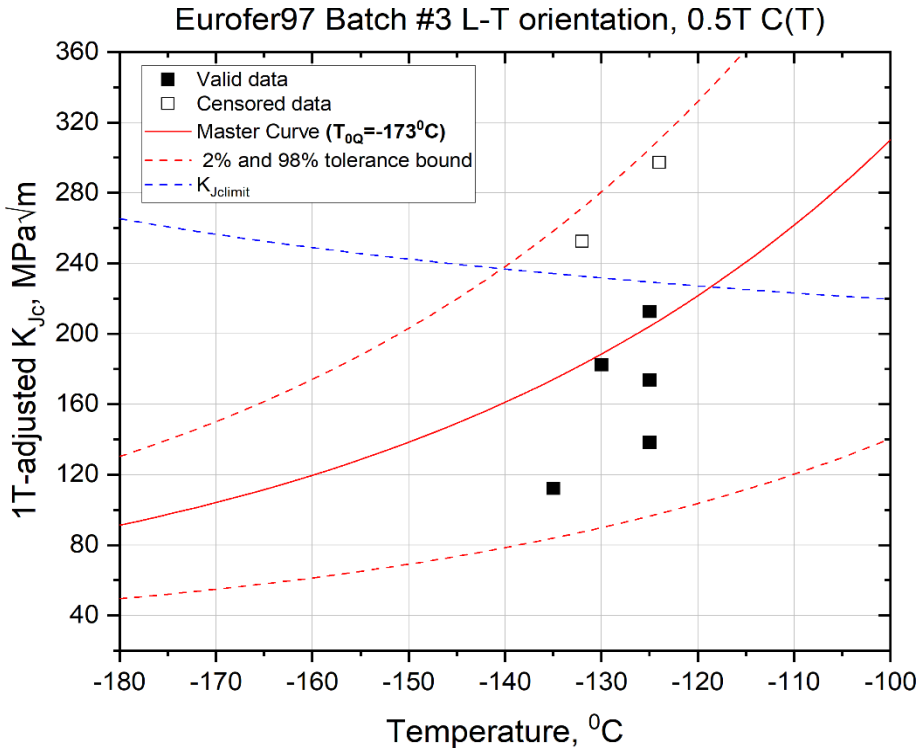

(a)

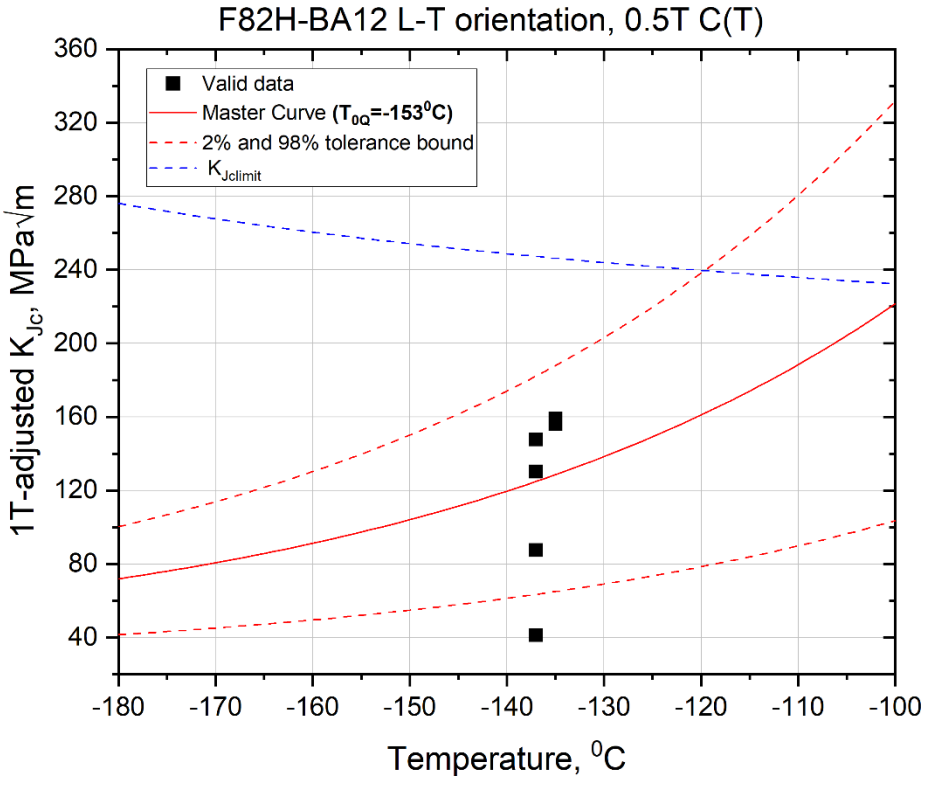

(b)

Figure 10. Master Curve plots from 0.5TCT specimens for Eurofer97-3 in (a) and F82H-BA12 in (b).

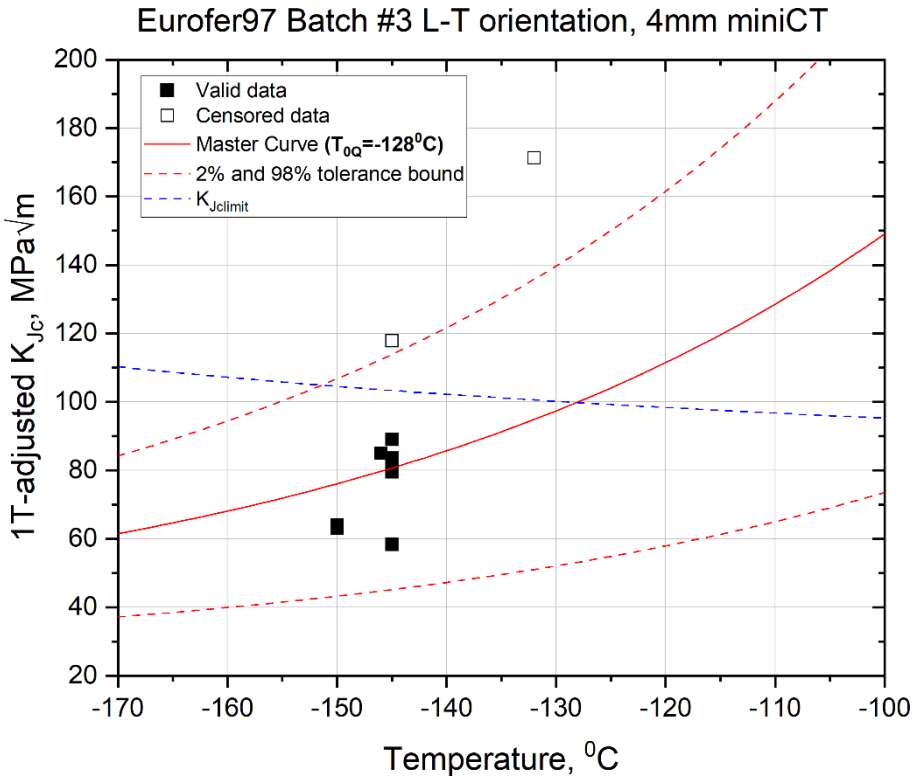

(a)

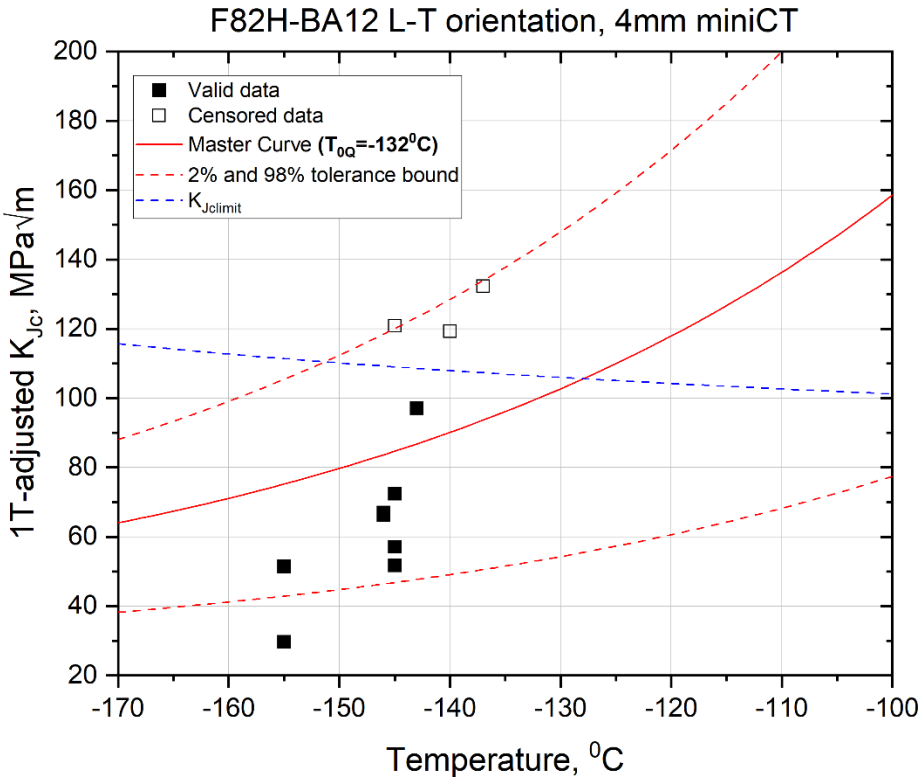

(b)

Figure 11. Master Curve plots from 4mm miniCT specimens for Eurofer97-3 in (a) and F82H-BA12 in (b).

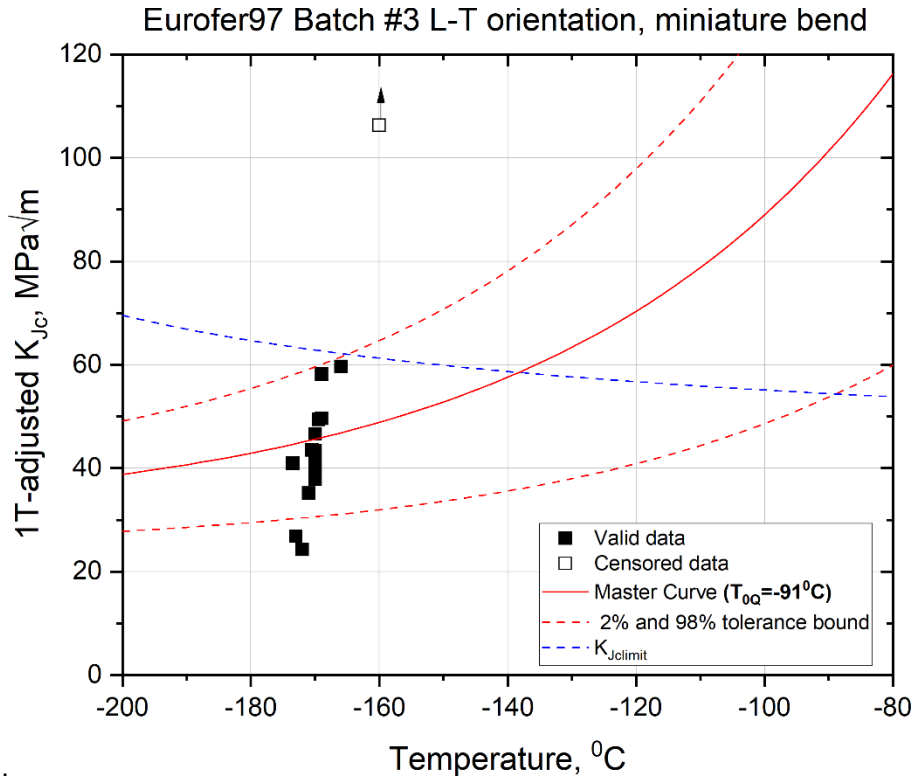

(a)

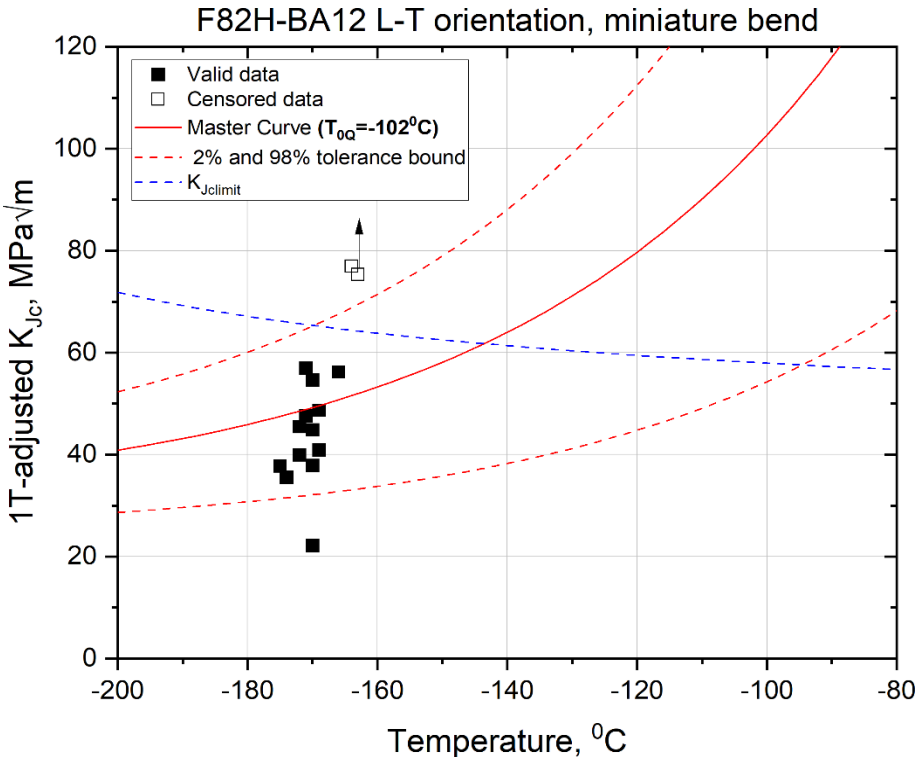

(b)

Figure 12. Master Curve plots from miniature bend bar specimens for Eurofer97-3 in (a) and F82H-BA12 in (b).

The specimen size and geometry effects on the determination of the Master Curve reference temperature T_{0Q} are evaluated in Figure 13. For either Eurofer97-3 or F82H-BA12, three different specimen types, namely 0.5TCT, 4mm miniCT, and miniature bend bars, yielded different nonoverlapping T_{0Q} values. In addition, T_{0Q} increased with decreasing specimen sizes. However, due to the skewed fatigue precrack front for 0.5TCT and 4mm miniCT specimens (Figures 7 and 8), it is questionable if T_{0Q} determined from these two specimen types are reliable. This is especially true for 0.5TCT specimens where the fatigue precrack did not initiate from a small portion of the initial machined Chevron notch, which would affect the crack front stress field. Indeed, it is very unlikely for both RAFM steels exhibiting T_{0Q} lower than -150°C as shown in 0.5TCT testing. In contrast, T_{0Q} from the miniature bend bars matched reported T_0 range for Eurofer97 and F82H in literature and therefore showing suitability of using such specimen geometry for Master Curve fracture toughness characterization. To evaluate the specimen size effect on T_{0Q}, a new testing campaign is needed for testing 0.5TCT and 4mm miniCT specimens with a straight fatigue precrack front. Nonetheless, when comparing T_{0Q} results obtained from the same type of specimen for both Eurofer97-3 or F82H-BA12, T_{0Q} results are similar between the two materials.

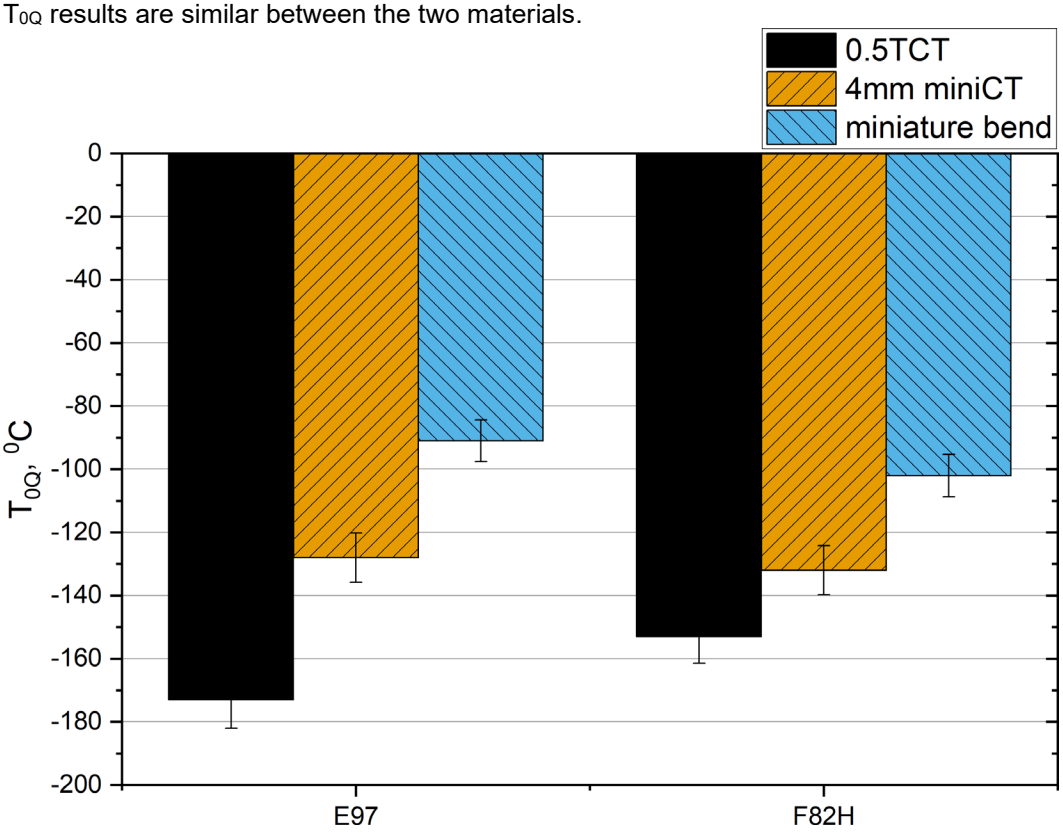

Figure 13. Comparison of the Master Curve reference temperature T_{0Q} determined from three different specimen types for Eurofer97-3 and F82H-BA12. Error bars correspond to ± 1σ (standard deviation).

Besides the fatigue precrack front straightness issues observed in 0.5TCT and 4mm miniCT specimens, which invalidate some test results and qualification of T_{0Q} as T_0, the cryogenic test temperature is another unique challenge in testing the miniature bend bar specimens. Not only the cryogenic test temperature is difficult to control and would affect the initial walk-in crack size estimate and post-test crack size check, but also it violates the current low test temperature limit, T_{0Q} – 50°C, set by the ASTM E1921. For example, fracture toughness testing on miniature bend bar specimens was performed near -170°C, which was approximately -80°C and -70°C lower than T_{0Q} of Eurofer97-3 and F82H-BA12, respectively. However, based on the Master Curve plots from Fig. 12, -170°C corresponds to the intersection point of the $K_{Jclimit}$ line and the 98% tolerance bound, meaning if testing had been performed at T > -170°C, the test result

would have a much higher chance of being censored. To address this issue, the low-test temperature limit needs to be relaxed in the ASTM E1921 standard.

References

[1] ASTM E1921-19be1, Standard Test Method for Determination of Reference Temperature, T_0, for Ferritic Steels in the Transition Range, ASTM International, West Conshohocken, PA, 2019, www.astm.org.

[2] X. Chen et al., "Guidelines for IAEA Small Specimen Test Techniques Master Curve Fracture Toughness Testing", ORNL/LTR-2020/27, July.

10.2 MATERIALS FOR FRONTIER US-JAPAN COLLABORATION—L. M. Garrison, Y. Katoh, J. R. Echols, J. W. Geringer, N. C. Reid, Hanns Gietl, Y. Yang (Oak Ridge National Laboratory), T. Hinoki (Kyoto University), N. Hashimoto (Hokkaido University), J. P. Allain (Pennsylvania State University), B. Cheng, L. L. Snead, J. R. Trelewicz (Stony Brook University), D. Dorow-Gerspach, V. Ganesh (Forschungszentrum Juelich GmbH), S. A. Humphry-Baker (Imperial College), E. Lang (University of Illinois, Urbana-Champaign), I. McCue (John Hopkins University)[j], J. Riesch (Max-Planck-Institut für Plasmaphysik), G. D. W. Smith (Oxford University), S. J. Zinkle (University of Tennessee)

Extended abstract of manuscript submitted to Physica Scripta, "Development of plasma-facing material joints and composites for neutron irradiation in the FRONTIER US-Japan collaboration"

The plasma facing components (PFCs) of future fusion reactors will have intricate structures and require multiple materials because no one material can simultaneously satisfy all the requirements of the component. Dissimilar material joints in PFCs must withstand extreme thermal and stress gradients under neutron irradiation. Irradiation defects, transmutation, and irradiation induced segregation can lead to deterioration and thus weaken or even deboned initially well bonded interfaces. The Fusion Research Oriented to Neutron Irradiation and Tritium Behavior at Material Interfaces (FRONTIER) US-Japan collaboration seeks to explore and explain the behavior of internal solid interfaces in PFCs under neutron irradiation. More than 25 materials have been developed including particle reinforced W, advanced Cu alloys, W-steel joints, W fiber composites, and additively manufactured W materials. Two of these materials are shown in Figure 1. These advanced fusion-relevant alloys, composites, and joints will be neutron irradiated in the High Flux Isotope Reactor (HFIR), a fission test reactor.

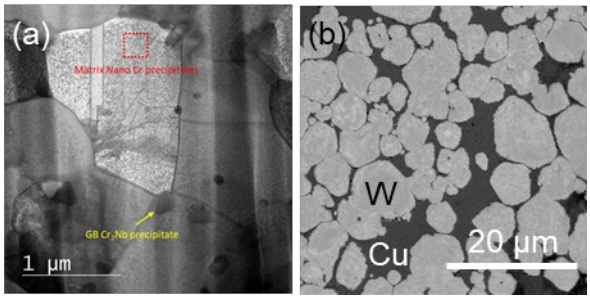

Figure 1. (a) The TEM bright-field micrograph showing the microstructure of direct current sintered/spark plasma sintered CuCrNbZr alloy with highlighted matrix nano Cr precipitates and a grain boundary (GB) Cr_2Nb precipitate. (b) SEM image of W-Cu sintered composite.

Acknowledgements

This work is part of the U.S. Japan FRONTIER Collaboration supported by the U.S. Department of Energy, Office of Fusion Energy Sciences and Ministry of Education, Culture, Sports, Science and Technology, Japan. Research is sponsored by the U.S. Department of Energy, Office of Fusion Energy Sciences, under contract DE-AC05-00OR22725 with UT-Battelle, LLC. The JRT acknowledges support from the U.S. Department of Energy, Office of Fusion Energy Sciences, under contract DE-SC0017899.

10.3 RECOIL SPECTRA IN W-Ni-Fe TUNGSTEN HEAVY ALLOYS—C. W. Trucks, G. Nandipati, W. Setyawan (Pacific Northwest National Laboratory)

OBJECTIVE

To generate database of recoil spectra at the front and back of ARIES-ACT2 divertor dome with W-Ni-Fe heavy alloys as a structural material. Two alloys with weight composition of 94.143W-4.1Ni-1.757Fe (denoted as W94) and 87W, 9.1Ni, 3.9Fe (W87) are considered.

SUMMARY

Recoil spectra have been calculated using SPECTRA-PKA code on the W phase and the Ni-Fe-W ductile phase of W94 and W87 alloys. Both alloys has a similar atomic composition in the ductile phase, namely 66 at. %Ni, 25 at. % Fe, 9 at. % W. These cases are considered separately, as transmutations and damage evolve differently in each part of the alloys. In addition, calculations are performed on pure Ni and Fe to compare the recoil spectra in the ductile phase from direct calculations on the ductile phase versus those from compositionally averaging the elemental calculations. Composition-averaged spectra tend to underestimate Ni recoils but overestimate Fe recoils, while the W recoils are similar. These spectra are needed for future damage accumulation and microstructure evolution modeling in these alloys.

PROGRESS AND STATUS

Tungsten Heavy Alloys (WHAs) are a promising candidate as a structural material for the divertor component of fusion reactors, boasting remarkable fracture toughness and improved durability compared to pure tungsten [1-4]. These WHAs are subject to intense neutron irradiation during operation that causes nuclear transmutation and atomic displacement damage. Molecular dynamics method is the state-of-the-arts technique to simulate atomic displacement cascades due to an energetic primary-knock-atom (PKA). The number of surviving defects (damage) depends on the PKA energy. To calculate the overall damage, the recoil spectrum of the PKAs due to these neutrons must be found.

The SPECTRA-PKA code is used to calculate the recoil spectra and dpa/s [5, 6]. Two data files are necessary to perform the calculation: the neutron flux and the nuclear reaction cross-section data. Our neutron fluxes are acquired from a neutronics simulation focused on the divertor dome of the US ARIES-ACT2 concept [7, 8], while our cross-section data is sourced from the TENDL-2015 library [9]. A manuscript reporting on the results of the neutronics simulations and activation analyses is being submitted to the journal of Nuclear Materials and Energy. The activation analyses show for use as a structural material in the ARIEST-ACT2 divertor for 10 years of operation, the Ni content in the WHAs should be limited to ~4.5 wt.% to satisfy the Class C low-level-waste (LLW) classification based on the NRC's specific activity limits for terrestrial waste disposal. If the Fetter's activity limits are employed, up to ~9.5 wt.% Ni may be used.

In the recoil spectra calculations, two WHAs with weight composition of 94.143W-4.1Ni-1.757Fe (denoted as W94) and 87W, 9.1Ni, 3.9Fe (W87) are of interest. The alloys satisfy the Class-C LLW based on NRC's and Fetter's limits, respectively. The calculations are performed on the iron, nickel, tungsten, and ductile phase, subject to fluxes found at the front and back of the ARIES-ACT2 divertor dome section that experiences a peak neutron wall loading of ~0.9 MW/m^2. Table 1 summarizes the total neutron flux at the front and back of the divertor dome for W94 and W87 and Figure 1 shows the neutron spectra. From Figure 1, the spectra found at the back of the divertor dome has slightly fewer neutron counts at energies above 10 keV and significantly greater counts below 10 keV compared to the flux at the front. Meanwhile, the shapes of the spectra between the two alloys are nearly identical. These trends indicate the energy shift in the neutron spectrum as it passes through the divertor, as higher energy neutrons undergo some moderation. This process is hardly affected by the change in alloy composition.

Table 1. Total neutron flux (in n/cm²s) at front and back of ARIES-ACT2 divertor dome made with W94 and W87 W-Ni-Fe heavy alloys

	front	back
W94	6.6465E+14	5.9585E+14
W87	6.5596E+14	5.9019E+14

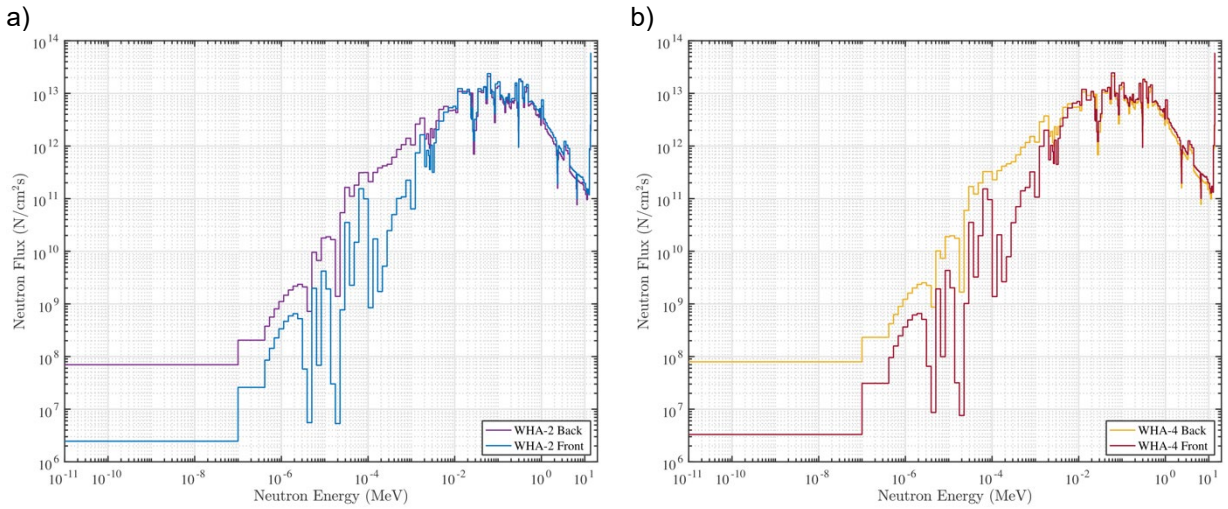

Figure 1. Neutron spectrum at front and back of divertor dome for a) W94 (WHA-2) and b) W87 (WHA-4).

Below is an example input file dpt_WHA-2_109.in, which is the case for the recoil spectra at the front of the divertor dome in the ductile phase of W94. On line 1, *flux_filename*="…" specifies the location of the flux file relative to the input file. Lines 3-5 set up the format for inputting the cross-section data. Line 5 specifies the purpose of each parameter given in lines 6-19, including the filename, the atomic percentage of the given isotope, the symbol and atomic number, and the atomic masses of the parent and daughter isotopes after a neutron absorption reaction. Subsequently, on line 24, *do_ngamma_estimate=.t.* enables the calculation of recoils from (n,γ) capture reactions, requiring the parent and daughter atomic masses. On line 20, *flux_norm_type=2* reads in the flux in units of n s^{-1} cm^{-2}. *do_mtd_sums=.t.* on line 22 allows SPECTRA-PKA to give summed results over different interaction types per species and *do_exclude_light_from_total=.t.* excludes light elements such as H and He from the total recoil spectra, useful for accurate damage calculations. *do_global_sums=.t.* on line 25 allows for the atomic percentages to be used in the calculations. *do_tdam=.t.* on line 26 is the setting that allows for the dpa to be calculated. *assumed_ed=44.5* on line 30 is the displacement threshold (E_d) in eV, which is taken as a weighted average of the 66 at. %Ni, 25 at. % Fe, 9 at. % W with E_d of 40, 40, and 90 eV respectively.

```
1   flux_filename="../../fluxes_WHA/WHA-2_109_Front.dat"
2   results_stub="dpt_WHA-2_109"
3   number_pka_files=14
4   num_columns=6
5   columns= pka_filename pka_ratios parent_ele parent_num ngamma_parent_mass ngamma_daughter_mass
6   "../../../pka/Ni058s.asc" 0.449308 Ni 58 57.935342 58.934346
7   "../../../pka/Ni060s.asc" 0.173072 Ni 60 59.930786 60.931056
8   "../../../pka/Ni061s.asc" 0.007523 Ni 61 60.931056 61.928345
9   "../../../pka/Ni062s.asc" 0.023988 Ni 62 61.928345 62.929669
10  "../../../pka/Ni064s.asc" 0.006109 Ni 64 63.927966 64.930084
11  "../../../pka/Fe054s.asc" 0.014613 Fe 54 53.939610 54.938293
12  "../../../pka/Fe056s.asc" 0.229385 Fe 56 55.934937 56.935394
13  "../../../pka/Fe057s.asc" 0.005298 Fe 57 56.935394 57.933275
```

```
14  "../../../pka/Fe058s.asc" 0.000705 Fe 58 57.933275 58.934875
15  "../../../pka/W180s.asc" 0.000108 W 180 179.946704 180.948197
16  "../../../pka/W182s.asc" 0.023850 W 182 181.948204 182.950223
17  "../../../pka/W183s.asc" 0.012879 W 183 182.950223 183.950931
18  "../../../pka/W184s.asc" 0.027576 W 184 183.950931 184.953419
19  "../../../pka/W186s.asc" 0.025587 W 186 185.954364 186.957160
20  flux_norm_type=2
21  pka_filetype=2
22  do_mtd_sums=.t.
23  do_exclude_light_from_total=.t.
24  do_ngamma_estimate=.t.
25  do_global_sums=.t.
26  do_tdam=.t.
27  flux_rescale_value=1.0
28  max_global_recoils=200
29  energies_once_perfile=.t.
30  assumed_ed=44.5
```

Figures 2-5 show the recoil spectra for Fe, Ni, W, and ductile phase at the front and back of divertor dome made with W94 and W87 alloys. The plotted spectra are differential spectra, i.e., spectrum per energy, given in PKAs/s/MeV. The shape of such plots is independent of the energy bins used.

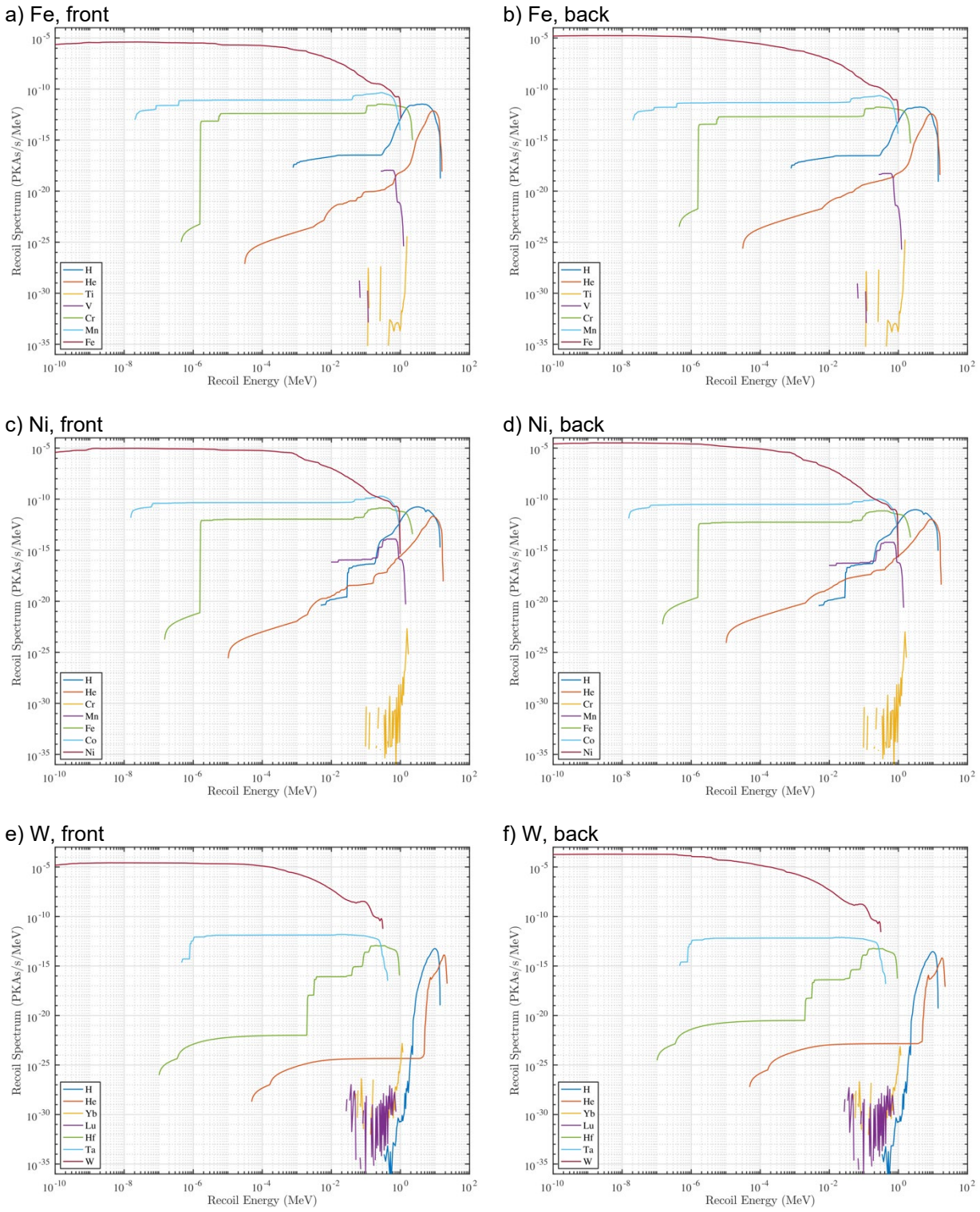

Figure 2. Recoil spectra in Fe, Ni, and W at the front and back of divertor dome made of W94 alloy.

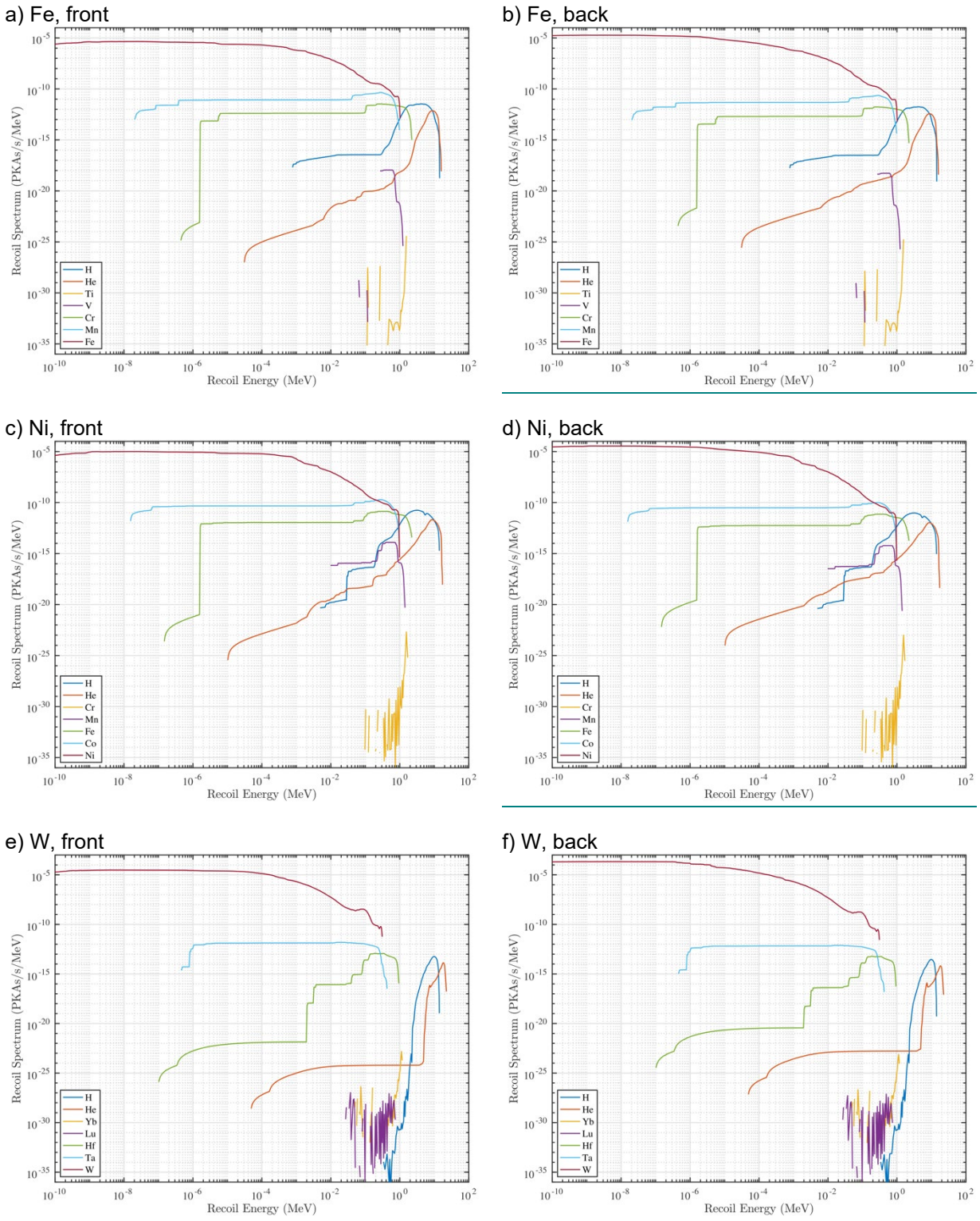

Figure 3. Recoil spectra in Fe, Ni, and W at the front and back of divertor dome made of W87 alloy.

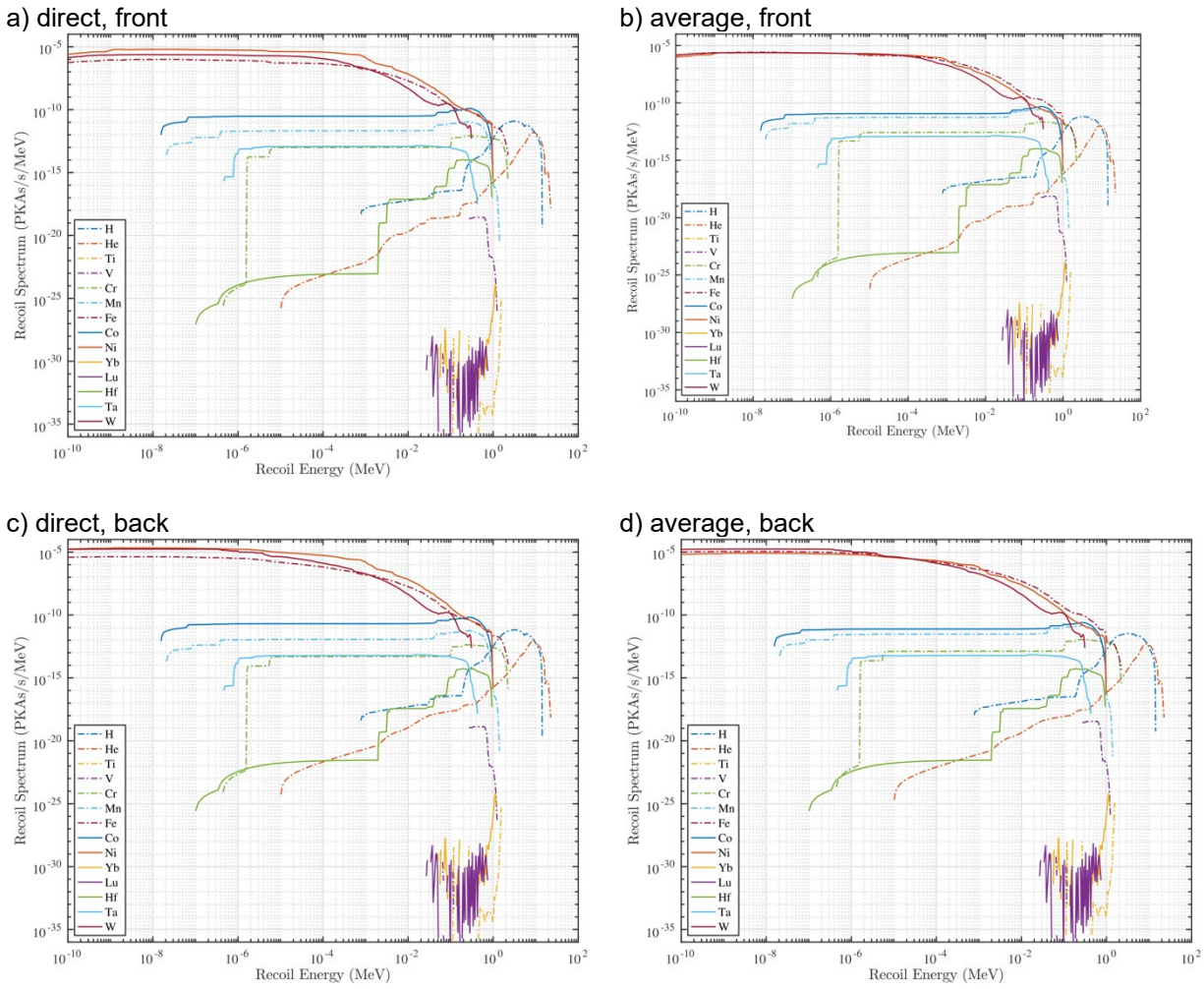

Figure 4. Recoil spectra in the ductile phase at the front and back of divertor dome made of W94 alloy. Data obtained from direct calculation with ductile phase (direct) are compared with data calculated as composition average of the elemental data (average).

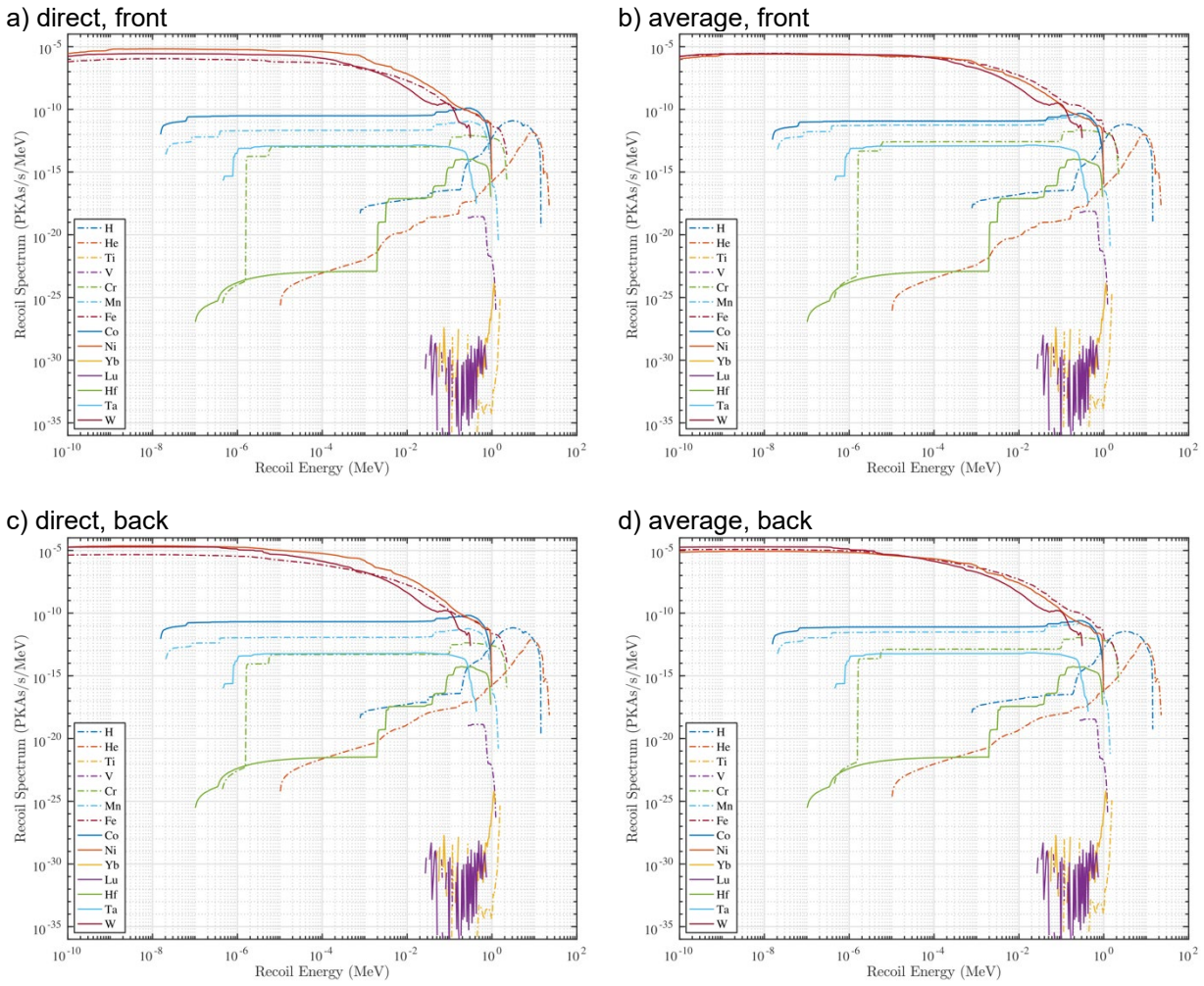

Figure 5. Recoil spectra in the ductile phase at the front and back of divertor dome made of W87 alloy. Data obtained from direct calculation with ductile phase (direct) are compared with data calculated as composition average of the elemental data (average).

The results show that the recoil spectra in both alloys are similar, due to the similarity in the neutron spectra. For the ductile phase, comparing the recoil spectra obtained from direct simulation versus from composition average of elemental data shows that taking the average tends to underestimate the Ni recoils and overestimate the Fe recoils. The W recoils seem to be approximated accurately, however this could simply be an artefact of the low atomic concentration or W in the ductile phase.

Table 2 summarizes the dpa level in Ni, Fe, W, and the ductile phase, over the course of 5 and 10 years of divertor operation assuming 13.5% down time. W94 exhibits a similar damage to W87, again due to the similarity in the neutron spectra. For 10 years of operation, the W phase will receive a damage dose of ~25 dpa (at front) and ~16 dpa (back), while the ductile phase receives ~78 dpa (front) and ~52 dpa (back). If one estimates the dpa in the ductile phase by averaging the dpa of Fe, Ni, and W, the estimated dpa will be about 8% overestimated.

Table 2. Dpa level in Fe, Ni, W, ductile phase, and composition average at 5 years (4.325 full power year) and 10 years (8.65 full power year) of divertor operation at the front and back of divertor dome made of W94 and W87 alloys. Composition average data is calculated by averaging elemental data based on the composition of the ductile phase of 66 at. % Ni, 25 at. % Fe, and 9 at. % W.

W94 Front:	Ni	Fe	W	ductile phase	average
dpa/s	3.5123E-07	2.8159E-07	9.1033E-08	2.8822E-07	3.1040E-07
5-year dpa	47.9	38.4	12.4	39.3	42.3
10-year dpa	95.8	76.8	24.8	78.6	84.7
W94 Back:					
dpa/s	2.3696E-07	1.8424E-07	5.7800E-08	1.9250E-07	2.0766E-07
5-year dpa	32.3	25.1	7.88	26.3	28.3
10-year dpa	64.6	50.3	15.8	52.5	56.6
W87 Front:					
dpa/s	3.4820E-07	2.8017E-07	9.0611E-08	2.8602E-07	3.0801E-07
5-year dpa	47.5	38.2	12.4	39.0	42.0
10-year dpa	95.0	76.4	24.7	78.0	84.0
W87 Back					
dpa/s	2.3559E-07	1.8402E-07	5.7733E-08	1.9163E-07	2.0669E-07
5-year dpa	32.1	25.1	7.87	26.1	28.2
10-year dpa	64.3	50.2	15.7	52.3	56.4

Acknowledgement

This research has been supported by the U.S. Department of Energy, Office of Science, Office of Fusion Energy Sciences and performed at the Pacific Northwest National Laboratory under contract number DE-AC05-76RL01830 and by the U.S. Department of Energy, Science Undergraduate Laboratory Internship (SULI) program (PNNL project #45260).

References

[1.] C.H. Henager, W. Setyawan, T.J. Roosendaal, N.R. Overman, B.A. Borlaug, E.L. Stevens, K.B. Wagner, R.J. Kurtz, G.R. Odette, B.N. Nguyen, K. Cunningham, Ductile-Phase Toughened Tungsten for Plasma-Facing Materials in Fusion Reactors, International Journal of Powder Metallurgy, 53 (2017) 53-69.

[2.] M.E. Alam, G.R. Odette, On the remarkable fracture toughness of 90 to 97W-NiFe alloys revealing powerful new ductile phase toughening mechanisms, Acta Materialia, 186 (2020) 324-340.

[3.] J.V. Haag, D.J. Edwards, C.H. Henager, W. Setyawan, J. Wang, M. Murayama, Characterization of ductile phase toughening mechanisms in a hot-rolled tungsten heavy alloy, Acta Materialia, 204 (2021) 116523.

[4.] M.E. Alam, J. Wang, C.H. Henager, W. Setyawan, G.R. Odette, The effect of hot rolling on the strength and fracture toughness of 90W–7Ni3Fe tungsten heavy metal alloys, Materials Science and Engineering: A, DOI https://doi.org/10.1016/j.msea.2021.141738(2021) 141738.
[5.] M.R. Gilbert, J. Marian, J.C. Sublet, Energy spectra of primary knock-on atoms under neutron irradiation, Journal of Nuclear Materials, 467 (2015) 121-134.
[6.] M.R. Gilbert, J.C. Sublet, Differential dpa calculations with SPECTRA-PKA, Journal of Nuclear Materials, 504 (2018) 101-108.
[7.] L. El-Guebaly, L. Mynsberge, A. Davis, C. D'Angelo, A. Rowcliffe, B. Pint, Design and Evaluation of Nuclear System for ARIES-ACT2 Power Plant with DCLL Blanket, Fusion Science and Technology, 72 (2017) 17-40.
[8.] The ARIES Project, http://aries.ucsd.edu/ARIES/.
[9.] TENDL-2015 nuclear data library, https://fispact.ukaea.uk/nuclear_data/PKA/TENDL2015data-n-pka.tar.bz2.

10.4 MINIATURE MECHANICAL TEST DEVELOPMENT FOR TUNGSTEN-BASED MATERIALS—L. M. Garrison, N. C. Reid, J. R. Echols (Oak Ridge National Laboratory)

OBJECTIVE

The aim of this work is to develop miniature mechanical test methods that can be used to evaluate neutron-irradiated tungsten and tungsten composite samples in LAMDA.

SUMMARY

Three-point bending, and shear punch will be used to observe failure modes in tungsten-based samples due to flexural and shear stresses, respectively. Because of simplicity and economy, they are fitting tests to perform on samples of TEM disk geometry that have been irradiated in HFIR. Three-point bending is conventionally performed on beams of rectangular cross sections and has been adapted to be performed on disk specimens at the plane of symmetry in the center of the sample. A fixture has been modelled and procured for testing of tungsten materials in LAMDA.

PROGRESS AND STATUS

The mechanical properties of fusion materials and joints need to be determined using a disk geometry. Many varieties of materials will be neutron irradiated in the FRONTIER US-Japan collaboration as 3 mm diameter disk specimens. A custom three-point bending fixture was designed to examine fracture and ductility of tungsten alloys and composites for fusion. Shear punch has also been explored as a technique to determine the shear yield and strength of small volumes of material. Both techniques are desired for determining the mechanical properties of neutron-irradiated disk specimens that are 3 mm in diameter, which is the typical size for transmission electron microscopy (TEM) disks.

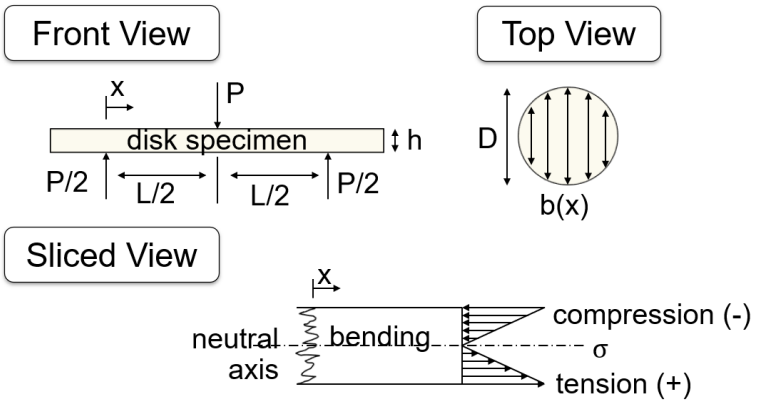

Figure 1. Three-point bend diagram in two dimensions showing the normal stresses that occur in the specimen due to the applied bending moment. The region of interest is at the plane of symmetry and the bottom surface, giving this technique the advantage of determining the tension stress that is highest at the surface for specimens with modified surfaces by either coatings, heat flux, or irradiations by ions.

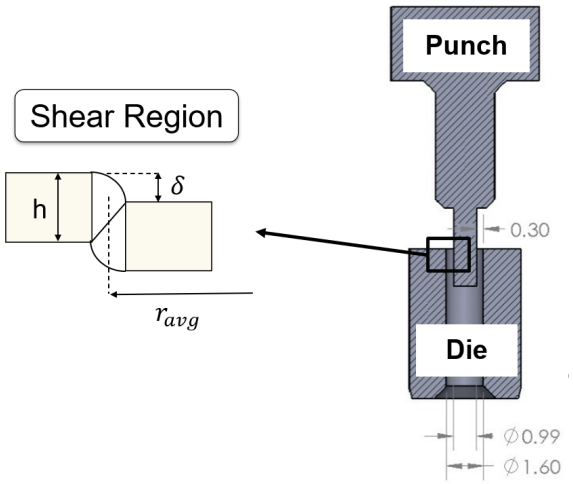

Figure 2. Shear punch diagram in two dimensions showing the shear stresses in the specimen due to the region of material sliding as the punch is driven into the die. This technique has the advantage of determining shear deformation mechanisms in the cylindrical plane of material surrounding the punch, and tensile information of the bulk material can be obtained through analysis using tensile-shear correlations.

These tests are complementary in that the fixtures have parts that are shared between the two and the tests apply stress fields of different configurations. For three-point bend (Figure 1), the load (P) is applied at the center of the specimen of diameter D and thickness h, which is supported by a span of 2 mm (L). The normal stress σ due to the applied bending moment is a function of location at the disk with changing width b(x), where x is the distance from the left support. For shear punch (Figure 2), the load is applied to the punch and shear deformation occurs in the gap between punch and die at radius r_{avg}. Normalized displacement (δ/h) is used to compare specimens of different thickness (h).

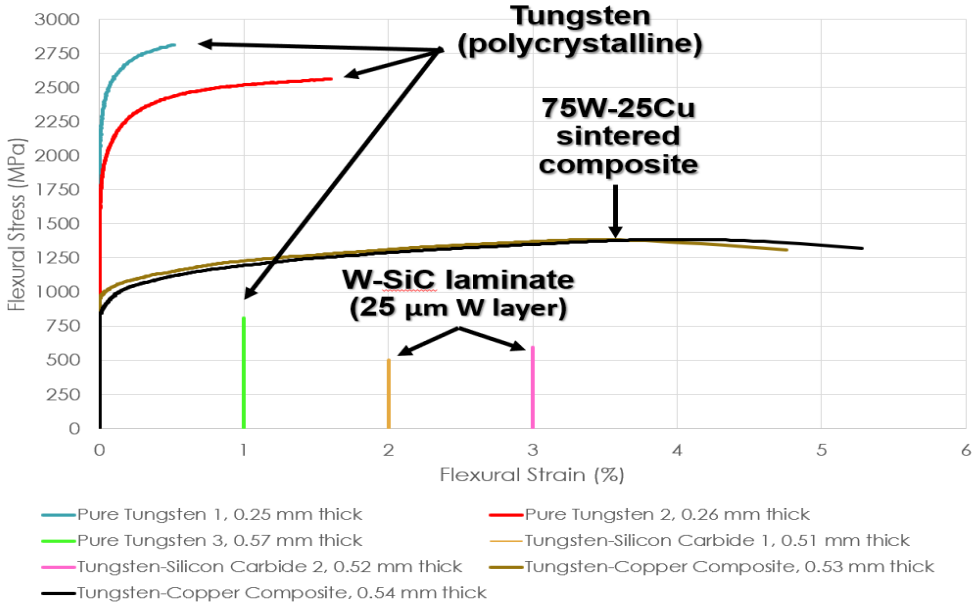

Figure 3. The bend test results showing plastic deformation of the 3 mm disks. Specimens were ½ mm thick except for polycrystalline tungsten (PC W) that was machined to a thickness of ¼ mm. Specimens were bent until fracture and the elastic region was removed. Only the ¼ mm thick PC W and tungsten-copper (W Cu) showed room temperature ductility. Tungsten-silicon carbide (W-SiC) fractured in the elastic region for the thicknesses tested.

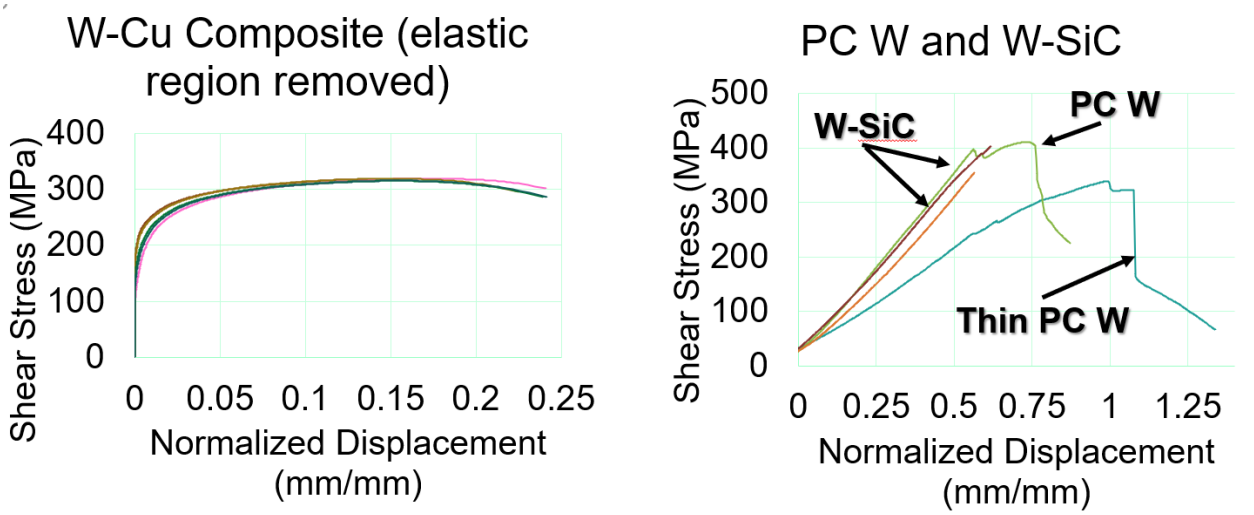

Figure 4. The shear punch results with tungsten-copper (W Cu) shown with the elastic region removed and other specimens with the elastic region due to having room temperature brittleness. Five shear punch tests were performed on W Cu tensile tabs. The other tests were performed on ½ mm thick tungsten-silicon carbide (W SiC) and polycrystalline (PC W) disks and on a ¼ mm thick PC W disk.

Specimens of polycrystalline tungsten (PC W), silicon carbide with a 25 μm thick tungsten foil layer (W SiC), and 75 wt% tungsten-25 wt% copper sintered composite (W Cu) were tested by three-point bending and shear punch using the MTS Insight Electromechanical Test Frame in LAMDA. The fracture surfaces were examined in the TESCAN MIRA3 GMH scanning electron microscope (SEM) in LAMDA. The load was measured by a 1 kN load cell from which the flexural and shear stress was calculated. The flexural strain and normalized displacement were calculated from the displacement measured by the crosshead of the MTS frame. Figure 3 shows the stress-strain curves of three-point bending and Figure 4 shows the stress-displacement curves of shear punch. Only the ¼ mm thick PC W and W Cu showed room temperature ductility in bend testing and only W Cu in shear punch testing. All other specimens showed highly brittle fracture at room temperature.

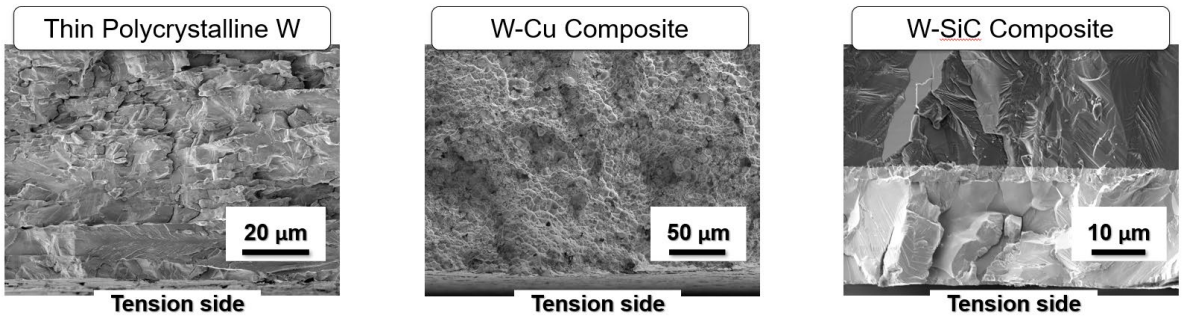

Figure 5. Fracture surfaces at the tension (bottom) side of the specimen for three-point bend.

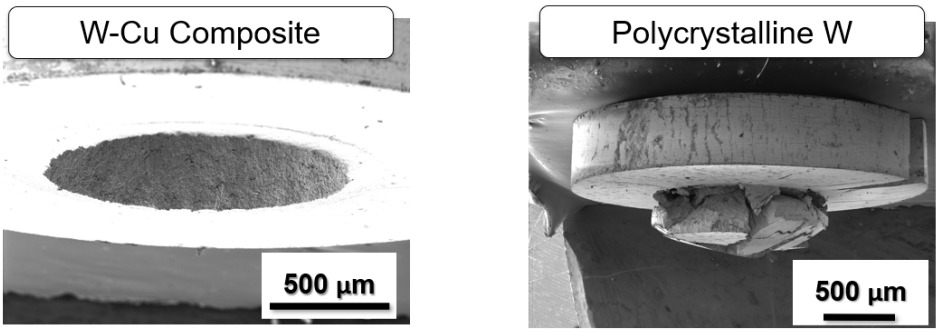

Figure 6. Fracture surfaces at the bottom side of the specimen for shear punch. The W Cu micrograph shows the inner fracture surface that was subjected to shear forces, which was possible to see in this micrograph due to the ductility of the Cu matrix and the center of the specimen being punched cleanly away. The PC W micrograph was only able to see the fractured center of the specimen, where the center of the specimen fractured before it could be punched out.

The SEM micrographs of the fracture surfaces are shown for three-point bend (Figure 5) and shear punch (Figure 6). For the bend test, the ¼ mm thick PC W and W SiC show signs of brittle cleavage, whereas the W Cu shows ductile knife edges of the Cu matrix around the brittle W particles. For the shear test, the W Cu hole was punched out cleanly with the ductility of the Cu matrix, whereas the PC W absorbed the energy of the punch in brittle cracks along weak grain boundaries in the interior of the punch.

Future Work

Three-point bend testing of thicknesses of tungsten between 0.125 mm and 1.000 mm is undergoing to determine the role effects of shear forces in bending contribute to the load-displacement curve. Bend tests will be performed on tungsten specimens of constant width (hence, cross-sectional area) for the role the curvature of the disk edge has on the stress state of the specimen. The flexural strength of tungsten with a width of 3 mm across the span will be compared to a specimen with a width of 12.7 mm while maintaining the same span-to-thickness ratio across both tests. Disk specimens of polycrystalline tungsten and single crystal tungsten with orientation in the (110) plane at the disk surface that were irradiated in the PHENIX campaign will be tested in LAMDA for their flexural strength and ductility by three-point bending.

10.5 HFIR IRRADIATION EXPERIMENTS—C. On, J. W. Geringer, J. L. McDuffee (Oak Ridge National Laboratory)

OBJECTIVE

The goal of this report is to describe the progress of the neutron irradiation experiments that were performed in the High Flux Isotope Reactor (HFIR) and the operating status.

SUMMARY

During the six-month period starting from January 1st to June 30th, 2021 a total of twenty-four rabbit capsules continued their irradiation. There were seven new capsules inserted into HFIR, while seventeen capsules were removed. The cycles 490 through 492 were completed during this period, but cycle 490 was split into three (490A, 490B, and 490C) due to a reactor scrams.

PROGRESS AND STATUS

Neutron irradiation experiments were performed in support of the research and development of fusion reactor materials using various materials irradiation facilities in the High Flux Isotope Reactor (HFIR). The reactor operating history for the period from January 1-June 30, 2021 is detailed in Table 1.

Table 1. HFIR operating record for the semi-annual FY2021

Cycle Number	Cycle End Date	Power (MWD)
490*	March 27	2107.27
491	May 8	2163.95
492	June 20	2165.66

*Cycle was in three parts, due to reactor scrams. Cycle 490A received 6.90 MWD, 490B received 22.33 MWD, while cycle 490C received 2107.27 MWD.

All the fusion materials program irradiation experiments performed during this period (FY2021) used the nominally two-inch rabbit capsules, with no full-length target rod nor instrumented reflector position capsules within that period. Twenty-four target zone rabbit capsules remain in the reactor to complete the scheduled irradiations. Table 2 lists the new capsules that were loaded into HFIR in cycle 490, and Table 3 lists the capsules that were removed from HFIR during cycles 490, 491, or 492. The capsules listed in Table 4 were inserted either during or before FY2021 and will continue in FY2021 and beyond. Tables 2 through 4 give condensed information on the material, specimen type, temperature, fluence, and period of irradiation.

Table 2. New capsules starting irradiation in cycle 490

Experiment Designation	Primary Materials	Specimen Types	Irradiation Temperature (°C)	Max Exposure (dpa)	Number of Reactor Cycles	HFIR Cycles Start – End
VNH1	W, Graphite, SiC, V	D6	400	0.1	31.5 hrs	490 - 490
VNH2	W, Graphite, SiC, V	D6	400	0.02	6.24 hrs	490 - 490
VH01	W, Graphite, SiC, V	D6	400	0.1	31.5 hrs	490 - 490
VH02	W, Graphite, SiC, V	D6	400	0.02	6.24 hrs	490 - 490
FH51	F82H-IEA, F82H-BA12	Tensile	300	5	3	490 - 492
FH61	F82H-IEA, F82H-BA12	Bend bars	300	5	4	490 - 493
FH62	F82H-IEA, F82H-BA12	Bend Bars	300	5	4	490 - 493

Table 3. The rabbit capsules removed from HFIR during cycles 490, 491, or 492

Experiment Designation	Primary Materials	Specimen Types	Irradiation Temperature (°C)	Max Exposure (dpa)	Number of Reactor Cycles	HFIR Cycles Start – End
VNH1	W, Graphite, SiC, V	D6	400	0.1	31.5 hrs	490 - 490
VNH2	W, Graphite, SiC, V	D6	400	0.02	6.24 hrs	490 - 490
VH01	W, Graphite, SiC, V	D6	400	0.1	31.5 hrs	490 - 490
VH02	W, Graphite, SiC, V	D6	400	0.02	6.24 hrs	490 - 490
ES01	EUROFER 97	Tensile/MPC*	220	20	12	479 - 491
ES03	EUROFER 97	Tensile/MPC*	275	20	12	479 - 491
ES04	EUROFER 97	Tensile/MPC*	300	20	12	479 - 491
ES05	EUROFER 97	Tensile/MPC*	325	20	12	479 - 491
ES06	EUROFER 97	Tensile/MPC*	350	20	12	479 - 491
ES07	EUROFER 97	Tensile/MPC*	375	20	12	479 - 491
ES02	EUROFER 97	Tensile/MPC*	275	20	12	480 - 492
ES11	EUROFER 97	Bend bars	220	20	12	479 - 492
ES12	EUROFER 97	Bend bars	240	20	12	479 - 492
ES13	EUROFER 97	Bend bars	275	20	12	479 - 492
ES14	EUROFER 97	Bend bars	300	20	12	479 - 492
FH51	F82H-IEA, F82H-BA12	Tensile	300	5	3	490 - 492
JCR11-07	SiC/SiC	Mini bend bars	950	100	47	444 - 492

Table 4. The HFIR fusion materials program rabbit capsules to continue irradiation in FY2021

Experiment Designation	Primary Materials	Specimen Types	Irradiation Temperature (°C)	Max Exposure (dpa)	Number of Reactor Cycles	HFIR Cycles Start – End
FMP07	F82H	Tensile	300	20	11	487 - 497
FMP08	F82H	Tensile	300	80	45	487 - 531
FMP11	F82H	Tensile	385	20	11	488 - 498
FMP12	F82H	Tensile	385	80	45	488 - 532
FMP14	F82H	Tensile	525	20	11	484 - 494
FMP16	F82H	Tensile/MPC*	650	20	11	484 - 494
FMP17	F82H	Tensile/MPC*	650	80	45	484 - 528
FMP22	F82H	Bend Bars	300	20	11	488 - 498
FMP23	F82H	Bend Bars	300	80	45	488 - 532
F13B4	FeCrAlY Steel	Tensile	300	50	29	451 - 497
JCR11-03	SiC/SiC	Mini bend bars	950	200	100	487 - 586
JCR11-05	SiC/SiC	Mini bend bars	950	200	115	444 - 568
JCR11-08	SiC/SiC	Mini bend bars	950	200	115	444 - 560
JCR11-11	SiC/SiC	Mini bend bars	950	100	55	448 - 524
SCF4	SiC/SiC	Miniature flexure bar	250	100	90	457 - 547
SCF5	SiC/SiC	Miniature flexure bar	250	200	45	457 - 511
SCF8	SiC/SiC	Miniature flexure bar	600	100	45	457 - 502
SCF9	SiC/SiC	Miniature flexure bar	600	200	90	457 - 548
SCF11	SiC/SiC	Miniature flexure bar	950	100	57	458 - 517
ES15**	EUROFER 97	Bend bars	325	20	12	479 - 494
ES16**	EUROFER 97	Bend bars	350	20	12	479 - 494
ES17**	EUROFER 97	Bend bars	375	20	12	479 - 494
FH61	F82H-IEA, F82H-BA12	Bend bars	300	5	4	490 - 493
FH62	F82H-IEA, F82H-BA12	Bend Bars	300	5	4	490 - 493

*MPC= Multi-Purpose Coupon

**ES15, ES16, and ES17= These capsules were removed at the end of cycle 483 and put back in cycle 487. The capsules missed 3 cycles.